Abstract of "Biomedical Spectroscopy in Clinical Applications and Implications of Liquid Crystal Filter Technologies" by John W. McMurdy, Ph.D., Brown University, May, 2009.

This dissertation discusses two related clinical applications of visible regime diffuse reflectance spectroscopy as well as two new configurations of liquid crystal microspectrometer suitable in these applications. Total hemoglobin concentration can be determined, and thus anemia diagnosed, using diffuse reflectance signals from the inner lining of the eyelid, the palpebral conjunctiva. Alternative technologies for anemia detection are explored, a theoretical model for light diffusion through the conjunctiva is presented, and predictive models are established relating spectral signatures to hemoglobin concentration. Two separate clinical trials were conducted showing accuracy of hemoglobin determination with respect to invasive determination of 5% and 8% of mean hemoglobin concentration, respectively. Local hemoglobin concentration can also be determined *in vivo* at individual vessels using a single fiber which is directly applicable in endoscopic and laparoscopic surgery. Clinical trials showed signal differentiation of different hemoglobin levels in laparoscopic cases when pressing the single fiber against an individual vessel, and donor/recipient differentiation in fetal endoscopy cases of twin to twin transfusion syndrome. Liquid crystal technologies can be used to create integrated chip-scale microspectrometers. In one configuration, analog tunable ferroelectric liquid crystals are applied to create a tunable filter spectrometer with resolution from 15-30 nm. In a second configuration, stressed liquid crystal polymer composites are used to create large phase modulators, subsequently applied as single panel Fourier transform spectrometers. Proof of concept studies show a 100 μm stressed liquid crystal polymer in double pass mode is capable of 60 nm resolving power.

Biomedical Spectroscopy in Clinical Applications and Implications of Liquid Crystal Filter Technologies

by

John W. McMurdy

B.S., University of Rochester, 2002

M.S., University of Rochester, 2003

Submitted in partial fulfillment of the requirements

for the Degree of Doctor of Philosophy in the

Department of Engineering at Brown University

Providence, Rhode Island

May, 2009

This dissertation by John W. McMurdy is accepted in its present form by

the Department of Engineering as satisfying the dissertation requirement

for the degree of Doctor of Philosophy

Date 10/19/08

Gregory Crawford, Director

Recommended to the Graduate Council

Date 9/24/2008

Gregory Jay, Reader

Date 9/27/08

Selim Suner, Reader

Date 9/24/08

Rashid Zia, Reader

Date 10/08/08

Dick Broer, External Reader

Approved by the Graduate Council

Date _____

Sheila Bonde

Dean of the Graduate School

Vita

John W. McMurdy was born in Latrobe, Pennsylvania on August 19^{th}, 1980. After completing high school in Indiana, PA, he attended the University of Rochester in Rochester, NY under support of the Rush Rhees Scholarship. John received his B.S. in May 2002 and M.S. in May 2003, both in optics. While at Rochester, John worked under Professor Andrew Berger exploring biomedical applications of non-resonant Raman spectroscopy for quantifying biofluids and wrote an M.S. essay entitled "NIR Diffuse Optical Methods for Functional Brain Monitoring." Following completion of his masters, John spent the following year working as a field service engineer for Digilab, LLC (now a division of Varian).

John began his doctoral studies in Fall 2004 under the supervision of Professor Gregory Crawford at the Display and Photonics Laboratory. In this duration, he was an author or co-author on 11 articles, 3 book contributions, 2 published abstracts, and 5 conference proceedings while presenting research in the Netherlands, India, San Jose, San Diego, Dayton, Cleveland, Keystone, and Boston. John spent the fall of 2007 working as a Mirzayan Science Policy fellow at the National Academy of Science and has worked over the past 2 years with Corum Medical, a company formed around key elements of his thesis and recently awarded both an NIH and NSF SBIR Phase I grant.

Over the course of four years at Brown, John's research was supported by a University Fellowship, the NASA GSRP fellowship, and several SPIE educational scholarships. He has also recieved an NCIIA Advanced Entrepreneurship Team grant, a runner up award at the 2006 NCIIA National BMEIdea competition, and a citation from the Rhode Island Lt. Governor Charles Fogerty in recognition of efforts to commercialize anemia technologies.

Publications

PEER REVIEWED PUBLICATIONS

1. McMurdy, J.W., Shelton, L.J. and Crawford, G.P., "Fourier Transform Spectroscopy using Stressed Liquid Crystal", *Optics Letters*, 2008, submitted.

2. McMurdy, J.W., Reichner, J.S., Mathews, Z., Markey, M., Intwala, S. and Crawford, G.P., "Diffuse Reflectance Spectroscopy as a Quantitative Metric of Vascular Leak", *Journal of Pharmacological and Toxicological Methods*, 2008, submitted.

3. McMurdy, J.W. and Crawford, G.P., "Image Processing and Deconvolution in Liquid Crystal Based Microspectrometers", *Journal of Applied Physics*, 2008, submitted.

4. McMurdy, J.W., Jay, G.D., Suner, S. and Crawford, G.P., "Noninvasive Optical, Electrical, and Acoustic Methods of Total Hemoglobin Determination", *Clinical Chemistry*, 2008, **54**(2): 1-9.

5. Suner, S., McMurdy, J.W., Jay, G.D. and Crawford, G.P., "Digital Imaging, spectroscopy, and liquid crystals in a hand-held, non-invasive device to determine hemoglobin concentration", *Journal of Society for Information Display*, 2007, **15**: 399-407.

6. Suner, S., Crawford, G.P., McMurdy, J.W. and Jay, G.D., "Noninvasive determination of hemoglobin by digital imaging of the palpebral conjunctiva", *Journal of Emergency Medicine*, 2007, **33**(2): 105-111.

7. McMurdy, J.W., Eakin, J.N. and Crawford, G.P., "Microspectrometer based on vertically aligned deformed helix ferroelectric liquid crystal", *Molecular Crystals and Liquid Crystals*, 2007, **476**: 61-76.

8. McMurdy, J.W., Jay, G.D., Suner, S., Trespalacios, F.M. and Crawford, G.P., "Diffuse reflectance spectra of the palpebral conjunctiva and its utility as a noninvasive indicator of total hemoglobin", *Journal of Biomedical Optics*, 2006, **11**(1): 014019.

9. McMurdy, J.W., Jay, G.D. and Crawford, G.P., "Monolithic microspectrometer using tunable ferroelectric liquid crystals", *Applied Physics Letters*, 2006, **89**: 081105.

10. McMurdy, J.W., Eakin, J. and Crawford, G.P., "Vertically Aligned Deformed Helix Ferroelectric Liquid Crystal Configuration for Reflective Display Device", *SID Symposium Digest of Technical Papers*, 2006, **37**.

11. McMurdy, J.W., Crawford, G.P., Jay, G.D. and Suner, S., "A novel medical diagnostic tool for non-invasively measuring hemoglobin utilizing switchable H-PDLC display technology", *SID Symposium Digest of Technical Papers*, 2005, **36**: 364-367.

12. McMurdy, J.W. and Berger, A.J., "Raman spectroscopy-based creatinine measurement in urine samples from a multipatient population", *Applied Spectroscopy*, 2003, **57**(5): 522-525.

BOOK CONTRIBUTIONS

1. Woltman, S.J., McMurdy, J.W., Crawford, G.P. and Gorkhali, S., "Biomimicking with Liquid Crystals", in *Liquid Crystals: Frontiers in Biomedical Applications*, Singapore: World Scientific Publishing Group, 2007.

2. McMurdy, J.W., Crawford, G.P. and Suner, S., "Liquid Crystals in Spectroscopy, Microscopy, and Hyperspectral Imaging", in *Liquid Crystals: Frontiers in Biomedical Applications*, Singapore: World Scientific Publishing Group, 2007.

3. Biga, F.Y., Luks, F.I., McMurdy, J.W. and Crawford, G.P., "Medical Displays", in *Liquid*

Crystals: Frontiers in Biomedical Applications, Singapore: World Scientific Publishing Group, 2007.

ABSTRACTS

1. Racht, J., McMurdy, J.W., Mathews, Z., Hughes, A., Crawford, G.P., Jay, G.D. and Suner, S., "Noninvasive Measurement of Hemoglobin Concentration in Emergency Department Patients using Fiber Optic Spectral Analysis of the Tarsal Plate", *Academic Emergency Medicine*, 2007, **14-S1**: S40-41.

2. Duffy, S.J., McMurdy, J.W., Kollet, M., Jay, G.D. and Crawford, G.P., "Using spectroscopy to assess the ages of bruises", *Academic Emergency Medicine*, 2007, **14-S1**: S43.

CONFERENCE PROCEEDINGS

1. McMurdy, J.W., Duffy, S.J. and Crawford, G.P., "Monitoring bruise age using visible diffuse reflectance spectroscopy", *Proceedings of SPIE*, 2007, **6434**: 643426.

2. Jay, G.D., Racht, J., McMurdy, J.W., Mathews, Z., Hughes, A., Suner, S. and Crawford, G.P., "Point-of-Care Noninvasive Hemoglobin Determination using fiber optic reflectance spectroscopy", *Proceedings of IEEE: Engineering in Medicine and Biology Society*, 2007, **1**: 2932-2935.

3. McMurdy, J.W., Jay, G.D., Suner, S. and Crawford, G.P., "Anemia detection utilizing diffuse reflectance of the palpebral conjunctiva and tunable liquid crystal filter technology", *Proceedings of SPIE*, 2006, **6177**: 61771-61710.

4. McMurdy, J.W., Duffy, S.J., Mathews, Z. and Crawford, G.P., "Using display configurations in spectro-photometric bruise aging applications", *International Display Research Conference Proceedings*, 2006, **26**: 387-391.

5. McMurdy, J.W., Crawford, G.P. and Jay, G.D., "Monolithic microspectrometers for routine and rapid display performance characterization", *International Display Research Conference Proceedings*, 2006, **26**: 383-387.

Acknowledgments

I first want to thank Prof. Gregory Crawford a wonderful experience in Providence. So many of the opportunities I have been given in working with a start-up company, traveling to foreign countries, networking with business leaders around the state, and pursuing opportunities outside of Brown are directly related to both his open mindedness and concern for my career, and I can't express my gratitude enough.

I also wish to thank many collaborators, researchers and friends for their great help during the past 4 years of research that has taken me to every square inch of Rhode Island Hospital. This includes Gregory Jay, Selim Suner, Francois Luks, Jonathan Reichner, Susan Duffy, Flor Trespalacios, Ashley Hughes, Zara Mathews, Sean Curran, Sunny Intwala, Mary Markey, Justin Racht, and numerous other highly tolerant people at both the RIH Emergency Department and Hasbro Childrens Hospital.

I want to acknowledge primary financial support from the NASA Graduate Student Researcher Program (NNG05GL57H) for three years of research as well as the SPIE Educational Scholarship Program, the RI Science and Technology Advisory Council (STAC) Grant, and the National Collegiate Innovators and Inventors Alliance (NCIIA) for additional financial support.

I am gracious to have worked with a great group of people in the Display Lab in the past years, especially those who i have worked closest with in Suraj, Matt, Jim, Scott, Leslie, Fred, and Maureen, all who have assisted in part with this thesis. Thanks for being friends, keeping life interesting, always having an open ear, and putting up with the frustrating times in the lab. A second round of gratitude goes out the rest of my other great friends from Brown and Rochester,

you know who you are and you know you are much appreciated! Special thanks to you, Sarah, for an amazing last couple months and I look forward to many more.

Lastly, I want to thank my mother, father, and grandmother for every imaginable kind of support over all 28 of my years. Its hard to imagine where life would be without your guidance and I know I can't thank you enough, but at least I can say it one more time here.

Contents

List of Tables

List of Figures

Chapter 1

Convergence of Liquid Crystals and Optical Microspectroscopy

1.1 Introduction: Thesis

With the current state of the art in biomedical spectroscopy in mind, the field has room to grow in two mutually *inclusive* directions: (1) the advancement of device performance through improved component performance, device assembly, device machining, or new materials and (2) the applications of both new and existing technologies technologies in new arenas of medicine, including both therapeutics and diagnostics. The mutually inclusive nature of these two pathways lies in the enabling nature of new device configurations to broaden impact of this technology in areas of biomedicine where spectroscopic diagnostics may have been previously limited. This chapter discusses research in *both* of these directions; the creation of new spectrometer technologies and investigation into new applications of biomedical spectroscopy.

As is likely the case in most spectrometer technologies, the drive for innovation is a direct result of the needs of a specific application. Our application and the core focus of this thesis is the development of a new method to quantify total hemoglobin and thus identify anemia without the need of a blood draw. This technique and its feasibility in medical practice, discussed in great

depth later, benefits significantly from durable, miniaturized visible regime spectrometers that can be manufactured at low cost. Chapter 1 discusses microspectrometer technologies investigated by other groups and their suitability as practical devices. Chapter 2 and Chapter 3 present two alternative spectrometer technologies investigated, one based on single panel tunable Bragg filters and one based on a new type of tunable LC retarder, both with distinct advantages over many of the devices previously studies. These devices may enable more straightforward and inexpensive fabrication of single chip microspectrometers. Chapter 4 discusses in great detail the need for a device to monitor hemoglobin and detect anemia, alternative technologies to approach this problem, theory and modeling of our approach to optically monitoring blood hemoglobin from the palpebral conjunctiva, and experimental results from separate clinical trials. Chapter 5 discusses an extension application of the conjunctiva hemoglobin study; using diffuse reflectance spectroscopy invasively as a diagnostic tool in endoscopic laparoscopy and fetal surgery. Although this application benefits less from microspectroscopy technologies, it leverages on the theory and experimental work from Chapter 4. The concluding chapter puts the results of this two phase research project in context and discusses future directions of these technologies. Appendix A discusses a third new application for biomedical diffuse reflectance spectroscopy in quantifying the degree of vascular leak; important for experimental immunochemistry.

1.2 Introduction: Microspectroscopy

Numerous examples exist of technological advancements in devices and device manufacturing that have subsequently allowed the application of spectroscopy to new areas of medicine. One such example is the complementary metal oxide semiconductor (CMOS) detector, an imaging detector with low-power consumption and the ability to incorporate integrated circuits into the detection elements of a single chip. CMOS detectors have enabled spectroscopic imaging in compact and portable devices, so compact that, in some cases, these devices have been integrated into pill-sized cameras for invasive imaging of the gastrointestinal tract using sensors small enough to be swallowed [1]. Vertical cavity surface emitting lasers (VCSELs) are another example of devices which

have enabled new applications in absorption spectroscopy, primarily as a result of their inexpensive fabrication costs (resulting from on-wafer device testing and two-dimensional array fabrication), low threshold currents and potential wavelength tunabilities [2].

Liquid crystal materials and devices act can as similar bridges, resulting in new applications for a variety of spectroscopic techniques in the biotechnology sphere. Through either device enhancement or device component replacement with a liquid crystal based material, spectroscopic techniques can benefit through improved performance, a reduction in device size, a reduction of device cost, or a combination of all three. Compact and inexpensive spectroscopic and spectral imaging devices have potential implications as point-of-care diagnostic tools, microchip *in vivo* sensors, rapid and real-time process control testing devices, as well as in numerous applications not yet considered. Here, three different classes of microspectrometers are introduced; (1) micrograting dispersive devices, (2) compact phase modulators for Fourier transform spectroscopy (both active phase modulators and passive wedge plates), and (3) tunable filter technologies (acousto-optic, liquid crystal, Fabry-Pérot). There exists several figures of merit to consider when evaluating the performance of a microspectrometer in the scope of potential commercial acceptance. This criteria can include the optical resolution, light gathering capability (*étendue*), optical throughput (product of resolution and *étendue*), data collection rate, quality (Q) factor (in tunable filter technologies), operating wavelength range, device dimensions, ease of fabrication, cost, operating voltages, and readout electronics. Technologies discussed here present a combination of positives and negatives in each of these facets, as a whole limiting the adoption of these devices in contemporary technologies and, for the most part, propagating the use of benchtop devices costing > \$1000. This chapter discusses aspects and current methods of microspectrometer fabrication, followed by a brief overview of liquid crystal physics relevant to this field, and concluding with a discussion of current attempts to construct liquid crystal based spectrometers.

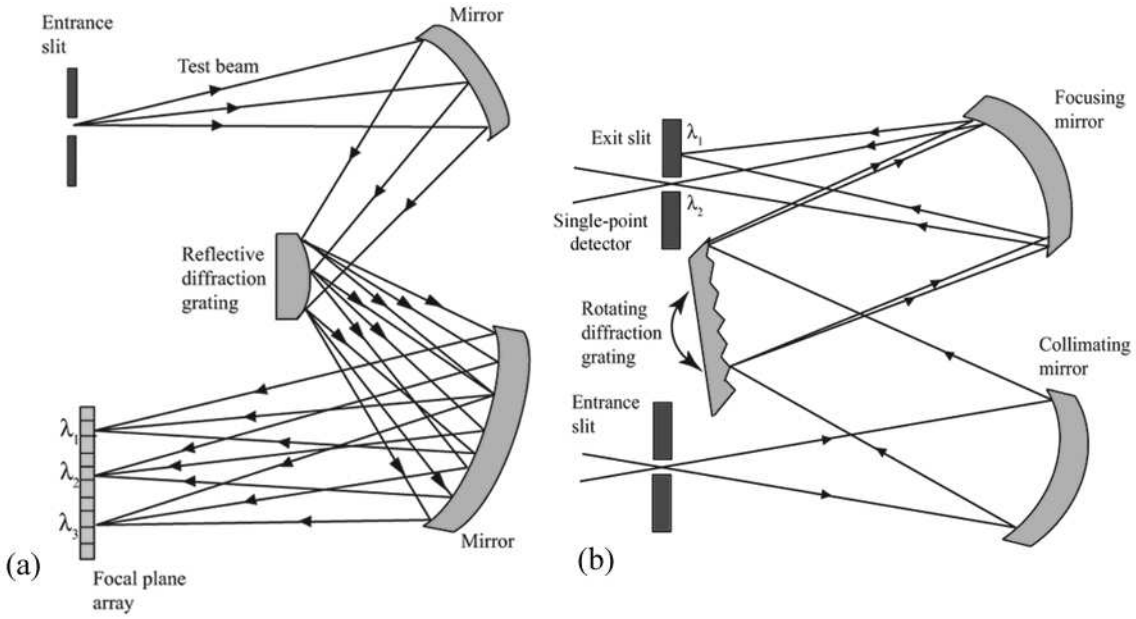

Figure 1.1: Scanning and fixed grating optical spectrometer: (a) Static grating spectrometer with all spectral components detected simultaneously by a focal plane array and (b) a scanning grating spectrometer with spectral components detected sequentially by rotating a diffracting grating and monitoring irradiation through the exit slit

1.2.1 Dispersive and Tunable Gratings

The most direct and commercially embraced methods of UV/Vis/NIR absorption spectroscopy are spatially dispersive techniques utilizing wavelength dispersive prisms or, more often, variants of holographic or etched diffraction gratings. Summarative discussion on grating fabrication, selection, and considerations can be found in the literature [3, 4]. With technological improvements in both grating fabrication and photon detection, these devices have steadily become more inexpensive and compact while maintaining high resolution benchmarks.

Operation of Dispersive Spectrometer

In a static diffraction grating configuration, operating in either transmission or reflection mode, the spectrum of interest is broken down into its relative frequency components by angular separation. The intensity of each spatially discriminated frequency is recorded simultaneously using a focal plane array such as a CCD or photodiode array, as is shown in Figure 1.1(a).

Using a diffraction grating, the angular separation as a function of wavelength, $\theta_m(\lambda)$, is determined from the grating relation:

$$m\lambda = \Lambda(\sin\theta_m(\lambda)) - \sin\theta_i) \tag{1.1}$$

where Λ is the grating period or pitch, θ_i is the incidence angle, and m is the diffraction order. The angular separation of each optical frequency is controlled by the grating periodicity, which may be periodic in transmission/reflection, an amplitude grating; refractive index, a phase grating; or in polarization, a polarization grating. These systems have no moving components and usually a fixed entrance slit, and as a result are used primarily for applications requiring less expensive, durable, and compact systems. The resolution of these systems is determined by the density of pixel elements in the focal plane array and the width of the entrance slit, most often a fixed width in static grating devices.

Alternatively, diffraction gratings can be implemented in a frequency sequential configuration by scanning the grating incidence angle to project a single spectral component on a single point detector, a configuration shown in Figure 1.1(b). While this method of collection requires more advanced mechanically scanning systems, it is the configuration of choice for experiments requiring high sensitivity and high resolution over a wide scanning range ($<$ 1 nm). The resolution of these systems is determined primarily by the width of the entrance and exit slits; wider slits have a higher sensitivity and lower resolution and the opposite is true for smaller slits, yielding a fixed optical throughput. Although these systems, as a whole, are more expensive as a result of the precise mechanical motors and optical system required to ensure accurate grating scanning, variable slit instruments offer a degree of flexibility attractive in an instrument used in a wide base of applications as well as the capability of higher resolution than capable in fixed grating instruments.

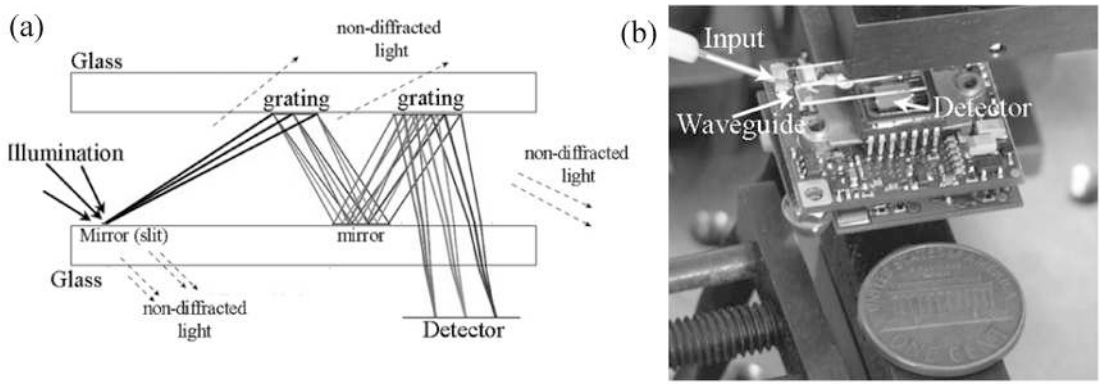

Figure 1.2: Integrated planar reflective grating waveguide: (a) Schematic of a integrated planar waveguide here gratings are fabricated into the waveguide interfaces to disperse spectral components and eventually focus on multilchannel detection element and (b) image of this class of device. Adapted from [6]

Micrograting Spectrometers

Advances in micro-machining techniques, assembly processes, and MEMS have propelled dispersive grating spectrometers, primarily the static grating type, to be realized in ultracompact form factors. The focus of these efforts has thus far been primarily on compact and inexpensive sensors for on-line spectroscopic characterization in process control applications, however these technologies are easily translated in biomedical applications, aerospace, or "lab on a chip" analytical devices. In many application spaces, potential decreases in performance are greatly outweighed by the reduction in device size, affording portability, durability, and inclusion in integrated systems. As one such example, Brennan and colleagues [5] have examined a free space propagation microspectrometer using a LIGA (a German acronym for lithography, electroplating, and molding) process to fabricate miniature, self-focusing, reflective diffraction gratings with an integrated multichannel silicon detector. The ability to manufacture miniature self-focusing reflective grating leads to two component devices, purely a single reflective grating and the array detector, and promotes full spectrometer operation on a single circuit board. [5]

Micro-grating spectrometers have also been realized through the integration of micro-fabricated diffraction gratings into optical waveguides using both planar reflective gratings [6–8], arrayed waveguide gratings [9], self-focusing phase transmission gratings [10,11], and combination microlens/planar waveguides [12] with an application foci on wavelength division multiplexing and de-multiplexing

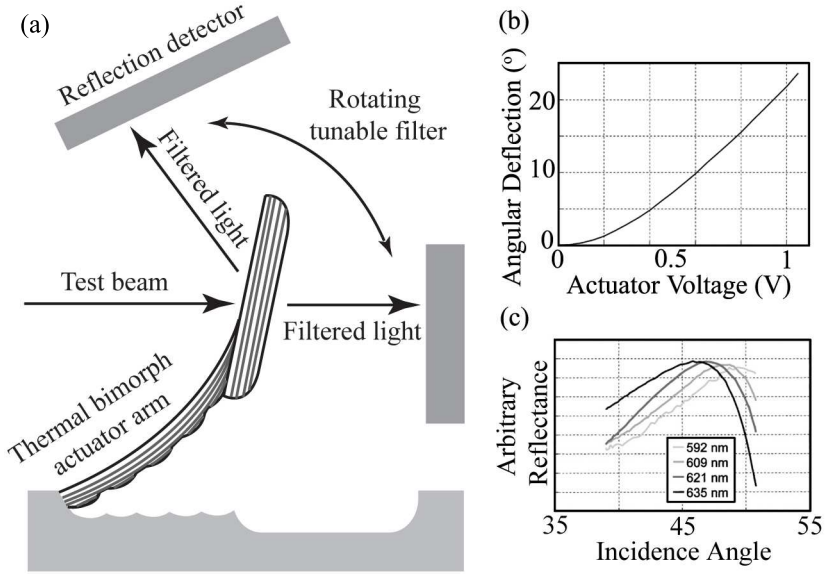

Figure 1.3: An opto-mechanical microspectrometer based on variable incidence Bragg reflection: Thermal bimorph actuators rotate the orientation of Bragg grating with respect to incidence beam using applied fields as depicted in (a) and experimentally shown in (b) while reflectance/transmission characteristics (c) are monitored using two multiple single point detectors. Data from [13].

devices in telecommunications as well as analytical spectroscopy across the visible/NIR range. Using a waveguide as a platform, the optical system of a microspectrometer can be simplified and the whole device can be integrated into a fiber optic platform, reducing device complexity and size by eliminating external optics, and in cases simplifying the alignment process beyond that of a free-space propagating system. The most recent example of a waveguide micrograting system, as described by Grabarnik and colleagues, is shown in Figure 1.2, achieving 3 nm resolution across 300 nm of dynamic range (with an light gathering efficiency of 9%). Fiber integrated gratings have been disclosed with optical resolution on the order of 10 nm [10, 11] across the visible regime and near infrared wavelengths (particularly at telecommunication wavelength $\lambda 1.5$ μm).

In a significantly different approach, Lammel and colleagues [13] disclose a microspectrometer with modified scanning grating configuration using a mechanically tunable optical filter based on a Bragg reflection grating of porous silicon. The silicon grating is mounted on a thermal bimorph actuator that rotates the grating with respect to incident light as a function of applied voltage mediated actuator deformation, as is shown in Figure 1.3. Rotating the Bragg grating changes the incidence angle and as a result, the bandgap and reflection notch are shifted according to the Bragg

diffraction equation. Monitoring the intensity reflected from the rotating grating as a function of applied voltage yields the spectrum of the incident beam, reported with a resolution < 20 nm in the visible spectral window. [13].

As a general observation, microspectrometers based on micromachining and MEMS technologies are limited primarily as a result of difficult alignment of micro-optic components, explicity all the difficulties of a commercial grating spectrometer in a package orders of magnitude smaller. As a result, the cost of manufacturing is driven up in these devices, compromising their attractiveness as process control and rapid optical sensors. As in most grating spectrometer systems, a trade-off most often exists in these systems between the dynamic range, optical resolution and *étendue*, e.g. wide range devices (> 300 nm) exhibit lower resolution (> 10 nm), while higher resolution devices (< 10 nm) most often only function over ~ 100 nm.

As a more simplistic alternative to micro-grating fabrication and waveguide system integration, low resolution spectral processing may be accomplished using an array of static notch filters and detectors. Focusing the spectral source of interest onto an array of filter/detector pairs with each pair tuned to a different transmission peak, the intensity of several discrete components can be determined simulataneously without moving parts. Several publications have disclosed such devices using paired Fabry-Pérot (FP) filters (see Section 1.2.3)with different resonance peaks and complementary metal oxide semiconductor detectors [14–16], although in principle this technique can be implemented using any type of holographic notch filter or other filter with narrow band transmission. Wang and colleagues have disclosed a complementary technology using integrated filters directly integrated in a CCD with resolution between 1.7 and 3.8 nm across a 100 nm range [17]. While these devices are extremely simple in integration and operation, as there are no electrically modulated components, higher uniformity spatial beam intensity is necessary across the device aperture to ensure accurate spectral recreation. Additionally, the resolution of this type of fixed device is not only governed by the characteristics of the filter arrays, but also by the number of filter/detector pairs in the device. Consequently, more panels improve device performance but also increase device size, cost, and the need for highly uniform beam intensity profiles across the detector aperture.

1.2.2 Fourier Transform Spectroscopy

Along with dispersive grating type devices, the other predominant class of spectrometer is a phase modulating Fourier transform (FT) device. While FT devices are, in general, much larger, complex and expensive than diffractive/dispersive systems, they offer numerous performance advantages justifying additional complexity. Efforts are ongoing to miniaturize FT devices using similar micromachining, MEMS, and fabrication techniques discussed above.

Operation of Fourier Transform Interferometer

The most common type of FT spectrometer is based on a modified Michelson interferometer. In this configuration, source irradiation is propagated through, or reflected from, the specimen of interest and then projected into one arm of a standard Michelson interferometer. As is shown in Figure 1.4(a), the beam is divided into two equal parts using a beamsplitter, with one beam propagating to a stationary mirror and other beam propagating to an axially scanning mirror with maximum deviation Δl. As the scanning mirror translates, a phase modulation, $\Delta\phi$, is created between the two beams where $\Delta\phi = k\Delta L$, $k = 2\pi/\lambda$, $\Delta L = n\Delta l$, and n is the refractive index. The two beams are recombined using the same beamsplitter and the frequency dependent interference effects are monitored on a single point photodetector. The superposition of the interference pattern from all frequency components appears superimposed into one interferogram, which can be transformed from a scanning mirror position versus intensity plot into a frequency versus intensity plot using the discrete Fourier transform. In this configuration, the resolution of the spectrometer is governed by the maximum $\Delta\phi$ (also referred to as retardance, $\Gamma = \Delta\phi$) generated in the scanning arm, i.e., higher resolution scans may be obtained simply by increasing Δl and subsequently increasing Γ. In this setup, the instrument dynamic range is limited by the source emission and detector sensitivity. A photograph of a commercial FTS instrument based on a scanning Michelson interferometer is shown in Figure 1.5.

A second type of FT spectrometer device is based on coupled polarizers and retarders. Variable retarders generate optical phase delay through varying the material refractive index n, rather than

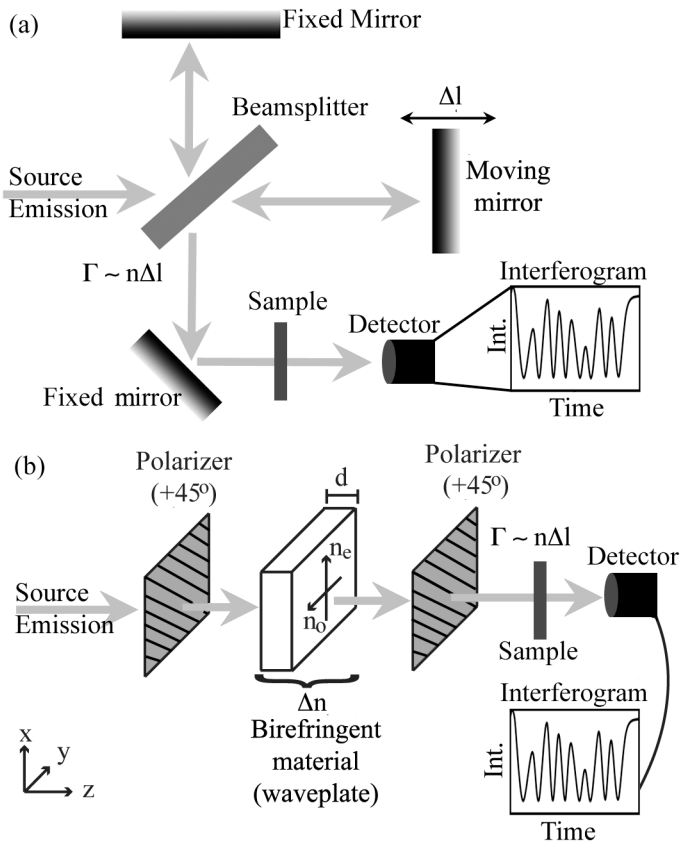

Figure 1.4: Basic operation of a Michelson Fourier transform spectrometer: (a) Modulation in phase through the movement of a mirror generates an interferogram which is Fourier transformed to determine the spectrum or (b) alternatively, a common-path Fourier transform spectrometer modulates polarization through a variable birefringent element oriented at 45° to the initial polarizer while an interferogram is monitored through the analyzer.

Δl as in the Michelson device, and can generate temporally varying interferograms in an analagous fashion, as depicted in Figure 1.4(b). A more complete discussion of this second type of FT spectrometer, most applicable in FT microspectrometers is presented below in Section 1.4.2 and in Chapter 3.

There are several reasons FTS is a preferred method of spectral decomposition over grating type spectroscopy. Analyzing spectra using FTS enables time-multiplexing of signals; explicitly, every wavelength in the detector range is incident on the detector at all times, after which signals are demultiplexed (Fourier transformed) to extract the spectral components. As this is the case, the detector integrates the signal for each frequency component over the entire duration of the scan, translating to a higher signal to noise ratio, and correspondent higher spectrometer *ètendue* than in

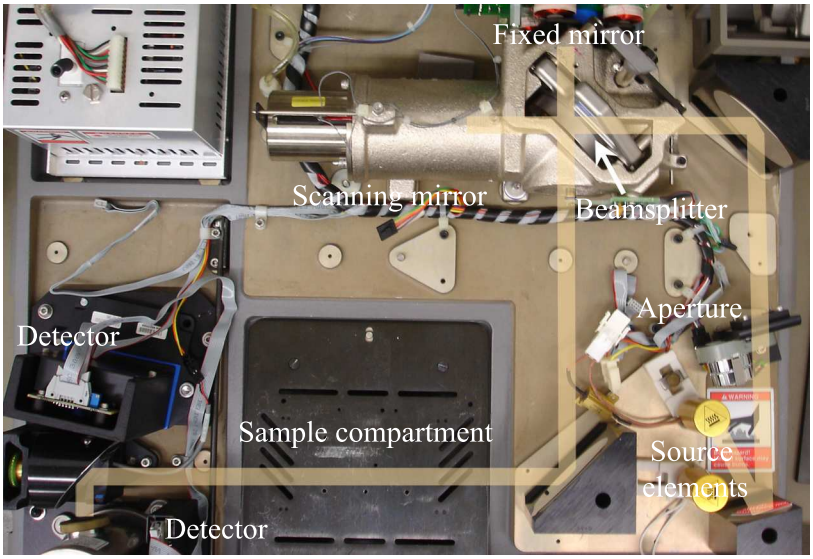

Figure 1.5: A commercial FTIR scanning Michelson interferometer

scanning grating spectrometers or tunable filter devices. The detection element of a FT spectrometer also has higher throughput than grating/filter spectrometers as the entire incidence irradiation spot is collected on the detector, rather than separating components into smaller fractions using a grating slit or tunable filter, a property known as the Fellgett advantage [18]. Although instrumentation is often more costly and complicated than that of a dispersive/scanning grating spectrometer, FTS is utilized almost exclusively in the infrared spectral range (FTIR) as a result of its enhanced sensitivity and reduced integration times necessary for detecting infrared molecular bond vibration absorptions, weaker than electronic transitions observed in UV/Vis spectroscopy.

Compact Fourier Transform Spectrometers

In Michelson FT spectrometers, phase modulation is performed through the mechanical movement of a mirror in one arm of the interferometer. A mechanical phase modulator has limitations in size, cost, and sensitivity to external vibrations. Several approaches have been examined to miniaturize and improve the design of the Michelson type FT interferometer enabling small portable FT spectrometers for sensor applications. Manzardo and colleagues [19] have investigated the fabrication of an ultracompact Michelson interferometer (5 mm $\times$ 4 mm) with a scanning mirror driven by electrostatic actuators on silicon, shown in Figure1.6(a). The electrostatic actuators are designed

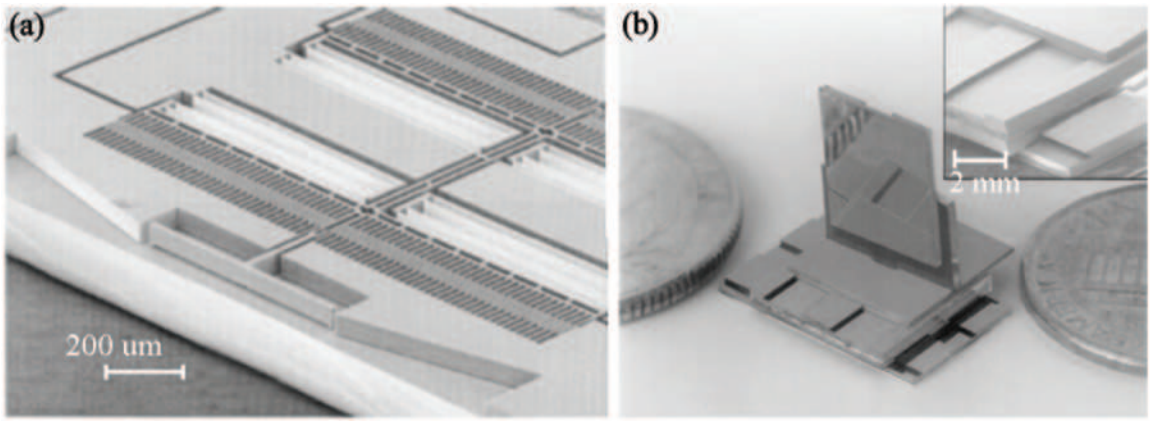

Figure 1.6: Micromachined scanning mirrors for integration in compact FT spectrometers: (a) electrostatic actuator driven module [19], and (b) etched microgroove mechanically scanning mirror [21].

with linear voltage-displacement response and the system yields resolutions <10 nm in the visible wavelength regime. Alternative solutions based on a tilted mirror configuration have also been reported [20]. Collins and colleagues [21] report on a method of micromachining a compact Michelson FT spectrometer using etched microjoints and dovetails to construct a scaled down movable mirror array for the scanning arm of the interferometer, shown in Figure1.6(b). While this device is larger than the microfabricated solution from Manzardo and colleagues, larger mirror translation capabilities in this device can allow for higher resolution scans to be acquired. Although these solutions are all passable for more compact FT spectrometers, they still require moving components and are less than ideal for truly compact and robust FT spectroscopic sensors in medical or other applications.

Unlike scanning phase modulators generating temporal interferograms, an alternative method of FT microspectrometer exists using static spatially varying phase modulators, called wedge FT spectrometers. A Fourier transform spectrometer is fabricated in this 'nonscanning' configuration using a static birefrigent material, most commonly a pure crystal [22–27], and a focal plane array. While the preceding devices create an interferogram through temporal phase modulation, an interferogram can alternatively be generated spatially using a birefringent material with a gradient in retardance. A schematic of the operation of a nonscanning FT spectrometer using birefringent materials is shown in Figure 1.7.

The source (test) beam is collimated, polarized at 45° with respect to the optic axis of the phase

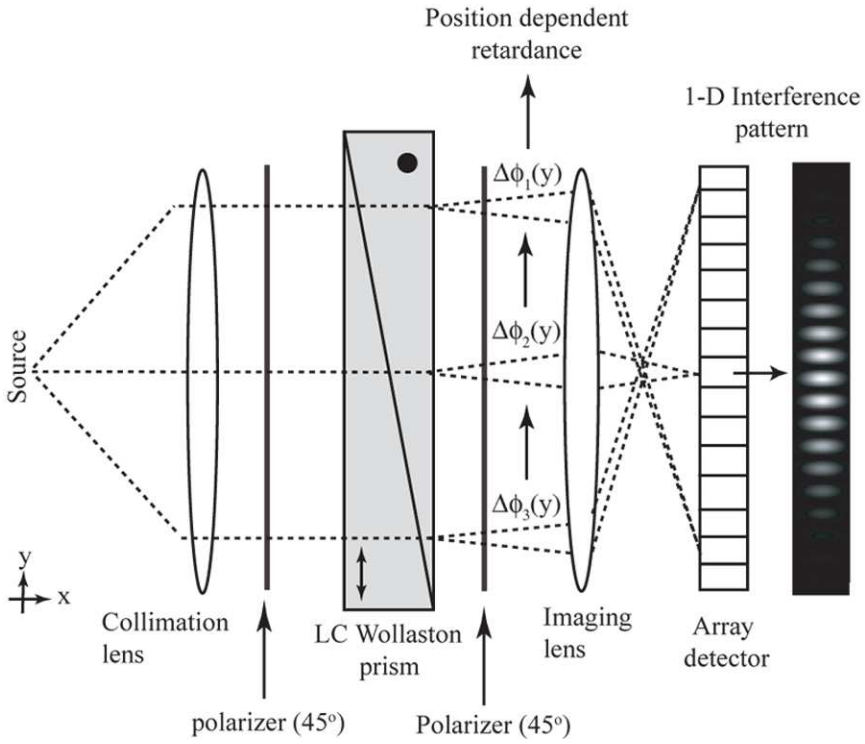

Figure 1.7: Operation of a nonscanning Wollaston Fourier transform spectrometer: A spatial phase delay, $\Delta\phi_i(y)$, is generated across the aperture of the prism inducing a frequency dependent polarization change and consequently, a spatial interferogram at the output sampled using a focal plane array.

delay component, and propagated through the static cell with a polarization dependent gradient of phase delay. The gradient of retardance causes a varying phase delay between orthogonal polarization components propagating through this cell, which depends on the position of the beam in the cell (in the y direction in Figure 1.7). The phase delay results in a position dependent polarization modulation that, when transmitted through another polarizer, produces a spatial interferogram. Taking the FT of this interferogram yields the incident spectrum. In the static FT spectrometer, the maximum phase delay, and consequently resolution, is dependent on both the device aperture size and the birefringence of the phase delay element. A measurement of the mercury lamp emission spectra using a Wollaston prism based FT spectrometer is shown in Figure 1.8, where effective aperture size is increased by stacking multiple shifted Wollaston prisms (e.g., two stacked Wollaston subprisms is analagous to a single Wollaston prism with twice the aperture size). The device aperture size directly correlates with device resolution.

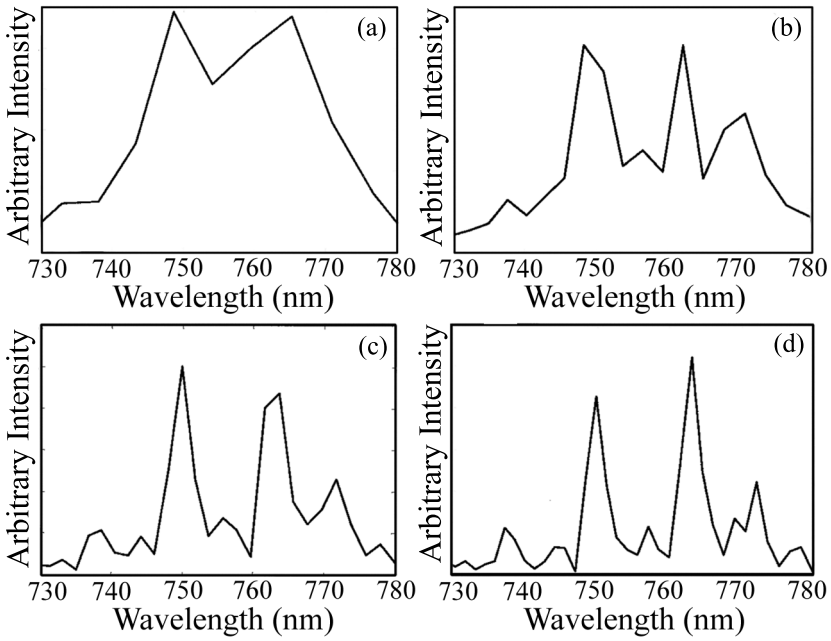

Figure 1.8: Performance of multiple Wollaston prism FT device: Recreation of the emission spectra of a mercury arc lamp using a Wollaston nonscanning FT spectrometer with one (a), two (b), three (c) and four (d) Wollaston subprisms. A Wollaston subprism array increases the the maximum phase delay by stacking multiple Wollaston prisms. Data from [27]

1.2.3 Tunable Optical Filters

The principal of operation behind tunable filter spectrometers is that intensity either reflected, transmitted, or diffracted from a dynamic filter can be recorded serially on a single pixel photodetector while the filter is modulated, yielding a temporal reading of intensity correlated to the light source impinging on the filter. The most critical parameters of a tunable filter spectrometer are the Q-factor (defined as $\lambda_o/\Delta\lambda$ for transmissive/reflective filters), throughput, dynamic range, and tuning speed.

Acousto-optic Tunable filters

An acousto-optic tunable filter (AOTF) operates by sending an acoustic wave through a crystalline solid which subsequently diffracts the light that interacts with these perturbations, as is shown in Figure 1.9. The acoustic modulations in the material can be used to shift the diffracted wavelength by varying the frequency of the perturbation, in turn changing the effective "pitch" of the acoustic grating. In these structures, the acousto-optic interaction occurs in an anisotropic medium, most

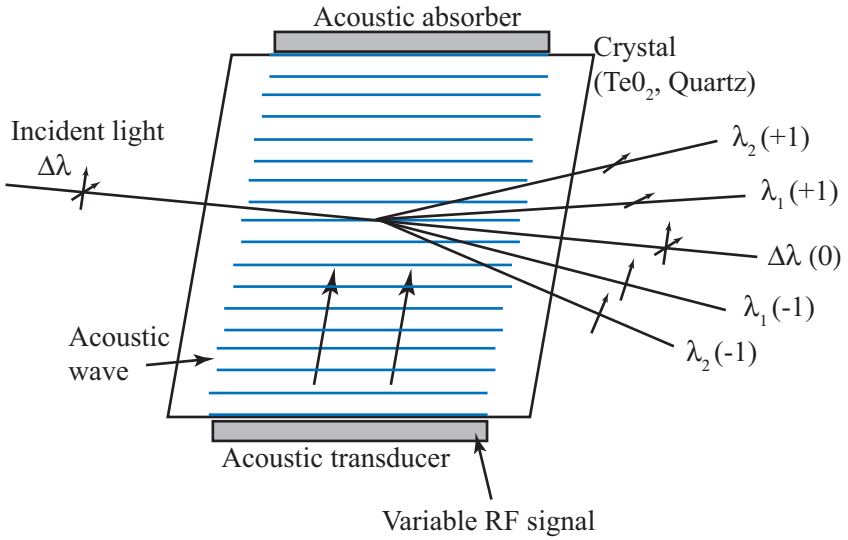

Figure 1.9: Operation of an Acousto-optic tunable filter: An acousto-optic tunable filter operates by transducer mediated acoustic perturbation inducing a diffraction of light, similar to a transmission grating, while the perturbation can be tuned by shifting the RF frequency generating the acoustic wave: (a) For incident unpolarized light, one polarization component is diffracted into the positive diffractive order while the orthogonal polarization is diffracted into the negative order, allowing for a straightforward discrimination of diffracted beams. Initial unpolarized broadband source is shown as $\Delta\lambda$ with positive diffracted $(\lambda_1(+1), \lambda_2(+1), etc.)$, negative diffracted order $(\lambda_1(-1), \lambda_2(-1), etc.)$, and undiffracted light $(\Delta\lambda(0))$. (b)

often TeO_2, quartz, or Tl_3AsSe_3 crystals, depending on the wavelength regime of interest. The operating wavelength regime is defined by the optical transparency of the material; these three common materials offer dynamic tuning ranges from $0.2 - 4.5$ μm in quartz, $0.35 - 5.0$ μm in TeO_2, and $1.0 - 1.6$ μm in Tl_3AsSe_3 [28], translating to a wide overall operating range for AOTF devices.

In an AOTF, tuning speeds are determined by the speed of the acoustic waves, or speed of sound, in the material; and more accurately, how fast the acoustic wave can be adjusted in pitch. Tuning speeds are often less than 100 μs, making these devices excellent for rapid wavelength selection in hyperspectral imaging applications. The resolution of an AOTF is determined by the incident wave interaction length with the acoustic wave, as well as the incidence angle on the crystal. Resolutions have been reported at <1 nm in the UV wavelength regime using quartz crystals, translating to Q factors > 350, and broadening to $15 - 25$ nm in the $1.5 - 2.4$ μm wavelength regime, correlating to Q-factors $\sim$100 using TeO_2 crystals [28]. Depending on the geometry of the acousto-optic crystal and the propagating acoustic wave, an AOTF may be fabricated in a collinear configuration, where the

diffracted and zero order beams are superimposed on each other, or in a noncollinear configuration, where the diffracted and zero order beams are separated spatially (more analagous to a transmission grating). The interaction of a polarized beam of light with the acoustic wave induces diffraction in a beam with orthogonal polarization (see Figure 1.9), allowing for the separation of diffracted from non-diffracted beams in collinear systems using a reflective polarizer (separation is not needed in the non-collinear case).

Tran [28–30] has presented several reviews of AOTF theory and operating principles while Bei and colleagues [31] present a review of the applications of AOTFs in analytical techniques. Numerous authors have reported on the performance of various AOTFs in hyperspectral imaging [32–34] and biomedical applications, such as the characterization of malignant tissues [35,36], ecophysiology [37], and surface enhanced Raman cellular imaging [38].

Tunable Fabry-Pérot Interferometers

A second class of tunable filter suitable as a microspectrometer is a Fabry-Pérot (FP) cavity. The FP cavity is formed by two highly parallel and reflective plates, alternatively referred to as an Etalon. When light is propagated through the cavity, only resonant frequencies of the FP cavity are transmitted, yielding a periodic bandpass structure. Resonant frequencies in the FP cavity occur at points of constructive interference between each reflected wave inside the cavity. The phase difference between successive reflections in the cavity, $\Delta\phi$, is the product of the optical path difference ΔL and wavenumber k, given by the equation $\Delta\phi = k \times 2ndcos\theta$, where λ is the wavelength, n is the cavity index, d is the cavity width, and θ is the incidence angle relative to normal incidence, as shown in Figure 1.10(a). Points of maximum intensity occur when $\Delta\phi = 0$, 2π, 4π ... and minimum intensity occur when $\Delta\phi = \pi$, 3π, 5π ... for each wavelength propagating through the filter. In the FP cavity, the spacing between adjacent resonant frequencies ($\Delta\lambda$ in Figure 1.10), or the free spectral range, is related to the wavelength and cavity parameters by the equation:

$$\Delta\lambda = \frac{{\lambda_0}^2}{2ndcos\theta} \tag{1.2}$$

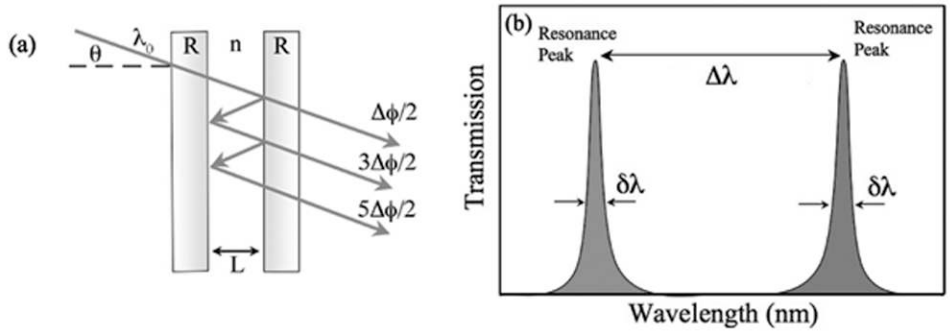

Figure 1.10: Operation of a Fabry-Pérot Etalon/Interferometer: (a) Light propagating through parallel mirrors encounters phase difference at each reflection and only constructively interfering resonances are transmitted, (b) example of transmission lines in a FP interferometer showing the bandwidth, $\delta\lambda$, and the free spectral range, $\Delta\lambda$.

where λ_0 is the center wavelength of the nearest transmission peak, as shown in Figure 1.10(b). The bandwidth of each transmission peak, $\delta\lambda$ can be related to the spacing between adjacent peaks by the spectrometer Finesse, $\mathcal{F}$, as defined by equation:

$$\mathcal{F} = \frac{\Delta\lambda}{\delta\lambda} = \frac{\pi}{2arcsin(1/\sqrt{F})} \tag{1.3}$$

where F is the coefficient of finesse, related to the Reflectivity, R, of the plates in the FP cavity by equation:

$$F = \frac{4R}{1-R^2} \tag{1.4}$$

In the case of a static FP filter, the transmission profiles is set by the cavity index and spacing; an FP interferometer is a FP cavity in which on or both plates are modulated to shift either the cavity spacing, d, or refractive index, n. This shift in cavity parameters shifts the transmission profile, tuning the wavelength(s) of transmitted peaks accordingly. In this fashion, a single FP interferometer can be used as a tunable filter and microspectrometer in conjunction with photodetector as microspectrometer. Tunability of fixed mirrors in FP cavities has been realized using a variety of techniques including electrostatically actuated membranes [39] and microelectronic deformable mirrors [40,41]. Examining equation 1.2 above, it is also evident that the FP cavity can be tuned by varying the incidence angle, e.g. rotating the FP to scan transmission profiles, as described in one

instance by Beard [42]. It is significant to note that rejection filters must be employed to eliminate adjacent transmission peaks of each cavity spacing, otherwise which would contribute excessive out of band leakage in a single pixel monitoring. This can be designed into the system through the addition of absorptive dyes or notch filters in the wavelength regions of choice.

Microspectrometers built upon FP interferometers have demonstrated excellent tuning ranges, $>$ 650 nm in a single cavity in the long wave visible/short wave near infrared region. Resolution across this 650 nm range have been documented at $<$55 nm [40], which can be minimized further by reducing this range. Fabry-Pérot instruments also demonstrate excellent potential as longer wave infrared, $>$ 2 μm, as a function of wide mirror spacings and large mechanical or electromechanical translations.

Although these configurations all have shown promise, liquid crystalline phased materials have been explored to improve and miniaturize these devices even further. A brief introduction to liquid crystal materials is given below in Section 1.3

1.3 Liquid Crystal Phase of Matter

The liquid crystal phase is a mesophase exhibited by certain classes of molecules between the crystalline solid and the isotropic fluid. In the case of thermotropic liquid crystals, the liquid crystal phase exists in a particular temperature range. These molecules exist in either rod-like (calamitic) or disk-like (discotic) organic molecules with dimensions on the order of a few nanometers. This section will focus on calamitic liquid crystals, which possess a shape anistropy in one direction greater than the other two. This shape anisotropy leads to material properties useful in designing tunable filters.

1.3.1 Structure

A standard thermotropic calamitic liquid crystal, 4'-*n*-pentyl-4-cyano-biphenyl, abbreviated 5CB, is shown in Figure 1.11(a) with its commonly represented simple structure shown in Figure 1.11(b). The calamitic molecules have a permanent dipole moment as a result of the polar CN head group; however, calamitic liquid crystal are represented as a cylinder with head and tail equivalence as the

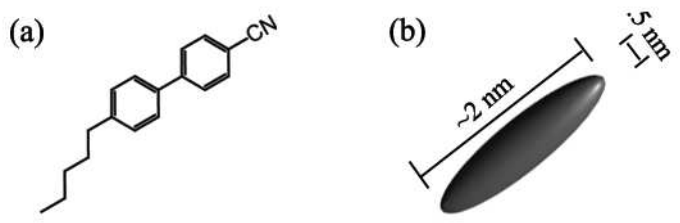

Figure 1.11: Molecular structure of 4'-n-pentyl-4-cyano-biphenyl (a) and the corresponding dimensions of the molecule (b).

CN group is equally likely to point up or down in a bulk system.

Liquid crystal molecules can exhibit a variety of phases, with the simplest phases shown in Figure 1.13. At highest temperatures, the LC material behaves as an isotropic fluid with no positional or orientational order and viscosity similar to that of water. As the temperature is decreased, the LC material transitions to the nematic phase, possessing some molecular orientational order but no positional order. The LC molecules are free to translate and shift around each other, as in a fluid, but remain with the long axis of the molecule preferentially oriented in one direction, called the nematic liquid crystal director and denoted as $\vec{n}$ in Figure 1.13. As the temperature is further reduced, certain materials will transition into a solid phase while others will transition into the Smectic A phase. The smectic-A phase has a higher orientational order than the nematic and also a partial positional order, in that the molecules form quasi-layered structures. Depicted in Figure 1.13 is an idealized configuration, in reality the LC molecules have an average layer distribution function which is periodic such that it is more likely molecules in one depth position than another. At lower temperatures still, some materials will exhibit the Smectic C phase, similar to the Smectic A phase but with the layers tilted with respect to the layered structure.

As Figure 1.13 shows, decreasing temperature increases the overall order in the system, with the highest order occuring in crystalline solid and lowest order in an isotropic fluid. In a liquid crystal, the amount of order, S, is quantified using the ensemble average of the second Legendre polynomial.

$$S =< P_2(cos\theta) >= \frac{3}{2}cos^2\theta - \frac{1}{2} \tag{1.5}$$

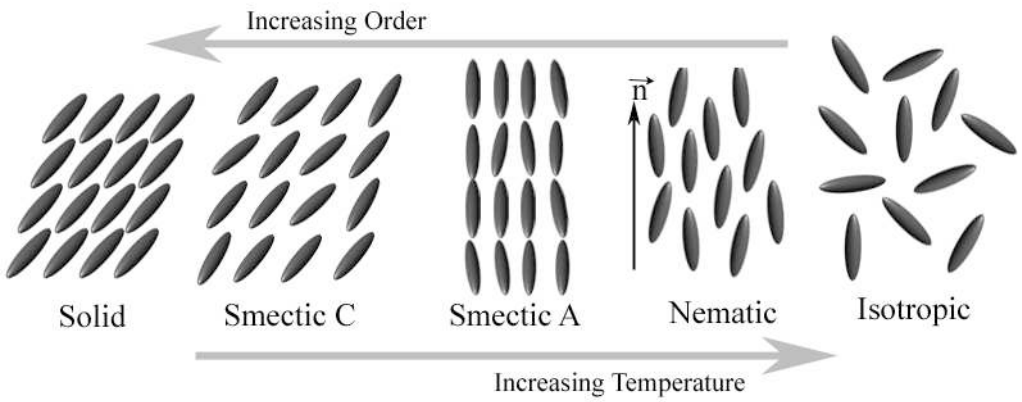

Figure 1.12: The isotropic, nematic, Smectic A, Smectic C, and crystal solid phases

where θ is angle between an individual molecule and the director and the function is averaged over many molecules. For a perfectly ordered solid, $< cos\theta >= 1$ and S = 1, while for an isotropic fluid, $< cos\theta > = 1/3$ and S = 0. In liquid crystals, S increases as temperature decreases and S has a value typically between 0.3 and 0.8

1.3.2 Dielectric and Optical Anisotropy

While the field of liquid crystal physics is expansive, the most significant properties of liquid crystals in their applications in devices are the optical and dielectric anistropy. The shape anistropy of a liquid crystal molecule is a function of its molecular structure, inducing the dielectric and optical anisotropy properties discussed here.

Applying an electric field to a liquid crystal material induces a charge separation and subsequent induced dipole moment. The degree of the induced dipole moment and direction of maximum direction of charge separation is a function of the molecular structure, specifically the dielectric permittivity, ϵ, and the electric field E. In a nematic phase liquid crystal, the dielectric permittivities vary perpendicular and parallel to the long axis of the molecule and are denoted as $\epsilon_{\perp}$ and $\epsilon_{||}$, respectively. The dielectric anisotropy of a liquid crystal is then defined as $\Delta\epsilon = \epsilon_{||} - \epsilon_{\perp}$. In the case where $\epsilon_{||} > \epsilon_{\perp}$ and $\Delta\epsilon > 0$, the LC has a positive dielectric anistropy, will have an larger induced dipole along the long molecular axis, and will subsequently tend to align the liquid crystal molecule

such that the nematic director $\vec{n}$ points along the direction of the applied field. In the case where $\epsilon_{||} < \epsilon_{\perp}$ and $\Delta\epsilon < 0$, the LC has a negative dielectric anistropy, will have an larger induced dipole along the short molecular axis, and will subsequently tend to align the liquid crystal molecule such that the long axis is perpendicular to the direction of the applied field.

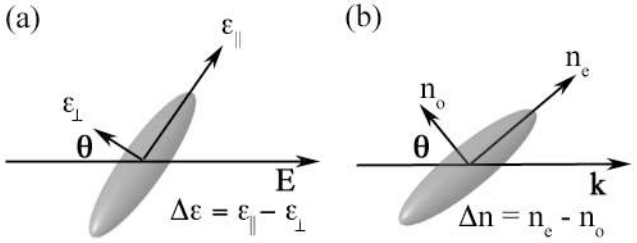

Figure 1.13: The $\perp$ and $||$ dielectric constants with dielectric anisotropy (a) and ordinary and extraordinary refractive indices with birefringence (b).

In addition to the dielectric anisotropy, the aspect ratio of a liquid crystal molecule induces an optical anistropy, or birefringence, into the system. As the refractive index n is proportional to the square root of the permittivity $\sqrt{\epsilon}$, polarized light along the two axes of the molecule experiences two different refractive indices, the extraordinary (along long axis) n_e and ordinary (along short axis) n_o. The birefringence, Δn is defined as the difference between the extraordinary and ordinary refractive indices such that $\Delta n = n_e - n_o$. An optical field propagating through a liquid crystal medium at some angle θ with respect to long molecular axis will experience an index of refraction as shown in equation 1.6.

$$n(\theta) = [\frac{cos^2\theta}{n_e^2} + \frac{sin^2\theta}{n_o^2}]^{-\frac{1}{2}} \tag{1.6}$$

Coupling the dielectric anisotropy and birefringence together, liquid crystals enable electric field reorientation of alignment textures, which in turn varies the optical properties of the LC. This is the underlying concept utilized in the majority of all LC based devices, including display, optical switches, sensors, etc. and is the underlying concept used in fabrication of liquid crystal microspectrometers discussed here and in Chapters 2 and 3.

1.3.3 Surface Alignment

In most devices, LC materials are sandwiched between two planar substrates at a fixed spacer defined thickness. In the absence of an electric field, the orientation of the anistropic LC materials is determined by the surface boundary conditions at the two substrates. The two most common classifications of LC surface anchoring are the planar and homeotropic alignment. These alignment conditions are most commonly achieved through either mechanical or chemical surface treatments.

An LC material is said to have planar alignment when the director is pointing parallel to the surface, most commonly with a preferential director orientation called the alignment direction, as shown in Figure 1.14(a). Planar alignment is primarily achieved by depositing a polymer layer on the surface of the substrate and then mechanically rubbing the polymer layer [43]. The abrasive rubbing creates microgrooves in the surface align the rubbing direction which induces the LC molecules to orient along these microgrooves through free energy minimization. More nonconventional methods of inducing LC surface anchoring include self-assembled monolayers [44], holographic UV exposure [45], and atomic force microscopy scribing [46], all with the same intention of creating homogeneously aligned LC textures.

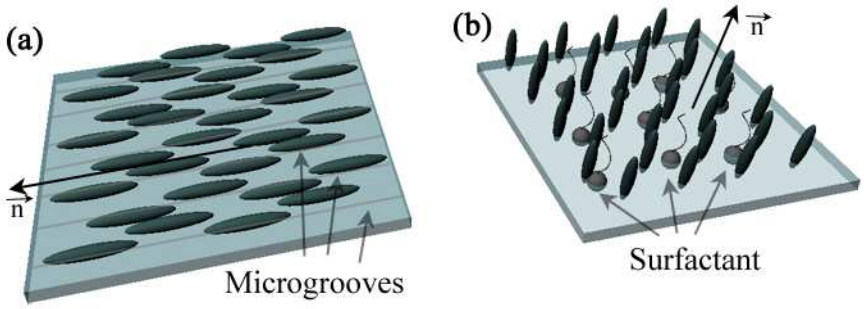

Figure 1.14: Microgroove induced LC planar alignment (a) and surfactant induced homeotropic alignment (b).

Homeotropic or vertical alignment is achieved using monolayer surfactants to induce LC directors perpendicular to the substrate. Typical surfactants used to induce homeotropic alignment are lecithin and silane [47]. These polar molecules are spin coated and evaporated from the substrates, causing the polar head of the material to attach to the substrate and the hydrocarbon tail to point away and perpendicular to surface. The LC molecules orient along the direction of the hydrocarbon

tails in the perpendicular condition, shown in Figure 1.14(b), as a result of intermolecular interaction between the two molecules.

Several intermediate alignment conditions exist between the homeotropic and homogeneous conditions where the LC molecules are aligned with a tilt angle $\neq 0°$ or $90°$. These are created using a variety of alternative polymer and surfactant treatments. The order introduced into the system as a result of surface boundary conditions penetrates only a few microns into the bulk of the system, meaning the alignment quality decreases close to the middle of the LC layer. In practice, the alignment quality often limits the thickness of LC layers.

1.4 Liquid Crystal Microspectrometers

The combination and complement of optical, mechanical, and electric properties of materials exhibiting a liquid crystalline phase has propelled them into numerous applications in photonics. Although liquid crystals are most prominently utilized in display technology, they have also gained traction in optical communications devices, beam steerers, shutters, adaptive optics, microscopy, and biological sensors. Evaluation of liquid crystal materials and configurations in these applications has also propelled their investigation as active/passive elements in ultracompact spectrometers. Contemporarily, liquid crystals have been implemented in numerous devices complementing microspectrometer technologies discussed above in Section 1.2. A brief summary of ongoing efforts in liquid crystal based microspectroscopy, consisting of tunable notch filters, variable phase modulators, and spatial encoders is presented here, followed by conclusions, discussion of target areas of improvement, and approaches to fill this these needs.

1.4.1 Electro-optic Liquid Crystal Filters

Easily the most utilized configuration of a liquid crystal tunable filter for spectroscopy and hyperspectral imaging is the Lyot filter, invented by the French astronomer Bernard Lyot in the 1920's. The implementation of Lyot filters in microspectrometer and hyperspectral imaging devices has been reported by numerous groups [48–54] as well as their subsequent applications in biomedical

photonics [55–59].

The Lyot filter is based on multiple stages of optical retardance filters, each having a variable bandpass structure. The optical radiation of interest, either an emission or irradation beam which interacts with a specimen through transmission/reflection/scattering, is propagated into an initial linear absorption polarizer. The emerging linearly polarized beam then passes through a static birefringent crystal retarder, followed by an electrically controlled liquid crystal retarder, both oriented at 45° with respect to the initial polarizer. As the two retardance elements are at 45° with the polarization direction, the two orthogonal polarization components corresponding to the fast and slow axis of the retarders, n_o and n_e, are subjected to a phase delay dependent on the retarder birefringence, Δn, thickness, d, and wavelength λ. The phase difference between two orthogonal linear polarization states, $\Delta\phi$, is wavelength dependent following propagation through both retarders with a total retardance of Γ:

$$\Gamma = \Delta\phi = \Gamma_c + \Gamma_{lc} = \frac{2\pi(d_c\Delta n_c + d_{lc}\Delta n_{lc})}{\lambda} \tag{1.7}$$

In the case of a Lyot filter, Γ is the sum of the retardance of the birefringent crystal, Γ_c, and the retardance of the liquid crystal, Γ_{lc}. With a phase delay between the constituent orthogonal polarization components, polarization interference effects can rotate the output polarization state depending on the wavelength and total phase delay. Another polarizer (or analyzer), parallel to the initial polarizer, is placed at the output of the paired retarders. Spectral components meeting the condition of $\delta = 2\pi$, and subsequently $\Gamma = m\lambda$ where m is an integer, will have high transmission through the analyzer as the output polarization state is parallel to both the analyzer and the initial polarizer. Spectral components meeting the condition $\Gamma = (m+1)\lambda$ will have minimal transmission as the phase delay from the retarders rotates the polarization state. Rotating the analyzer 90° will reverse the wavelength selection criterion.

The configuration and transmission spectra of a single static filter are shown in Figure 1.15(a). As is noted, the separation between each peak transmission wavelength is dependent on the total retardance Γ. Multiple sets of retardance filters can function as a narrowband filter if (1) each set

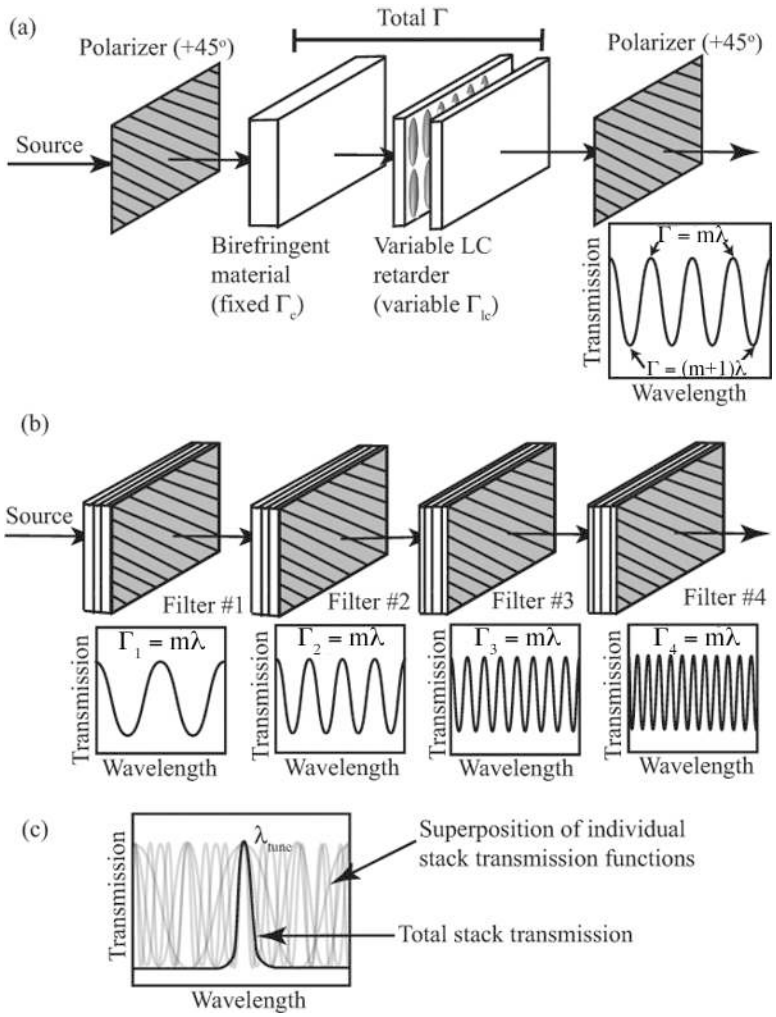

Figure 1.15: Operation of a Lyot filter: (a) A single birefringent filter with periodic transmission based on retardance, (b) stacked Lyot filter in which each stack has different transmission periodicity based on birefringence and thickness and (c) an overlay of the transmission spectra of all filters yielding a transmission peak at λ_{tune}.

has a different retardance value and subsequent peak spacing, but (2) all have a transmission peak at the wavelength of interest, denoted by λ_{tune}. Figure 1.15(b) shows the configuration of a four-stack Lyot filter showing the variation in the transmission spectra while Figure 1.15(c) shows the superimposed transmission spectra yielding a transmission notch at λ_{tune}. As the total retardance Γ depends on both the retardance of the birefringent crystal (Γ_c) and the electrically controlled variable retardance liquid crystal cell (Γ_{lc}), the total retardance and thus transmission properties of each filter set can be modified by an applied voltage.

The liquid crystal device configuration used most often in the Lyot filter configuration is a

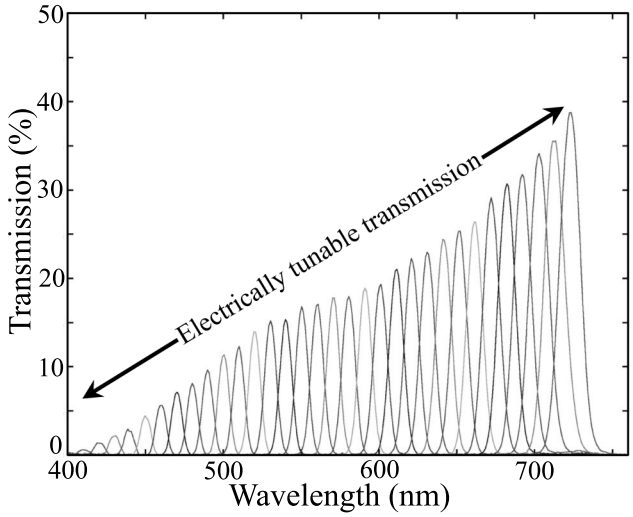

Figure 1.16: Transmission spectra from a Lyot filter: Electro-optic control of liquid crystal retardance in a Lyot filter configuration can shift the transmission peak across the visible regime and into the NIR. Data from [52].

planarly aligned nematic liquid crystal cell ($\Delta\epsilon > 0$) with conductive coatings on both substrates to electro-optically rotate the nematic liquid crystal parallel to the surface normal, as is the case for molecules possessing a positive dielectric anisotropy. In the deactivated planar configuration, Γ_{lc} is the product of the birefringence of the liquid crystal and the thickness of the LC layer in the cell. In the fully activated perpendicular configuration, Γ_{lc} is approximately zero, as both polarization states experience the ordinary refractive index of the liquid crystal. As all intermediate states are possible with intermediate voltage levels, the retardance may be electro-optically tuned from $\Gamma = \Gamma_c$ to $\Gamma = \Gamma_c + \Gamma_{lc}$. This configuration is the most common type of liquid crystal electrically controlled birefringence (ECB) cell, also referred to as an LC variable retarder.

Because of the periodically spaced transmission peaks, Γ_{lc} need only be capable of shifting the retardance value through one period of the transmission profile of the individual Lyot filter, translating to a wide device tuning range even though Γ_{lc} is much less than Γ_c. The resolution in these devices is limited by the device with the minimum Γ, corresponding to the transmission peaks spaced closest together and with the smallest bandwidth, as is shown in Figure 1.15(b). Numerous sequential stacks are necessary for adequate out of band rejection, ensuring no additional overlap in the stack transmission profiles. However, although device performance increases with the number of stacks,

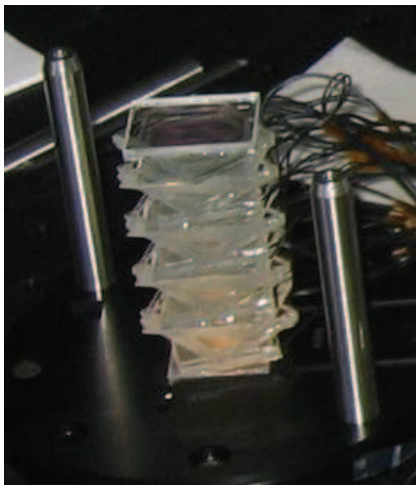

Figure 1.17: A commercial Lyot LCTF filter stack: Image courtesy of Andrew Dionne, Meadowlark Optics.

transmittance through these filters decreases as a result of absorption, reflection and scattering from imperfect polarizers and birefringent elements. In addition to the transmission efficiency compromise, increasing the number of stacks increases the devices cost as a result of added complexity of the electro-optic drivers for precision tuning control of each individual stack. Lyot filters in practice have as many as 12 individual filters and are inherently expensive, limiting their utility in compact and routine analytical tools. Electro-optic tunable Lyot filters using liquid crystals have shown wavelength tuning ranges from the UV/visible regime to the material-determined upper wavelength limit of ∼1700 nm. The notch bandwidths (determined as full-width half-maximum(FWHM)) are 10 nm or less (as noted by numerous authors [50, 53, 60]) in the UV/visible wavelength regime and broaden toward 20 nm at longer wavelengths (the reflection notch bandwidth increases by λ^2 with λ_o), translating to Q-factors ~ 50 . Figure 1.16 shows typical tuning spectra for a liquid crystal ECB Lyot filter, while Figure 1.17 shows a commercial Lyot filter with associated electronics, processors, and housing elements. For further explanation of the operating principles of a Lyot filter, Miller [61] provides an in depth account of Lyot filter fabrication.

While the Lyot filter configuration is the most commonly utilized LCTF spectroscopy device, its limitations, namely low transmission and costly multicomponent fabrication process, have led to investigations of other potential devices. LCTFs can broadly be grouped into two categories:

(1) retardance filters using polarization interference as just described and (2) electro-optic photonic crystals with a liquid crystal material enabling shifting or switching of the photonic bandgap. Tunable or switchable photonic crystals have a stop-band in which, based on coupled mode theory [62], a frequency band of light will be reflected while frequencies outside this band will be transmitted. In this fashion, if the bandgap can be shifted, the reflected frequencies can also be shifted, allowing for temporal spectral scanning analagous to other nondispersive methods. The main limitation in these devices is again their resolution, determined by the bandwidth of the reflection notch in the photonic crystal. While multistack Lyot filter configurations have shown resolution capabilities less than 10 nm in the visible spectrum, single panel tunable liquid crystal photonic crystals have not yet approached this benchmark; some configurations are as much as an order of magnitude lower in resolution. Nevertheless, these devices have been explored as a result of their inexpensive cost and simplicity of fabrication in comparison to multi-stack devices. Alternative configurations of a single panel liquid crystal tunable filter such holographically formed polymer dispersed liquid crystals, chiral nematic liquid crystals, and, in particular, deformed helix ferroelectric liquid crystals will be explored further in Chapter 2.

1.4.2 Liquid Crystal Fourier Transform Spectroscopy

In contrast to monitoring amplitude interference effects using mechanical optical path length modulation, as described in Section 1.2.2, frequency dependent polarization interference can be recorded to generate similar information. As is depicted earlier in Figure 1.4(b), incident radiation passes through a polarizer, a birefringent retarder with its long axis at 45° with respect to the polarizer, a second polarizer parallel to initial polarizer, and a single point photodetector. The phase delay generated between the two polarization components induces a rotation in the polarization director dependent on the birefringence of the material and the frequency of the incident light. In the same fashion as a Lyot filter, a variable retarder is introduced in addition to a static birefringent retarder to provide external control over the polarization output for each frequency in the FT spectrometer. However, unlike a Lyot filter, the intensity is recorded continuously as the variable retarder is tuned,

explicitly measuring an intensity versus optical path difference relation. The temporal interferogram generated by a variable retarder-mediated polarization state modulation can then be Fourier transformed to determine the spectrum, identical to the Michelson configuration. The resolution of this device again depends on the maximum $\Delta\phi$ possible by modulating the variable retarder, thus the maximum phase difference. The advantage of measuring spectra in FTS using polarization is the common path configuration, which translates to a higher tolerance for vibration and air current fluctuations.

Modulating the phase in an FT spectrometer using dynamic liquid crystal variable retarders collapses this device into a compact monolithic interferometer that may be produced for a fraction of the cost of a commercial FT spectrometer. The most important consideration in designing an FT spectrometer using a liquid crystal variable retarder is the maximum $\Delta\phi$ obtainable by electro-optic tuning of the liquid crystal material, correlating to the resolution of the device. Because the phase delay between polarization states in a birefringent material is the product of the thickness of the material and the birefringence, these are the two most important parameters to be considered. As the birefringence in a liquid crystal is fixed by the material properties, optimization of the liquid crystal molecule used can only improve the maximum phase delay by a certain amount, implying that the path length is the significant design parameter to be considered. While in theory the optical pathlength of a liquid crystal cell could be increased until the resolution needs are met, fabricating arbitrarily thick liquid crystal variable retarders is unfeasible as (1) a surface induced alignment only penetrates so far into the cell and (2) very high driving voltages are needed to adjust the retardance of these cells at an acceptable speed. As this is the case, other approaches have been taken to optimize the resolution of a liquid crystal based FT spectrometer.

One solution to the problem of limited optical phase delay is to operate the liquid crystal variable retarders in a double pass reflective mode, doubling the maximum retardance value. Itoh and colleagues [64] disclose a single liquid crystal cell based common path interferometer using a single homogeneously planar aligned nematic liquid crystal cell driven in the double pass reflective mode. While this is a simple device to fabricate, its resolution characteristics are still limited by the small

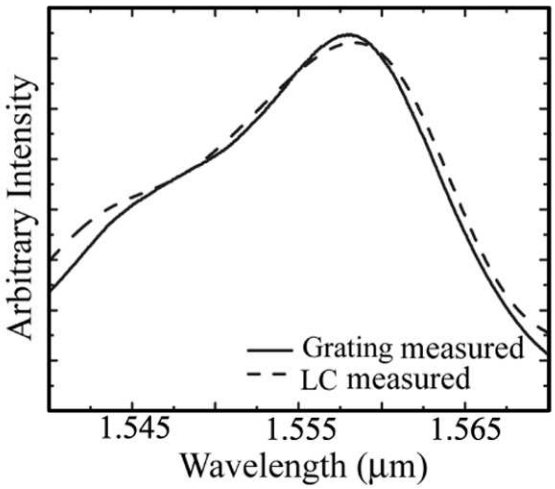

Figure 1.18: Performance of a six-stack LC-FT device: Spectrum of a broadband infrared source as determined by a grating spectrometer and a six-stack liquid crystal FT spectrometer. Data from [63].

phase delay of a single cell, even when doubled. The more effective solution to the problem of limited phase delay in liquid crystal variable retarders is to stack multiple retarders together for the additive retardance effect, as has been reported by numerous groups [51,63,65–68]. Lu and colleagues [63,66] report on the fabrication of liquid crystal FT spectrometers using stacked planarly aligned nematic cells. In this scope, a six stack ECB cell FT spectrometer has demonstrated capabilities of spectral recreation in the visible and NIR range [63]. Figure 1.18 shows the spectrum of a NIR source as measured by both a grating spectrometer and the six stack liquid crystal FT spectrometer.

By stacking multiple liquid crystal retarders together, variable phase delays can be attained using a combination of binary phase switches in place of continuously variable retarders. Several publications [65,67,68] have reported that stacked achromatic phase switches using surface stabilized ferroelectric liquid crystals may be used as phase modulation components. The basic switch consists of two perpendicular or parallel polarizers with two static birefringent plates and an achromatic switchable FLC half-wave plate sandwiched in the middle. In the applied electric field state, the FLC half-wave plate switch rotates the polarization state by 90°, while in the non-applied field state, the polarization remains unchanged. As this is the case, light propagating through the stack can either experience the sum or the difference of the static birefringent retarders, depending on the state of the FLC switch, as is shown in Figure 1.19. With each switch having two discrete retardance

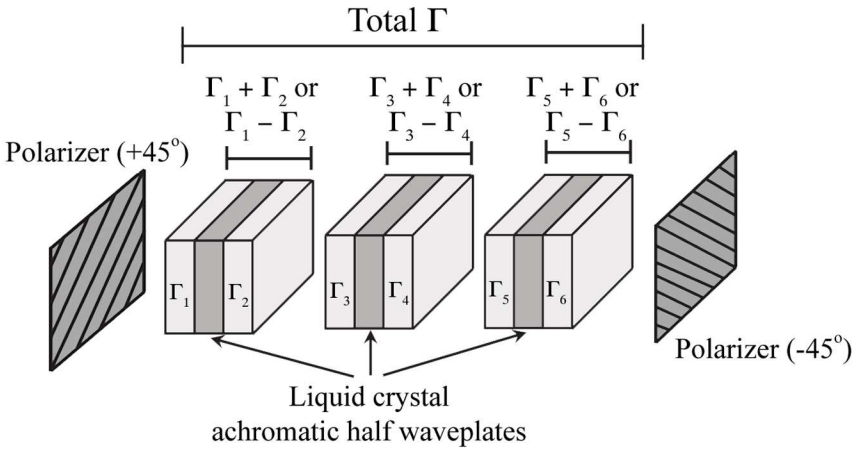

Figure 1.19: An FT spectrometer operating with stacked FLC achromatic half wave switches: Each switch can either provide the sum, Γ_1+Γ_2, or difference, Γ_1-Γ_2, of the retardance of two static retarders by switching the dynamic liquid crystal half-wave plate. The value of Γ can be chosen arbitrarily for each static retarder ($\Gamma_3, \Gamma_4, \Gamma_5, \Gamma_6$) yielding a summed retardance of Γ.

values, stacking N switches together will yield 2^N potential retardance states. Progressively and systematically activating and deactivating stack switches, while monitoring intensity through the output analyzer, generates a discrete point temporal interferogram that can be Fourier transformed to yield the spectrum. Ferroelectric liquid crystals in the surface stabilized mode (see Chapter 2) are attractive here because of their bistability, lowering the device driving voltages of progressive activation/deactivation during scans as voltage does not need to be maintained to hold alignment. The resolution in these devices depends on the maximum phase delay and, accordingly, on the number of switches and amount of retardance at each switch. Chao and colleagues [67, 68] report a potential resolution of 2.68 cm^{-1} and 0.67 cm^{-1} in the NIR wavelength range for 11 and 13 stage devices, respectively. While the potential resolution is high for these devices, some potential weak points of this technology include a more complex electrical driving scheme and low optical throughput with numerous stacked liquid crystal devices, as was the case with the Lyot filter. It is also noteworthy that numerous switches are also necessary to measure enough points in the interferogram such that high frequency modulation components are adequately sampled.

As an alternative method of increasing the maximum phase delay and subsequent resolution while maintaining device simplicity, Davis and colleagues [69] present a waveguide integrated liquid crystal

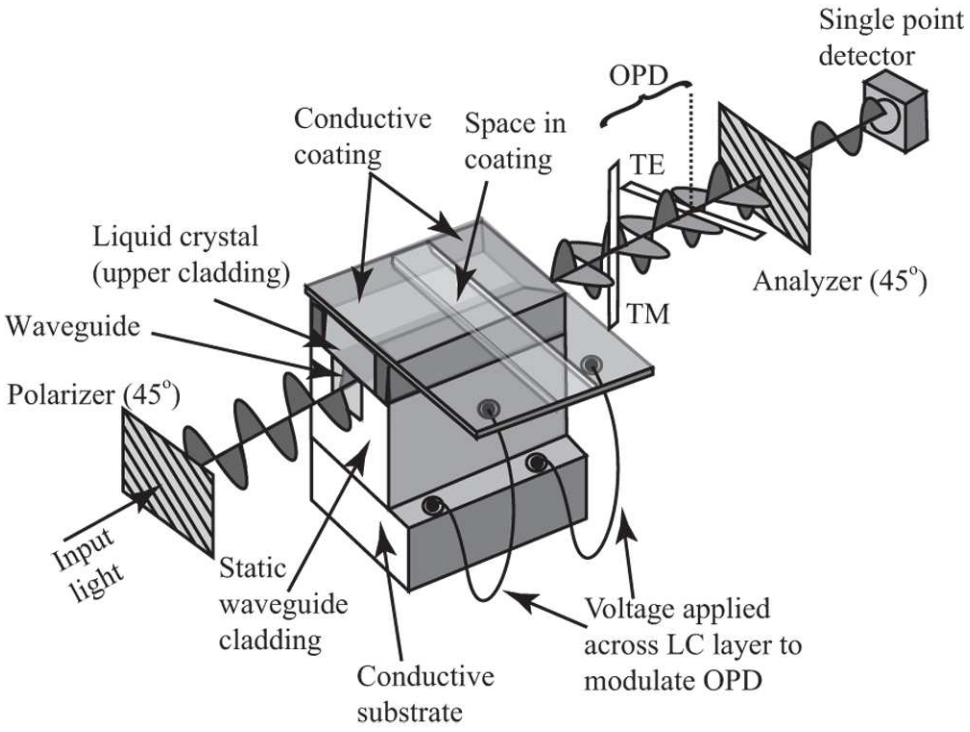

Figure 1.20: A variable retardance Fourier transform spectrometer integrated into a waveguide: Electrically rotating liquid crystal material at one waveguide interface modulates the index profile for one polarization state and generates a phase delay with the orthogonal polarization. The phase delay is frequency dependent and is used to generate an interferogram and determine the spectrum of the propagating beam; integration allows for high phase modulation values decoupled from the thickness of the liquid crystal layer. Adapted from [69].

Fourier transform spectrometer. As shown in Figure 1.20, a planar slab waveguide is fabricated where one surface has an electro-optically controllable layer of nematic liquid crystal, with the other three surfaces acting as static cladding. Using conductive layers integrated along the length of the waveguide, a field can be applied across the liquid crystal material and vary the refractive index at the waveguide interface. For unpolarized light, one linear polarization will experience a waveguide index profile independent of applied voltage (cladding on both sides), while the other polarization component will experience a relative phase delay as a result of the shifted liquid crystal refractive index profile. Similar to the common-path polarization interferometers already described, the phase delay is frequency dependent and will generate a temporal interferogram when detected through a polarization combining element. The foremost advantage of this device is that the light interaction length with the liquid crystal material is dependent on the length of the waveguide as opposed to

the thickness of the liquid crystal layer, as is the case in other liquid crystal FT spectrometers. This decoupling of the phase delay from the thickness of the liquid crystal layer allows for single component manufacturing with large optical path differences and high resolution.

While multiple groups have reported on the use of birefringent Wollaston prisms fabricated using inorganic crystals [22–25, 27], in the fashion described in Section 1.2.2 polymerized liquid crystals in a Wollaston prism configuration have also been investigated. [70, 71]. Polymerized liquid crystals enable surface or electric field induced liquid crystal alignment to be retained over a wide temperature range by locking in this structure with a polymer. This enables cost effective and simple to fabricate liquid crystal phase plates. The advantage of liquid crystals in static FT spectrometers lies in their patterning ability and material properties, rather than the elecro-optic properties exploited in the majority of other applications. Traditional liquid crystal materials have a higher birefringence than the crystals used in Wollaston prisms, enabling a smaller aperture size to obtain the same phase delay. Utilizing polymerized liquid crystal cells also allows more complex structures to be patterned in a liquid crystal Wollaston prism. Boer and colleagues [70, 71] report that a twisted nematic configuration patterned into the wedge of a Wollaston prism effectively reduces the angular dependence of the phase shifts and improves device resolution. In the case of conventional Wollaston prisms, off axis irradiation encounters improper phase delays and blurs out the interferograms, lowering the resolution. Integration of liquid crystal patterned birefringent materials minimizes this blur effect. These devices are exceedingly simple to fabricate with only a few components; although, it is noted that this method requires high density focal plane arrays for sufficient interferogram sampling and high resolution FT spectroscopy.

FT spectrometers using temporal interferograms can be used in conjunction with imaging devices to fabricate spectral imaging devices. In this configuration, a temporal interferogram is produced at each pixel that can subsequently be Fourier transformed to yield the spectral composition of the pixel in object space. Integration of liquid crystal tunable elements in FT spectrometer imaging systems requires additional device requirements, most importantly uniform liquid crystal phase retardance across the device aperture and for varying incidence angles. Wide acceptance angles are

of greater importance in imaging applications as incident irradiation cannot be perfectly collimated for specimens of finite size (as opposed to a point source or uniform sample). Two potential liquid crystal variable retardance cells meeting these requirements are the π cell [72] and the Kaye pair cell [73]. Miller and colleagues [51] report the use of a single Kaye pair cell as a variable retarder in a common path interferometer imaging configuration and have demonstrated the resulting spectral performance by testing uniform bandpass filters and collecting spectral images of tissue samples.

1.4.3 Liquid Crystal Hadamard Transform Spectroscopy

Hadamard transform spectrometers are a subclass of FT spectrometers coupling liquid crystal spatial light modulator arrays with wavelength dispersive elements rather than variable phase delay elements. In these systems, the incident radiation is spatially decomposed into spectral components using a wavelength discriminate element, such as paired reflective grating dispersive filters (paired gratings are needed to re-collimate the dispersion) [74] or static wedge interference filters [75], to produce a spatial gradient of color. The collimated beam with a gradient of optical frequencies is then propagated through a one-dimensional spatial light modulator. The spatial light modulator is used to amplitude modulate each spectral component and 'encode' it with a different frequency. By encoding each spectral component with a different frequency, the encoded beam can be recombined into a single spot and collected on a single point detector. The optical spectrum can then be determined by deciphering the superimposed frequency components, similar to the inverse Fourier transform applied in FTS. The most prevalent method of spatial light modulation is through the use of a one-dimensional pixelated liquid crystal spatial light modulator that encodes each spectral component at a different frequency depending on the liquid crystal driving frequency [74–77]. As liquid crystal encoding masks for Hadamard transform spectroscopy, passive nematic LC spatial light modulators [75, 76], and more recently faster switching (<1 ms) FLC light modulators [74, 78] and thin-film transitor twisted nematic light modulators [77] have all been investigated.

A schematic of the Hadamard technique (using paired gratings) is shown in Figure 1.21. While this technique requires multiple components for operation, the use of a single detector to measure

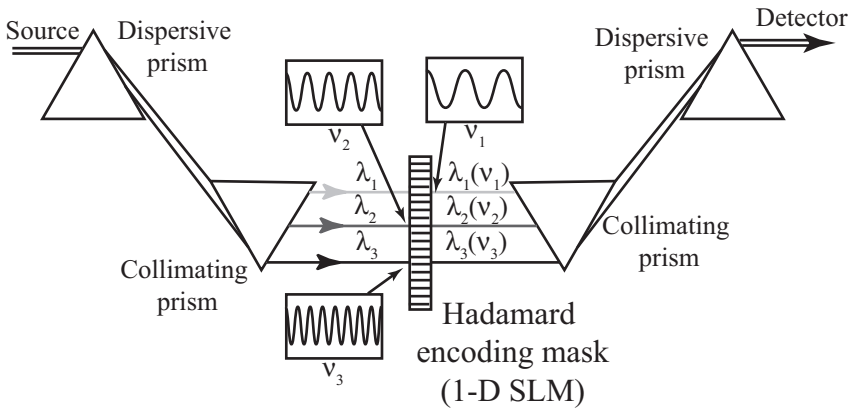

Figure 1.21: Configuration of Hadamard transform spectrometer: A schematic of a combination dispersive prism and liquid crystal spatial light modulator forming a Hadamard transform spectrometer. Incident radiation is broken into its relative spectral components, by a dispersive element, paired prisms in this case, after which each component is encoded at a different frequency $(\lambda_1(\nu_1), \lambda_2(\nu_2), \lambda_3(\nu_3), ...)$ using a one dimensional spatial light modulator. Spectral elements are then recombined and collected at a single detector, and subsequently decoded.

Fourier encoded spectral components leads to the same advantages of conventional FTS, namely good signal to noise ratio and fast collection times while maintaining no mechanically moving components. Limitations on this method of FTS are primarily based on the liquid crystal mask. Resolution limits are determined by the number of discrete liquid crystal pixels encoding each spectral component; scanning speeds are correlated to liquid crystal switching speeds, making fast responding FLCs an appropriate technology for this application. As noted by Funk and Moore [74], resolution proves to be a significant problem when dealing in the IR regime, where resolutions on the order of 0.25 cm^{-1} are desired along with dynamic ranges across the mid-infrared regime $(400 - 4000\ cm^{-1})$. These requirements translate to a 1-D liquid crystal SLM with >14,000 elements. The less stringent device requirements in UV/visible spectroscopy make this device more applicable in this window.

Hadamard transform spectrometers using liquid crystal spatial light modulators, like conventional FT systems, may be applied in spectral imaging systems, and have been evaluated as such in the scope of fluorescence spectroscopy by Hanley and colleagues [77], transmission and reflectance spectroscopy (specifically display emission characterization) by Macgregor and colleagures [79], and Raman spectroscopy by Bohlke and colleagues [80]. A comparison and assessment of the advances in Hadamard transform methods has been given by Tang [81], while an early discussion of fundamental

advantages and disadvantages of Hadamard transform spectroscopy versus Fourier transform spectroscopy is presented by Hirschfield [82]. Hadamard transform spectroscopy has not been heavily investigated more recently, even with the advancement of liquid crystal spatial light modulators and consequent improvements in spectral encoding methods, likely as a result of the improvements of conventional FT and FTIR spectrometers.

1.5 Conclusions

This chapter has discussed contemporary methods of fabricating microspectrometers, material properties of liquid crystals, and how to integrate these materials into new classes of microspectrometer. The implementations of LC materials thus far as analog tunable filters, coupled with photodetectors, as active/passive spectrometers have not yet gained traction in applications which benefit from this technology, which may include 'lab on a chip' devices, biomedical sensors, or on-line process diagnostics. In the subsequent two chapters, two alternative device configurations are investigated. The first, a tunable Ferroelectric liquid crystal device, falls into the class of tunable photonic crystal LC devices and the second, a thick polymer composite phase retarder, falls into the class of tunable LC-FT spectrometers. Each device element has benefits and drawbacks over existing technologies and have the potential for impact across application noted above as well as others.

Chapter 2

Deformed Helix Tunable Ferroelectric Liquid Crystals

2.1 Introduction: Ferroelectric Liquid Crystals

Liquid crystal materials aligned in different configurations enable devices with an optical reflection notch which may be tuned or deactivated with applied voltage. Two such configurations include holographically formed polymer dispersed liquid crystals (H-PDLCs) or cholesteric liquid crystals (CLCs). CLC materials have been utilized in reflective display applications in a notch activated/deactivate fashion [83] as well as other applications in which the peak reflection wavelength may be tuned using in-plane electrodes to deform the helical structure in a CLC [84]; however the typical wide bandwidth of the reflection notch (FWHM $\sim$ 70nm) coupled with polarization sensitivity of reflection (reflects only one circular polarization state) make these materials less than ideal for microspectrometer applications. H-PDLCs, which have also been explored as reflective displays [85] and as color separation devices [86], have the advantage of a narrow bandgap in the transmission spectra (FWHM $\sim$ 15nm) making the technology more applicable for spectroscopy applications, however, these devices have only shown a tunability of 15 nm [87] in a single panel and concomitantly require multiple panels to achieve full visible spectral coverage. We propose the

use of vertically aligned deformed helix ferroelectric liquid crystals (VA-DHFLC) as a single panel solution. VA-DHFLC's couple the full spectrum tunability of a cholesteric liquid crystal with the narrow bandgap reflection notch (15-30 nm) and relative polarization insensitivity of an H-PDLC Bragg reflection grating. A VA-DHFLC microspectrometer has no moving components, actively scans spectral features using applied fields or temperature, and requires only a single pixel photodiode, making it ultra-compact, inexpensive, and easy to manufacture.

2.1.1 Ferroelectric Liquid Crystal Material Properties

In addition to the smectic A and smectic C phases discussed in Chapter 1, other smectic phases exist including ones that can generate form chirality as a result of molecular structure of the material. These materials exhibit a helical structure chirality, similar to the cholesteric LC, but arising from a different mechanism. The distance between successive rotations in the helix is defined as the 'pitch' of the material. The most prevalently investigated chiral smectic material is the SmC* phase, exhibiting the least viscosity of the chiral smectics [88]. A typical SmC* molecule is shown in Figure 2.1(a). The SmC* phase is organized similar to the SmC phase in that the LC layers form a stratified lameller structure with some predefined tilt angle, θ_{tilt}, as depicted in Figure 2.1(b). As a function of the chirality of the molecules, the tilt direction relative to the surface normal gradually changes from layer to layer, forming a helix rotating around a cone angle equal to twice the tilt angle, shown in Figure 2.1(b), with a polar angle around the the cone, ϕ. The tilt angle in SmC* liquid crystals also has some temperature dependence, such that at higher temperatures, the tilt angle decreases and increases the pitch length of the chiral structure, and at lower temperatures, the tilt angle increases and decreases the pitch length.

In tilted molecules of the SmC* phase, the molecular symmetry is drastically reduced from the achiral SmC phase to two-fold axis of rotation symmetry. This reduction in symmetry causes an inequivalence in the dipole moments of the LC molecules and, in contrast to nematics or chiral nematics, creates a permanent dipole moment, or spontaneous polarization P_s shown in Figure 2.1(b) along the axis perpendicular to the long axis of the molecule [47, 89]. As the molecular axis

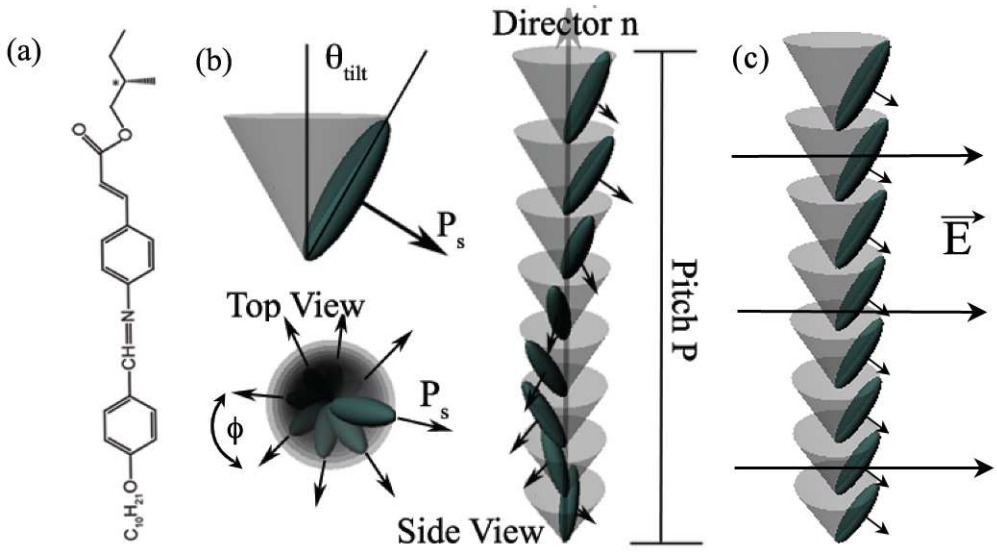

Figure 2.1: Molecular structure of a typical SmC*/ferroelectric liquid crystal (a), structural view of a helical arranged ferroelectric liquid crystal from multiple views (b), and electric field/thermally unwound ferroelectric liquid crystal helix (c).

rotates along the cone angle, the direction of the spontaneous polarization processes around the cone as well. Observing along the helical axis of the ferroelectric cone in Figure 2.1(b), the bulk spontaneous polarization is zero in the plane of the substrate and averages to yield a net dipole along the helical axis. As such, SmC* are often referred to as ferroelectric liquid crystals. Because of this dipole moment, an electric field can be applied to perpendicular to helical axis and reorient LC molecules along one polar angle as shown in Figure 2.1(c).

2.1.2 Device Configurations

The permanent dipole in these materials enables fast switching on the cone and subsequent high performance optical switches and filters using FLC's. Ferroelectric LC's have been applied primary in devices and displays in two different configurations, the surface stabilized condition using long pitch length FLC's and the vertically aligned condition using short pitch FLC's.

Surface Stabilized FLC

Surface stabilized ferroelectric liquid crystals (SSFLC) were the first configuration of FLC's to be implemented as practical devices. Clark and Lagerwall created a SmC* structure in which the

spontaneous polarization is utilized for fast switching while the helical pitch is suppressed through mechanical confinement leaving all molecules on one polar angle of the conical rotation [90]. This is achieved by sandwiching the FLC material between substrates with parallel alignment layers and a cell gap thinner than the helical pitch of the material, explicitly the SSFLC configuration. The surface anchoring of the substrates supresses the pitch of the FLC and causes the material to align in the parallel conditions. The boundary conditions force the molecules to one of two positions at the two edges of the cone, one in which all the dipoles are pointed upward and one in which they are all pointed downward. The permanent dipoles also allow the positions, denoted at $+\theta_{tilt}$ and $-\theta_{tilt}$, to be selected through the application of DC electric fields applied in either the +z or - z direction across the cell. Furthermore, after selection of the molecule position, the cell exhibits bistability in each orientation as a significant energy gap exists between the two states. With these two states, bistable and rapidly switchable waveplates can be created by aligning a polarizer in the dimension of one the two stable LC director states.

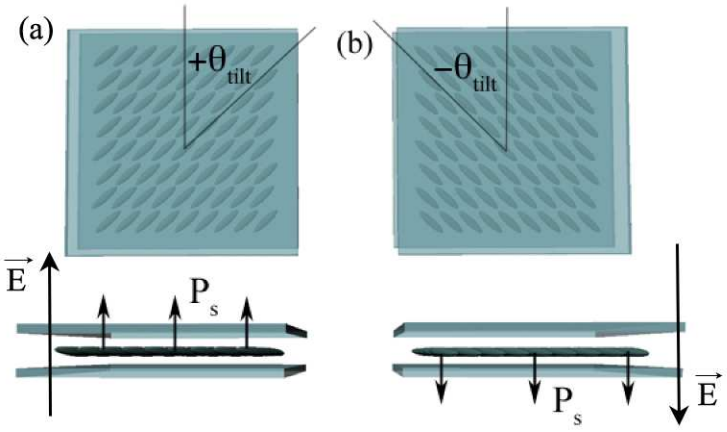

Figure 2.2: One state of a surface stabilized ferroelectric liquid crystal with helix suppressed in the $+\theta_{tilt}$ state (a) and the other state at $-\theta_{tilt}$ (b).

Deformed Helix FLC

The more suitable configuration for spectroscopy purposes is the use of the short pitch DHFLC materials in the vertically aligned condition, as this condition is capable of continuously distorting the helical pitch of the FLC, creating analog tunable devices. The primary configuration of DHFLC's

has been in the total switching mode where alignment is switched from helical to non-helical where molecules at θ_{tilt} now have a uniform polar angle ϕ, as shown in the change from Figure 2.1(b) to (c). Because the helical and non-helical textures have different phase modulation values, a rapid phase modulator has been created. Properties of DHFLCs have been exploited in several applications, the majority of which utilize this full switching mode with in-plane electrodes. VA-DHFLC materials have been implemented in a waveplate configuration such that the waveplate axis is manipulated using circularly patterned in-plane electrodes to modulate FLC alignment [91]. VA-DHFLCs also have been shown to function as intrinsic and tunable feedback mechanism in a laser cavity and, when doped with fluorescent dyes, enable mirrorless lasing [92]. DHFLCs act as rapid cavity resonance modulators in fabry-perot etalons, enabling rapid tuning of etalon transmission properties [93] while similar properties have been applied in dynamic FLC holograms in WDM optical networks [94]. The literature also shows numerous configurations of DHFLCs being used in liquid crystal display technology. One novel method uses a VA-DHFLC sandwiched between a single linear polarizer and $\lambda/2$ waveplate/metallic reflector stack [95]. In-plane electrodes generate an electric field that is sufficiently strong to remove the DHFLC pitch and force the initially bulk zero retardance cell to a bulk optically anisotropic state and modulate pixel output. Short pitch FLCs as well have shown promise in a polymer dispersed configuration, denoted polymer dispersed ferroelectric liquid crystals (PDFLCs), creating a bandgap structure analogous to an H-PDLC [96, 97]. The permanent dipole of the FLC material in the PDFLC overcomes slow switching times inherent in more conventional polymer dispersed liquid crystal devices; however the tunability is still small and limited by the finite birefringence values is not suitable for monolithic microspectrometers. The pitch has been shown to be continuously tunable as well [98] in the scope of grayscale for displays, a facet that will be exploited later in the creating of FLC microspectometers. Using a VA-DHFLC cell as a microspectrometer with continuously tunable helical pitch length is a new concept and well suited due the optical and electrical properties of these materials.

2.2 Tunable FLC Bragg Filters

A VA-DHFLC aligned vertically between two substrates has periodic planes of differing refractive index and can be treated as a reflective grating structure exhibiting many of the properties of a photonic crystal [99]. The grating characterization parameter, Q, given in equation 2.1 (and not to be confused with the quality factor) can be used to describe this structure where λ is the wavelength of incident light, d is the grating thickness, and Λ is the grating pitch.

$$Q = 2\pi \frac{\lambda d}{n\Lambda^2} \tag{2.1}$$

For cases when Q << 1, the cell behaves in the Raman Nath regime. In the case of short pitch FLC materials, Λ is on the order of λ and thus Q>>1, causing the grating to behave in the Bragg regime. In the vertically aligned condition, the FLC helical axis and thus Bragg planes will be mostly perpendicular to the substrate normal and operate in a coherent reflection mode dependent on index profile. In this vertically aligned configuration, the index profile of a VA-DHFLC cell for every incident polarization state as a function of the depth z and the incidence angle can be represented by equation 2.2.

$$n(z, \theta_{inc}) = n_{avg}(\theta_{inc}) + n_m(\theta_{inc}) cos(K(\theta_{inc})z) \tag{2.2}$$

where n_{avg} is the average index as a function of θ_{inc}, the angle between the FLC helical director and the incident wavevector, n_m is the index modulation as a function of θ_{inc}, and $K = 2\pi/\Lambda$ is also a function of θ_{inc}. Using the standard equation describing the average index in a liquid crystal shown in equation 2.3

$$\frac{1}{{n_{avg}}^2} = \frac{cos^2(\theta_{tilt})}{{n_o}^2} + \frac{sin^2(\theta_{tilt})}{{n_e}^2} \tag{2.3}$$

where θ_{tilt} is the tilt angle of the liquid crystal molecule, n_o is the ordinary index and n_e is the extraordinary index, the VA-DHFLC Bragg reflection can be modeled. Manipulating equation (3)

for a VA-DHFLC configuration, the effective birefringence Δn_{eff} experienced by each polarization state propagating through the VA-DHFLC cell can be written as a function of the FLC tilt angle, θ_{tilt}, angle of incidence between helical director and incident wavevector (in the liquid crystal), θ_{inc}, and ordinary and extraordinary index of the FLC material, n_0 and n_e. Equation 2.4 is for the case when $\theta_{inc} < \theta_{tilt}$ while equation 2.5 holds for the case when $\theta_{inc} > \theta_{tilt}$

$$\Delta n_{eff} = \sqrt{\frac{1}{(\frac{cos^2(\theta_{tilt}+\theta_{inc})}{n_0^2}) + (\frac{sin^2(\theta_{tilt}+\theta_{inc})}{n_e^2})}} - n_o,\ \theta_{inc} < \theta_{tilt} \tag{2.4}$$

$$\Delta n_{eff} = \sqrt{\frac{1}{(\frac{cos^2(\theta_{tilt}+\theta_{inc})}{n_0^2}) + (\frac{sin^2(\theta_{tilt}+\theta_{inc})}{n_e^2})}} - \sqrt{\frac{1}{(\frac{cos^2(\theta_{tilt}-\theta_{inc})}{n_0^2}) + (\frac{sin^2(\theta_{tilt}-\theta_{inc})}{n_e^2})}},\ \theta_{inc} > \theta_{tilt} \tag{2.5}$$

Plotting equations 2.4 and 2.5 as a function of incidence angle for several FLC tilt angles, the effective birefringence value is maximized at $\theta_{inc} = 45°$ when $\theta_{inc} < \theta_{inc}$. The effective birefringence achieves its absolute maximum value ($\Delta n_{eff} = \Delta n_{flc}$) at $\theta_{tilt} = 45°$ and $\theta_{inc} = 45°$. The effective birefringence maximum is maintained when $\theta_{tilt} > 45°$ by decreasing the incidence angle. Minimum effective birefringence is observed at normal incidence (of all feasible $\theta_{inc} < 80°$) because the effective birefringence is much lower than that of the liquid crystal molecule ($\Delta n_{eff} << \Delta n_{flc}$). Figure 2.3 shows the modeled normalized effective birefringence as a function of θ_{tilt} and θ_{inc} as described by equations 2.4 and 2.5.

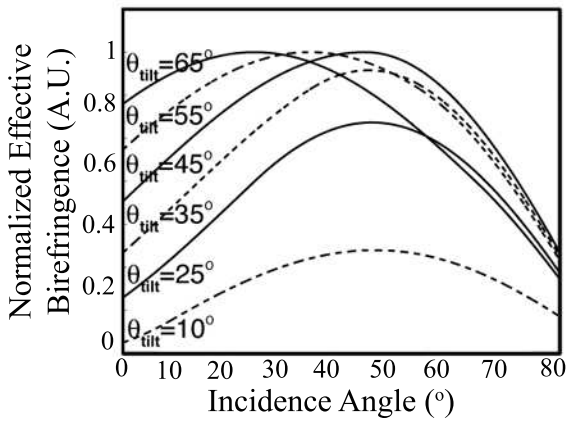

Figure 2.3: Plot of the calculated effective birefringence of the VA-DHFLC

The reflection efficiency, ϵ, is determined by treating the VA-DHFLC cell as a volume phase grating and using a simplified version of the phase grating reflection efficiency equation as is shown in equation 2.6.

$$\epsilon(\theta_{inc}) = tanh^2(\frac{\pi \Delta n_{eff}(\theta_{inc})d}{2\lambda_0}) \tag{2.6}$$

where d is the cell thickness and λ_0 is the reflected peak center wavelength. It is noted that the reflection efficiency variation with reflection notch wavelength is considered purely as a function of the number of Bragg planes while dispersion and birefringence modulation with decreasing order parameter are excluded in this equation. For a microspectrometer, the bandwidth of the reflection notch should be minimized while maximizing the reflection notch depth. The bandwidth of the cell, given in equation 2.7 from that of a Bragg reflection grating, shows that while increasing the effective birefringence increases the peak reflectance, it also increases the reflectance bandwidth and subsequently decreases resolution.

$$\Delta\lambda_{refl}(\theta_{inc}) = \lambda_0 \Delta n_{eff}(\theta_{inc}) \tag{2.7}$$

The trade off between peak reflectance and reflection bandwidth is important when designing a VA-DHFLC cell as a microspectrometer. Equations 2.6 and 2.7 and the material properties of the FLC can be used to model the reflection spectra of a VA-DHFLC as a function of peak reflection wavelength and device orientation as is shown later in Figure 2.7.

2.3 Thermally Tuned Ferroelectric Liquid Crystal

2.3.1 Filter Fabrication

Thermally tunable VA-DHFLC samples were prepared using Nissan SE-120 polyimide (Brewer Science, Ltd, Rolla, MO) spin-coated on glass substrates, chosen because it promoted homeotropic alignment of liquid crystals. The alignment layer was first spin-coated at 3000 rpm for 30 seconds

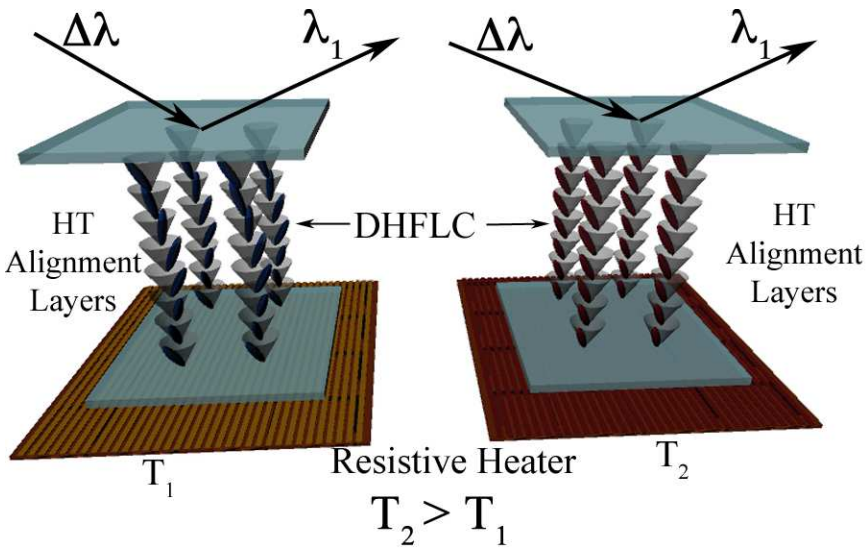

Figure 2.4: A schematic of a thermally tuned VA-DHFLC where a resistive contact heater is used to tune VA-DHFLC pitch. Substrates are coated with a homeotropic (HT) alignment layer to induce vertical alignment of DHFLC helix. λ_1 and λ_2 are the peak reflection wavelengths from broadband illumination $\Delta\lambda$ at two different temperature T_1 and T_2 where when $T_2 > T_1$, $\lambda_2 > \lambda_1$.

to achieve a layers thickness of $\sim$ 200 nm. Following spin-coating, the polyimide was processed by heating on a hotplate at 100° C for 10 minutes to remove the solvent followed by an imidization in an oven at 180° C for 90 minutes. Empty cells were constructed using two pieces of the polyimide coated glass having a constant cell gap of 10 μm maintained by glass fiber spacers. The larger cell gap and consequent improved reflection efficiency is enabled by operating the device in the thermal mode. Specially fabricated deformed helix ferroelectric liquid crystal material (ROLIC 10855, Rolic Research, Allschwil, Switzerland) with a pitch length < 200 nm at room temperature, a spontaneous polarization (Ps) of 98 nC/cm^2, a tilt angle (θ_{tilt}) of 38°, a birefringence (Δn_{flc}) of 0.07 at 550 nm, and phase sequence of Smectic C*/FLC < 83° C < Nematic* < 93° C < Isotropic. The VA-DHFLC was capillary filled into the empty cell under a vacuum in the isotropic phase and cooled to

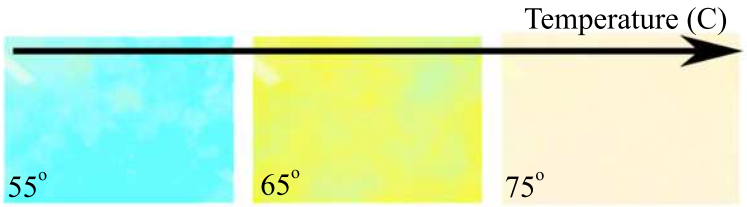

Figure 2.5: Images of thermally tuned VA-DHFLC cells.

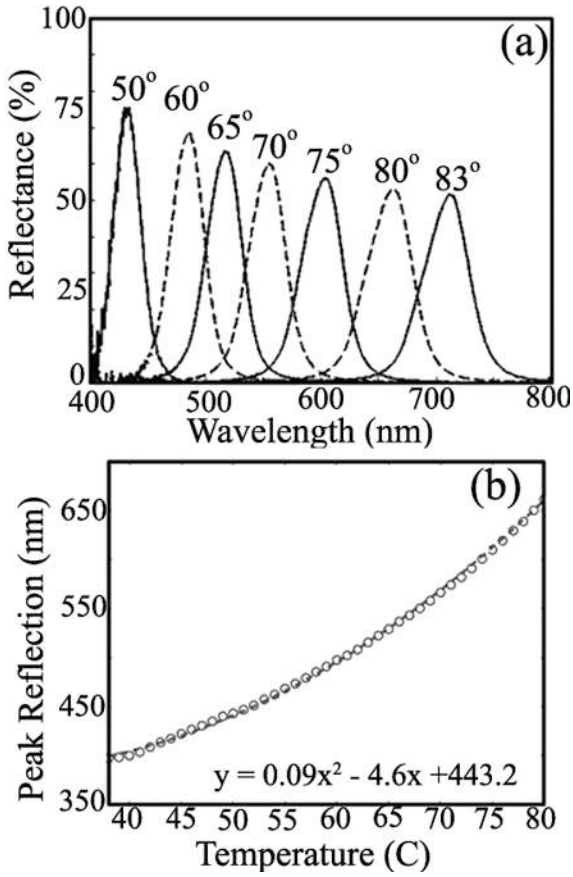

Figure 2.6: (a) Reflection spectra of a 10μm VA-DHFLC as a function of temperature (in ° C collected at $\theta_{air} = 45°$ and (b) the peak reflectance wavelength as a function of temperature.

room temperature under ambient conditions. The cell was then sealed with UV epoxy and cured to maintain stability. A schematic of the thermally tuned VA-DHFLC is depicted in Figure 2.4.

2.3.2 Tuning Performance

Thermal tuning was performed using a contact resistive heating stage with a 0.5° C resolution (Instec, Boulder, CO). To investigate reflection notch characteristics when operating in thermal mode, the VA-DHFLC cell was mounted on the heating stage and illuminated with a broadband white light halogen source. Images of the thermally tuned VA-DHFLC are shown in Figure 2.5

Reflection spectra from the VA-DHFLC were collected using a visible/near infrared grating spectrometer (USB2000, Ocean Optics, Dunedin, FL) with 4 nm resolution and operating range from 330 nm to 1030 nm. The cell was tuned from $50 - 83°$ C to fully examine the dynamic range

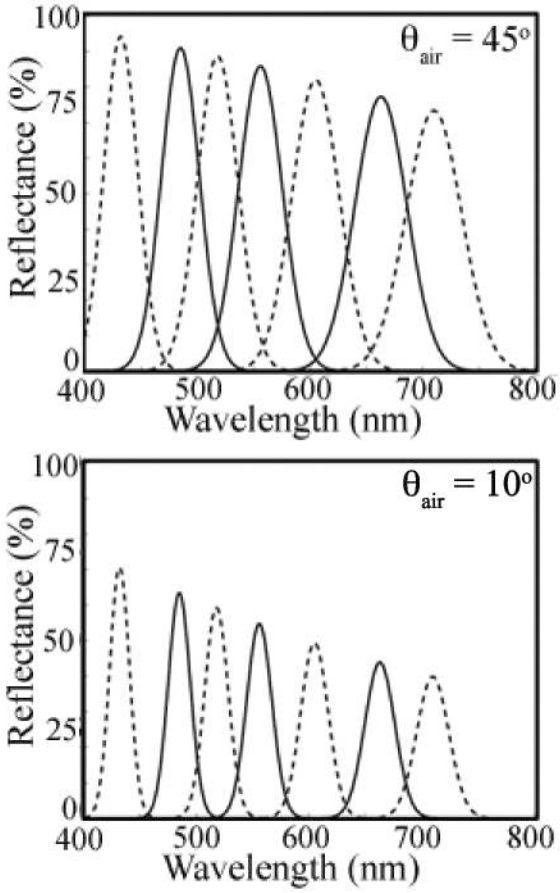

Figure 2.7: (a) Modeled reflection spectra of a VA-DHFLC at 45° incidence and (b) 5° incidence using equations 2.7 and 2.6.

of the sample before crossing the FLC-Nematic* phase transition point and disrupting the helical configuration. The cell was oriented at an incidence angle in air, θ_{air}, of 45° with respect to the collimated halogen source to demonstrate the full visible/NIR spectral range of tunability as shown in Figure 2.6(a) with the peak reflection shown as a function of temperature in Figure 2.6(b).

Experimentally determined reflection characteristics can then be compared to the results of the theoretical model treating the VA-DHFLC as a Bragg reflection grating with angular-dependent birefringence and subsequent peak reflection and bandwidth. Using an FLC material with birefringence $\Delta n = 0.07$, tilt angle θ_{tilt}= 38, d = 10 μm and orientation of $\theta_{air} = 45°$ ($\theta_{inc} = 28°$ as a result of refraction at substrates), equations 2.4 and 2.5 are used to derive the index modulation in the Bragg grating. The index modulation is then used in equations 2.6 and 2.7 to determine maximum reflectivity and bandwidth. Several Gaussian reflection spectra with central reflection wavelength

corresponding to experimentally recorded data were plotted using model-determined parameters as shown in Figure 2.7(a). The modeled data was also plotted with orientation $\theta_{air} = 10°$ ($\theta_{inc} = 6.8°$) to highlight the angular dependent resolution of these samples, and is shown in Figure 2.7(b).

2.3.3 Filter Characteristics

Several additional parameters are discussed in the scope of experimental and modeled data relevant to behavior of this configuration as a microspectrometer. In the experimental data, in the short wavelength visible spectrum (peak at 420 nm), the VA-DHFLC shows a peak reflectivity of 75% for unpolarized light. Shifting to the long wavelength visible regime, the peak reflectivity decreases to 50% (peak at 710 nm) as a result of the decreased number of Bragg planes for longer wavelength light before losing all selective reflectivity beyond the nematic* phase transition temperature at 83° C. Reflectivity and thus sensitivity is maximized in the high incidence angle ($\theta_{air} = 45°$) alignment. In this configuration, the FWHM in short wavelength visible regime is ∼25 nm and broadens to ∼45 nm in the long wavelength visible regime. The shift in reflection characteristics as a function of peak reflection wavelength is in agreement with the modeled reflection spectra as are shown in Figure 2.7(a). The tunable Bragg grating model shows a similar decrease in reflection efficiency and increase in bandwidth with increasing λ_0. The modeled results have a peak reflectivity of 94% and FWHM of 35 nm at the short wavelength visible peak (420 nm) and a peak reflectivity of 73% and FWHM of 60 nm at the long wavelength visible peak (710 nm) using an index modulation of 0.058 estimated using equations 2.6 and 2.7 with $\theta_{air} = 45°$ ($\theta_{inc} = 28.1°$), $\theta_{tilt} = 38°$, and cell thickness, d, of 10 μm. The increased peak reflectivity and increased bandwidth for the modeled system compared to the experimental system can likely be attributed to the model assumption of perfect alignment of the Bragg planes along the incidence wavevector. Alignment imperfection decreases the total index modulation experienced and has the effect of lowering the peak reflectivity as well as the notch bandwidth, as is the case here. Figure 2.7(b) is the modeled reflection notch characteristics with an incidence angle $\theta_{air} = 10°$, a significant improvement in notch bandwidth and resultant resolution as compared to the modeled reflection notch characteristics with incidence angle $\theta_{air} =$

45° as shown in Figure 2.7(a). At $\theta_{air} = 10°$, the FWHM = 18 nm at a short wavelength visible peak (420 nm) and FWHM = 30 nm at a long wavelength visible peak (710 nm) with a calculated effective birefringence, $\Delta n_{eff} = 0.036$. The resolution can be improved further through the use of smaller birefringent FLC materials assuming there still remain enough Bragg planes for significant reflection, translating to thicker LC layers.

As shown in Figure 2.6, the thermally tuned VA-DHFLC device with this FLC material has a dynamic range in the visible spectrum from 400 - 750 nm. The upper threshold is defined for thermally tuned devices by the FLC-n*(CLC) phase transition point after which the FLC no longer maintains is helical structure. The dynamic range of a thermally tunable cell can be shifted to longer wavelengths and near-infrared by integrating an FLC material with a larger helical pitch at room temperatures such that the window of tunable reflection wavelengths is shifted for temperatures in the smectic C* phase. An electrically controllable cell with patterned ITO described in Section 2.4 has a larger dynamic range as the phase transition does not sharply limit the upper bound; however, the upper bound is limited by the reduced number of Bragg planes at long wavelength helical pitches causing a decrease in the peak reflectivity (see equation 2.6 where λ_0 is increasing and d remains constant). A tunable FLC NIR spectroscope is most effectively fabricated using a thermally tuning VA-DHFLC cell using longer pitch FLC materials and a thick VA-DHFLC cell gap (>20 μm) to assure numerous Bragg planes even at the upper limit of the device dynamic range. These thick cells must be thermally addressed because of the inability of feasible electric fields to effectively deform the helical pitch uniformly though this larger cell gap.

As represented in Figure 2.7, the incidence angle is of particular importance in designing the microspectrometer as the resolution and sensitivity are directly correlated to the index modulation and thus the operating incidence angle. Figure 2.8 shows the experimentally measured VA-DHFLC transmission spectra as a function of incidence angle in air. This angular sensitivity was verified by monitoring the transmission of the VA-DHFLC cell as a function of the incidence angle again using a grating spectrometer and collimated broadband source. Explicitly, the VA-DHFLC cell was placed on a rotational heating stage and heated to 65° C inducing a reflection notch at 550 nm.

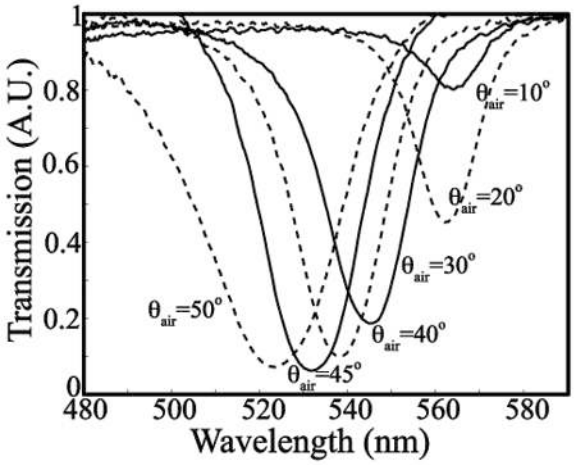

Figure 2.8: Variation of bandwidth and efficiency of transmission spectra as a function of incidence angle in a $10\mu m$ VA-DHFLC cell.

Transmission spectra were analyzed in this case to eliminate small variability in alignment while adjusting setup for different geometrical configuration. Transmission spectra were monitored as a function of θ_{air} from 10° to 50° (θ_{inc} from 6.8° to 30.7°); below θ_{air} =10° the effective birefringence was sufficiently small causing minimal Bragg reflection and above θ_{air}=50° the overall transmission signal was weak due to the reduced size of the VA-DHFLC clear aperture and initial waveguide losses in transmission mode.

At a low incidence angle $\theta_{air} = 10°$, the FWHM = 14 nm. As the incidence angle is increased to $\theta_{air} = 50°$, the reflection bandwidth increases to 35 nm as a result of increased index modulation. The slight drop in reflection intensity from $\theta_{air} = 45°$ to $\theta_{air} = 50°$ is likely the result of initial waveguide losses in substrates as the continued broadening transmission notch suggests the effective birefringence is continuing to increase as the model predicts.

Last, polarization sensitivity of the VA-DHFLC cell was characterized by monitoring reflected intensity for both right and left handed circularly polarized light from a 532 Argon Ion Laser (Coherent, Santa Clara, CA). The cell was thermally tuned to a center reflection maximum of 532 nm (to correspond to the laser emission maxima) and a fiber spectrometer was used to measure the reflected emission intensity while rotating a 532 nm quarter waveplate by 90°. Figure 2.9 shows the reflected intensity for right handed and left handed circularly polarized light (the two spectra

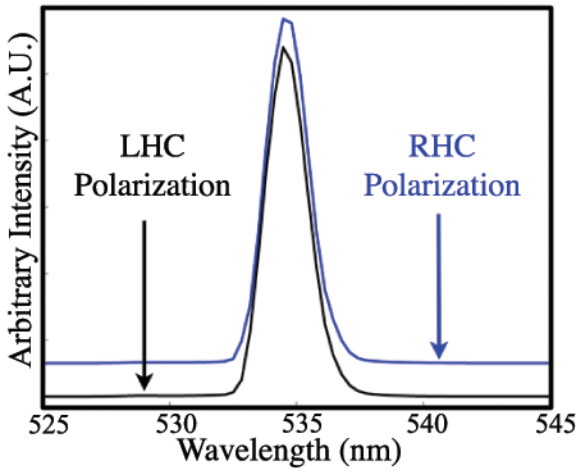

Figure 2.9: Reflection intensity of a 532nm Argon-ion laser with left-hand and right-hand circular polarization (Offset for clarity).

are offset for clarity). The variation in the peak reflected laser intensity is 1.3% between the two orthogonal polarization states, showing that the VA-DHFLC is mostly polarization insensitive more analogous to an H-PDLC as opposed to a CLC. This allows a microspectrometer based on this technology to be inherently more simple and sensitive by not requiring one filter for each circular polarization.

2.4 In-Plane Tuned Ferroelectric Liquid Crystals

2.4.1 Filter Fabrication

Electrically tunable cells can be fabricated analogous to thermally tunable cells except one substrate is coated with indium-tin-oxide (ITO) prior to coating with polyimide varnish. ITO patterns or interdigitated electrodes were formed on one of the two substrates substrates using ITO with resistance of 15 Ω / square, 25 μm electrode width, and 25 μm electrode spacing fabricated by laser patterning of bulk ITO sample. Additionally, the cell gap was reduced from 10 to 6 μm to attempt to minimize drive voltages

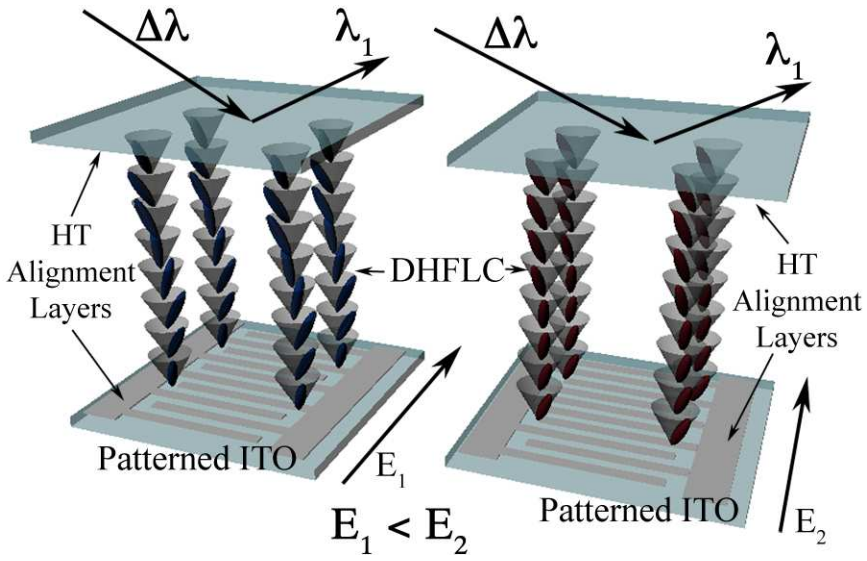

Figure 2.10: A schematic of a electically tuned VA-DHFLC where patterned ITO substrates are used to tune VA-DHFLC pitch. Substrates are coated with a homeotropic (HT) alignment layer to induce vertical alignment of DHFLC helix. Λ_1 and Λ_2 are the peak reflection wavelengths from broadband illumination $\Delta\lambda$ at two different electric field strengths E_1 and E_2 where when $E_2 > E_1$, $\lambda_2 > \lambda_1$.

2.4.2 Tuning Performance

Due to low spatial uniformity of reflection notch characteristics from the in-plane tuned VA-DHFLC, reflectance tuning was observed under a reflectance microscope with sample tilted to $\theta_{air} = 25°$ using a slanted microscope slide. A collimated broadband halogen source was used to irradiate the sample, although in this configuration projected through illumination arm of the microscope. Specular reflectance was captured in the microscope and images collected on a CCD camera. The device was tuned from 0 - 700 V using 100 kHz AC signal and sample observed at $\sim$ 25 V steps. The resulting tuned reflection notches are shown in Figure 2.11 with the electric field in V/μm. Note the VA-DHFLC tuning domains pictured here are small, on the order of the size of the electrodes.

As a result of the small areas of reliable tuning domain in the IPS VA-DHFLC cells, reflection spectra were difficult to obtain with adequate signal level. While peak positions visually appear to be repeatable in particular domains (such as those shown in Figure 2.11), as a whole, samples were not consistent in the spatial optical characteristics varying with applied voltage. Microscope images of a larger spatial area of the FLC sample are shown in Figure 2.12. This image depicts

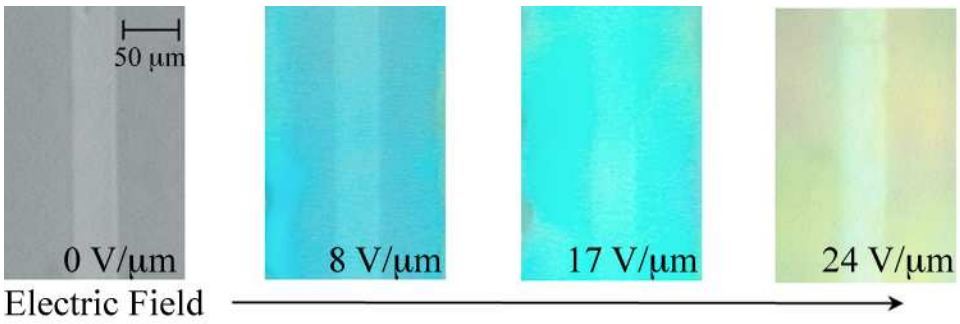

Figure 2.11: Microscope images of in-plane electrode tuning of 6 μm thick VA-DHFLC as a function of applied voltage.

multiple facets about in-plane FLC tuning in this configuration. First, aggregate LC defects are formed above some of in-plane electrodes, likely resulting from local electric field vector pointing perpendicular to the sample. This defects tend to appear after one or two tuning cycles and remain under all electric fields until the material is heated above isotropic clearing point. Second, many of the in-plane electrodes are non-functional, possibly as a result of broken electrodes, but more likely a result of the aggregate defects affecting both local alignment and field directions. The low fraction of functional electrodes, empirically estimated at $\approx 40\%$ across most samples, drastically reduces the overall peak reflectivity of the sample. The source of these defects is a concept requiring future study to produce more spatially uniform FLC samples. As a result of these drawbacks in reliable IPS-FLC tunable filter construction, thermal VA-DHFLC cells are considered in microspectrometer tests with anticipation that IPS-FLC can at some point perform analogously with modified voltage driving scheme and electrode patterning.

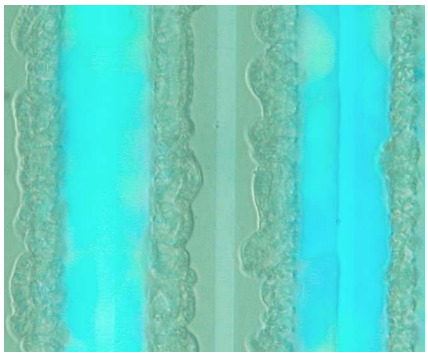

Figure 2.12: Microscope image of a IPS tuning VA-DHFLC showing both aggregates of defects shown appearing above electrodes, and several non-functional electrodes.

2.5 Microspectrometer Performance Validation

The performance of the VA-DHFLC as a microspectrometer is assessed theoretically and experimentally. As reference emission standards, a liquid crystal display (LCD) and a mercury arc lamp were interrogated using the microspectrometer device. The emission of both standards was first measured using the same grating spectrometer as above. Using these spectra, modeled reflection spectra of a VA-DHFLC device (as determined using the method described in section 2.2 with $\theta_{air} = 25°$) were applied as weighting factors and then signals summed to simulate the incident power on a single pixel diode and emulate microspectrometer performance. The modeled microspectrometer performance was broken down into 350 discrete VA-DHFLC reflection notches ranging from 400 nm to 750 nm and the summed intensity from each notch was then recombined with its central wavelength to recreate the spectrum. To verify microspectrometer performance experimentally, the emission standards were focused onto a single pixel photodiode (Melles-Griot, Rochester, NY) using a high clear aperture lens after reflecting from the VA-DHFLC sample at an incidence angle $\theta_{air} = 25°$ ($\theta_{inc} = 16.3°$). The incidence angle was chosen at an angle to compromise high signal to noise with angular resolution dependence. The VA-DHFLC was thermally tuned from 50-83° C to cover the full visible regime at a rate of 3°C/min.

The emission spectra of an the mercury arc lamp as measured by a grating spectrometer and as determined both theoretically and experimentally using a VA-DHFLC microspectrometer are shown in Figure 2.13(a)-(c) while the same is shown for an LCD in Figure 2.13(d)-(f). Note the expermental/modeled spectrometer intensities are scaled by the reflectance notch characteristics. Although the loss in resolution is present from a commercial fiber based spectrometer to the LC system, analogous spectral features between data are clearly observable. The modeled spectral signatures are in good agreement with experimentally determined signatures with a slight improvement in resolution in experimental results arising from decreased effective birefringence from alignment defects as described previously. The peak in the mercury spectrum at 436 nm has an experimentally determined FWHM of 18 nm using the VA-DHFLC operating at $\theta_{air} = 25°$ and a model determined FWHM of 23 nm with the same parameters. This is a result of the discrepancy in ideal modeled effective

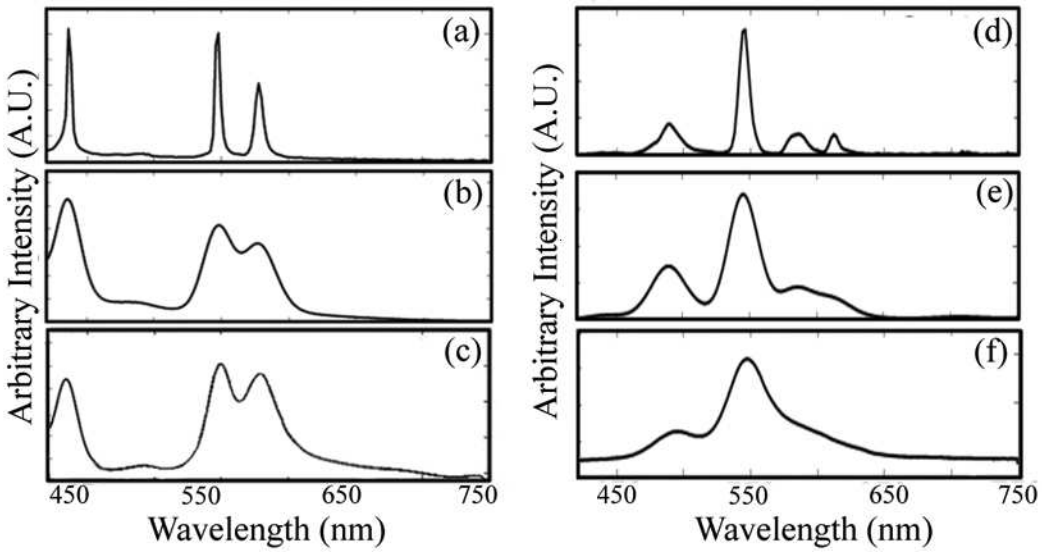

Figure 2.13: Emission spectrum of a mercury lamp measured using (a) a grating spectrometer, (b) modeled VA-DHFLC performance, and (c) fabricated VA-DHFLC. Emission spectrum of the green pixels of an LCD measured using (d) a grating spectrometer, (e) modeled VA-DHFLC performance, and (f) fabricated VA-DHFLC.

birefringence as opposed to actual effective birefringence narrowing the peak linewidth and thus features linewidth as explained previously. Both experimental and theoretical spectra demonstrate this device is capable of resolving the doublet in the mercury spectra at 546 nm and 579 nm. The recreated LCD emission spectra shown in Figure 2.13(d)-(f), demonstrates that the VA-DHFLC device is also suitable in monitoring more broadband spectral lineshapes as opposed to narrow emission lines, as is the case in many biomedical spectroscopy applications.

2.6 Spectral Imaging Configuration

The performance of the VA-DHFLC tunable filter in a hyperspectral imaging device was demonstrated by replacing the silicon photodiode in the previous setup with a CCD array. A pattern of RGB stripes was displayed on the same display and focused using a biconvex lens (f = 10 cm) onto a 512 x 128 back-thinned CCD array (HC230, Hamamatsu, Japan). The VA-DHFLC was again oriented with an incidence angle of 25 for resolution/sensitivity compromise. The VA-DHFLC cell was tuned at 3° C/minute from 40° to 83° and an image collected once per minute with integration

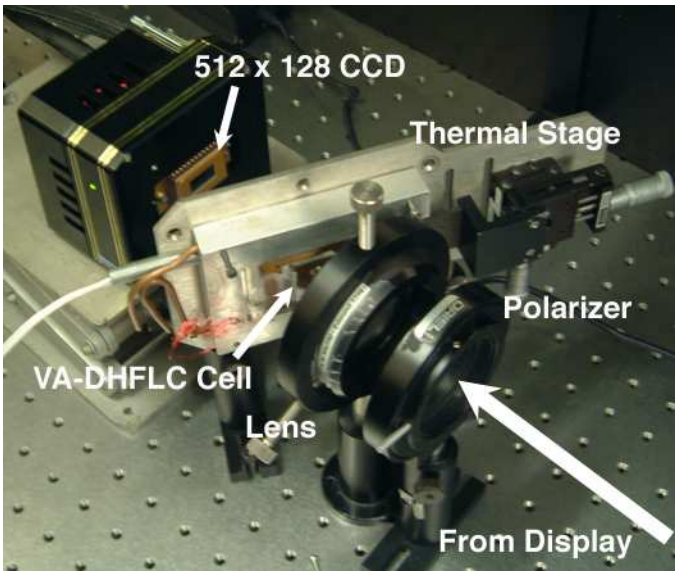

Figure 2.14: Benchtop prototype of hyperspectral imaging device using tunable VA-DHLFC cell.

time of 500 ms for each pixel. Pixel intensities were normalized for wavelength responsivity variation to produce a uniform baseline image. Figure 2.14 shows a hyperspectral imaging setup using a thermally tunable VA-DHFLC, focusing lens, polarizer (for intensity control of the test display) and an array detector operating in the transmissive mode.

The CCD captured intensities of a patterned display emission pattern transmitted through the VA-DHFLC cell demonstrate the capability of hyperspectral imaging using this setup. Figure 2.15(a) shows the RGB patterned stripe array while Figure 2.15(b) shows the imaged intensity on the CCD for temperature T = 40°C when the reflection notch is in the UV range and Figure 2.15(c) for temperature T = 70°C where the reflection notch is tuned to 550 nm. Since this measurement is taken in transmission, at the green pixel stripes in the display pattern, the CCD intensity is minimized as the emission is reflected from the filter away from the detector. A small difference is also observable between the red and blue striped patterns as the emission of the blue pixels has some intensity overlapping that of the green pixel while the red pixel overlap is minimal (as can be seen in Figure 2.15(d)). Small variations in intensity across the length of the stripe pattern can likely be attributed to VA-DHFLC variations in tuning. Minimization of these non-uniformity effects in a hyperspectral imaging device can be managed by focusing the emission down to a small aperture

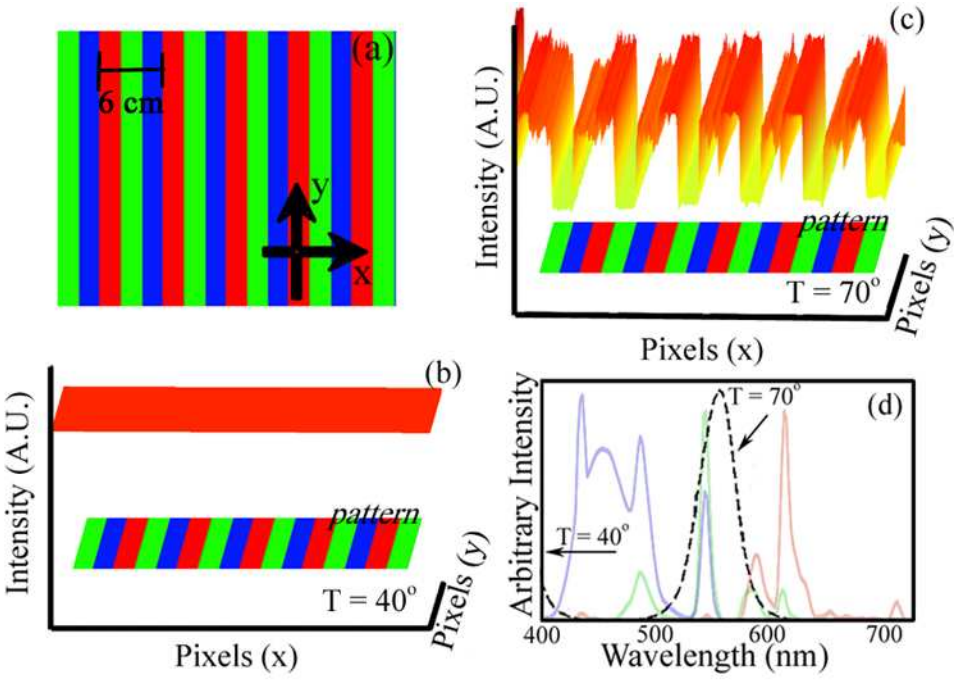

Figure 2.15: (a) Display emission image to be captured using hyperspectral image device pictured in Figure 2.14. (b) Hyperspectral image captured at VA-DHFLC tuned in UV reflection regime and (c) at $\sim$ 550 nm reflection peak. (d) Emission spectra of three display pixel colors with overlay of FLC reflection spectra at 40° and 70°.

size such that only the tunable filter only interrogates a small area of emitted light. The large area of displays emission makes a tight focus difficult in this particular example, however other applications utilizing this hyperspectral imaging device to interrogate a smaller field of view can easily overcome small sample tuning variations.

2.7 Resolution Enhancement through Post Processing

In an imaging setup, the quality of the image is determined by the overall point spread function (PSF) of the optical system coupled with the resolution and characteristics of the detection system. This concept can be applied to the microspectrometer system discussed above where the PSF is the spectral reflection/transmission profile of the tunable LC filter, the "real" image is the actual spectra being passed through the system and the "blurred" image is the spectra recorded on the photodiode or photodiode array after serially tuning the LC filter. Carrying this analogy further, postprocessing image enhancements techniques such as various deconvolution algorithms can be

applied to enhance the spectral resolution in serially tuned microspectrometer systems. As spectral transmission/reflection profile of the LC filter are known, the effective PSF of the system is known. This known blur function can then, for example, be deconvolved with the blurred spectrum to recreate the initial spectrum. One added caveat of this variant of image processing is that instead of having a constant PSF as in an optical system, the LC panels have a spectrally varying blur function, i.e. the transmission/reflection profiles shift at longer wavelengths. Although this dilutes performance, a benefit from this post-process technique is still observed.

2.7.1 Spectral Deconvolution

Investigated here are several types of deconvolution algorithm applied LC spectrometer obtained data. Considering the cursory equation shown below in equation 2.8

$$g = H * f + \epsilon \tag{2.8}$$

where g is the blurred spectra recorded on the photodiode/FPA, H is the PSF or spectral blur function introducted by the liquid crystal filter, f is the "true" spectral signature, ϵ is noise introduced into the system from the detection system, and $*$ indicates that a convolution is being performed. The discrete form of equation 2.8 is shown below in equation 2.9 (for a 1-dimensional system).

$$g(m) = \sum_{n=-\infty}^{\infty} H(n-m) \cdot f(n) + \epsilon \tag{2.9}$$

where n is the number of discrete points described in the real spectra, f, and m is the number of discrete points recorded in the blurred image, f. Note that the real spectra is the spectra that would be observed either using an infinitely high resolution spectrometer, or theoretically based on molecular/atomic structure. As this operation is performed inherently by the LC filter when recreating the spectral signature, the important operation is the inverse operation, a deconvolution to recreate an estimate of f from a recorded g and known H. The four most commonly used deconvolution algorithms used for this estimation in image processing are (1) deconvolution with

the Wiener filter, (2) deconvolution with a Regularized filter, (3) deconvolution with the Lucy-Richardson (LR) Algorithm, and (4) blind deconvolution (BD). Each of these algorithms has a slight variations in how it recreates the original image, or spectrum as is the case here.

Deconvolution using the Wiener filter and regularized filter both utilize least squares solutions in determining the real image/spectrum, and work optimally when some information is known about the PSF as well as about both the noise added in the system by optical/detection system and some frequency aspects of the real image/spectrum. This is difficult in the case of the tunable microspectrometer as the noise varies across the spectra as the blur function changes as the filter redshifts. Additionally, this algorithm should be applied in this case without *a priori* knowledge of real spectrum properties. The iterative algorithmic approaches of Lucy-Richardson deconvolution and blind deconvolution are more suited to this application as all that is required is knowledge of the PSF of the system, and not even that in latter case. The LR and BD algorithms both iterate and maximize the likelihood that the convolution of their solution with given/estimated PSF results in the recorded blurred spectra/image, and in this fashion optimize the solution to the deconvolution, making this most effective when little information is known about the noise in the system. The LR algorithm explicitly takes the PSF of the system as an input and optimizes around this blur function as described in the following summation [100].

$$f^{h+1}(n) = f^{h}(n) \sum_{m=-\infty}^{\infty} \frac{g(m)H(n-m)}{\sum_{n=-\infty}^{\infty} f^{h}(n)H(n-m)} \tag{2.10}$$

where h is the number of cycles through the algorithm, and f^h at h = 0 is an initial guess of the object function. Examining the elements of this function, in each iteration h, the previous estimated real spectra f is scaled by the the convolution of the known point spread function, H, and ratio of the initial blur function g to the "new" blur function (convolution of iteratively determined real spectra, f^h). It is found that when the summation over m converges to one, and thus f^h is unchanging for each cycle, f^h is the highest probability solution for f. Equation 2.10 is derived from the Bayes probability theorem [101]. The blind deconvolution algorithm works in a similar fashion; however, initial guesses exist for both the PSF and the initial object function [101].

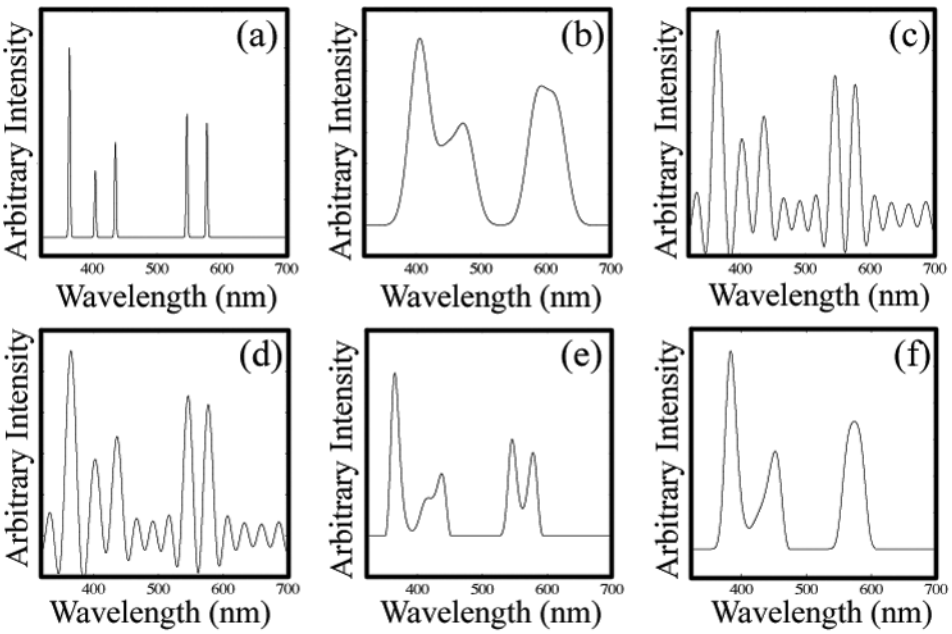

Figure 2.16: Simulate spectra of a mercury emission lamp (a), convolution of simulated spectra with 25 nm gaussian PSF (b), and deconvolutions applied to simulated blurred spectra using Wiener filter (c), Regularized filter (d), Lucy-Richardson (e), and blind deconvolution (f).

2.7.2 Modeled Enhancement

In order to demonstrate the theoretical capability of deconvolution techniques on improving resolution, a simulated mercury emission spectra was created through superimposing several narrow gaussian emission peaks at mercury emission wavelengths (Figure 2.16(a)). This spectra is then convolved as in equation 2.9 with a 25 nm gaussian curve, representing the average blur function observed in the VA-DHFLC microspectometer at an orientation of $\theta_{inc} = 25°$, and is shown in Figure 2.16(b). It is import to note that this is not a perfect simulation of what is happening in the VA-DHFLC system as a contant PSF function is being assumed where, in practice, the PSF is spectrally varying. For the purposes of exploring each deconvolution method, this should be a suitable assumption. This blurred spectra is then deconvolved using the Wiener and Regular filters, shown in Figure 2.16(c) and (d), respectively, and using the Lucy-Richardson and Blind Deconvolution algorithms, shown in Figure 2.16(e) and (f), respectively.

As anticipated, the Lucy-Richardson algorithms performs the best of these four algorithms in recreating the initial spectra as information on the initial PSF is known and passed to algorithm,

while noise information is not needed in this iterative process. While the blind deconvolution also appears to work well in enhancing resolution, it is a less straightforward algorithm as the PSF is modulated during the algorithm and adds another degree of freedom not wanted in this particular case (however, in experimental data with spectrally varying PSF, the blind deconvolution may perform equally as it can optimize the PSF used to be whatever best fits the varying system, as is examined in section 2.7.3). The Wiener and Regular Filters both improve resoluton a bit, but suffer from ringing as a function of the discrete Fourier transform applied. This can be removed through either low pass filtering the resulting deconvolution or smoothing the functions prior to applying algorithms, but is not anticipated these will perform as well as the algorithmic approaches for the reasons stated above. It is also important to note that this this simulated system is an idealized one with a perfectly uniform PSF and no additive noise.

2.7.3 Experimental Enhancement

The capability of deconvolution in resolution enhancement is verified in experimental data. Consider the spectrum of a mercury lamp as determined by a 2 nm resolution spectrometer, depicted in Figure 2.17(a), the convolution of this data, depicted in Figure 2.17(b), and the VA-DHFLC experimentally determined spectrum, depicted Figure 2.17(c). Deviation between the FLC experimentally determined blurred spectra and the convolution of high resolution data with a 25 nm gaussian ((b) and (c)), specifically the intensity variation, is a result of the spectrally varying notch filter properties. As the bandwidth of the reflection notch is more constant in the lower wavelength regime, the spectra is more similar between experimental and convolved data, while the significant difference in the later states is a result of the broadening reflection notch as the filter redshifts.

Both the Lucy-Richardson and blind deconvolution algorithms are applied to the experimentally blurred function, using a 25 nm gaussian as the input PSF for the former and as the initial guess PSF in the latter. The results of these two deconvolutions are shown in Figure 2.17(d) and Figure 2.17(e) below. As is observed, the enhancement through the Lucy-Richardson algorithm over the blind deconvolution is not apparent in this case as the system has a varying PSF and the algorithms

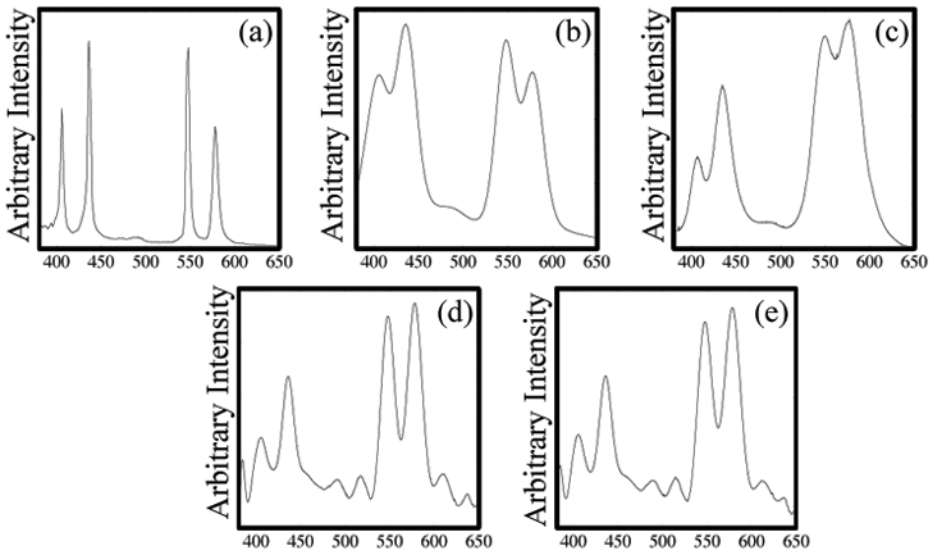

Figure 2.17: Experimentally recorded spectra of a mercury emission lamp (a), convolution of experimental spectra with 25 nm gaussian PSF (b), data when collected with a VA-DHFLC device (c) and deconvolutions applied to experimental spectra using Lucy-Richardson (d), and blind deconvolution (e).

performs just as adequate in estimating the PSF with an initial guess. Incremental resolution enhancement is gained in this system with the application of either of these functions.

2.8 Conclusions

A VA-DHFLC microspectrometer has been fabricated using homeotropically aligned ferroelectric liquid crystal and a single pixel photodiode. This device can be tuned with a narrow reflection notch fully through the visible spectra regime using thermal modulation or potentially applied in-plane electric fields. The reflection notch characteristics were investigated both experimentally measured reflection spectra and modeled reflection spectra treating the VA-DHFLC as a tunable Bragg reflection grating and estimating the effective birefringence through the geometrical configuration. Performance tests involving emission spectra from a liquid crystal display have demonstrated the feasibility and resolution of a microspectrometer created with a single vertically aligned deformed helix ferroelectric liquid crystal and a single pixel photodiode. The VA-DHFLC device was also explored as the active element in a hyperspectral imaging configuration using a spatially resolved

detection element.

A VA-DHFLC based spectrometer is advantageous over other reported methods of fabricating microspectrometers as it only requires two components for operation, does not depend on high resolution focal plane arrays for wavelength resolution, and is straightforward to fabricate and align. While the inexpensive nature of a VA-DHFLC microspectrometer allows it to replace more expensive and bulky spectrometers in rapid and routine screening applications, the ultra-compact aspect of this device enables new applications of spectral analysis where prior instrumentation has limited functionality.

Chapter 3

Stressed Liquid Crystal Fourier Transform Spectrometer

3.1 Introduction: Liquid Crystal Polymer Devices

The previous two chapters have discussed many potential technologies as miniature spectrometers, both LC and non-LC based, and a new technology for tunable filters using ferroelectric liquid crystals. Chapter 3 discusses the application of another novel LC technology as the active retardance element in a Fourier transform spectrometer. As described in Chapter 1, numerous technologies have been explored as alternatives to a Michelson interferometer as the phase modulating element in an FT spectrometer. These include machining of ultra-compact scanning mirror interferometers using electrostatic actuators [19], scanning tilted mirror configurations [20], and other micro-machined and etched moving mirror arrays [21]. Alternatively, static FT devices have been explored using static birefringent materials with spatially resolved detectors [22–27]. The primary design goal of these technologies is to optimize the phase delay while maintaining throughput, size, and scanning repeatability. An optimization of phase delay subsequently maximizes the FT spectrometer resolution through the scaling relation that the frequency bandwidth is inversely related to time/position bandwidth $\Delta v \sim 1/\Delta x$.

Electro-optic and birefringent properties of LC materials enable variable retarders to be constructed and used as the phase modulating element in an FT spectrometer. In this case, the device resolution depends on the maximum amount of optical retardance, subsequently depending on the birefringence and thickness of LC layer with which light interacts. Although electrically controlled birefringence (ECB) cells using nematic liquid crystal can in theory be used, the thin LC layer in most ECB devices (<20 um) translates to a low maximum retardance and low resolution. Methods of increasing the pathlength of light through the samples have been explored as a way to increase resolution without increasing LC layer thickness, as described in Chapter 1. These methods include double-pass systems [64], multiple stacked ECB retarders [63, 66], and multiple stacked retardance switches using SSFLC's [51,65,67,68]. Although adding multiple LC panels increases the retardance of the device, it can also add complexity to the voltage driving schemes in order to synchronize the panel tuning, as well as decreasing optical throughput by increasing the number of optical interfaces. The application of a liquid crystal polymer composites to increase maximum retardance in a single LC panel through increased layer thickness is investigated here.

Liquid crystal polymer composites have been studied in several instances as tunable and photo-reactive diffraction gratings [102–106] because of the capability of photo-patterning these materials while maintaining electrical manipulation of optical properties. Other areas explored for LC polymer composites include variable focus lenses [107, 108] and flexible display materials [109]. These applications benefit from either periodic polymer/LC interfaces, or polymer stabilized LC orientation generated through conventional LC alignment techniques. Alternatively, polymer materials have been used to induce LC alignment themselves in several configurations including micro-contact printing with polymers [110], polymer templating and surface relief structures [111–113], stretched polymer films [114], and polymer filaments [115].

Stressed liquid crystal (SLC) polymer devices are a class of polymer alignment controlled liquid crystals first formally reported by West and colleagues [116–119] for phase retarders and beam stearing applications and subsequently investigated by another group [120] as mechanically tunable gratings and lenses. These materials are low polymer concentration (<20%) composites (lower

than a polymer dispersed liquid crystal (30-50% polymer) but higher than a polymer stabilized liquid crystal (<10% polymer)) that use mechanical deformation to align liquid crystals along the direction of the deformation. The polymer induced volume alignment can stabilize liquid crystal alignment throughout the cell and decrease response times at the cost of an increased drive voltage. Although most applications benefit more from this decreased response time, the implementation of these devices as phase retarders in single panel FT spectrometers benefit from the uniform volume alignment of the LC *throughout* the sample rather than just due to surface boundary conditions. This allows SLC samples to fabricated more than an order of magnitude thicker than would normally be possible in surface aligned LC ECB devices. The subsequent increase in resolution from increased LC layer thickness allows the FT-SLC spectrometer to be a suitable configuration for a chip-sized microspectrometer. Theoretical performance of the SLC as well as experimental results are presented below.

3.2 Stressed Liquid Crystal Polymers

Stressed liquid crystal polymer cells are formed using a mixture of low concentration monomer and nematic liquid crystal to produce a modified ECB cell between two conductive substrates. The monomer is polymerized using a bulk UV exposure, forming a low density polymer matrix around the nematic LC and binding the LC into domains around the polymer fibers. Following polymerization, the LC material is oriented with random director fields due to the lack of surface alignment coating or patterned polymerization, as depicted in Figure 3.1(a). As observed in Figure 3.2, these samples are highly scattering in the unsheared state. This scattering results from both the index mismatch between randomly aligned LC domains as well as the index mismatch between LC and polymer fibers.

A mechanical shear force is applied to the sample by holding one substrate fixed and displacing the other substrate. Because the polymer network is low density, the samples are easily mechanically deformed. This shearing causes the polymer fibers traversing the sample to stretch and deform along the shear axis, as shown in Figure 3.1(b). As documented by other studies, the randomly oriented LC

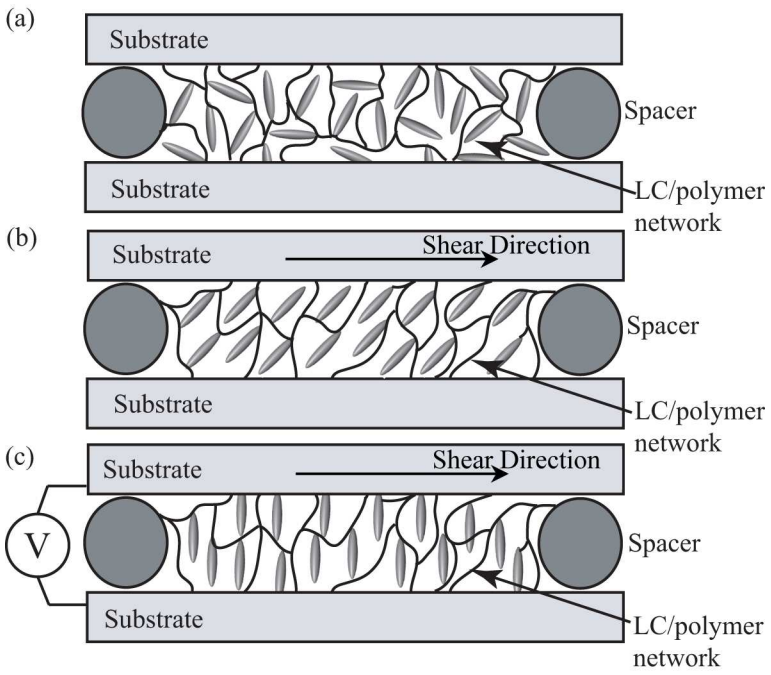

Figure 3.1: Schematic of a stressed liquid crystal in the unsheared (a), sheared (b), and voltage tuned (c) states.

domains in Figure 3.1(b) are aligned as a result of the increased ordering of the polymer system from shearing, subsequently increasing ordering in the LC system [116, 121, 122]. As the polymer fibrils traverse the entire volume of the SLC mixture, the increased ordering is assumed to be highly uniform across the sample apart from small surface defects, inducing uniform LC director profiles that also are uniform across the volume. Unlike surface alignment in conventional ECB cells, the alignment of the LC material is effectively decoupled from the thickness of the cell. The decoupling effect in principal allows LC devices of arbitrary LC layer thickness to be constructed while maintaining passable alignment characteristics. This is limited in practice by scattering effects that remain in the sheared state due to polymer/LC domain index mismatches. Although the LC material is chosen with ordinary index matched to that of the polymer, perfect index matching would only be evident in a perfectly aligned system at the homeotropic zero retardance state.

Analogous to a nematic LC ECB device, applying an electric field across the uniform coated ITO substrates rotates molecules in the LC domains from the planar to homeotropic state, as depicted in Figure 3.1(c). The change in LC alignment with applied voltage changes the effective birefringence of

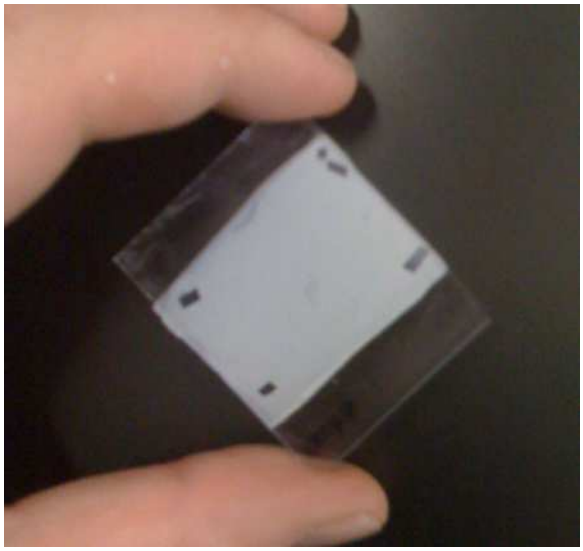

Figure 3.2: Digital image of a 100 μm thick stressed liquid crystal cell of 5CB:NOA65 before shearing at V = 0

the cell caused by the > 80% LC, and consequenly changes the retardance of the sample. Removing the electric field, the polymer induced alignment reorients LC molecules to a planar state along the shear direction. As a result of the volume alignment of the LC, the relaxation times are increased for these samples therefore allow the cells to be driven with switching times < 1 ms reported (for thinner cells) [116], much faster than conventional surface aligned nematic liquid crystal cells.

3.3 Modeled SLC Fourier Transform Spectroscopy

While the concept of FT transform spectrometers were described in an overview in Section 1.2.2, a more complete understanding is necessary to explore the potential performance and complications of implementing an SLC as the retardance element in an FT device. Consider using the SLC retardance element in the same configuration as described in Section 1.2.2 and as shown in Figure 1.4(b) to generate a temporal interferogram for an incoming light source with spectral characteristics denoted by S. Initially, the discrete Fourier transform equation is considered as shown in equation 3.1

$$S'(k) = \frac{1}{\sqrt{N}} \sum_{m=0}^{N-1} s(m) exp \frac{-i2\pi km}{N} \tag{3.1}$$

where s is the measured intensity as function of retardance (or interferogram) over m points in real space, S' is the complex number frequency space FT of the interferogram over k points in frequency space, and N is the maximum number of time points measured in the S. N is correlated to a combination of maximum phase delay $\Delta\phi \sim \Gamma$ generated by the SLC retarder and number of data points sampled in that range. The power spectrum, or intensity at each frequency value, is calculated by the magnitude of the complex vector S', such that $S = |S'^2|$. To understand the effects of retardance and sampling rate on resolution, it is important to note the argument of the exponential in equation 3.1, $-i2\pi km/N$. As N is increased either by increasing the maximum retardance or sampling rate, the frequency spacing between adjacent sinusoids (as k increases) used in the Fourier series is increased. Increasing the number of closely packed sinusoids applied in the Fourier transform equation also increases the frequency/wavelength resolution of the incident light, and thus the FT spectrometer.

The sampling rate requirements also need to be considered in context of the Nyquist frequency. The Nyquist-Shannon theorem states that sampling frequency needs to be twice that of the highest frequency in the system in order to eliminate aliasing in the system. Considering a visible spectrometer, the highest frequency wave to be sampled would be at 400 nm = 7.5×10^{14} Hz, requiring a minimum sampling frequency of 15×10^{14} Hz = 200 nm. In practice, sampling is done more frequently than every 200 nm, at least an order of magnitude faster sampling rate at 20 nm step sizes. The sampling rate is determined by the reliability of the retarder generating small phase shifts will small voltage steps. If the sampling rate is kept constant, resolution enhancement is achieved entirely by the total phase shift range, $\Delta\phi$, and thus maximum retardance avaiable.

Theoretical performance of an SLC can be evaluated using LC material properties. The relationship determining the maximum phase shift $\Delta\phi$ and assuming perfect alignment in the planar and homeotropic conditions is shown in equation 3.2

$$\Delta\phi = d\Delta nv \tag{3.2}$$

where v is the volume fraction of LC in the SLC mixture, Δn is the birefringence, and d is the LC

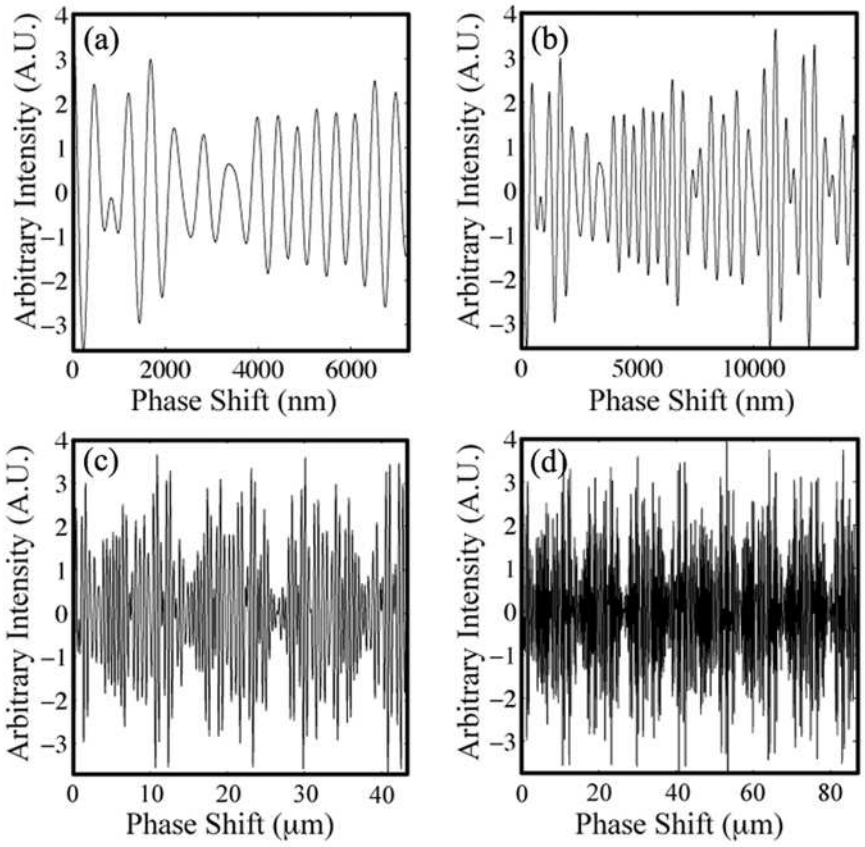

Figure 3.3: Simulated interferograms using Δn = 0.175, v = 0.85, and d = 50μm (a), 100μm (b), 300μm (c) and 600μm (d) for an four frequency system.

layer thickness. Simulated interferograms are then generated using $\Delta\phi$ as the maximum phase shift and assuming a sampling rate of 20 nm. The emission spectra of mercury is chosen as a simulation standard for clarity with peak emissions at λ = 406, 436, 548 and 578 nm, all with intensity of 1 arbitrary unit. Using a 85:15 LC:NOA65 mixture by weight, v = 0.85, and Δn = 0.175 with four LC layer thicknesses of 50, 100, 300, and 600 μm, simulated interferograms are shown in Figure 3.3(a)-(d) while calculated power spectra of each interferogram are shown in Figure 3.4(a)-(d).

Significant increase in resolution is observed with increasing layer thickness, highlighted by the resolution of the doublet at λ = 548 and 578 nm. The FWHM of the peak at 406 nm decreases at d = 100 μm , 300μm and 600 μm from FWHM = 20nm, 4nm, and 3 nm, respectively. The 50 μm cell does not resolve peaks at 406 and 436 nm. Note that the intensity of peak values is difficult to isolate using perfectly periodic functions as the intensity of the peak depends on how close the

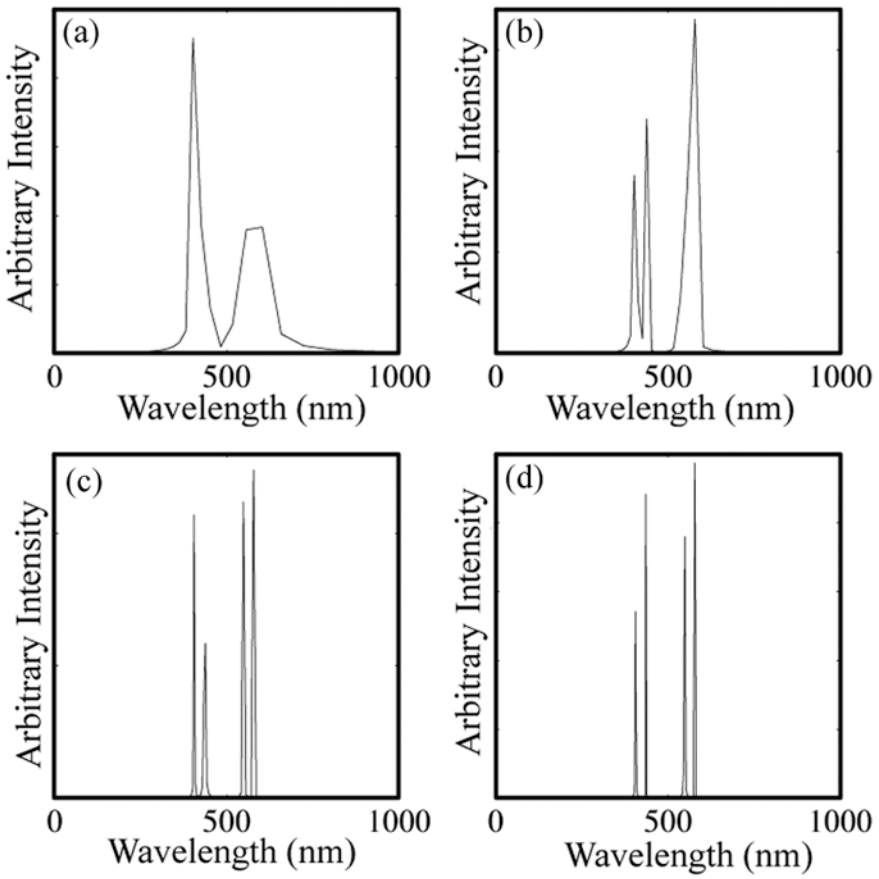

Figure 3.4: Power spectra calculated from FT of simulated interferograms of four frequency system in Figure 3.3 for d = 50μm (a), 100μm (b), 300μm (c) and 600μm (d).

sinusoids used in the FT are to the actual peak values.

Deviations from an ideal signal may result from the SLC tuning and detection components. These deviations include noise in the intensity from detection (shot) noise and fluctuations in the phase shift position of peaks from potential filter tuning variability, both in a random (normal distribution around phase shift expected at a given peak) or systemic (overall nonlinearity in the phase shifts caused by improper calibration of filter tuning characteristics). The effects of these three deviations can be observed in Figure 3.5 (a)-(c) showing the FT results on the 300 μm cell (with ideal simulated mercury power spectra pictured in Figure 3.4(c)).

Figure 3.5 (a) shows the power spectra with severe shot noise applied to the interferogram; noise is of normal distribution with SD = 25% of maximum intensity of the interferogram. Because the periodicity is stable and the noise is randomly fluctuating, little effect is observed in the power spectra

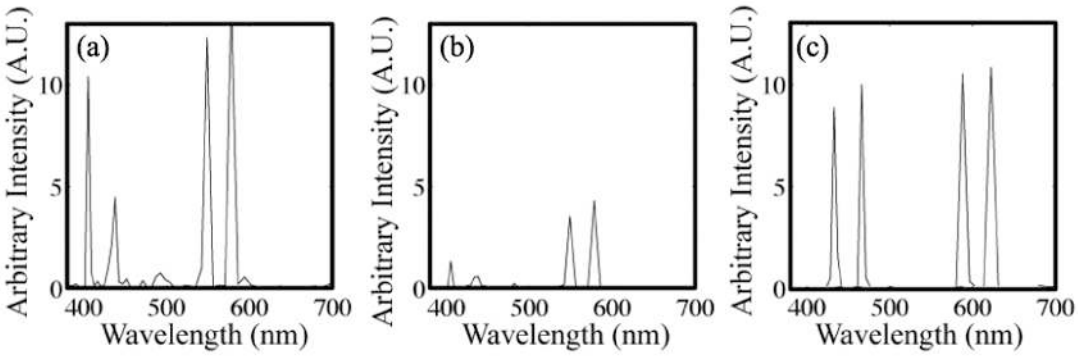

Figure 3.5: Using the modeled interferogram of a 300 μm shown in Figure 3.3(c), the effect of detector noise (a), noise in the phase delay (b), and an incorrectly calibrated phase delay curve (c) on the FT spectra.

of simulated mercury spectra. Figure 3.5 (b) shows the effect of random fluctuations of the phase shift corresponding to the intensity data, simulating noise in the calibration of the retardance vs. voltage curve of the SLC. Again, assuming the noise is normally distributed around the correct phase shift, the FT calculates accurate spectral distribution of emission wavelengths; however, because the periodic functions have been blurred and are now less defined, the intensity of each peak has decreased due to less overlap with each sinusoid in the Fourier transform. This is of concern in weak signals without a lower signal to noise ratio than in simulated data. Figure 3.5 (c) shows the effect of an improper retardance vs. voltage curve in the SLC, causing the periodicities of oscillating signals to be incorrect and the frequencies calculated in each component to also be incorrect, clearly evident by the shifted peaks. Note that changing the frequencies of the peaks also changes the intensities for the same reason stated above for perfect sinusoids, and is not a result of this improper retardance vs. voltage calibration.

While the above issues are of concern, they can be minimized by measuring an accurate retardance calibration for the SLC filter. The most significant change occurs from the optical scattering of the filter, which varies with tuning voltage and subsequently causes changes in both the mean signal level and the modulation depth in the interferogram. The scattering change results from increased LC/polymer index matching as the sample tends toward homeotropic where the ordinary index and polymer index are matched ($n_p \approx n_o$). This correlates to variation in the interferogram where the

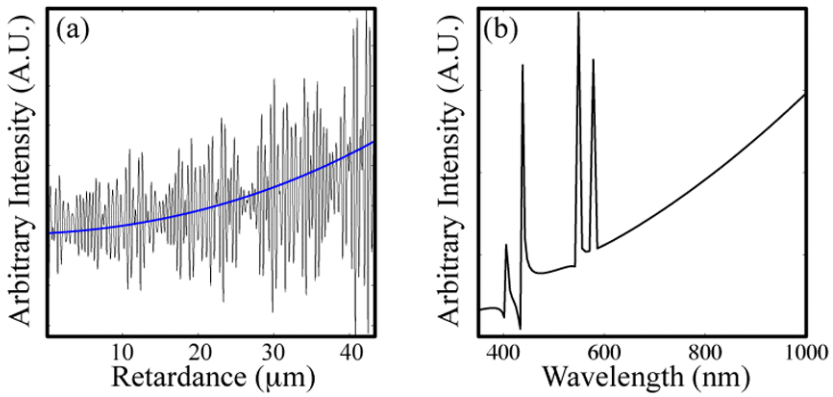

Figure 3.6: Deformation of interferogram with addition of scattering scaling factor dependent on retardance (a) and resulting deformation of the power spectra of simulated mercury emission (b).

intensity has a higher mean signal and modulation depth at lower retardance values. The resulting effects on the interferogram can be observed by adding these effects to simulated sinusoids, as shown in Figure 3.6 (a), and subsequent FT power spectra, as shown Figure 3.6 (b), again using a simulated 300 μm thick cell. The scattering deformation induces a background broad signal in the FT, distorting the features of the emission spectra, and as such should be accounted for in signal processing of these FT signals.

The above modeling studies highlight three key factors in designing the SLC spectrometer. First, at least 100 μm thick cells are needed to obtain useful spectral information. Second, a well fitting calibration is needed between the retardance and voltage applied to the filter to ensure accurate wavelength determination. Lastly, the effects of scattering in distorting the interferogram need to be removed to preserve spectral recreation without large defects.

3.4 SLC Phase Modulator Construction

The potential performance of SLC phase modulators as FT spectrometers encourages further investigation into fabrication of thick SLC cells, verification of their performance as phase modulators, and testing of their performance as spectrometers on single frequency optical sources.

3.4.1 Filter Fabrication

Constructing SLC polymer devices is a relatively straightforward three step process. Nematic liquid crystals, either 5CB, E7, or BL038 (EMD Chemicals, Hawthorne, NY) are mixed with a small amount of UV activated polymer, Norland Optical Adhesive #65 (NOA65, Norland, Cranbury, NJ). Mixture concentrations, by weight %, can range from 80:20 to 95:5 LC:polymer depending on several design parameters such as cell thickness, desired optical throughput, and amount of shear applied. Preceding publications have reported successful device fabrication using mixtures of 90:10 LC:polymer [116, 118] using 22 μm and 40 μm cell gaps, respectively, 85:15 LC:polymer [120] at 25 μm cell gaps, and 94:6 LC:polymer [119] at 12 μm cell gap. As the focus of this application is on constructing larger cell gap materials for large phase modulation devices, higher percentage polymer mixtures were explored to ensure mechanical stability across cell gap. It was found that the 90:10 mixture often delaminated during shearing of thick cells (> 50 um), thus an 85:15 LC:polymer and 80:20 LC:polymer mixture were investigated. The 5CB:NOA65 system was chosen because it has the best index matching between polymer and LC, allowing scattering to be minimized through a thick cell. 5CB has ordinary index of 1.531 and birefringence of 0.175 and the refractive index of NOA65 is 1.52 at room temperature. Unfortunately, the 5CB also has a low isotropic temperature (T_i = 35°C) and therefore, heating of the sample through optical absorption must be kept to a minimum through lower light intensities.

The LC/polymer mixture is stirred on a hot plate at 100°C for 30 minutes, well above the LC clearing point. Substrates are prepared using 1 mm thick cleaned glass plates coated with indium tin oxide. The bottom substrates have a dimension of 3.75 cm × 3.75 cm and the top substrates have a dimension of 3.75 cm × 2.54 cm to allow a 2.54 × 2.54 cm active area with border around allowing for simple electrode placement or alligator clips to be attached. The target thickness was a cell with 100 μm cell gap, achieved using mylar film spacers at approximately this thickness. Small areas of the mylar film spacers were deposited at each corner of the bottom substrate, the material pipetted onto the center, and the top substrate placed over the spot and lightly pressed onto the spacers. A balloon press was not used due to squeezing of material from the sample edges in such a

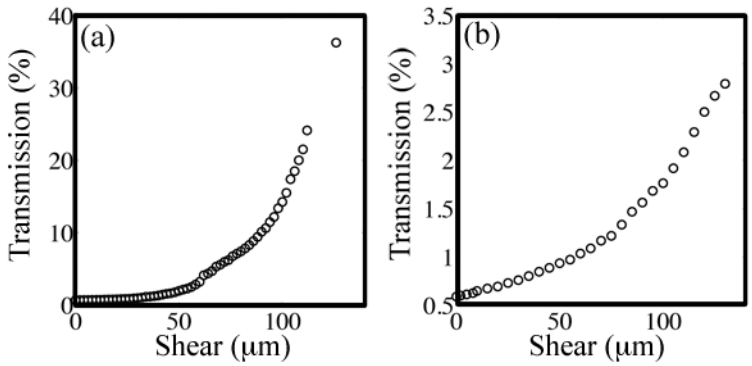

Figure 3.7: Plot of the transmission through a 100μm SLC as a function of shearing distance over a solid angle of 5° (a) and 1° (b).

thick sample. An image of a fabricated sample is shown in Figure 3.2

The samples were exposed in a silver halide UV exposure box for 120 minutes. Samples were exposed while holding the LC in the isotropic state on a hotplate at 100° C, leading to higher transparency in samples as noted by West and colleagues [116]. We hypothesize that this allows polymer threads to freely form through the sample while LC is in the isotropic state, and ultimately reduce scatter through uniform polymer fiber and LC droplet formation. Following exposure, cells were allowed to cool before inducing alignment through shear. Transmission through the cells before shearing is primarily below 1%.

3.4.2 Mechanical Shearing

Shearing of SLC samples was performed with an in-house assembled μ-precision shearing stage using a single dimension translation stage. Based on personal communcations with the West lab at Kent State, shearing was applied slowly, at no greater that 10 μm per 5 second period, and with maximum shear amount of ∼120% of the cell gap, or ∼120 μm. Shearing of the sample produces an obvious and easily observable increase in the transmission through the sample indicating the mechanically induced induced alignment of the LC through pulling of the polymer threads. A plot of the transmission spectra and percent transmission versus amount of shear is shown in Figure 3.7. The transmission of a 100 μm cell reaches its maximum just beyond 120 μm shear displacement with the percent transmission approximately 35% over an angle of approximately 5°. Reducing the

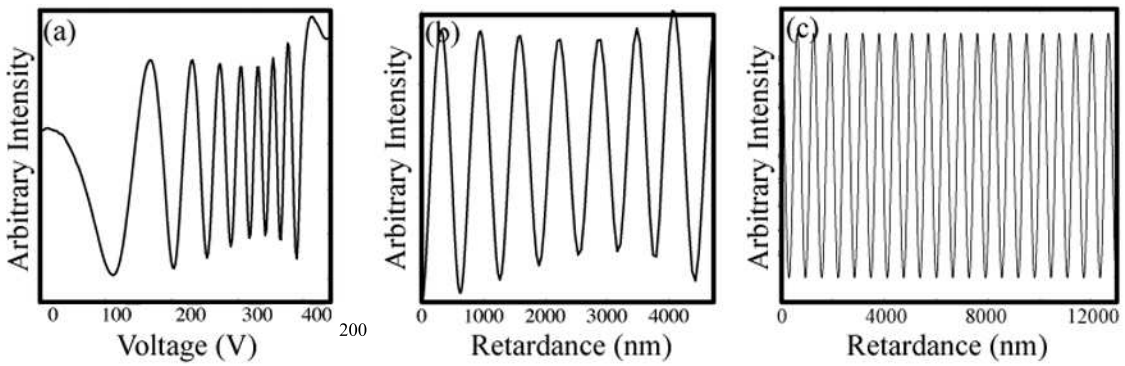

Figure 3.8: Intensity modulation of a Helium-Neon laser monitored through 100 μm thick SLC driven from 1-400 V (a) and the subsequent interferogram created by fitting the voltage to retardance values (b). The modeled interferogram assuming a perfect SLC retardance filter of thickness 100 μm, LC 5CB and 85 % LC vs. polymer

solid angle of collection from 5° to 1°, the maximum transmission decreases to $\sim$ 3%. Figure 3.7 (a) shows the transmission of the unscattered and paraxially scattered light while Figure 3.7 (b) more closely represents light transmitted through the sample that is completely unscattered.

3.5 Microspectrometer Performance Validation

The ability of the SLC to function as a microspectrometer was examined by looking at various sources and quantifying the ability to recreate the emission spectra.

3.5.1 Single Pass Laser Measurement

The capability of generating interferograms and subsequent FT spectra was validated in proof of concept experiments using a single frequency laser emission passing through the SLC retarder in two configurations. The first group of SLC retarders were fabricated using a 85:15 mixture of liquid crystal 5CB:NOA65 fabricated as described above using 100 μm mylar spacers. The samples were cured and sheared in the μ-shearing device to a displacement of $\sim$120 μm. Leads were soldered onto the exposed ITO at the sample edges and attached to function generator and amplifier for driving voltage. The sample was driven from 0 - 400 V PP using a 1 kHz sine wave in 1.5 V increments. Data was read from a p-i-n photodiode (Melles Griot, Rochester, NY) through a wide-band amplifier and multimeter interfaced to PC using HP-VEE software package (Hewlett Packard). The raw intensity

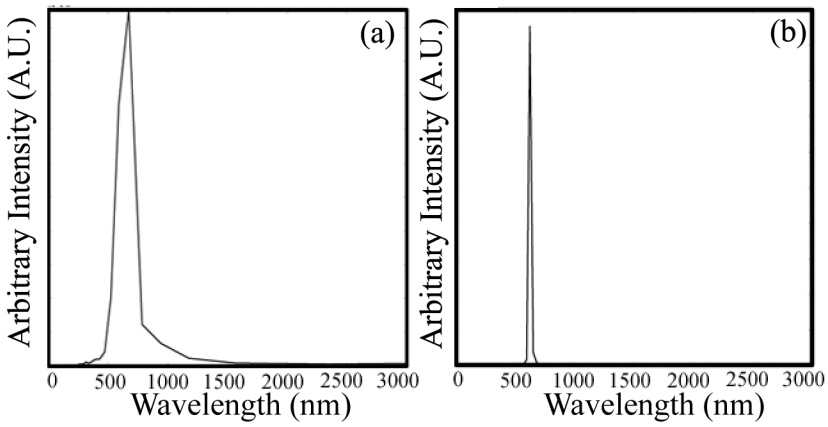

Figure 3.9: Power spectra from 100 μm thick SLC retarders using experimental (a) and theoretical optimized (b) system.

pattern observed in these samples is shown in Figure 3.8(a) using a 632.8 nm Helium Neon laser at 5 mW power with SLC oriented at 45° with respect to polarizer and analyzer.

As observed, the change in retardance, and corresponding variation in LC alignment begins at 20 V and gradually continues to phase shift at low voltages. Above 100 V, the phase shift becomes roughly linear with applied voltage, until the LC is aligned in the homeotropic condition and the intensity remains constant at its maximum value above 400 V. As the voltage/retardance relation is not linear throughout the phase shift range, the calibration is established using a piecewise spline fit between the position of each maximum peak location, corresponding to 632.8 nm of retardance. A plot of the intensity versus phase shift (interferogram) using the spline fit calibration is shown in Figure 3.8(b). The fitting has forced the modulation to a linear periodic function which can be Fourier transformed without defects from the nonlinearity of phase shift with voltage at low voltages (simply, the fitting allows the whole intensity pattern to be used and not just the higher voltage linear segment).

An interferogram is also generated using the experimental parameters of v = 85%, $\Delta n = 0.17$ and d = 100 μm shown in Figure 3.8(c). This function represents the ideal case of perfect planar and perfect homeotropic alignment in the two system states as well as a scattering free system. The experimental interferogram shows a maximum retardance of $\sim$4.5 μm while the theoretical interferogram shows a maximum retardance of $\sim$12 μm. This indicates factor of three deviation

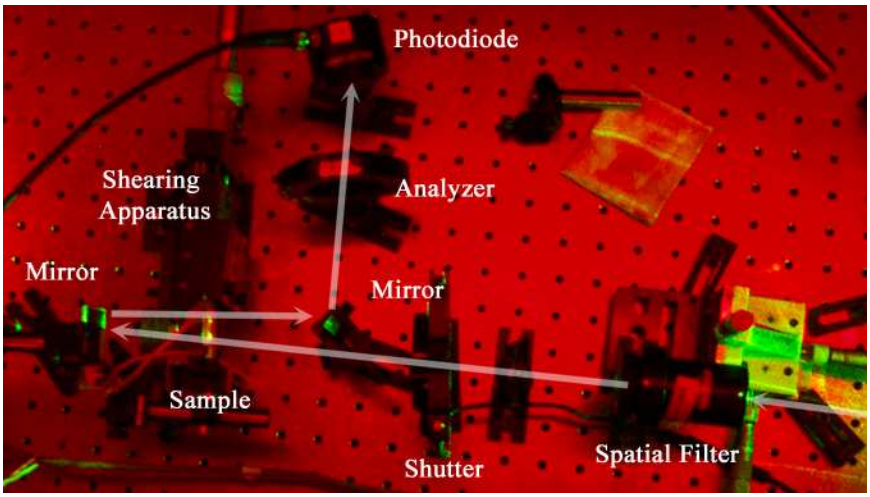

Figure 3.10: The experimental configuration for a double pass FT spectrometer using the SLC retardance filter

from ideal performance as a result of non-ideal planar/homeotropic alignment in the sample.

The FT is calculated and power spectra plotted for both the experimental and theoretical interferograms shown in Figure 3.9 (a) and (b). The reduction in maximum phase delay in the experimental versus theoretical optimized model accounts for the significant reduction in the resolution. The FWHM of the laser peak as recorded by the experimental interferogram is 160 nm while the theoretical FWHM is 50 nm. This degree of resolution is likely not suitable for most applications. In order to improve the resolution of this system, the sample was probed using a double pass system in the same fashion as described by Itoh and colleagues [64].

3.5.2 Double Pass Laser Measurement

A system for two passes through the SLC retarder to generate additional phase shift was constructed and is pictured in Figure 3.10. Samples to be used in the double pass SLC phase retarder were fabricated identically to the single pass SLC measurements above, except that the liquid crystal concentration v was decreased to 80% to attempt to eliminate delaminating effects over time observed in thick samples with lower polymer concentration. A plot of intensity versus retardance of a double pass setup is shown in Figure 3.11 (a) for voltage 1-500 V. The data presented is clipped to the useful voltage range exhibiting index modulation from V = 80-400V. A solid state Verdi laser at λ

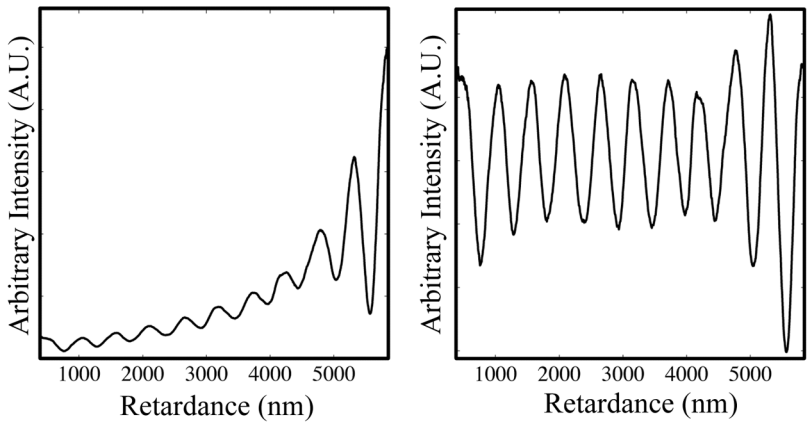

Figure 3.11: Interferograms generated using double pass SLC retardance filter (a) and the intensity corrected version (b) accounting for scattering change with LC alignment

= 532 nm was used to straightforwardly characterize and quantify the spectrometer performance of this system. The laser source was switched from a He:Ne to Verdi in order to obtain a higher quality beam profile through spatial filtering apparatus aligned with the latter.

The increase in polymer concentration for 15% to 20% coupled with the increase in pathlength generates additional scattering in the system which manifests as both (1) reduced modulation in intensity over each period and (2) an average intensity pattern which varies more significantly with applied voltage, explicitly the average intensity increases with increased LC alignment as n_o is matched with n_p. This intensity can be corrected by measuring the intensity transmission through the sample without the second polarizer (analyzer), eliminating variation in intensity not attributed to the phase modulation. The voltage versus intensity can be fit and subtracted from the interferogram to yield phase only intensity modulation, and then the interferogram normalized by the fit to adjust the modulation intensity. The resulting intensity corrected interferogram is shown in Figure 3.11 (b).

The power spectra calculated from the FT of the interferogram for the double pass system is shown in Figure 3.12. As shown, the additional increase in effective pathlength results in an increased maximum retardance from 4.5 μm to $\sim$ 6.0 μm which correlated to an increased resolution from 180 nm to 60 nm FWHM for the single and double-pass configurations, respectively. Two factors of note; first, retardance does not increase purely by a factor of two as a result of (1) the increased

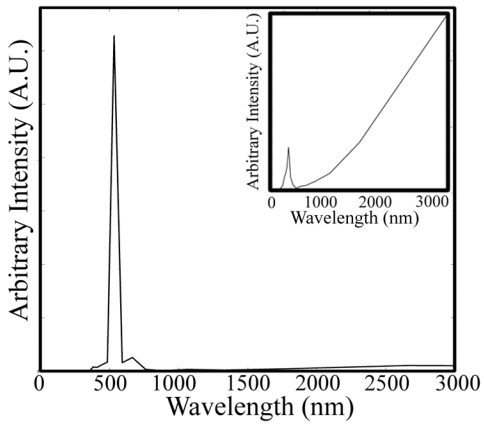

Figure 3.12: Spectra obtained for $\lambda = 532$ nm laser collected using double pass system INSET: FT of non-intensity corrected interferogram

polymer concentration decreasing LC birefringence and (2) increased scattering limiting the amount of light passing through the sample, and thus the low voltage modulations in intensity cannot be observed (where scattering is at a maximum). Second, part of the increase in resolution is due to the higher frequency source used in the double pass system. The higher frequency translates to more periods being samples and subsequently, a lower FWHM. The inset shows the resulting FT from the non-scattering corrected interferogram to highlight the need to correct the intensity before processing, similar to the effects observed in simulations of Section 3.3.

3.6 Conclusions

Constructing a modified ECB cell with low density polymer network stabilizing LC alignment enables the fabrication of high retardance phase modulators, and subsequent FT spectrometers using fewer panels than conventional ECB devices. Proof of concept study showed a spectrometer using a single SLC panel capable of 60 nm resolution of a single frequency system using a two-pass system. Pushing the upper limit of cell thickness while maintaining the best possibly transmission through index matching and optimized director profiles will continue to increase the resolution of these single panel microspectrometers.

Chapter 4

Noninvasive Hemoglobin Determination

4.1 Introduction: Causes and Manifestations of Anemia

Chapter 2 and 3 presented novel approaches for the design of miniature spectrometers. Chapter 4 discusses the primary motivation for studying these devices: the development of a new technology for the diagnosis of anemia. Initially presented are the clinical definitions, causes, and clinical manifestations justifying the need for anemia screening, followed by alternative approaches to this problem, and concluded with an in depth look at the theory and experimental results of a new approach to detection.

4.1.1 Clinical Definition

Anemia is clinically defined as a significant reduction (two standard deviations (SD)) in either the number of red blood cells (RBCs) per unit volume of whole blood, the amount of packed RBCs per unit volume of whole blood, or most generally the amount of the oxygen/CO_2 transporting protein hemoglobin (Hgb) from the clinically determined 'normal' value [123]. The World Health Organization (WHO) has defined the lower bound Hgb concentration for healthy vs. anemic patients

(adults over 18 years of age) as 13.0 g/dL for males and 12 g/dL for females based upon the normal range determined from a large population of healthy individuals [124]. This value has been accepted by the Center for Disease Control and similar values are reported in several hematology textbooks [125–127]. Discrepancy between male and female Hgb concentration is caused by the male sex hormone androgen's effect on the release of erythropoietin from the kidneys. Erythropoietic is the growth factor regulating synthesis of RBCs from pluripotent hematopoietic stem cells (RBC precursor cells). According to the National Anemia Action Council (NAAC), anemia affects 3.4 million Americans and millions more may be undiagnosed or at increased risk of developing anemia [128]. The WHO reports anemia may affect 2 billion people worldwide using their clinical definition, or roughly one-third of the world's population [129].

4.1.2 Pathological Causes

Although hundreds of types of anemia exist, the underlying mechanisms of anemia can be divided into four primary categories, hemorrhagic, hemolytic, inhibited RBC synthesis, and anemia of chronic disease. These categories are not mutually exclusive; the reduction in hemoglobin concentration may be a result of numerous factors.

Hemorrhagic Anemia

Hemorrhaging is the most serious casue of anemia in terms of mortality and the most common cause seen in clinical practice. Bleeding can be a result of trauma, surgery, or acute/congenital bleeding disorders and causes a reduction in the number of circulating RBCs and thus hemoglobin concentration. The reduction of hemoglobin concentration following acute blood depends on the elapsed time. Immediately following blood loss, the total blood volume decreases but the hemoglobin concentration remains constant because plasma and RBCs are lost in equal proportion. Gradually fluid from tissues replenishes blood volume in circulation and dilutes the hemoglobin concentration over the successive hours. The fall in hemoglobin concentration from acute hemorrhage is observable around three hours following onset depending on severity; thus, a hematological examination will

not provide insight into acute hemorrhages in the earliest stages [127]. Further, acute anemia inhibits adaptive physiological responses due to rapidity of disease onset. Slowly manifesting hemorrhagic anemia or chronic anemia stimulates compensatory responses including tachycardia, decrease in vascular resistance, decrease in renal blood flow, enhanced oxygen dissociation, and the stimulation of new RBC production through an increase in the production of erythropoietin by the kidneys. Acute anemia stimulates rapid physiological responses including hypovolemia, vasoconstriction, and increased ventricular stroke volume, all of which are detrimental to cardiovascular function. One of the most common causes of hemorrhagic acute anemia is heavy menstruation in women of reproductive age. Menohhagic (heavy menstruation) anemia represents a serious problem for otherwise healthy women as well as those with pre-existing conditions such as iron-deficiency anemia or other hereditary anemias [130]. Another common location for internal hemorrhaging is the gastrointestinal tract.

Hemolytic Anemia

Hemolytic anemia is characterized by a premature destruction of RBCs such that bone marrow production of RBC cannot compensate, leading to a reduction in hemoglobin concentration. The average lifetime of a RBC following production from the bone marrow is 120 days, after which RBCs are broken down in the spleen and iron content is recycled into new cells. Hemolytic anemia can occur either due to intrinsic RBC defects, or extrinsic disorders causing destruction and may be the result of congenital or acquired conditions. Intrinsic RBC defects are primarily the result of congenital conditions while extrinsic hemolytic disorders are primarily acquired anemias. Example intrinsic defects include (1) RBC membrane disorders such as hereditary spherocytosis, a disorder marked by a congenital defect of the primary erythrocyte membrane component causing RBC to weaken structurally and be susceptible to spontaneous hemolysis, (2) enzymatic defects glucose-6-phosphate dehydrogenase (G6PD) or pyruvate kinase (PK) deficiency affect RBC metabolism and cause a premature destruction of the RBC either extravascularly (in the spleen) or intravascularly, and (3) hemoglobin defects causing RBCs to be perceived as aberrant and broken down in the spleen.

Hemoglobin defects include hereditary sickle cell anemia, a physical abnormality occuring from a polymerization of defective hemoglobin molecules in the RBC causing a deformation of membrane into a crescent/sickle shape along with concurrent obstruction of microvascular pathways resulting in premature hemolysis. Other forms of hemoglobin defect are various thalassemias, characterized by an imbalance in the production of either the α globin chain (α-thalassemia major) or β globin chain (β-thalassemia major). The most common extrinsic hemolytic anemias is autoimmune hemolytic anemia (AIHA), the result of an antibody binding to an antigen on the RBC membrane and shortening RBC lifetime. AIHA has several forms and severities depending on binding antibody being utilized, however, common causes for AIHA include chronic leukemia, lymphoma, and immune disorders such as AIDS. Extrinsic hemolytic anemias also may be drug induced immune reactions. Hypersplenism is the increased activity of the spleen causing increased RBC destruction and corresponding hemolytic anemia. Damaged microvascular structures constitute an extrinsic disorder and can damage RBCs structural integrity and cause premature hemolysis, resulting in microangiopathic hemolytic anemia.

Inhibition of Red Blood Cell Synthesis

The inhibition of RBC production from the bone marrow is influenced through nutritional inadequacies, kidney disorders, and bone marrow disorders. Nutritional anemias are the predominant worldwide form of anemia, especially in regions of economic depression. According to the WHO and International Food Policy Research Institute, nine out of ten anemics live in developing countries [131]. The three chief types of nutritional anemias are iron, vitamin B12, and folic acid deficiency. Iron is the primary component of the oxygen binding heme unit present in the transport protein hemoglobin as well as the storage protein myoglobin. Iron deficiencies occur either from increases in iron requirements (growth, pregnancy, etc.) or inadequate iron supply (insufficient dietary iron or impaired absorption of ingested iron), both of which restrict RBC production or stimulate production of hypochromic (low mean cell hemoglobin concentration) and microcytic (undersized) RBCs. Vitamin B12 (Cobalimin) and Folic Acid deficiency are both deficiencies causing abnormal

RBC production. Vitamin B12 deficiencies occur both through dietary inadequacies or inadequate absorption of ingested B12. Pernicious anemia is a chronic progressive anemia in older adults due to an inadequate absorption of B12 because of an autoimmune destruction of B12 absorbing substances. Folic Acid appears in blood serum proteins, and deficiency occurs primarily in malnourished individuals. However, folic acid deficiencies do occur as a result of drugs, diseases of the intestine (where folic acid is absorbed), and HIV. Chronic Kidney Disease (CKD) frequently causes anemia through inhibition of erythropoiesis (RBC synthesis). Kidney disorders inhibit production of erythropoeitin (EPO), the growth hormone regulating production of RBCs from the bone marrow, and thus often cause anemia. It has also been shown that CKD concurrent with anemia has increased the risk of stroke [132]. Disorders affecting RBC precursor cells in the bone marrow include acute and chronic leukemia. Aplastic anemia suppresses the development of RBC precursors cells and is often a spontaneously occurring disorder.

Anemia of Chronic Diseases

Apart from the overview of the pathological causes above, anemia may manifest itself with other diseases based on disturbances of iron homeostasis and erythropoiesis. These are termed anemias of chronic diseases (ACD) and are the most frequent anemias in hospitalized patients [133]. While iron is essential to the erythropoietic process, its physiological presence must be highly regulated as it is detrimental to surrounding tissues as it may catalyse the formation of highly toxic hydroxl radicals [134]. Chronic inflammatory diseases such as cancer, chronic infections, rheumatoid arthritis and autoimmune diseases disturb iron homeostasis and remove iron from bone marrow regions of erythropoiesis. ACD is an active immune defense system which withdraws the growth factor iron from invading pathogens to improve cell-mediated immunity [133]. Anemia of chronic disease also inhibits the response of bone marrow RBC production to compensatory increased erythropoietin levels. As an example study, Baer *et al* reported on the erythropoietin (EPO) levels in response to anemia for patients with and without rheumatoid arthritis (RA) and found a blunted response in EPO production to anemia for the RA patients as compared to those without, indicating the

inflammatory disease inhibits the triggered anemic responses of increased RBC production [135].

4.1.3 Clinical Manifestations

The myriad of causes highlighted previously lead to numerous clinical manifestations of anemia; however, there are several uniform symptoms. Acute anemias, mostly hemorrhagic anemias, result in ultra-low blood pressure (hypotension), loss of consciousness, and shock. More chronic anemias or slowly manifesting hemorrhagic anemias result in tissue oxygen shortages. Tissue hypoxia leads to fatigue, difficulty breathing, cognitive abnormalities, and pain caused by a lack of blood flow to a particular region (angina). As stated previously, anemia also manifests itself as tachycardia, heart palpitations, or possibly congestive heart failure. Hemolytic anemias frequently result in jaundice as a result of increased serum bilirubin levels, a breakdown product of hemoglobin. Hemolytic anemias also form pigment gallstones from high turnover of iron (heme). Sickle cell anemia is characterized by "sickle cell attacks", painful episodes resulting from abnormally shaped RBCs occluding blood flow of of microvascular blood flow. Vitamin B12 and Folic Acid deficiencies often exhibit nonhematological symptoms including effects on epithelial tissues causing a more red appearance, especially on the tongue, as well as nueropsychiatric disorders including sensory difficulties, optic atrophy, and psychiatric issues. Anemia of chronic diseases is obviously manifested as symptoms of the inflammatory disease itself.

4.2 Diagnoses Methods

Exhibition of aforementioned symptoms is only a precursor to discerning the mechanism of anemia and treating the disorder. Suspicion of anemia prompts hematological examination of the patient, specifically RBC characteristics. Red blood cell characteristics can be obtained using several methods.

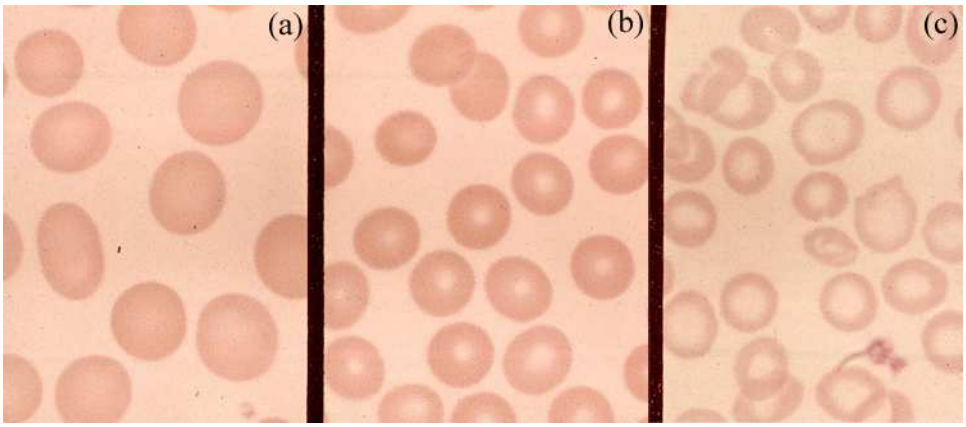

Figure 4.1: Microscope images of Macrocytic (a), Normocytic (b), and Microcytic (c) RBCs. Adapted from Marist College [136]

4.2.1 Invasive Diagnostics - The Complete Blood Count

Invasive determination of blood hemoglobin levels remains the dominant form of anemia diagnoses and the method most clinically embraced. The complete blood count (CBC) examination necessitates collection of blood either by intravenous blood draw or lancet finger prick. Collected blood is mixed with an anticoagulant to prevent clotting and analyzed for complete plasma cellular propoerties. The amount of diagnostic information that may be obtained from a CBC is vital to accurate diagnosis of the anemia mechanism. The CBC reports seven primary RBC indices, in addition to white blood cell (WBC) counts, platelet counts, and differential counts of each of the five white blood cell types (basophils, monocytes, lymphocytes, eosinophils, and neutrophils). The most critical RBC indices are (1) the hemoglobin concentration (Hb), amount of hemoglobin per unit whole blood, and the hematocrit (Hct), the percent volume of whole blood occupied by RBCs. Either of these parameters may initially be used to detect anemia. Following detection, the remaining five indices coupled with the Hb and Hct become significant for anemia classification. The red blood cell count is the absolute number of RBCs per volume of whole blood. This parameter can be supplemented with a reticulocyte count. A reticulocyte is young erythrocyte just released into circulation from the bone marrow which is biochemically and morphologically different from a mature RBC, allowing the two cells to be discerned. The reticulocyte count is expressed as a percentage of reticulocytes amongst all RBCs and is valuable in determining bone marrow function in response

Figure 4.2: A commercial CBC instrument from Sysmex (Kobe, Japan).

to anemia. As an example, hemorrhagic blood loss or hemolytic anemias will induce more RBC production and increase the reticulocyte count, while bone marrow disorders will inhibit RBC production and lower the reticulocyte count. The average reticulocyte count is 2 percent, however the erythropoeitic system is capable of increasing RBC production up to eightfold from normal RBC synthesis rates [126]. The mean cell volume (MCV) is a determination of the mean RBC volume. The MCV is utilized to discriminate mechanisms causing microcytic (undersized - iron deficiency anemia, hemoglobin defects, certain anemias of chronic disease), normocytic (normal-sized - acute hemorrhagic anemia, CKD, bone marrow disorders), or macrocytic (oversized - vitamin B12 and folic acid deficiency, chronic bleeding anemia, drug induced anemias), as shown in Figure 4.1. The mean corpuscular (cell) hemoglobin and mean corpuscular (cell) hemoglobin concentration represent how much hemoglobin is in each cell and are both used to discern certain anemias causing hypochromic (lowered cellular hemoglobin content) or normochromic (normal cellular hemoglobin content) RBCs. The last RBC indice is the red blood cell distribution width (RDW) which is a distribution of MCV's providing information on the size variability of RBCs aiding in discerning factors inducing microcytic, normocytic, and macrocytic anemias. Parameters of the CBC are obtained using biochemical assays, flow cytometry, and analysis of blood smears, contemporarily in a fully integrated workstation. Although remaining invaluable as a test for many specific anemias, CBCs are time consuming, costly, and increase risks of phlebotimist exposure to blood-borne pathogens.

If the full CBC results are not necessary, blood can be centrifuged at the bedside providing a hematocrit determination (termed small volume devices); however, this remains an invasive technique and creates cross-contamination possibilities for neighboring patients and physicians.

4.2.2 Contemporary Non-invasive Hemoglobin Monitoring

In the contemporary climate of non-invasive diagnostics, the CBC and finger prick methods remain antiquated. While it is not anticipated that non-invasive techniques in their infancy will provide as much diagnostic information as the CBC, a rapid screening tool will alert physicians to a patients anemic hemoglobin levels and encourage further investigation/CBC analysis. The time and cost associated with a CBC have likely prohibited this parameter from becoming part of routine physical examinations.

Repeated anemia screening for high risk demographics including pregnant women, children, and elderly would also draw great benefit from rapid non-invasive anemia detection. The necessity of an enhanced technique to rapidly screen for anemia has resulted in investigations on numerous non-invasive hemoglobin measurement methods. Yamakoshi *et al* early reported on abilities to monitor hematocrit by submerging the finger in an electrolyte solution and calculating the electrolyte concentration necessary to eliminate pulsatile changes in resistivity (blood resistivity varies with hematocrit) [137]. Yamakoshi *et al* further reported that hematocrit could be determined by simultaneously measuring finger resistance and pulsatile volume changes and inferring volume normalized changes in resistivity from patient to patient [138]. Rice *et al* has reported on potentials of using standardized retinal imaging as an indicator for hemoglobin, serum bilirubin, and glucose [139]. While these techniques have shown promise, they have struggled to gain clinical acceptance due to expensive costs, complicated instrumentation, and inaccuracies comparative to CBC blood testing. Clinical noninvasive devices require simple operation and compact size in order to replace/supplement heavily relied upon tests such as the CBC

Because hemoglobin is one of the primary chromophores in cutaneous tissues (absorption spectra shown in Figure 4.3), optical techniques have been extensively evaluated. Pulse oximetry, arguably

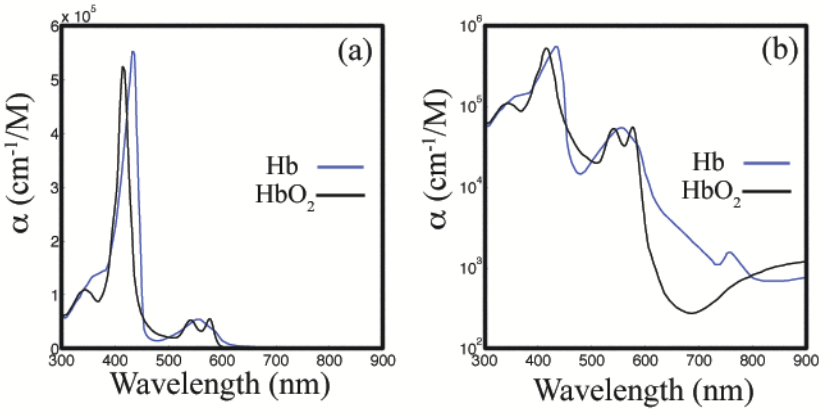

Figure 4.3: Pure spectra of oxy and deoxyhemoglobin in terms of molar extinction coefficient α (a), and same plot on a log scale (b).

the most successful noninvasive spectroscopic technique, utilizes spectroscopic characteristics of oxy- and deoxyhemoglobin to determine relativistic concentrations of each species; however, a viable and accepted analogous noninvasive method for *total* hemoglobin concentration has yet to be developed. A survey of potential optical methods of total hemoglobin measurement is presented here.

Photometric evaluation coupled with vascular imaging has been explored as a method of hemoglobin measurement. Kanashima *et al* reviewed the performance of the Astrim© noninvasive hemoglobin monitor, a commercial product from Sysmex (Kobe, Japan) utilizing NIR transmission through the fingertip along with CCD blood vessel imaging to calculate hemoglobin concentration [140]. The fingertip is illuminated with numerous discrete spectral components and imaged at the opposite side. Photometric measurements in the vascular portions of the image are coupled with an estimation of vascular diameter (assuming circular vessel cross sections) to estimate the concentration of the hemoglobin chromophore. This group reports an anemia diagnostic sensitivity and specificity of 78.3% and 69% respectively with correlation coefficients of 0.531 for anemic patients and 0.345 for patients without anemia [140]. It is unclear why this recent study has shown this device to be so much more inaccurate than the initial report on the Sysmex Astrim reporting a correlation coefficient of 0.896 [141]. Although the sensitivity/specificity are lacking in this study, it does report high precision enabling the potential use of continuous intrapatient monitoring of hemoglobin for hemorrhagic patients.

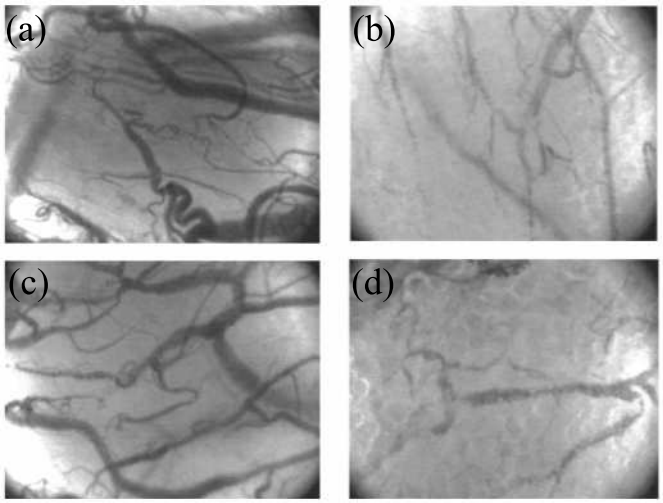

Figure 4.4: Microcirculation images collected using orthogonal polarization spectral imaging of a healthy patient (a,c) and an anemic patient (b,d). Adapted from [142].

Nadeau and Groner reported on a similar method of imaging analysis for anemia detection [142]. This technique uses orthoganol polarization spectral (OPS) imaging of the sublingual mucosal surface to measure hemoglobin noninvasively based upon computational estimation of microvascular network density and photometric intensity of spectral reflectance in vessel regions. Illuminating with a polarized source at a discrete spectral region of high hemoglobin absorbance (∼550 nm), a crossed polarizer is placed at the focal plane array to reject light which is not depolarized through deep penetration into tissue (via scattering). Images collected from anemic and healthy patients using the OPS technique are shown in Figure 4.4. This group has reported an excellent accuracy correlation coefficient of r = .093 [142]; however, imaging technique such as this or techniques reported by Kanashima *et al* may be limited in a clinical setting by complex expensive imaging equipment and computing hardware necessary.

NIR transmission spectroscopy is the embodiment of choice in the majority of studies on total hemoglobin detection. Aldrich *et al* reported on the utility of using NIR transmission through the fingertip at a single pseudo-isosbestic wavelength (905 nm) coupled with a sonomicrometer to monitor pulsatile changes in the optical pathlength through the finger [143]. Sonomicrometers were positioned at opposite sides of the finger to acoustically monitor the pathlength through the finger and fluctuations in this pathlength during blood pulsation, as depicted in Figure 4.5. The

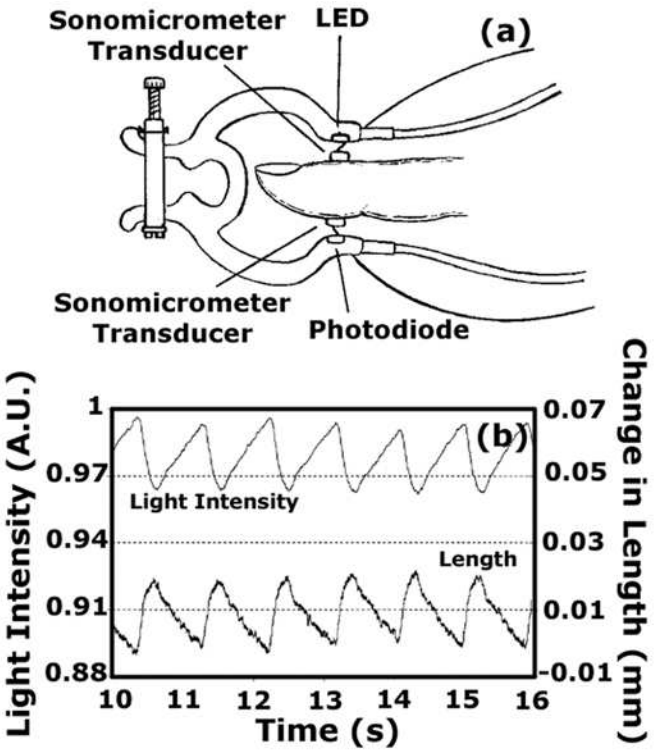

Figure 4.5: Setup of transcutaneous illumination coupled with path length modulation detection using sonomicrometer transducers (a) and the detected variation in light intensity corresponding to the sonomicrometer detected variation in optical pathlength (b). Adapted from [143].

transmission of an LED through the finger at the same position was normalized to the calculated pathlength, and this parameter compared to *in vitro* hemoglobin determination. In a clinical study with 24 participants, this group reported a correlation coefficient of 0.84 for their calculated parameter, a sensitivity and specificity of 94% and 78% respectively, and mean error of prediction of 1.1 g/dL [143]. This technique is unlikely to gain clinical utilization in its current embodiment as the sonomicrometers are extremely sensitive to positioning, applied pressure, and patient movements.

Several groups have reported that using a simple attenuance ratio at multiple wavelengths, similar to pulse oximetry, correlates to total hemoglobin concentration. Steuer *et al* reported that transmitted NIR attenuance measurements across the earlobe at multiple isosbestic wavelengths of oxy- and deoxyhemoglobin correlated to the hematocrit. Schmitt *et al* and Jeon *et al* [144] both reported as well that hematocrit could be estimated using ratios of the attenuance at multiple wavelengths. These particular three studies have failed to gain clinical acceptance due to associated inaccuracies.

Rendell *et al* has explored NIR transmission through the fingertip as a marker of total hemoglobin concentration with some success [145]. Unlike most other NIR transmission measurements, this group recreated broadband NIR transmission spectral characteristics using multiple (n=14) infrared emitting photodiodes rather than a single discrete photometric measurement. Progressively activating photodiodes, a single detector captures intensity transmitted through the fingertip at each frequency band. Applying a regression algorithm to the each discrete spectral point point, this group reports an optimal correlation coefficient of r = 0.862 and mean error of prediction of 1.28 g/dL

Geva *et al* has examined a technique termed occlusion spectroscopy that also uses transmitted NIR radiation through the fingertip to infer hemoglobin concentration [146]. This transmitted signal is enhanced by initially occluding the blood flow which in turn accelerates RBC aggregation, and subsequently releasing the occluding finger cuff and allowing RBCs to disaggregate [147]. The enhanced contrast in these two signals allows for a more accurate determination of RBC/hemoglobin concentration. This research has been adopted by Orsense (Rehovat, Israel) in their NBM-100 hemoglobin monitor. Clinical evaluation of the NBM-100 has shown average error values of 0.78 g/dL [148].

Several studies have also been published using visible/NIR diffuse reflectance spectroscopy. Zonios *et al* described the use of visible regime diffuse reflectance spectra from the forearm and back to measure total oxy- and deoxyhemoglobin concentration (as well as melanin content) [149]. In this particular study, the utility of reflectance signals in monitoring total hemoglobin was demonstrated intra-pateint by showing the diffuse signals ability to monitor reactive hyperemia following an occlusion and release of blood flow; however, inter-patient predictive ability was not discussed. Wu *et al* also examined the use of visible diffuse reflectance spectroscopy to measure total hemoglobin concentration [150]. This group uniquely took one step further in improving accuracy by locally controlling the skin temperature, which has been shown to affect absorption and scattering coefficients of tissues by altering cutaneous blood flow [151]. Wu *et al* reported a correlation coefficient for hemoglobin amongst participants of varying skin types of 0.8 and mean error of prediction of 0.9 g/dL. Zhang *et al* reported on the utility of visible/NIR diffuse reflectance spectroscopy as

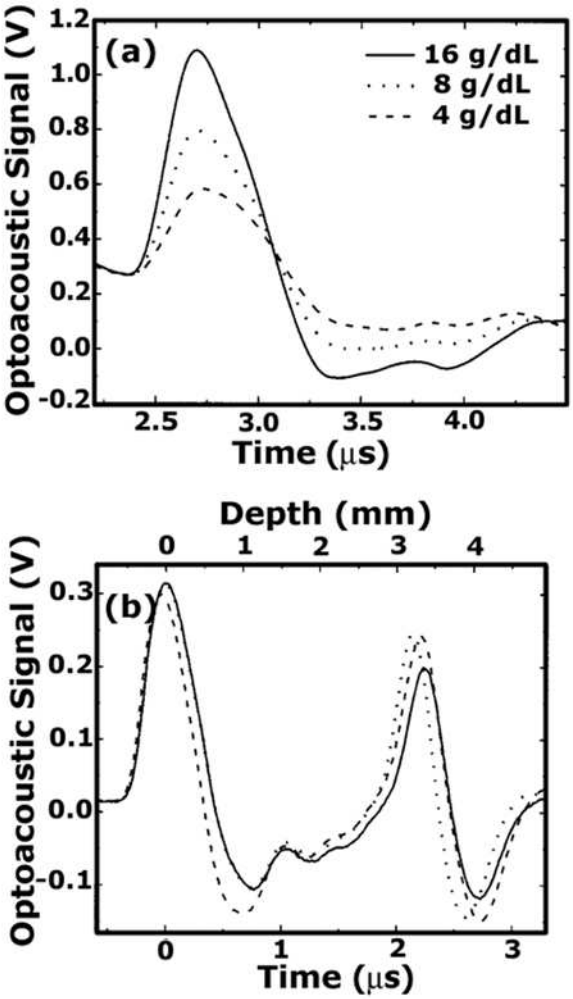

Figure 4.6: Modulation in optically generated acoustic wave as a function of hemoglobin concentration in a radial artery tissue phantom (a) and temporal variation in optoacoustic signal generated in the radial artery during saline infusion (b). Adapted from [155].

an indicator of hematocrit [152]. Using a partial least squares multivariate calibration [153, 154], Zhang reports an intrapatient correlation coefficient of 0.844 assessed by measuring fluctuations in hematocrit during heart surgery and recording reflectance spectra accordingly, and an interpatient correlation coefficient of 0.509 assessed by comparing cross patient data using a single model [152].

Petrova *et al* explored a different approach to predominant methods reported in the literature using optoacoustics spectroscopy [155]. Irradiating the finger with a pulsed Nd:YAG Laser (λ = 1064 nm) causes the heating and subsequent rapid expansion of tissue. The expansion of the tissue creates an optoacoustic (pressure) wave of which the characteristics of the wave, amplitude, phase,

depend on the characteristics of the absorbing substance(s). As can be observed in Figure 4.6, reflected optoacoustic waves were measured using sensitive piezoelectric transducers. In this pilot study, Petrova *et at* did not report on the interpatient assessment of anemia, but did show changing responses of optoacoustic waves with changing hemoglobin concentration by monitoring signals during an intravenous saline infusion (hemoglobin dilution) [155]. Variations of this technique have been reported in numerous journals by this group [156, 157]. A summary of anemia detection methods reported here is shown in Table 4.1

Table 4.1: A listing of literature on noninvasive hemoglobin monitoring techniques reported in the literature focused on anemia detection with the corresponding technique

Author	Technique
Aldrich 2002	Photoplethymography (Finger)
Dullenkopf 2004	Reflectance spectroscopy of various regions
Ernsting 2001	Digital Imaging of the conjunctiva
Faubert 1999	Retinal Spectral Imaging
Genzel-Boroviczeny 2000	Orthogonal Polarization Imaging
Geva 2004	NIR Occlusion Spectroscopy (Finger)
Iftimia 2006	Retinal Tracking and Low Coherence Interferometry
Jeon 2002	NIR Transcutaneous Spectroscopy (Finger)
Kanashima 2005	NIR Transcutaneous Imaging (Finger)
Kinoshita 2002	NIR Transcutaneous Imaging (Finger)
Nadeau 2001	Orthogonal Polarization Imaging of Sublingual Mucosa
Petrova 2005	Optoacoustics
Powell 2005	NIR Transcutaneous Spectroscopy (Finger)
Rabe 2005	Reflectance spectroscopy of forearm
Rendell 2003	NIR Transcutaneous Spectroscopy (Finger)
Rice 2001	Retinal Spectral Imaging
Sanchez-Carillo 1989	Conjunctiva color comparison chart
Secomski 2003	Ultrasound
Shapiro 2004	Conjunctiva color comparison chart
Winkelman 1991	Conjunctiva Capillary Imaging
Wu 2000	Reflectance Spectroscopy (Forearm)
Yamakoshi 1980	Electrical Admittance Plethysmography (Finger)
Zhang 2000	Reflectance Spectroscopy (Forearm)
Zonios 2001	Reflectance Spectroscopy (Forearm/Back)

4.3 Physiology of the Palpebral Conjunctiva

Previously discussed techniques, aside from the OPS imaging technique examining sublingual mucosa, explore cutaneous tissues as analytical locations. Cutaneous tissue, while easily accesible,

present difficulties due to interracial/interpatient melanin fluctuation, high scattering in turbid media, and weak signals due to the tissue absorptions even at NIR wavelengths. These factors have influenced the necessary instrumentation and have likely inhibited the acceptance of noninvasive technologies in a clinical setting.

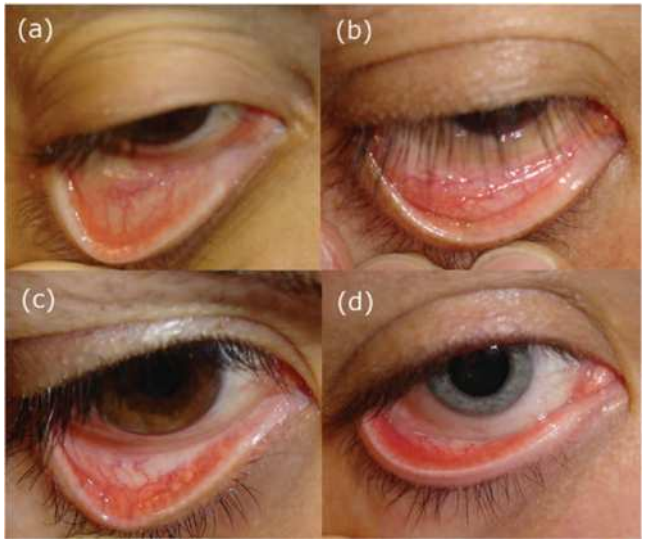

Figure 4.7: Digital photographs of the palpebral conjunctiva of four patients with hemoglobin concentrations of (a) 7.3 g/dL, (b) 12.7 g/dL, (c) 14.0 g/dL, and (d) 14.5 g/dL

As a quick examination for severe anemia, clinicians expose the inner lining of the lower eyelid, the palpebral conjunctiva, and visually look for a pale and uniform tint across the surface indicating anemia as opposed to a bright red tint in healthy patients [158–161]. An example of the gradient of hemoglobin concentrations in the palpebral conjunctiva is shown in Figure 4.7.

The conjunctiva is an attractive location to diagnose anemia as it is a highly vascular area, the capillaries vessels are close to the surface, and the mucous membrane of the conjunctiva is highly transparent. The conjunctiva itself is made up primarily of nonkeratinizing squamous epithelium, goblet cells, Langerhans cells, and sparse dendritic melanocytes. Nonkeratinizing squamous epithelial cells are a flattened scale like structure which do not keratinize and become rough and horny as they do in cutaneous surfaces. Goblet cells serve to secrete mucous and provide a hydrophilic mucin layer across the cornea/sclera. This is the lower most layer of the stratified tear film and allows watery layers to stay layered on the otherwise hydrophobic surfaces. Langerhans' Cells serve to

initiate immune responses to infections encountered at the surface of the conjunctiva (among other skin-environment interfaces). Dendritic melanocytes supply melanin to keratinocytes; however, the fact that the conjunctiva surface is non-keratinizing limits the necessity for melanin supplies, thus the dendritic melanocytes are sparse in the vicinity.

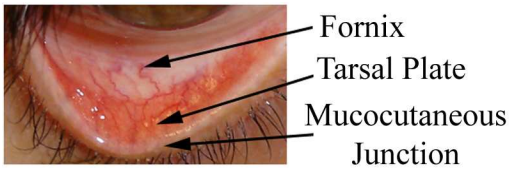

Figure 4.8: Major features of the palpebral conjunctiva.

The basic features of the conjunctiva are shown in Figure 4.8 while a detailed structural diagram of the eyelid/eye is shown in Figure (4.9). The cornea and lens are responsible for refraction of light and imaging capabilities of the eye, while the iris serves as a variable aperture to deliver appropriate photon counts to the photodetectors of the retina. The conjunctiva, as explained above, is a mucosal membrane lining the eyelid (palpebral conjunctiva), the fold in the eyelid (forniceal), and the sclera (bulbar conjunctiva). The tarsal plate is the fibrous region at the edge of the eyelid providing rigidity to the eyelid. As mentioned above the tear film is a three level stratified structure; a lipid/oily layer, an aqueous layer, and a mucin layer. The tear film is necessary to lubricate the eye, provide a smooth optical surface for refraction, provide oxygen and nutrients to the eye, and fight off surface bacteria (lysozyme) While the goblet cells of the palpebral/forniceal/bulbar conjunctiva are responsible for the mucin layer, the aqueous layer is formed by secretions of the Glands of Krause and Wolfing and the lacrimal sac (for large tear production during crying or irritation), and the liped layer is formed by the Meibomian glands beneath the palpebral conjunctiva at the tarsal plate. An aqueous layer provides the majority of oxygen and nutrients while the lipid layer keeps the aqueous layer from evaporating. Eyelid movement is controlled using the orbicularis muscle (eyelid closing) and the tarsal muscle (eyelid retraction). The orbital septum serves to constrain the orbital fat which extends from the socket into the lid.

More than 90% of physicians report the conjunctiva is the most attractive anatomical location

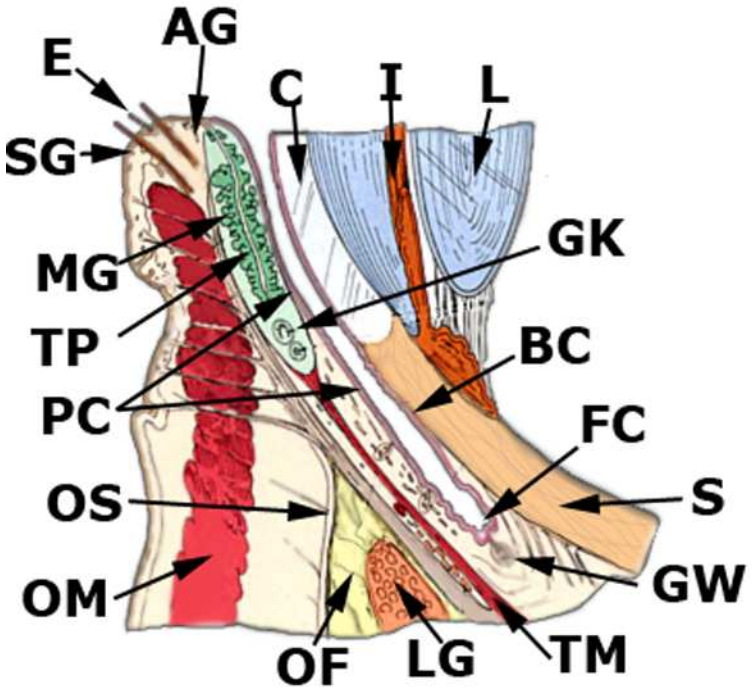

Figure 4.9: Diagram of palpebral conjunctiva and surrounding structures. Cornea (C), Iris (I), Lens (L), Gland of Krause (GK), Bulbar Conjunctiva (BC), Forniceal Conjunctiva (FC), Sclera (S), Gland of Wolfring (GW), Tarsal Muscle (TM), Lacrimal Glands (LG), Orbital Fat (OF), Orbicularis Muscle (OM), Orbital Septum (OS), Palpebral Conjunctiva (PC), Tarsal Plate (TP), Meibomian Glands (MG), Sebaceous Glands (SG), Aprocrine Glands (AG), and the Eyelashes (E) labeled accordingly. Adapted from [162]

for diagnosing anemia rather than nail beds, palmar creases, or the tongue [163]. Hung *et al* reports that a clinician's qualitative examination of the conjunctiva has only been shown to be, at best, 75% sensitive and 75% specific in diagnosing anemia independent of training [163]. Adjusting the anemia lower bound criterion to severe anemia (< 8 g/dL) was shown to improve these statistics. Hung *et al* also reports the visual diagnoses of anemia at the palpebral conjunctiva is independent of ethnicity/gender [163]. Another report has shown visually diagnosing anemia using the palpebral conjunctiva hue (PCH) is 80-90% specific but only 40% sensitive and leaves numerous cases undiagnosed [159]. Kent *et al* also reports that anemia detection is independent of ethnicity. Sanchez-Carrillo *et al* reports intraobserver agreement on conjunctival hue to range from 38-87% for anemic patients and ranging from 70-76% for non-anemic patients [164].

Current attempts to take the examination of the conjunctiva from a qualitative inspection to

a quantitative evaluation have been limited to the use of CIE based color charts as comparative tools; however, this is still subject to clinician interpretive color matching and has only moderately improved the sensitivity and specificity of conjunctival anemia diagnosis. Sanchez-Carillo reports that using a colorimetric chart as a reference with observation has a sensitivity of 63% and specificity of 72%, not a significant improvement over unaided observation [165]. Shapiro *et al* likewise has reported on the utility of an objective color scale to aid clinical anemia diagnosis. Subtle levels of hue were matched to the tarsal region of the palpebral conjunctiva and assessed using standard regression analysis [166]. In detecting severe anemia (hematocrit less than 30%), this tool has been shown to be 81% sensitive and 83% specific, however a statistical analysis based upon the WHO definition of anemia was not presented. Other groups have reported similar results using variations of comparative color matching with a color chart. [167, 168]

The simplicity of a quantitative examination of the conjunctiva coupled with the lack of resources in many developing countries and prevalance of nutritional/congenital anemias have lead to its widespread use in deprived areas. The limitations of widespread CBC blood testing in third world areas leaves numerous cases of anemia undetected. Anemias concurrent appearance with malaria and hookworm infections further influence this problem. Numerous groups have reported on the utility of clinical pallor to detect anemia in prevalant areas claiming that the tool is useful but not optimal. [161, 169–173] An inexpensive tool, more along the lines of a color chart type device, is suitable for such an application as the technical training necessary is minimal and the manufacturing costs are minimal.

A preliminary study done in collaboration with the *Rhode Island Hospital* examined the utility of using digital photography of the palpebral conjunctiva and subsequent analysis of the intensity of the three color channels [174]. The intensity of each channels was iteratively weighted to optimally correlate with the in vitro measured hemoglobin. This model resulted in correlation coefficients of 0.634 for the calibration set and 0.522 for a predictive set [174, 175].

4.4 Tissue Diffusion

Our hypothesis is that total hemoglobin concentration can be determined using visible broadband diffuse reflectance spectroscopy at the palpebral conjunctiva because the blood vessels are visible through a translucent mucosal surface. The tarsal plate is the most vascular location on the palpebral conjunctiva containing blood vessels from palpebral branches of nasal and lacrimal arteries throughout the squamous epithlium and capillary beds running in underlying dense fibrous tissue interspersed with sebaceous meibomiam glands. Photons impinging on the conjunctiva will diffuse throughout the conjunctiva, tarsal plate, and underlying orbicularis muscle and dermis, interacting through absorption and scattering with both hemoglobin molecules in intact RBCs and free hemoglobin, subsequently modifying the relative amounts of each spectral component. Assuming the light scattering, and thus photon diffusion properties, are comparable in different patients (as is acceptable with the low concentration of melanosome granules at the palpebral conjunctiva), backscattered visible light from the tarsal plate will have spectra primarily varying dependent on the hemoglobin concentration encountered during diffusion process. A calibration relation is developed between these reflection signals and known hemoglobin concentration, and is subsequently used to determine unknown hemoglobin concentrations. It is also assumed that a large irradiation spot (>1 mm) is necessary to ensure the interaction of diffusing photons with numerous blood vessels, creating a spectral averaging effect such that spectra do not scale with local variations in blood vessel density. Lastly, as oxy- and deoxyhemoglobin have similar absorption spectrum in the visible regime (Figure 4.3), it allows a measurement of total hemoglobin to take place without *a priori* knowledge of oxygen saturation in active sites of metabolism at capillary beds.

A critical step in assessing light diffusion through the tarsal plate is to identify the relation between diffuse reflectance R_d and hemoglobin concentration c. A model of the stratified structure of the eyelid is shown in Figure 4.10. As is depicted, the palpebral conjunctiva is the upper most mucosal lining of the inner eyelid; however, it is conventionally used to describe the whole structure including tarsal plate.

Light diffusion through the palpebral conjunctiva is considered using the Beer-Lambert law

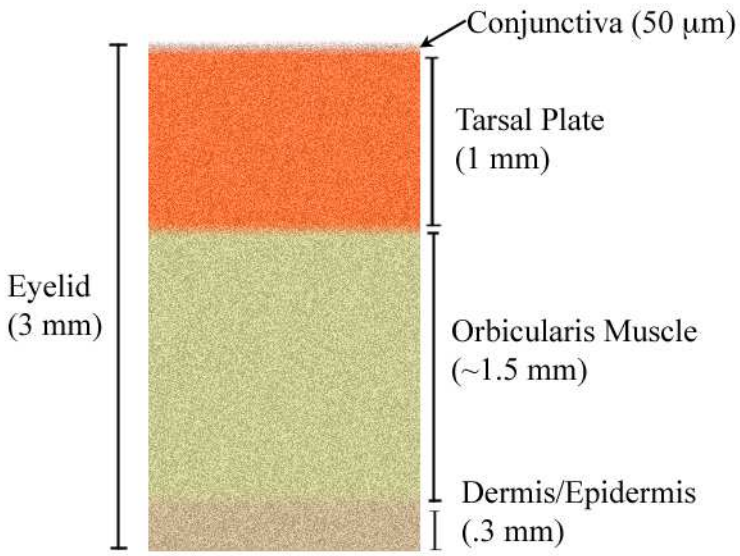

Figure 4.10: The stratified structure of the eyelid with dimensions based on average thicknesses in adults.

relating absorption to the pathlength, absorption coefficient, and concentration as shown in Equation 4.1.

$$A = \alpha L c = K c \tag{4.1}$$

which is derived from the equation for output intensity I_1 and input intensity I_0

$$I_1 = I_0 e^{-\alpha L c} \tag{4.2}$$

where the logarithmic absorbance A = -ln I/I_0 depends on the molar absorptivity of the material α, pathlength L, and concentration c. K is the molar absorptivity product. In the scope of the diffusion of light through tissue, this equation is more commonly described in terms of the absorption coefficient μ_a such that the diffuse reflectance $R_d = I_1/I_0$ from a sample is written as

$$R_d = e^{-\mu_a L} = e^{-\alpha L c} = e^{-\rho_a \sigma_a L} \tag{4.3}$$

where σ_a is the cross sectional area, related to the efficiency of absorption of the material and its

diameter, and ρ_a is the number density of absorbers, analogous to the concentration. This equation can be used to estimate transmission or absorption from a sample assuming the pathlength, L, is constant; however, the effects of cellular structures such as nuclei, mitochondria, collagen, and other membranes in biological materials induce elastic light scattering in the tissue. Inclusion of elastic light scattering terms in equation 4.3 varies the pathlength of light, L.

As in absorption, elastic scattering is a wavelength dependent event and is represented by $\mu_s = \rho_s \sigma_s$, with ρ_s and σ_s being the density of scattering particles and scattering cross section, respectively. The size and density of scattering particles vary light diffusion through turbid media, and consequently in diffuse reflectance studies, affect the optical pathlength/absorptivity and subsequent reflectance profiles. The directionality of the scattering event, dependent on the size of the scattering particles relative to wavelength of light (larger particles scatter light through directional Mie scattering while smaller particles scatter light through isotropic Rayleigh scattering), is expressed through the scattering anistropy parameter $g =< cos(\theta) >$, where θ is the scatter angle relative to the angle of incidence. A new parameter, the reduced scattering coefficient μ_s' is defined such that $\mu_s' = \mu_s(1-g)$. When g = 1, $\mu_s' = 0$ and the scattering term is eliminated; all scattering is in the forward direction. In an isotropic scattering condition, g = 0, $\mu_s' = \mu_s$ and scattering can occur in any direction at each scattering event; the photon has no "memory" of its prior direction at each event. These two scattering coefficient are used to define two additional parameters, the mean free path (MFP) = $1/\mu_s$ and the reduced mean free path MFP' = $1/\mu_s'$, which can be interpreted as the average length between all scattering events and the average length between isotropic scattering events, respectively.

Biological tissues usually have scattering anisotropy parameter of g $\approx$ 0.90-0.95 while human skin has reduced scattering coefficients on the order of magnitude of 100 cm^{-1} across the visible spectra, translating to a MFP of 100 μm [176]. Generally speaking, whenever a measurement is taken after numerous scattering events, μ_s' is sufficient to describe the diffuse behavior of light in tissue, simply the frequency of isotropic scattering events. In the context of the scattering from the tarsal plate of the conjunctiva, based on the similarity of cellular content and structures, it is assumed that

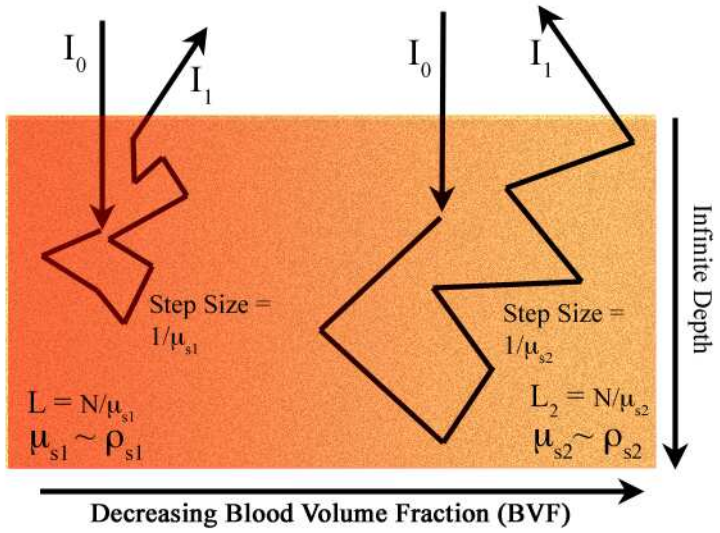

Figure 4.11: Light diffusing through an infinite segment of tissue with varying blood volume fraction and dependence on scattering coefficient μ_s

scattering coefficients have interpatient similarity aside from hemodynamic variations. Although molecular hemoglobin does not scatter visible light, cellular structures in whole blood including membranes in erythrocytes, leukocytes, and thrombocytes are scatterers, such that variability in the relative amounts of each blood fraction can modify the pathlength of light as it scatters through the tarsal plate.

Consider the situation shown in Figure 4.11 where a section of tissue has a gradient in blood volume fraction (BVF). As the reduced scattering coefficient μ_s' is proportional to the volume fraction of scattering particles ρ_s, increasing the concentration of RBCs will increase the scattering coefficient μ_s' and reduce the mean free path. As the total pathlengh L and absorption cross section $\rho_a \sim \mu_a$ determine the absorption characteristics of diffusely reflected light, decreasing the concentration of RBCs will decrease ρ_a but increase the MFP' and L in propotional amounts. Thus, in a infinite depth material as shown, the absorption characteristics will be the same for all blood volume fractions, making R_d independent of these parameters.

In the tarsal plate, the layers of tissue with significant BVF do not behave as infinite layers. In the finite case shown in Figure 4.12, the differing pathlength L does not fully offset the concentration difference because the pathlength is physically constrained by the layer dimensions. At some

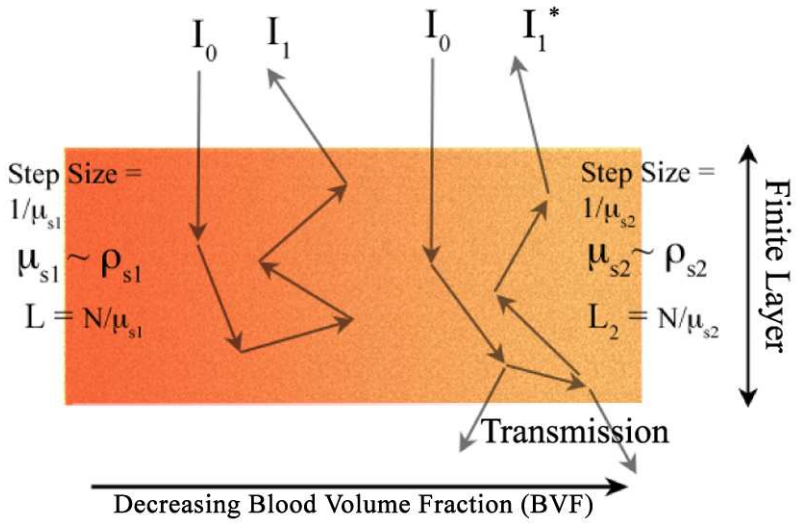

Figure 4.12: Diffuse reflectance of light diffusing through a discrete segments of tissue with varying blood volume fraction scales with MFP' and $1/\mu_a$; however, this scaling is unbalanced due to transmission to another layer.

minimum concentration of scatterers, ρ_s, light penetrating deeper into the tissue (longer MFP') either encounters a different BVF or transmits through the tissue and is never backscattered to the detector. In this configuration, the amount of diffuse reflectance R_d depends on a combination of ρ_a and the MFP'. In the case of the palpebral conjunctiva, a fraction of the irradiation is always transmitted through the lid, indicating that at all ρ_s, it always behaves as a finite layer system; thus, R_d will always vary in some relation with ρ_a.

If light takes N steps to exit the conjunctiva, the total pathlength L is the product of the MFP' and N, such that increasing RBC concentration decreases the total pathlengh of light, as expected. The generic equation for the Beer-Lambert law in Equation 4.3 in a highly scattering medium now becomes:

$$R_d = e^{-\mu_a MFP' N} = e^{-\mu_a N/\mu_s'} \tag{4.4}$$

As we have seen, the number of steps to exit the conjunctiva has dependence on both the scattering/absorption coefficients, geometry, and index of the refraction of the material, translating to a more complex equation in practice than that shown in Equation 4.4. The dependence of the

pathlength L on μ_a and μ_s' has been numerically approximated through fitting diffuse reflectance curves to analytical equations for biological tissues and factoring in Fresnel reflection from the surface [176], and is given as:

$$L = A'\delta = A'\sqrt{\frac{1}{3\mu_a\mu_t}},\ \mu_t = \mu_a + \mu_s' \tag{4.5}$$

where A', not to be confused with absorption, is a scale factor that is usually 7 or 8 for biological tissues, the index n is assumed to be that of water (n=1.33), and μ_t is the total attenuation parameter correlating to the absorption and scattering coefficients. This scaled pathlength allows for a straightforward Beer Lambert law calculation again using equation 4.3

$$R_d = e^{-A\mu_a\sqrt{\frac{1}{3\mu_a\mu_t}}} = e^{-\frac{A}{\sqrt{3(1+\mu_s'\mu_a)}}} \tag{4.6}$$

Solving for μ_a in this case yields

$$\mu_a \propto c = \frac{\mu_s'}{\frac{A^2}{3(ln(R_d))^2} - 1} \propto ((ln(R_d))^2 \tag{4.7}$$

The crucial and relevant part of this equation is the nonlinear dependence of R_d on μ_a, and subsequetly on ρ_a, which correlates to hemoglobin concentration. The following section discusses the linear prediction model for extracting hemoglobin concentration based on measured R_d, while the post processing fitting to correct for the nonlinearity observed in equation 4.7 to estimate unknown concentrations $c \propto \mu_a$ is discussed in the results section.

4.5 Multivariate Calibration and Prediction

Considering that several analytes with significant absorption coefficients in the visible regime vary from patient to patient and independent of total hemoglobin concentration, the most appropriate method of extracting concentration information is a multivariate regression technique. Since the system is nonlinear, as just shown, either a nonlinear fitting algorithm can be applied, or a linear

algorithm can be applied with nonlinear biasing of solutions after fitting.

The most straightforward multivariate regression technique is a classical least squares (CLS) approach in which a calibration set can be produced with known amounts of each varying analyte (chemical). Although this is unfeasible in the palpebral conjunctiva as the amount of each analyte cannot be known beforehand, multivariate regression can best be explained in the context of a example system using CLS. Assume a system with l analytes varying independently in m samples and n discrete wavelength values. Starting with equation 4.1, the logarithmic wavelength dependent reflectance $R = -ln(R_d)$ (at each wavelength for each sample) of the system can be written as a function of the pathlength/molar absorptivity product K (for each analyte at each wavelength) and concentration C (of each) for the calibration set:

$$R_{m,n} = K_{1,n}C_{m,1} + K_{2,n}C_{m,2} + K_{3,n}C_{m,3} \ldots K_{l,n}C_{m,l} \tag{4.8}$$

which can be easily written in matrix form as:

$$\begin{pmatrix} R_{1,1} & R_{1,2} & \ldots & R_{1,m} \\ R_{2,1} & R_{2,2} & \ldots & R_{2,m} \\ \vdots & \vdots & \vdots & \vdots \\ R_{n,1} & R_{n,2} & \ldots & R_{n,m} \end{pmatrix} = \begin{pmatrix} K_{1,1} & K_{1,2} & \ldots & K_{1,l} \\ K_{2,1} & K_{2,2} & \ldots & K_{2,l} \\ \vdots & \vdots & \vdots & \vdots \\ K_{n,1} & K_{n,2} & \ldots & K_{n,l} \end{pmatrix} \begin{pmatrix} C_{1,1} & C_{1,2} & \ldots & C_{1,m} \\ C_{2,1} & C_{2,2} & \ldots & C_{2,m} \\ \vdots & \vdots & \vdots & \vdots \\ C_{l,1} & C_{l,2} & \ldots & C_{l,m} \end{pmatrix} \tag{4.9}$$

In the case of the calibration set, the **R** and **C** matrix are known and are used to solve for the **K** matrix. The least squares solution for the pathlength/molar absorptivity product is the approximation $\hat{\mathbf{K}} = \mathbf{RC'}/\mathbf{CC'}$, with the $\hat{hat}$ denoting a least squares approximated variable/matrix. After solving for **K**, the resultant matrix can be used in conjunction with measured spectra **a** to approximate concentration **c** of unknown samples as in the following matrix:

$$\begin{pmatrix} a_1 \\ a_2 \\ \vdots \\ a_n \end{pmatrix} = \begin{pmatrix} K_{1,1} & K_{1,2} & \dots & K_{1,l} \\ K_{2,1} & K_{2,2} & \dots & K_{2,l} \\ \vdots & \vdots & \vdots & \vdots \\ K_{n,1} & K_{n,2} & \dots & K_{n,l} \end{pmatrix} \begin{pmatrix} c_1 \\ c_2 \\ \vdots \\ c_l \end{pmatrix} \tag{4.10}$$

after which the concentration of each species can be estimated using the same least squares approximation $\hat{\mathbf{c}} = \mathbf{a}\hat{\mathbf{K}}'/\hat{\mathbf{K}}\hat{\mathbf{K}}'$.

Because the CLS shown here requires *a priori* knowledge of the concentration of every analyte in the **C** matrix in order to approximate **K**, this exact solution method is not ideal in the palpebral conjunctiva system. This is a result of the interpatient fluctuations in other analytes (small amounts of melanin, bilirubin, cytochrome c oxidase, hemoglobin saturation state) inhibiting explicit calibration. Alternatively, a 'soft' modeling technique is utilized to extract concentration information of total hemoglobin in the presence of these unknown fluctuating species. The partial least least squares (PLS) [153, 154] is the most common soft modeling technique used in systems such as this, although other techniques such as principal component regression (PCR) [177] and hybrid linear analysis (HLA) [178] are potential solutions. Principal component regression and PLS are in fact quite similar. PCR uses least squares approximation to finds vectors accounting for maximum variance in a sample set, correlated to the main "components," while PLS finds vectors accounting for maximum correlation with the known concentration value of one analyte, and subsequently uses these vectors to predict unknown concentration values of the same analyte.

The PLS calibration operates as follows: Consider an array **R** of several calibration spectra in which only the concentration **C** of the analyte of interest (hemoglobin) is known. The first step is to find the least squares solution to equation 4.11 below where **w** is the PLS weight vector which, when scaled by the concentration of hemoglobin in each patient, most similarly approximates the recorded calibration spectra. The weight vector is approximated using the same least squares approximation used in CLS above to calculate **K**, except that the weight vector **w** only fits to the analyte of interest instead of each varying species independently. The h subscript is the number of "loops" through the algorithm. **R** is the recorded spectra in the first iteration, and then becomes the residual spectra,

which will be made clear later.

$$\mathbf{R}_h = \mathbf{w_h}\cdot\mathbf{C} \Rightarrow \text{ L.S. Solution } \hat{\mathbf{w_h}} = \mathbf{R'C}/\mathbf{CC'} \tag{4.11}$$

Once the weight vector has been created, another approximation is made to determine the relationship of this vector to each calibration spectra through a term called the score vector $\mathbf{t}$. Note that if the sample only has only one varying analyte and little noise, the weight vector is the pure spectra of the analyte, the score vector is the concentration of the analyte in each sample, and only one pass through this algorithm is necessary; however, in practice this is most often not the case, nor is it here.

$$\mathbf{R_h} = \mathbf{t_h}\cdot\hat{\mathbf{w_h}} \Rightarrow \text{ L.S. Solution } \hat{\mathbf{w_h}} = \mathbf{R'w_h}/\mathbf{ww'} \tag{4.12}$$

The score vector $\mathbf{t}$ is then related to the concentration of the analyte using a coefficient termed the score coefficient $\mathbf{v}$. Again, in a perfect system with a single analyte, the score coefficient is one because the score vectors are the concentration values; however, this again gets more complicated in multivariate systems with multiple passes through the algorithm. The score coefficient is approximated through:

$$\mathbf{C} = \mathbf{v_h}\cdot\hat{\mathbf{t_h}} \Rightarrow \text{ L.S. Solution } \hat{\mathbf{v_h}} = \hat{\mathbf{t_h}}'\mathbf{C}/\hat{\mathbf{t_h}}\hat{\mathbf{t_h}}' \tag{4.13}$$

To ensure that each weight vector is orthogonal to the previous one as the algorithm is iterated, the PLS loading vector $\mathbf{b}$ is created using the least squares determined score vector and measured spectra $\mathbf{R}$ through the following equation.

$$\mathbf{R} = \hat{\mathbf{t_h}}\cdot\mathbf{t_h} \Rightarrow \text{ L.S. Solution } \hat{\mathbf{b_h}} = \mathbf{R'}\hat{\mathbf{t_h}}'/\hat{\mathbf{t_h}}\hat{\mathbf{t_h}}' \tag{4.14}$$

Once orthogonal "weight vectors" have been formed, this weight vector is subtracted from each spectra creating a residual spectra $\mathbf{E_R}$, while the initial concentration approximation (through the

score vector/score coefficient product) is subtracted from the known calibration concentration to yield concentration residual $\mathbf{e_c}$ through the following equations

$$\mathbf{E_R} = \mathbf{R} - \hat{\mathbf{t_h}} \cdot \hat{\mathbf{b_h}}, \ \mathbf{e_c} = \mathbf{C} - \hat{\mathbf{v_h}} \cdot \hat{\mathbf{t_h}} \tag{4.15}$$

$\mathbf{R}$ is then replaced with $\mathbf{E_R}$ and $\mathbf{C}$ replaced with $\mathbf{e_c}$ and the algorithm is repeated from the first step with another weight vector formed of the residual, etc. Simply stated, (1) the algorithm finds the vector that best fits the recorded spectra when it is scaled by the known concentration values (weight vector), (2) it finds the how it should be scaled in each calibration spectra (score vector), (3) finds how well this scaling is matching the true concentration value (score coefficient), (4) adjusts the vectors so there is no collinearity (PLS loading vector), (5) removes the scaled orthogonal weight vectors from each calibration spectra, (6) removes how much of the concentration has been "predicted" in this loop through the score vector and coefficient, and (7) starts over. As expected, in each successive loop the weight vector will have less correlation with the changing analyte concentration until eventually the model begins trying to fit noise. The number of loops through the algorithm should be much less than the number of calibration spectra in order to prevent overfitting and artificially improved performance.

In order to predict unknown concentration values from measured spectra, the weight vectors $\mathbf{w_h}$ and score coefficients $\mathbf{v_h}$ are needed from the calibration. Again, assume a sample with measured spectra $\mathbf{a}$ and unknown concentration c. The calibration determined weight vector and measured unknown spectra are used to determine the score vector (e.g. how much of each weight vector is in the unknown) as shown in equation 4.16.

$$\mathbf{a} = \mathbf{t_h} \cdot \hat{\mathbf{w}}_\mathbf{h} \Rightarrow \text{ L.S. Solution } \hat{\mathbf{t_h}} = \mathbf{a}' \hat{\mathbf{w}}_\mathbf{h}{}' / \hat{\mathbf{w}}_\mathbf{h} \hat{\mathbf{w}}_\mathbf{h}{}' \tag{4.16}$$

Once the score vector $\mathbf{t_h}$ is known, the calibration determined score coefficient $\mathbf{v_h}$ can be used to determine the concentration value through equation 4.17

$$\hat{\mathbf{c}} = \mathbf{t_h} \cdot \hat{\mathbf{v}}_\mathbf{h} \tag{4.17}$$

The predictive algorithm is looped through h times with the concentration prediction updated with the inclusion of each weight vector, stopping when h reaches a sufficient number of cycles to model all varying analytes, but significantly less than the number of calibration samples. The "rule of thumb" commonly used in modeling using PLS is the number of weight vectors used should be at a minimum of four times less than the number of calibration samples. As is shown in results later in Figure 4.18, plotting the predictive accuracy as a function of the number of weight vectors, the accuracy increases rapidly over the first couple loading vectors with only moderate gains at higher numbers of vectors. This algorithm coupled with nonlinear biasing of the results based on the relation determined in Section 4.4 are used in multiple clinical trials to assess the feasibility of this method.

4.6 Clinical Trial using Modified Ophthalmoscope

As the first proof of concept study to test this theory, a large grating spectrometer was used in a modified ophthalmoscope configuration to collect diffuse reflectance spectra from the tarsal plate as shown in Figure 4.13.

4.6.1 Patient Enrollment

Thirty-two patients from the emergency department at the Rhode Island Hospital (RIH) were enrolled in this study. All patients were at least eighteen years of age, able to give written and verbal consent, and willing to participate. The institutional review board (IRB) of RIH approved this study. Recruited patients were all ambulatory and had been approved for participation by an attending physician. Individuals with a variety of complaints were enrolled to simulate a random patient population. Patients with acute cardiac symptoms, musculoskeletal injuries inhibiting comfortable relocation to the research location, symptoms of stroke, patients not yet seen nor cleared by a physician and critically ill patients were excluded from this study. Of the thirty-two consented

patients, thirty were able to participate. Two patients were unable to participate; one due to nausea and abdominal pain during the enrollment procedure, and one because the conjunctiva could not be sufficiently exposed for spectroscopic measurements. Additionally, only patients with oxygen saturation > 90 % were enrolled to exclude hypoxic patients during preliminary evaluation of the efficacy of this technique.

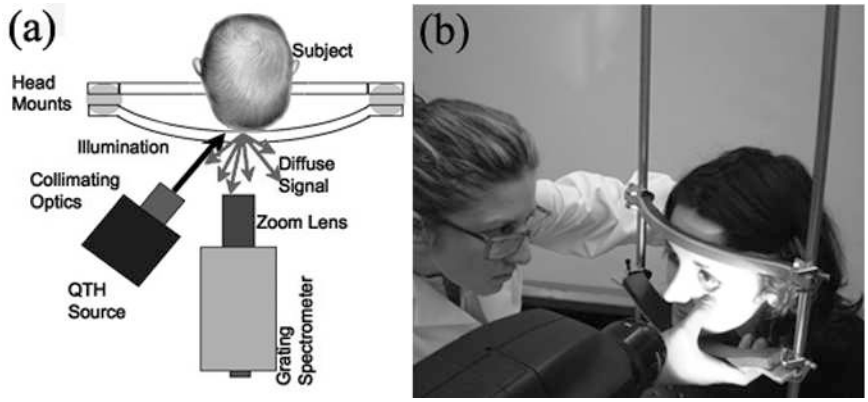

Figure 4.13: Schematic of a modified opthalmoscope configuration with grating spectrometer (a) and a photograph of data collection taking place (b).

4.6.2 Diffuse Reflectance Spectra Collection

Patients were seated with their heads resting on a custom built mount to stabilize conjunctiva exposure location. A visible spectrophotometer from Photoresearch (PR-705, Chatsworth, CA) with eyepiece to target collection region was mounted on a variable height platform with a separation of approximately 7 cm from the spectrometer to the exposed conjunctiva. The conjunctiva was illuminated through free space with a quartz-tungsten-halogen (QTH) source from Lot-Oriel (Surrey, UK) at an illumination angle of 50° with respect to the plane of the conjunctiva and a separation of ~ 15 cm from source element to conjunctiva. 30 watts of total broadband source power was used for all measurements, chosen to be as intense as possible without causing the subject discomfort. The irradiance of this source does not exceed 0.1 W/nm $\times$ m^2 across the visible wavelength range and thus does not pose a radiation exposure risk according to ANSI Z136.1 standards for incoherent radiation exposure [179]. As a comfort measure, patients averted their eyes opposite the direction of illumination to avoid prolonged retinal exposure to illumination. Source spectral characteristics

were recorded and behaved as expected for a QTH source with the intensity increasing close to linearly with increasing wavelength across the visible regime. Collimating optics were affixed to the source tower to provide uniform illumination of the conjunctiva allowing rapid measurement of various spatial locations. Ambient sunlight and room lights were normalized from data by collecting reference source spectrum each day and normalizing conjunctiva spectra to this spectra. This method of ambient light correction was the optimal available technique as a dark room facility was unavailable during early clinical trials.

All spectra were collected in reflectance mode across with a 1° field of view, translating to an aperture size of approximately 4.5 mm^2 for spectrometer to conjunctiva separation of 7 cm. While a smaller aperture is more suited to collect reflectance spectra from single capillary vessels, random movements of patients during acquisition prevented this procedure. A larger aperture allowed reflectance signal from numerous capillaries to be integrated together as discussed above in Section 4.4, eliminating artifacts from the aperture moving off and on individual capillaries. Acquisition times were varied by the software platform to integrate until a benchmark total signal level was obtained, but were on average $\sim$ 3 seconds. Varying integration time allows reflectance signals to be comparable in intensity despite small patient-to-patient variations in conjunctival structure, illumination angles, and source/spectrometer/patient separations (although data also normalized below). Three spectra were collected and averaged from each patient.

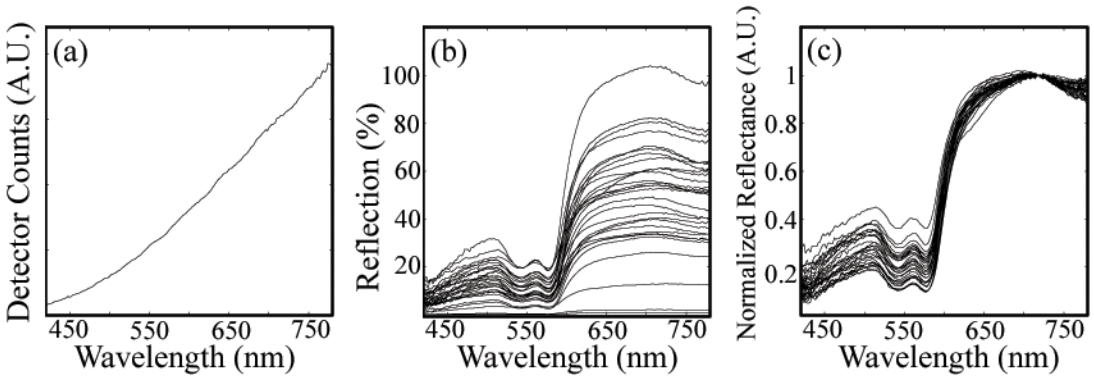

Figure 4.14: Emission spectra from QTH source (a), mean spectra from thirty patients with varying hemoglobin concentrations (b), and same data normalized to reflection peak at 720 nm (c).

4.6.3 Clinical Trial Results

Among the thirty patients recruited for the study, the average age was 42 years old with 14 males and 16 females. 21 of these patients were Caucasian, 6 were Hispanic, and 3 were African-American. The mean hemoglobin concentration was 13.6 ± 2.1 g/dL with range: 7.3 - 16.7 g/dL. The average oxygen saturation was 98.3 ± 1.5%. Using the WHO anemia definition, the sample set contained seven patients with clinical anemia. Of these seven, two were a result of congenital hemoglobin defects thalassemia and sickle cell anemia respectively, and a third from pregnancy. The cause of anemia for the remaining four patients in this subset was not determined.

The emission spectra from the QTH source is shown in Figure 4.14(a) where the the output is in arbitrary unit of detector counts. The source characteristics were recorded before each data collection session. The raw data, with source information normalized, is shown in Figure 4.14(b). The high variability in overall signal levels is attributed to variability in separation from source-patient-detection systems resulting from physiological differences. To emphasize changes in relative reflectance, spectra are normalized at the peak reflectance intensity at 720 nm, as shown in Figure 4.14(c). In the instance that oxy- and deoxyhemoglobin are the primary contributors to reflectance intensities, plotting the ratio of the intensity of two isosbestic points with two absorption coefficients for the two species should correlate with the total hemoglobin concentration. Using isosbestic points near 780 nm and 530 nm (as seen in Figure 4.3), the ratio of these two intensities for all patients are plotted versus the concentration value as shown in Figure 4.15.

Although a correlation is observable (Pearson correlation coefficient r = 0.439), the poor result is a function of the interfering analytes and amount of data collected that is not being used in correlation (of the 189 digitized points collected after clipping noisy spectra regions in UV, only 2 are used in the ratio calculation). As a result, the partial least squares calibration and prediction model is used as described in Section 4.5. The performance of the PLS algorithm on this data set was verified using a leave-one-out cross validation where 29 samples were used to determine weight vectors and score coefficients, and subsequently used to predict the remaining unknown sample. A plot of the PLS determined loading vectors are shown below in Figure 4.16 for the first 15 cycles

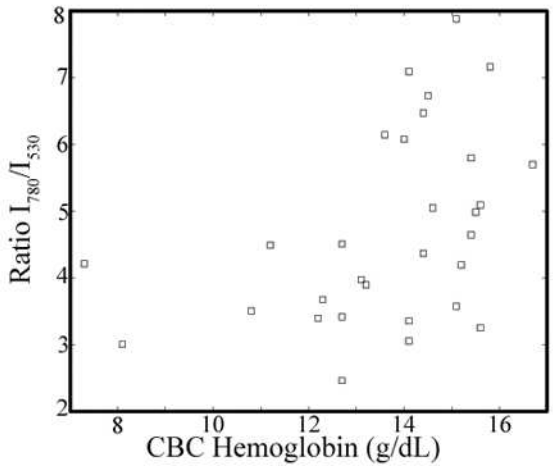

Figure 4.15: Plot of the ratio of reflected intensites at $\lambda = 780$ nm and $\lambda = 530$ nm plotted as a function of CBC determined total hemoglobin concentration.

through the algorithm for one set of 29 samples.

Among the important facets to note in the loading vector plots are (1) the h = 0 loading vector is the simply the mean of all calibration spectra and not used in the prediction algorithm and (2) spectral data is mean centered using the average calibration spectra, therefore changes in each spectra (and loading vector) are with respect to this mean spectra (zero line is no change). Important features appearing repeatedly in the loading vectors are a doublet peak around 550 nm, and inflection points appearing around 600 nm where the correlation goes from positive to negative, indicating a negative/positive correlation shift. The appearance of the double peak is expected as it is the defining feature in oxyhemoglobin as shown in Figure 4.3. The high degree of activity around 600 nm is representative of where the largest change in absorption coefficient (per nm) for hemoglobin occurs, causing the algorithm to heavily utilize this area to correlate to hemoglobin concentration.

Although the intensity scale of the loading vectors is irrelevant as it is the correlation of the weight vector to the *residual* and not measured spectra in each cycle, the more significant parameters to examine are the score coefficient $\mathbf{v}$ and score vector $\mathbf{t}$. The score coefficient $\mathbf{v}$ relates the amount of each loading vector in the spectrum (the score vector $\mathbf{t}$) to the hemoglobin concentration, i.e. the more significant a vector is to the prediction, the larger the score coefficient for that vector. The score *coefficient* cannot, however, be interpreted independent of the the score *vector*. While a vector

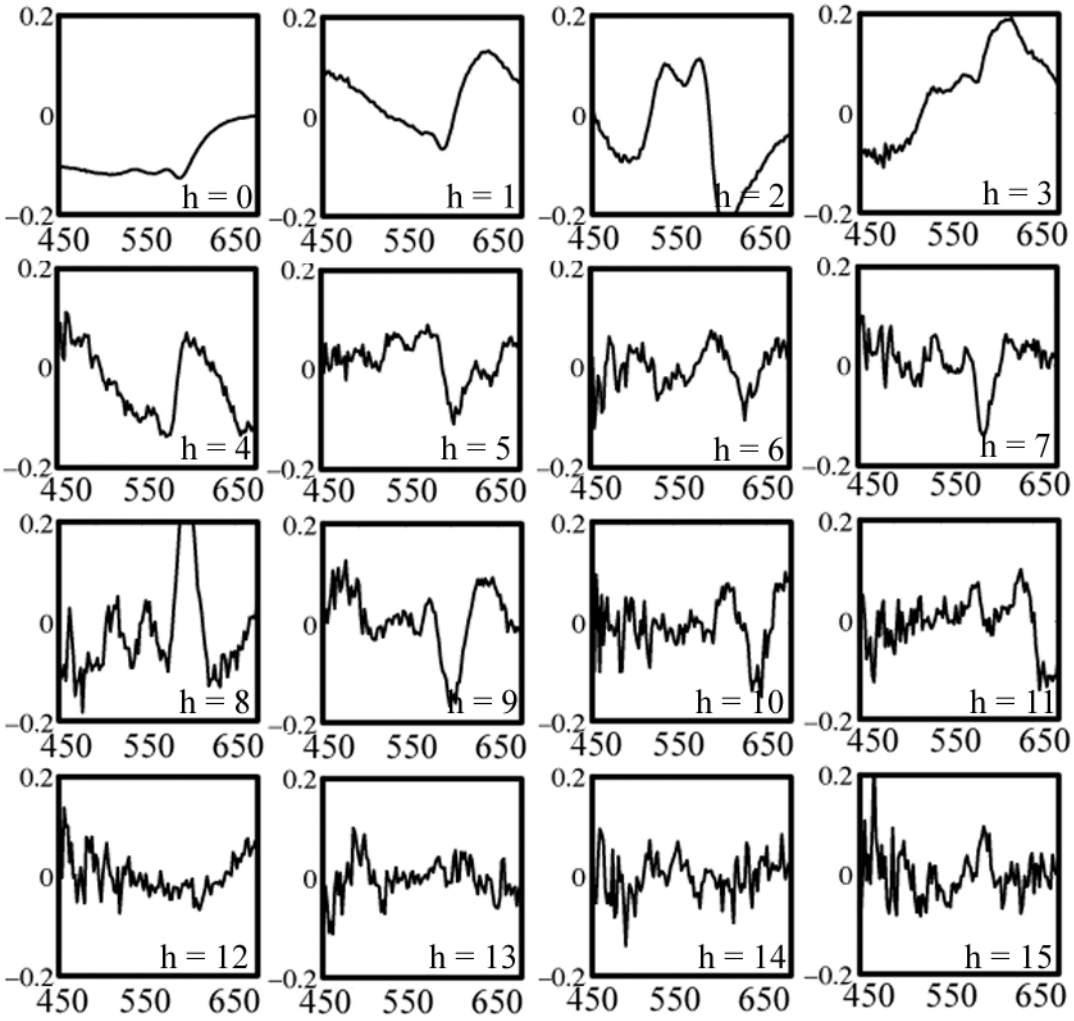

Figure 4.16: Plot of the PLS loading vector for h = 16 loops through the algorithm using 29 samples to establish calibration model. Y-axis values are relative amounts of correlation for each point in each iteration through the calibration algorithm.

may have high significance in the prediction and a high **v** value, there may be little of that vector in the varying spectral signatures (recall equation 4.17 where concentration $\sim \mathbf{v} \times \mathbf{t}$). Figure 4.17(a) shows a plot of the score coefficients versus the # of PLS loading vectors and Figure 4.17(b) shows the root mean square (RMS) of each loading vector across the entire data set. Because the data is mean centered, the score vector is < 0 for some spectra and RMS is thus used for comparison. As anticipated, the score vector is largest for the first loading vector and progressively decreases. The score coefficient varies and reaches a peak at the 5th loading vector, implying this vector is the component most free of interference from other analytes. The product of these two values,

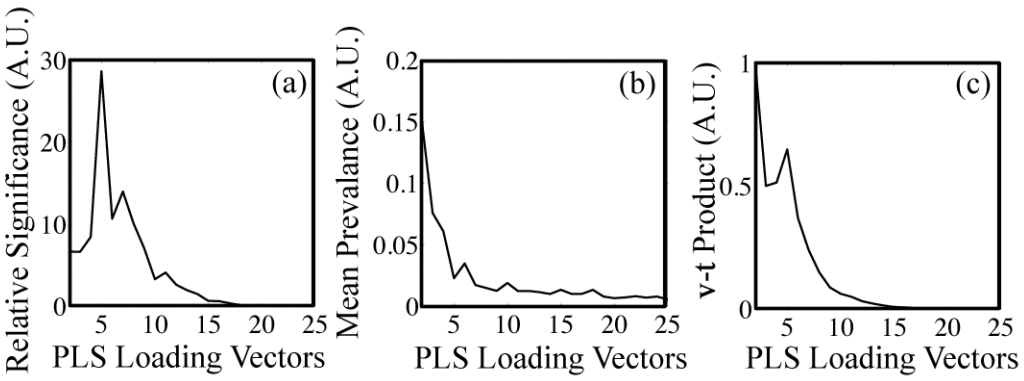

Figure 4.17: Plot of score coefficients versus # of loading vectors showing relative significance of each (a), RMS of score vectors across the whole data set showing relative prevalance of each (b) and product of these two curves showing the how significant each loading vector is in the prediction of hemoglobin.

depicted in Figure 4.17(c), shows the significance of each of the loading vectors in the hemoglobin determination.

Using these loading vectors to predict hemoglobin concentration from reflectance spectra from patients with unknown hemoglobin concentration shows a correlation related to the number of loading vectors used shown in Figure 4.18(a). The accuracy increases quickly using only a couple loading vectors, and beyond 8-9 loading vectors, the performance remains stable as the loading vectors begin to model simply the noise and have less defined features, as was observed in Figure 4.16 and in Figure 4.17

A plot of the PLS predicted hemoglobin concentration vs. CBC determined hemoglobin concentration using the leave one out cross validation with 8 loading vectors is shown in 4.18(b). While a high correlation is presented (correlation coefficient r = 0.936), the PLS linear prediction algorithm, in general, overpredicts low hemoglobin values and underpredicts high hemoglobin values. The prediction yields an agreement with standard deviation of error (standard error (SE)) = 0.887 g/dL and root mean squared error of prediction RMSEP = 0.881 g/dL. The over/under prediction at the boundaries is consistent with the concentration dependent pathlength variation; lower concentration values of hemoglobin enable a longer pathlength, and thus decrease the amount of Reflectance, making the algorithm believe the concentration is higher than the actual value. As was shown in Equation 4.7, the relationship between observed reflectance R_d and μ_a is a nonlinear one, accounting

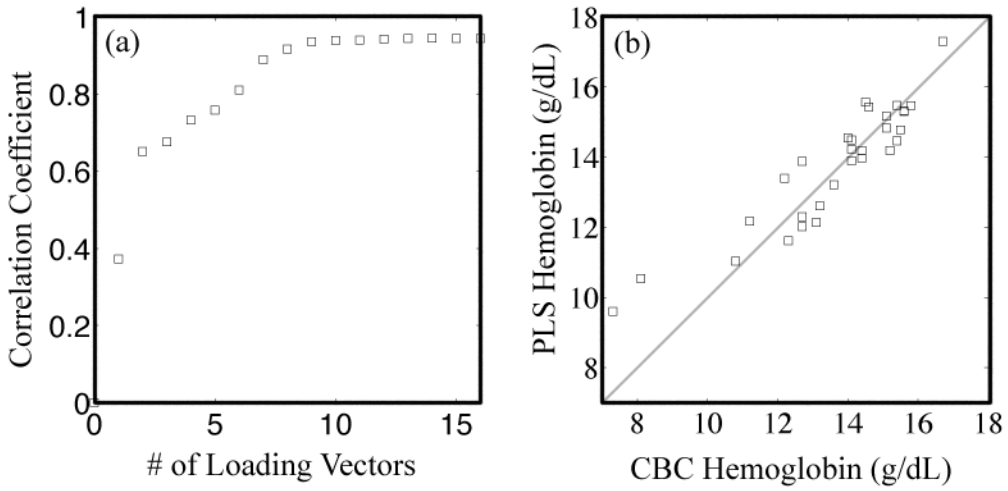

Figure 4.18: Plot of the correlation coefficient between CBC determined hemoglobin and PLS determined hemoglobin concentration as a function of the number of loading vectors (a), and prediction plot showing PLS vs. CBC determined concentration using 8 loading vectors (b).

for the biasing in prediction using a linear algorithm. From Equation 4.7, rearranging and assuming that PLS concentration predictions $\hat{\mathbf{c}} \propto R_d$, while the actual concentration c $\propto \mu_a$, then:

$$\hat{\mathbf{c}} \propto (R_d) \propto e^{\sqrt{\mu_a}} \rightarrow \ ln(\hat{\mathbf{c}}) \propto \sqrt{c} \tag{4.18}$$

The natural logarithm of PLS concentration prediction $\hat{\mathbf{c}}$ is then related to the absorption coefficient, which is proportional to the actual concentration, through a quadratic fit. This establishes a scaling algorithm for correcting PLS predictions for the nonlinearity of diffuse reflectance intensity. Using a leave-one-out cross validation to determine quadratic fits for PLS predictions and then applying this bias to the predictions themselves, the new concentration predictions $\hat{\mathbf{c}}$' compared with CBC predictions are shown in Figure 4.19. This model yields a pearson correlation coefficient r = 0.932, SE = 0.781 g/dL, and RMSEP = 0.621 g/dL.

The sensitivity and specificity of the prediction should be passable for diagnosing most cases of anemia. Using the WHO definition of anemia for males and females, the PLS/nonlinear model can be evaluated as a binary predictor of clinical anemia. For the seven patients whose CBC results found them clinically anemic, the PLS algorithm predicted six to be clinically anemic, resulting in a sensitivity of 86%. For the 23 patients whose CBC results showed them to have normal hemoglobin

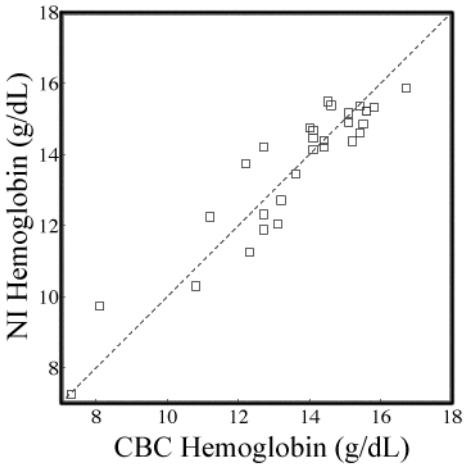

Figure 4.19: Prediction plot showing nonlinear corrected PLS vs. CBC determined concentration using 8 loading vectors

levels, the PLS algorithm predicted 21 to have normal hemoglobin levels, resulting in a specificity of 91%. This is an enhancement in both factors over color comparison charts or traditional clinician inspection methods. The utility of the PLS algorithm across ethnicities is additionally assessed. The results of the PLS/quadratic algorithm are presented as a Bland-Altman plot in Figure 4.20 [180]. This figure shows the predictive capabilities for the Caucasian, Hispanic, and African American demographics to be comparable. The RMSEP using the PLS model for the Caucasian population (n = 21), Hispanic population (n = 6), and African-American population (n = 3) were 0.564 g/dL, 0.866 g/dL, and 0.526 g/dL respectively. However, the limited numbers of participants of varying ethnicity limit clear assessment of the accuracy of the technique for each skin type. As stated previously, it is expected that a larger clinical trial will show little variation of accuracy amongst skin types because melanin content is minimal at the mucosal conjunctiva surface. This study included no participants of Asian decent.

Examining Figure 4.16, the spectral bandwidth of features in the first couple loading vector iterations are relatively large (>10 nm). To investigate the relationship of spectrometer resolution with predictive accuracy using the PLS nonlinear model, the same algorithm is applied to progressively blurred spectral curves using the 2 nm resolution raw data. Blurring is achieved through the convolution of gaussian profiles as the convolution kernel with increasing bandwidth with raw data

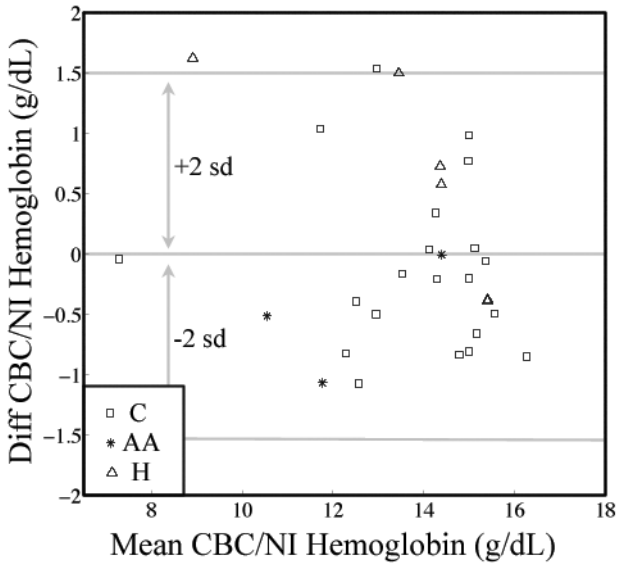

Figure 4.20:]
Bland Altman plot showing difference in nonlinear corrected PLS (NI) and CBC hemoglobin determination versus mean value plotted as a function of ethnicity. C = Caucasian, AA = African American, H = Hispanic

as shown in equation 4.19, where **n** is the number of discrete wavelength values, G is a gaussian function, and FWHM is the gaussian full width at half max.

$$\mathbf{R}' = \mathbf{R} \star G = \sum^{n} \mathbf{R} \times exp^{-(x-n)^2/2\sigma^2}, \sigma \approx \frac{FWHM}{2.355} \tag{4.19}$$

The resulting blurred spectra ranging from no blur to a gaussian profile with $1/e^2$ full width of 100 nm, as depicted in Figure 4.21. This plot shows that $\sim$ 10nm of blurring only affects the correlation coefficient by approximately 12%. Thus, a lower spectral resolution can be tolerated, an important parameter to consider when designing a portable spectrometer for this application.

4.7 Clinical Trial using Fiber-optic Reflectance Probe

While the free space propagation device showed potential technique performance, the form factor and requirement of relocation and stabilization of enrolled patients logistically made it difficult to enroll a larger patient population, as can be envisioned from Figure 4.13. To expand the data set and subsequently perform a more extensive statistical analysis of results, a second device was fabricated

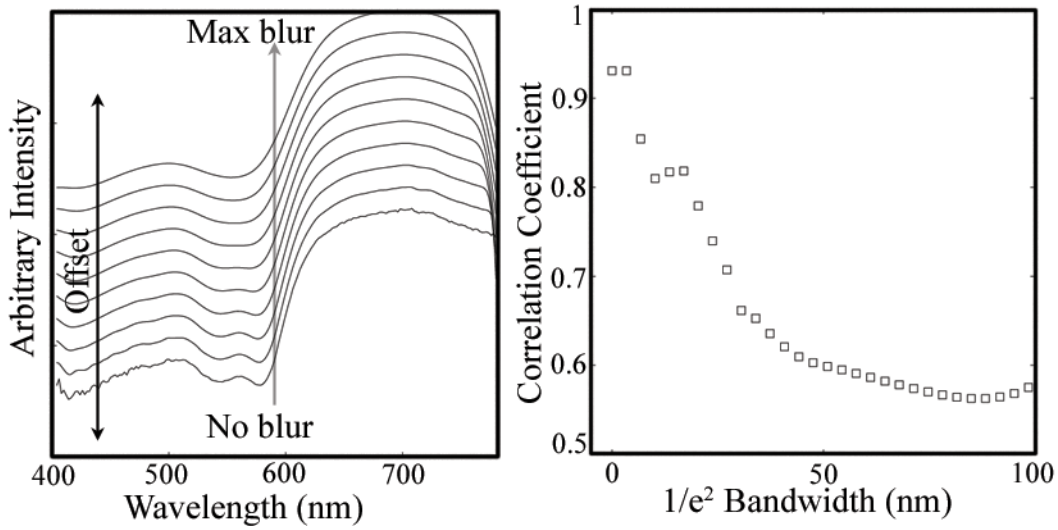

Figure 4.21: Plot of one example spectra blurred through convolution with gaussian functions of varying bandwidth (a), and the resulting correlation coefficient of PLS/nonlinear model applied to the blurred functions (b)

a fiber optic collection probe enabling bedside collection.

4.7.1 Patient Enrollment

The second clinical trial was again conducted in the emergency department (ED) at RIH and approved by the RIH IRB. Subsequent to enrollment, study volunteers were situated in a supine position. A research assistant everted the lower eyelid by pulling downward at the lashes while directing the patient to look upward, fully exposing the mucocutaneous junction, tarsal plate, and fornix. Age, sex, ethnicity, chief complaint, full CBC results, pulse, SpO_2, and blood pressure were recorded following enrollment. Patients were then classified as normal (Hgb 13-17 g/dL male, 12-16 g/dL female), anemic (Hgb $<$ 13 g/dL male, $<$ 12 g/dL female), severely anemic (Hgb $<$ 10 g/dL male, $<$ 9 g/dL female), or polycythemic (Hgb $>$ 17 g/dL male, $>$ 16 g/dL female) based upon CBC determined values. Adult patients in the ED were identified as study candidates following determination of the need for a CBC in the course of their treatment and within 6 hours of data collection. Patients with substance or alcohol abuse were excluded, as well as patients with active bleeding in the ocular region.

Figure 4.22: Photograph of data collection using fiber optic probe and collinear collection/irradiation fibers.

4.7.2 Diffuse Reflectance Spectra Collection

A metal ferrule with six 200 μm fiber oriented in a hexagonal pattern around a single 200 μm collection fiber and collimating lens affixed to the end of the probe (see Figure 4.22) was oriented such that the tarsal plate was irradiated. Collimating optics establish a consistent spot size of 2 mm independent of fluctuation in the separation from probe to conjunctiva. Illumination was achieved using a white LED (Ocean Optics, Dunedin, FL) coupled to irradiation fibers with operating range from $\sim$ 450-650 nm. Spectral monitoring was performed using a commercial miniature static grating spectrometer with 4 nm resolution (USB2000, Ocean Optics, Dunedin, FL) with collection fiber inserted at input port. Overhead fluorescent lights were turned off to remove contributions of sharp fluorescent emissions in spectra. The miniature grating spectrometer was interfaced to a PDA where the integration time was set to 50 ms per spectrum. Two reflection spectra were collected from the tarsal plate from each eye of the study volunteer, resulting in four spectra collected for each patient. The probe was removed and patients were instructed to blink between each collection to maximize comfort.

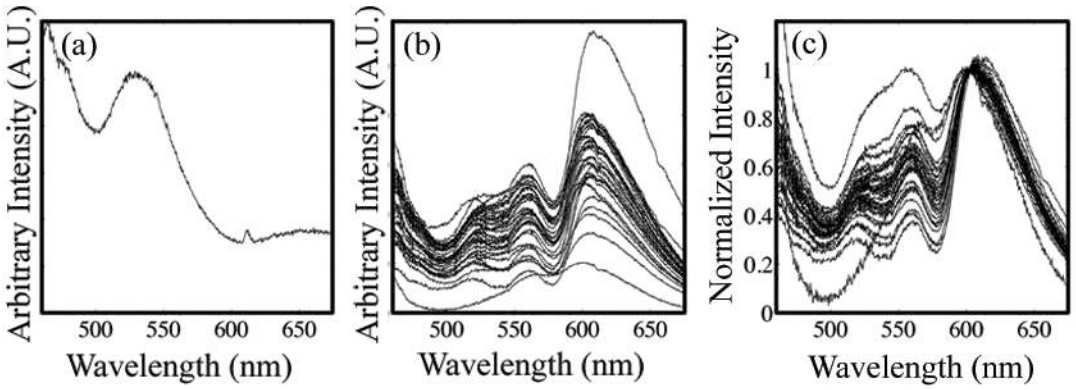

Figure 4.23: Emission spectra from white LED source (a), mean spectra from 34 of the 102 with varying hemoglobin concentrations (b), and same data normalized to reflection peak at 600 nm (c).

4.7.3 Clinical Trial Results

One hundred two patients were enrolled in this study of which 60% (N = 61) were female. The average age was 54 years (range 18-92 years, SD 21.4 years). The average CBC hemoglobin concentration was 12.9 g/dL (range 6.9-17.1 g/dL, SD 2.4 g/dL), with 65% (N=66) in the normal hemoglobin range, 31% (N=32) with in the anemic range with subset of 7% (N=7) with severe anemia, and 4% (N=4) in the polycythemic range. The breakdown in ethnicity among the 102 patients was 14% (N=14) African-American, 14% (N=14) Hispanic, 2% (N=2) Asian, and 60% (N=62) Caucasian.

The same PLS/nonlinear model used above in Section 4.6 was used to extract hemoglobin concentration again using a leave-one-out cross validation. The source, raw data, and normalized data (analagous to Figure 4.14 in Section 4.6) is shown in Figure 4.23. For figure clarity, only the mean spectra for every third patient is shown in Figure 4.23(b) and (c). Applying the PLS algorithm, vectors are constructed in a similar fashion and shown in Figure 4.24. Many of the same spectral characteristics in the predictive vectors observed from the fiber-optic data are comparable to the vectors observed in the initial study, specifically high activity around the inflection point at 600 nm and the doublet at 550-570 nm. This validates a similar predictive model is acting on the data set while using a different optical configuration.

The score coefficients $\mathbf{v}$, score vectors $\mathbf{t}$, and product of the two for the loading vector set shown in Figure 4.24 are shown in Figure 4.25(a-c). The score vectors appear analogous to the initial trial

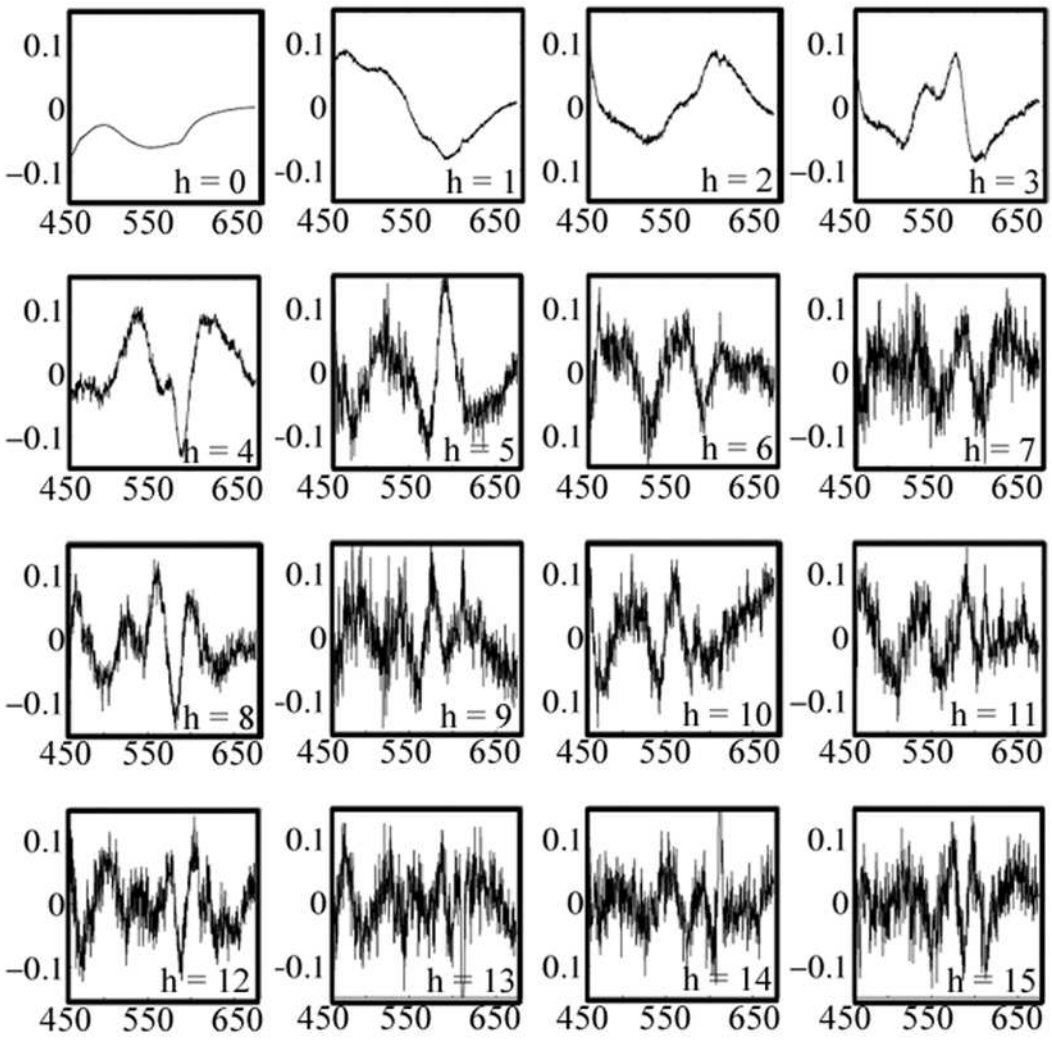

Figure 4.24: Plot of the PLS loading vector for h = 16 loops through the algorithm using 101 samples with fiber-optic device to establish calibration model. Y-axis values are relative amounts of correlation for each point in each iteration through the calibration algorithm.

while the score coefficients also appear quite similar. However, the peak in the score coefficient takes three more cycles to be reached, as is anticipated for a large sample size. With three times more patients in the calibration set, there is greater variation in spectral curves unattributable to hemoglobin, creating more interference in the earlier loading vectors.

Figure 4.26 shows the prediction plot using the linear PLS model alone (a), the Pearson correlation coefficient as a function of the number of loading vectors (b), and the prediction plot using the quadratic fitting function defined previously (c). As can be seen in Figure 4.26(a), the linear model again tends to overpredict low hemoglobin values and underpredicts high values. The plot

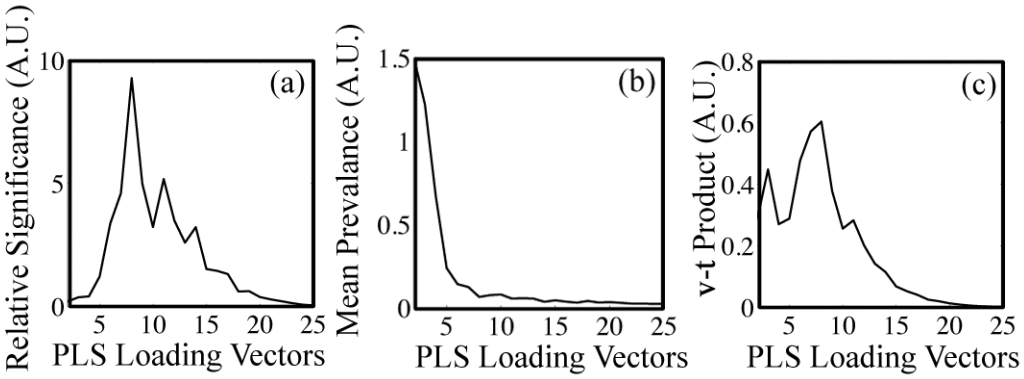

Figure 4.25: Plot of score coefficients versus # of loading vectors showing relative significance of each (a), RMS of score vectors across the whole data set showing relative prevalance of each (b) and product of these two curves showing the how significant each loading vector is in the prediction of hemoglobin

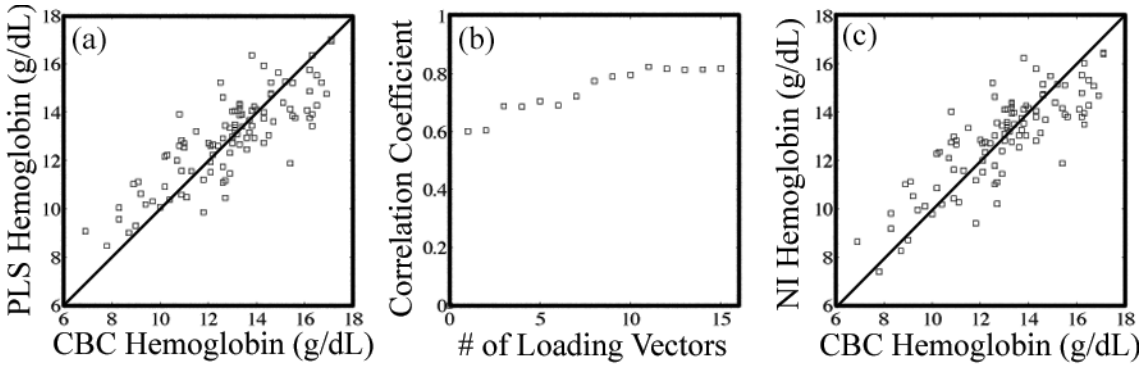

Figure 4.26: Plot of PLS determined vs. CBC determined hemoglobin using linear model with 11 loading vectors (a), change in the correlation coefficient with the number of loading vectors used (b), and prediction plot of PLS/Nonlinear model determined vs. CBC (noninvasive NI) determined hemoglobin (c).

of the correlation coefficient as a function of the number of loading vectors shown in Figure 4.26(b) again shows the majority of correlation is generated from the first couple loading vectors, consistent with the initial study and Figures 4.24 and 4.25. The maximum correlation is reached around 11 loading vectors, so this is the number used in this data set model. As mentioned earlier, the four additional loading vectors required for this model as compared with the initial trial may be a function of greater variation being calibrated in the 102 patient set. Using the nonlinear adjusted prediction model gives the prediction plot shown in Figure 4.26(c)

In this plot, the Pearson correlation coefficient is r = 0.818 with mean predicted hemoglobin of 12.9 g/dL (range 7.31-16.5 g/dL, SD = 1.9 g/dL), mean error of 1.02 g/dL (range 0.01 - 3.53 g/dL

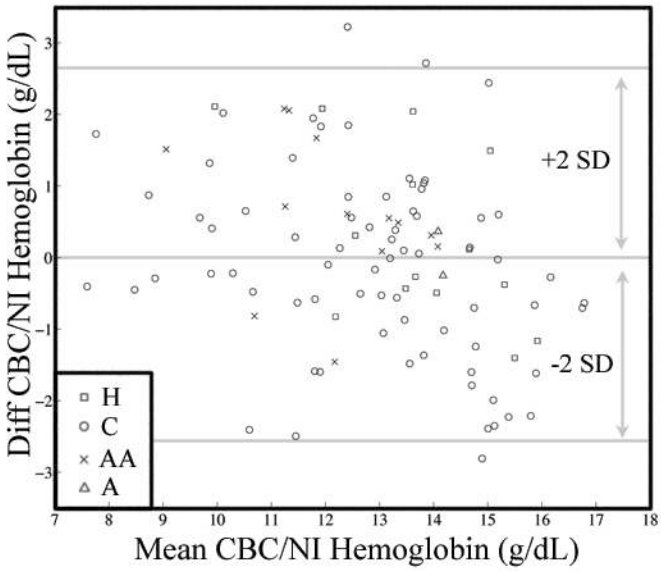

Figure 4.27: Bland Altman plot showing difference in nonlinear corrected PLS (NI) and CBC hemoglobin determination versus mean value plotted as a function of ethnicity. C = Caucasian, AA = African American, H = Hispanic

SD = 1.307 g/dL), and standard deviation of error (SE) of 1.307 g/dL in comparison to the CBC. A discussion of the change in performance is discussed below. Predictive accuracy can be broken into subcategories of anemic patients, severely anemic patients, normal patients and polycythemic patients as well as ethnic group. A Bland-Altman plot in Figure 4.27 shows the relative error vs. mean of two observations grouped in each of the four represented ethnic groups to highlight comparable performance across varying skin pigments using the nonlinear corrected PLS model.

A larger sample size allows a more thorough analysis of the anemia detection capability. Sensitivity and specificity are calculated based on predicted versus real observation of each subclass of hemoglobin concentration value. Normal value patients (N=66) are predicted with sensitivity of 86% (95% CI: 80% to 91%) and specificity of 81% (95% CI: 72% to 83%). Anemic patients (N=32) are predicted with sensitivity of 81% (95% CI: 75% to 84%) and specificity of 91.5% (95% CI: 89% to 94%). The subset of severely anemic patients (N=7) are predicted severely anemic with sensitivity of 71% (95% CI: 57% to 85%) and specificity 96% (95% CI: 95% to 97%). The subset of severely anemic patients (N=7) are predicted anemic with sensitivity of 100% (95% CI: 100%) and specificity 100% (95% CI: 100%). Polycythemic patients (N=4) are predicted polycythemic with sensitivity of

75% (95% CI: 50% to 75%) and specificity of 97% (95% CI: 95% to 98%).

As far as repeatability studies, reflectance measurements from each eye can be considered independent observations and compared for inter-rater reliability through an interclass correlation coefficient (as continuous variable) and Kappa score (discrete model). Assuming the spectra for two eyes are independent measurements, and applying the model established by the mean spectra from each eye to each individual eye, the intraclass correlation is calculated as ICC = 0.72 (95% CI 0.62 to 0.80). This is a relatively low ICC between the two measurements. In the following section, we discuss how variations in sample collection could lead to such discrepancies.

4.8 Clinical Trial Result Comparison

There are several potential sources of error amplified in the second clinical trial, most significantly the variability in sampling location using a fiber probe at the tarsal plate. This technique is predicated on maintaining uniform experimental conditions from one patient to the next, e.g. that the illumination light is sampling vessels in the palpebral conjunctiva and interspersed with the meibomian glands in the underlying tarsal plate. Error in the orientation of the fiber probe, caused by operator hand movement and/or difficulty fully exposing the tarsal plate in taught eyelids translates directly to an error in predictive hemoglobin concentration. The variation in accuracy of the fiber study from the initial study is dependent on the experimental configuration. In the initial study, the conjunctiva was fixated in a stabilization apparatus and spectral sampling performed using an objective lens grating spectrometer, allowing for high interpatient repeatability of measurement conditions. The introduction of a fiber-optic probe in this contribution allows for this technique to be performed at the bedside, but introduces significant variation in data collection, likely the primary source of error in this study (as described above in limitations).

Ongoing clinical studies are being designed for two alternative data capture techniques. First, reflectance signals can be collected using a spectral imaging device with two dimensional photodetector such that reflectance data is resolved in the vertical position dimension along one axis of the photodetector and in the wavelength regime along the other dimension. Second and alternatively, a

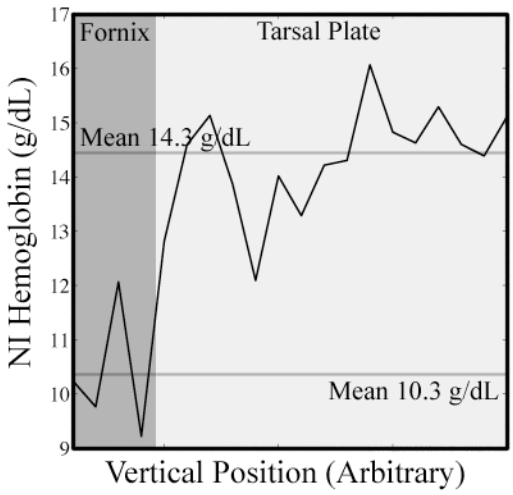

Figure 4.28: Plot of PLS/nonlinear (NI) prediction of hemoglobin as fiber optic probe is scanned vertically from the fornix to the tarsal plate.

single point fiber optic spectrometer can capture reflectance signals in kinetics mode while the probe is physically scanned vertically. The signal from the optimal positioning on the tarsal plate can be identified by the strongest hemoglobin absorption signal and the data processing algorithm applied to this signal only.

The degree of error can be assessed by scanning the fiber probe through the bulbar conjunctiva, fornix, tarsal plate, and mucocutaneous junction and observing the fluctuating hemoglobin determinations using the PLS model. This quantification was performed on four additional patient volunteers through collecting data dynamically while vertically scanning the fiber probe ≈ 2 cm and applying the optimal calibration algorithm to each one of the signals. It is noted that vertically scanning the probe is imprecise as a function of the operator movements in this difficult data collection technique, causing significant signal fluctuations from physically moving the probe. As shown in Figure 4.28, in most cases the data was noisy and erratic preventing good quantification of how much the hemoglobin prediction varied during scanning. However, on average, it appears that the using the PLS/nonlinear model, concentration prediction can vary as much as 7 g/dL from fornix to tarsal plate.

Another potential error in both studies stems from the time difference between the blood draw used for CBC laboratory analysis and data collection using the fiber-optic technique. Theoretically,

changes in hemoglobin concentration may occur due to on-going hemorrhage, fluid administration and shifts in plasma volume from other causes. There was no control in place for these variables in either clinical study.

4.9 Conclusions

The numerous pathological causes of anemia coupled with its concurrent appearance with several serious disorders and the stress it puts on both the cardiovascular/circulatory/renal systems justify the routine screening for anemia. Although the CBC provides a large amount of vital information for anemia characterization, the invasive nature of the examination and associated cost and time prevent it from being a standard procedure during physical examination. As the NAAC estimates millions of anemics go undiagnosed in the United States, rapid anemia detection is desirable in the United States and even more so abroad where statistics show the situation is more serious. Prior and contemporary spectroscopic studies involving characterization of cutaneous tissues have several technical hurdles and have hindered acceptance into clinical settings. Characterization of the mucosal surface of the inner eyelid, the palpebral conjunctiva, removes many of these hurdles and enables rapid noninvasive anemia detection in a compact and inexpensive fashion, suitable for application in domestic hospitals/physicians offices as well as anemia stricken developing countries.

A rapid, non-invasive portable tool for anemia screening could make a difference at emergency department triage points, in field treatment centers during large scale disasters and in austere environments where rapid triage and treatment decisions are based on few clinical data points. The use of devices that require blood may not be suitable or preferred in these settings. This device may serve to provide further information to triage patients with traumatic injuries or gastrointestinal bleeding. While the theory and two clinical studies presented here demonstrate the potential for a noninvasive device, the technologies presented in the preceding chapters allow for an even smaller, significantly cheaper, and more compact spectral sensor to perform a similar measurement, as well as introduce additional features such as spatially resolved imaging to eliminate addition sources of error, as discussed in Section 4.6. Furthermore this technology may be utilized to non-invasively

assess treatment interventions with transfusion. A complementary application of such techniques using fibers in laprascopic surgery is presented in the Chapter 5.

Chapter 5

Endoscopic Determination of Blood Parameters in Local Vessels

5.1 Introduction: Fetal Twin to Twin Transfusion

Measuring hemoglobin from the palpebral conjunctiva is based on integration of diffuse reflectance signals over numerous μm sized capillary vessels in the mucous membrane and muscles of the tarsal plate. These signals are monitored using collection optics / fiber arrays to localize optical detection over larger spatial area ($> 1mm$). This concept can be expanded to measure total hemoglobin *in vivo* from individual blood vessels using similar calibration and detection techniques; however, using single optical fibers to localize data collection over significantly smaller area. Although this identification of individual blood vessel parameters may have broad medical significance, particularly in neuroscience for identifying problematic brain areas from local hemoglobin indices, the suitability of this technology in identifying problematic anastomoses in fetal twin to twin transfusion syndrome (FTTTS) is discussed here.

FTTTS is believed to result from unbalanced transfusion between fetuses through placental anastomoses. These communications can have a strictly superficial course and connect homonymous vessels (arterio-arterial, AA, or veno-venous, VV), or they connect one twins artery with the other

twins vein through a shared cotyledon (AV anastomosis). It is well known that one or more such anastomoses are present in virtually all twins in the same fetus but different amnoitic cavities (diamnoitic monochorionic). While some bidirectional transfusion is therefore present in almost all these gestations [181], only a small percentage will go on to develop FTTTS.

FTTTS occurs in 10-15% of all diamniotic-monochorionic pregnancies (identical twins). If left untreated, mortality approaches 100% in severe cases [182,183]. In addition, up to 30% of survivors may exhibit severe neurological and/or cardiac anomalies [184, 185]. Laser ablation of the problematic communicating vessels through intrauterine endoscopy has gained in popularity, and is now the best available treatment for severe disease [186, 187]. Currently, only visual inspection of the placental vessels is used to determine which anastomoses to seal with the endoscopic laser. It is of great importance to only seal problematic vessels and leave regular maternal communicating vessels unchanged [188].

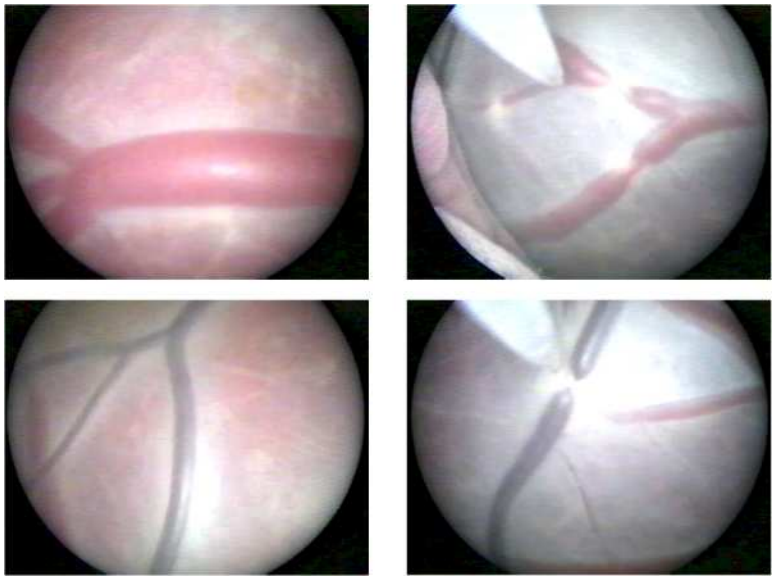

Figure 5.1: Endoscopic images of an artery and vein being photoablated using a fiber laser in the fetus. Images courtesy of Dr. Francois Luks, Hasbro Childrens Hospital, Providence, RI

As twin fetuses suffering from FTTTS have, by definition, different levels of hemoglobin (one fetus is anemic, the other polycytemic), hemoglobin determination is an ideal way to differentiate the origin of the vessels. The theory is that hemoglobin can be assessed through reflectance spectrometry using a single fiber-optic collection fiber during laparoscopic and endoscopic procedures.

The end goal of this investigation is to develop more accurate tools to differentiate causative from innocent placental vessels in the surgical treatment of TTTS, as well as techniques of non-invasive, intraoperative determination of hemoglobin during other laparoscopic operations where immediate or repeat hemoglobin determinations are needed (trauma, acute blood loss, etc.). As a result of both the small number of FTTTS events performed and the difficulty in obtaining quantitative hemoglobin concentration value in a fetus, two studies were collected in parallel: (1) collection of reflectance spectra from individual blood vessel using a single fiber during various laparoscopic procedures for probe calibration and (2) observation of varying signals from donor/recipient artery/vein during FTTTS procedures available for patient enrollment.

5.2 Laparoscopic Clinical Study

As a result of the infrequent treatment of FTTTS patients at the test site, the fiber optic probe was additionally tested on patients undergoing routine laparoscopic procedures such as appendectomy, cholecystectomy, or hernia repair.

5.2.1 Spectral Collection Technique

The most crucial and challenging aspect of this study is obtaining a repeatable spectral vessel measurement technique in a turbid and difficult endoscopic working environment. Unlike the conjunctiva study presented in the preceding chapter where signals are collected over many vessels, isolating reflectance signals from a single vessel requires precise fiber positioning, collection angle considerations, and mechanical fiber stability. The geometry of the collection fiber, explicitly the numerical aperture and fiber to vessel separation, determines the solid angle over which reflectance signals are collected. In an ideal case, (1) only reflectance signal would be collected from the vessel of interest and not background tissue and (2) the fiber geometry would be constant between patients and vessels.

Compared to the regression analysis techniques in Chapter 4, the relatively small data set size does not allow the same class of correlation analysis. In order to extract a quantitative parameter

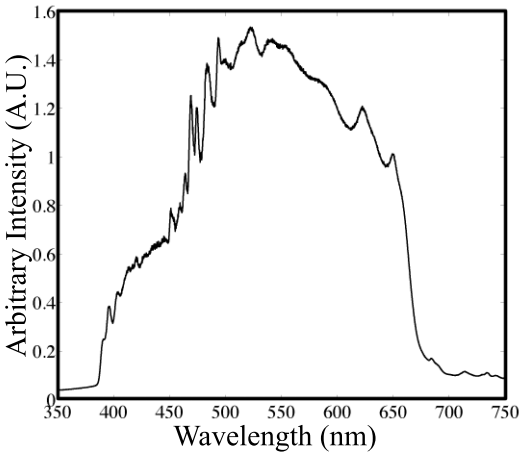

Figure 5.2: Endoscopic irradiation source normalized spectral intensity curve

correlated with total hemoglobin concentration, reflectance spectra were normalized by the irradiation source (shown in Figure 5.2) and then normalized to peak vessel reflection at $\lambda = 625$ nm. An estimation of the amount of total hemoglobin is calculated by the intensity ratio at two spectral points with significantly different absorption coefficients, $\lambda_1 = 625$ nm and $\lambda_2 = 575$ nm. Ideally, two isosbestic points for oxy- and deoxyhemoglobin would be compared; however, the similarity of absorption coefficients of five isosbestic points in the working spectral range ($\Delta\lambda$ = 400-700 nm) make this comparison less precise. The error introduced by varying oxy- and deoxyhemoglobin absorption coefficients at λ_1 and λ_2 is significant, but likely tolerable in preliminary experimentation. FDA regulatory procedures did not permit the introduction of longer wavelength NIR irradiation into the system, eliminating the potential to apply algorithms similar to pulse oximetry for saturation detection. This artificially generated ratio value is termed the hemoglobin ratio parameter (HRP) and increases correlated with total hemoglobin concentration.

Three optical sampling techniques were investigated over the course of proof of concept laparoscopic studies. First, the collection fiber was oriented in proximity to the blood vessel of interest (at $<$ 2 cm fiber to vessel separation) and single reflectance spectra were acquired. Because the broadband irradiation source is colinear with the collection fiber, the orientation of the fiber can be determined by the illumination spot. Second, the fiber held at a fixed separation and translated

across the blood vessel of interest (similar to a bar code reader) while reflection spectra were acquired in rapid collection mode. The theory of the scanning technique is that at one time point, the fiber is oriented perfectly over the vessel of interest, which should generate a spike in the HRP to be used in comparison with other vessels. This eliminates possible fiber misalignment or movement artifacts beyond individual acquisition events in the first technique. Lastly, the fiber was gently tapped against the blood vessel of interest, again generating peaks in the HRP correlating to the fiber contact points.

Even assuming repeatable collection techniques, making quantitative measurements of hemoglobin concentration requires a calibration for varying blood vessel thickness. Thicker blood vessels will translate to an artificially high HRP; and subsequently need to be corrected as vessels ranging from 500 μm to 2 mm are of significance. Digital images of blood vessels being investigated are captured, and the fiber probe itself is used as a reference to standardize image magnification.

5.2.2 Patient Enrollment

Eight patients undergoing laparoscopic procedures in the Hasbro childrens hospital surgical department were enrolled, and one patient was subsequently excluded due to equipment failure. Patients had a preoperative hemoglobin determination (CBC) within 24 hours of the operation and all patients with active hemorrhage were excluded. At the beginning of the laparoscopic procedure, a 10 Fr. endoscopic sheath containing a 1.9 mm telescope and collection fiber optic is introduced into the peritoneal cavity. For patients 1-4, the collection fiber is a custom silica fiber coated with a buffer layer to improve fiber durability with a total diameter $\sim$ 500 μm and low numerical aperture. The custom fiber is affixed to one of the entry points of the fiber sheath using an in-house fabricated adapter. For patients 5-7, in order to satisfy arising IRB concerns, the collection fiber was switched to a commercially manufactured endoscopic fiber with diameter of $\sim$ 700 μm; the same fiber used for Nd:YAG laser ablation. Illumination is colinear with collection fiber along the same endoscope using a broadband halogen source with spectral characteristics as shown in Figure 5.2. The broadband source is the same source used for endoscopic imaging. Denoting the enrolled laparoscopic patients

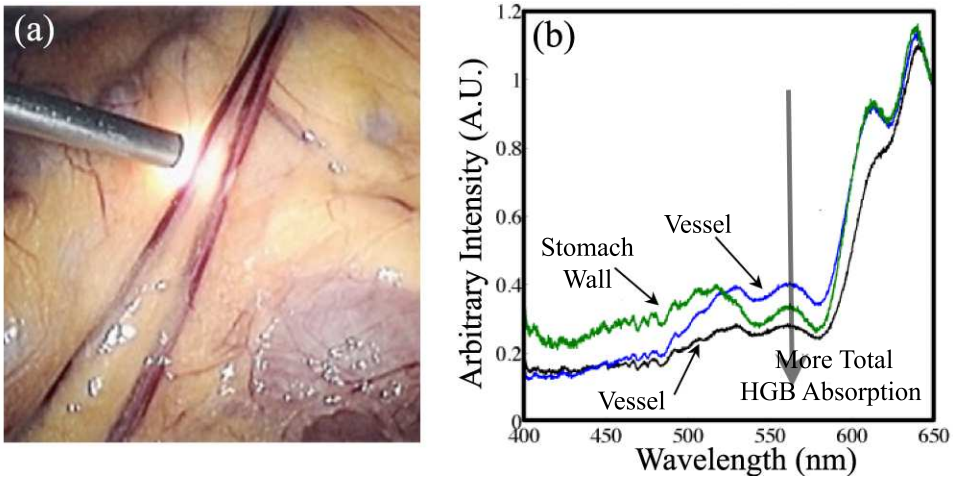

Figure 5.3: Endoscopic images of a bIood vessel in the stomach lining collected using a single fiber collection system (a) and two spectra from a single vessel in multiple captures as well as spectra from the adjacent stomach wall (b).

numerically L1-L7, spectra were collected from patient L1 using the single frame collection method, spectra were collected from patients L2-L4 using the scanning collection method, and spectra were collected from patients L5-L7 using the tapping collection method.

At least four individual blood vessels (mesentery, omentum, bowel wall) are illuminated in each patient and spectra collected. Total measurement time is < 1 second per measurement using the static measurement method, and between at 10-20 seconds using the scanning and tapping measurement technique. This procedure cumulatively adds approximately 1-3 minutes of operative time. Digital image collection software is supplementally used to collect multiple images of blood vessel of interest, as states above, for image processing, vessel diameter normalization, and blood vessel localization following collection of spectral signatures. Results of each group of data collection techniques are shown below.

5.2.3 Laparoscopic Clinical Trial Results

Single Frame Readings

A preliminary effort at collecting single frame vessel spectra was performed in patient L1. The fiber optic probe was positioned in proximity to the vessel of interest, < 2 cm, and spectrometer integration time adjusted to prevent saturation from high intensity halogen source. Integration

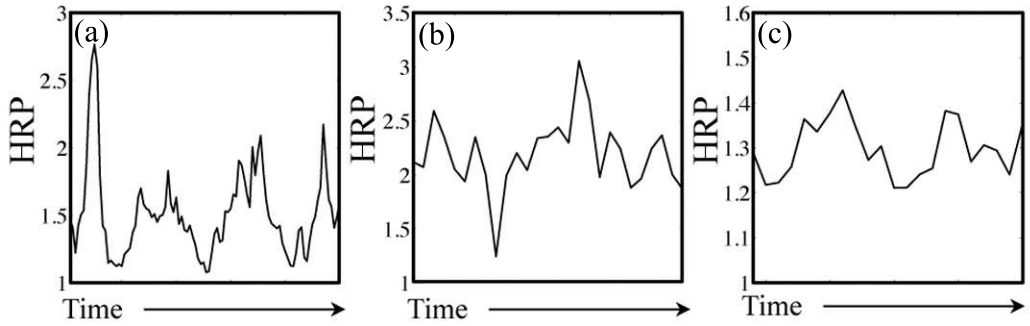

Figure 5.4: The HRP for multiple rapidly acquired signals while holding the fiber at a blood vessel in LP2 (a) and translating the probe over a blood vessel in LP3 (b) and LP4 (c).

time was on average $\sim$ 25 ms. Spectra were acquired with the irradiation spot centered on vessel of interest for four vessels of interest on the stomach lining and other accessible areas. A digital image of the single capture configuration on a vessel of the stomach lining is shown in Figure 5.3(a). Following normalization and removal of irradiation source characteristics, two spectral acquisitions from one particular vessel are shown in Figure 5.3(b).

Looking at the two spectra collected from the same vessel, the difference in the HRP is $> 30\%$, clearly demonstrating significant intra-vessel variation in signal acquisition from movement and fiber orientation. Although some repeated single capture spectra from other vessels are more similiar in appearance, this error is not tolerable for determining quantitative information. Additionally, a spectra is captured from the tissue wall just beside the vessel probed in Figure 5.3(a). This spectrum, also shown in Figure 5.3, indicates a significant amount of optical interaction with the adjacent blood vessel is still recorded due to fiber optic collection cone. Spectral absorption profiles from background fatty tissue are also observed (the increased reflectance from 400-500 nm). These results indicate that a single spectrum capture method is not sufficient to reliably sample from one vessel without interferance from background tissue and operator fiber positioning.

Positional Fiber Scanning

To eliminate some of the operator variability in acquiring a single spectra while holding collection fiber position stable, the instrument settings were changed to collect spectra in rapid acquisition mode. The fiber was either held stationary (laparoscopic patient L2), or translated positionally

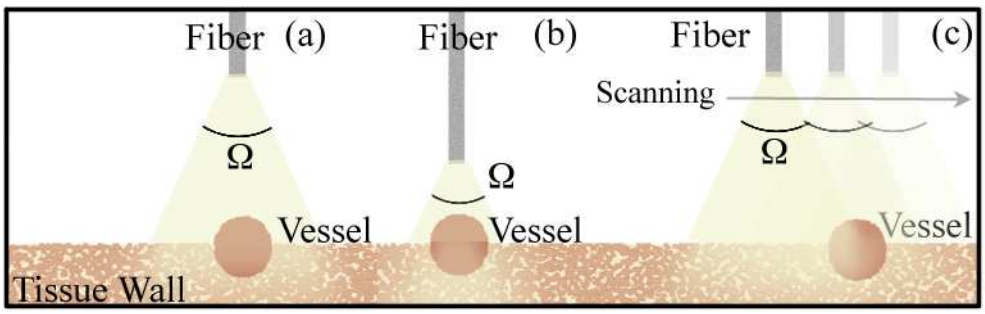

Figure 5.5: The amount of background tissue sampled depends on the solid angle of collection, Ω, and distance from fiber to tissue (a). Decreasing this distance decreases the interference from background and artificially increases signal from vessel (b). Scanning across the vessel, as in Figure 5.4(b-c), may not produce a peak in HRP depending on the solid angle and separation because the sampling area is large and modulation in background tissue are also detected (c).

across the blood vessel of interest (laparoscopic patients L3 & L4) while multiple spectra acquired (> 30). Data collection was taken over 15 s with average integration time at ~ 20 ms. The resulting HRP is plotted as function of time for rapid collection while positioning fiber over vessel of interest for patient L2 (Figure 5.4(a)) and while translating the fiber position across the vessel of interest in patients L3 and L4 (Figure 5.4(b) and (c), respectively).

Figure 5.4(a) shows modulation in the HRP corresponding to variations in hemoglobin signal from slight changes in fiber orientation with respect to vessel while holding fiber stable. Although local HRP maxima are observed in this function, the variability from fiber numerical aperture, fiber separation, and background tissue make this value an unreliable quantitative indicator. Changing the separation of fiber to vessel changes the proportion of vessel to background tissue sampled, as depicted in the change from Figure 5.5(a) and (b). This becomes a more significant problem when the tissue background characteristics have different absorption profiles, such as in two entirely different tissues (e.g. placental wall vs. fatty tissue). Physically translating the fiber across the vessel of interest, as shown in Figure 5.4(b) and (c) for patients L3 and L4, respectively, experiences this same issue. The HRP signal should be a function with a peak in the center as the probe is positioned over the vessel; however background tissue variation and probe orientation variation corrupts this signal with noise. Additionally, depending on the collection solid angle, the HRP may not have a peak in the translation position because the vessel is sampled in many scanning locations, as depicted in Figure 5.5(c).

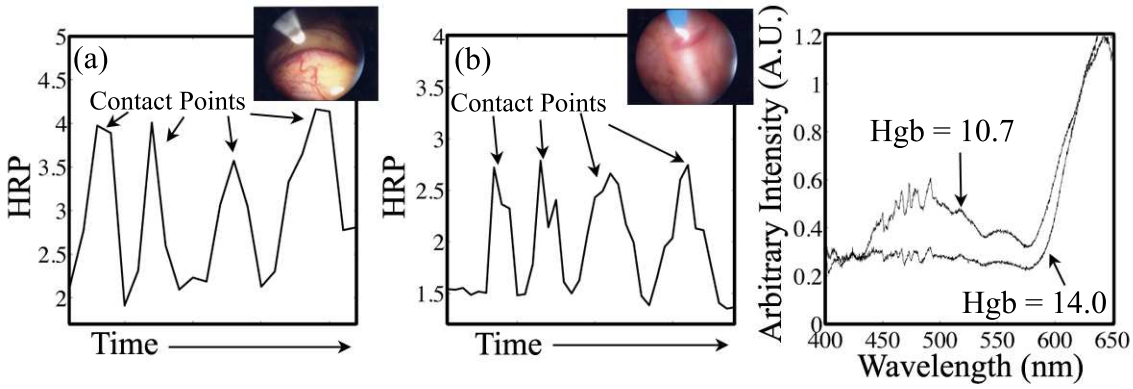

Figure 5.6: Change in the HRP correlating to hemoglobin as fiber is touched to vessel of interest in patient with hemoglobin of 14.0 (a), and 10.7 (b). Insets show the particular vessel probed in each case. Overlayed reflectance spectra correlating to a peak in the HRP for each patient are shown in (c).

In general, too many variables remain in data collection to ensure reliable data collection using this technique. Any permutation of these parameters can scale the HRP and add significant defects to the system. Placing the fiber in contact with the vessel helps minimize these variables for more reliable collection and is likely the optimal configuration.

Fiber Vessel Tapping

Data was collected from the last three patients (LP5-7) using rapid spectral acquisition with tapping the blood vessel of interest. The advantage of the tapping technique is it both assures that the blood vessel of interest is sampled with minimal interference from surrounding tissues while also assuring a repeatable technique from vessel to vessel. In patient LP5, an arbitrary number of fiber vessel contact events were initiatied, between two and six, for each vessel. It was observed that this process made it more difficult to isolate local maxima due to random peak spacing in the HRP, and in the two subsequent data collection elements, the tapping was fixed at four contacts per vessel. The integration time was varied slightly at each vessel to maximize signal without A/D saturation, but generally at $\sim$ 10 ms per spectra over 10 s of data collection. As shown in Figure 5.6(a) and (b), the peaks in HRP clearly show the four peaks from vessel/fiber contact for the final two patients. Pictured is the HRP as a function of time for two vessels of comparable size in patient 6 and patient 7, with hemoglobin concentrations of 14.0 and 10.7. The average HRP from contact points in Figure

5.6(a) is 3.9 with SD of 6% of mean peak value, while the average HRP from contact points in Figure 5.6(b) is 2.7 with SD of 2% of mean peak value, translating to a 35% greater HRP for patient 6 over patient 7 and correlating with the difference in hemoglobin concentration from 10.7 g/dL to 14.0 g/dL.

Although perfection of this sampling method along with collection of additional data is necessary to establish an accurate calibration relation between HRP and total hemoglobin, the above result shows the proof of principle that this technique can be used to quantify total hemoglobin from individual blood vessels.

5.3 *In Utero* Clinical Study

For proof of concept in the use of this technology for FTTTS patients, quantitative measurement of hemoglobin is not explicitly necessary but rather a comparison and identification of individual vessels from the recipient (polycythemic) twin and donor (anemic) twin based on relative total hemoglobin concentration. Comparing and grouping the relative sets of vessels can show the potential of this technique without quantitative analysis.

5.3.1 Patient Enrollment

Three patients undergoing necessary FTTTS procedures were enrolled for study participation. Patients undergoing endoscopic laser ablation of placental vessels for severe TTTS are treated according to standard-of-care protocols. Placental vessels are examined endoscopically, and communicating vessels (AV, VA, AA and VV) are occluded using Nd:YAG or diode laser, as per operative guidelines. Prior to ablation of the vessels, each vessel crossing the equator (membrane between twins) is probed using the collection fiber as described above. In each patient, at least 4 vessels from each fetus, measured close to the umbilical cord insertion, will be sampled; one artery and vein from the donor and recipient.

5.3.2 Spectral Collection Technique

While the tapping method was found to be the most reliable technique for obtaining repeatable data, the risk factor of vessel perforation *in utero* from physical contact with a bare fiber prevented this sampling technique from being employed. The scanning data collection technique was applied in all three FTTTS patients enrolled for data collection. Although the concerns of the background tissue interference observed in laparoscopic patients persist, the background of the placental wall should be, at a minimum, more spatially uniform around each vessel of interest, making the interference constant for all data. The fiber probe was scanned horizontally across the blood vessel and the spectra corresponding to the maximum HRP used for comparison. Digitial images were again collected for all vessels sampled. An image of the collection fiber in proximity to a the recipient artery is shown in Figure 5.7

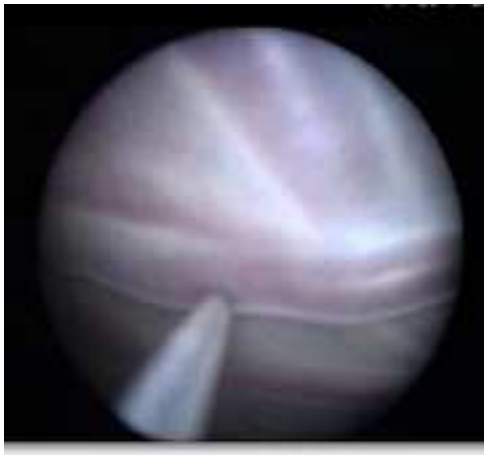

Figure 5.7: Digital image of fiber collection from recipient artery *in utero*

5.3.3 *In Utero* Clinical Trial Results

A plot of the spectra of all four vessel types corresponding to the maximum HRP is plotted for FTTTS patient 1 and 2 in Figure 5.8(a) and 5.8(b), respectively. As this figure shows, the vein and artery of the donor and recipient twin are differing in the HRP with the recipient twin having a higher HRP, as anticipated. Additionally, there are small but consistent differences between the artery and vein or each individual twin. Patient 1 has an average HRP difference of 26% for donor/recipient,

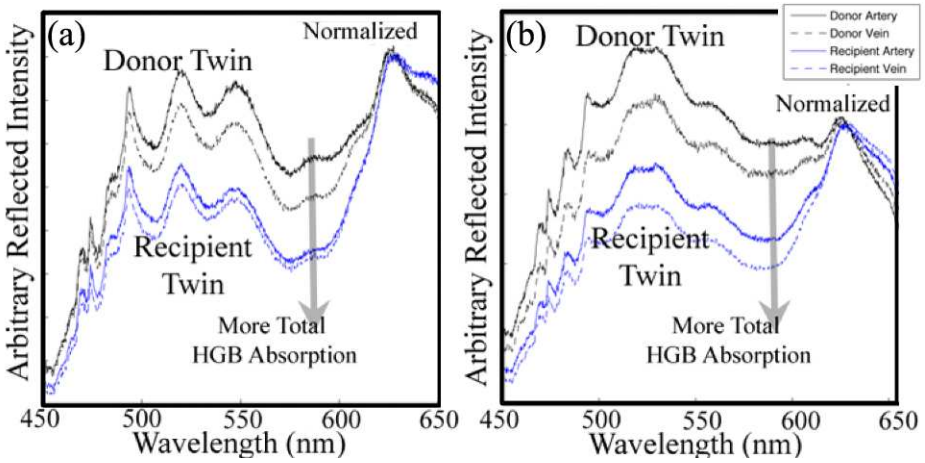

Figure 5.8: Reflectance spectra from donor/recipient vein/artery for two sets of twins with FTTTS

10% difference for donor vein/artery and 1% difference for recipient vein/artery, while patient 2 has an average HRP difference of 31% for donor/recipient, 9% difference for donor vein/artery and 12% difference for recipient vein/artery. The vein/artery difference is likely is a facet of variation in the absorption coefficients of oxy and deoxyhemoglobin at the two ratio points since they are non-isosbestic for these two proteins. This is consistent when looking at Figure 4.3 such that the ratio of absorption coefficients at $\lambda = 625$ nm and 575 nm is greater for oxyhemoglobin, therefore, the HRP will be greater for the vessel with higher concentration of total hemoglobin *and* higher saturation. This is the observed Figure 5.8(a) and (b) as the vein has the maximum HRP in both donor and recipient (and fetal blood is analogous to pulmonary circulation in adults such that arterial blood is oxygen poor and venous blood is oxygen rich).

While the figure above leads to promising conclusions, the third patient enrolled in the FTTTS did not fit the above pattern of grouping, but rather showed that the HRP was at a maximum for the vein of both donor and recipient while the artery of both donor and recipient were significantly lower (average difference of artery and vein 15%). This would be the case if there was little difference in total hemoglobin between the donor/recipient was small while the saturation difference was large; however, it cannot be stated with much certainty until the fiber optic probe has both been sufficiently calibrated to read quantitative values, and the tapping sampling method can be employed to ensure reliability of of data collection.

5.4 Conclusions

Evaluating this extension of research on hemoglobin concentration determination for individual blood vessels during endoscopic procedures has shown potential application in these first steps. The use of a single fiber to sample a single vessel has shown some capability of determining quantitative parameters related to hemoglobin concentration by placing fiber in contact with vessel to be sampled. Additionally, the fiber system has been shown to differentiate donor from recipient blood vessels in FTTTS; the main thrust of this investigation. The necessary major next steps in the laparoscopic arena involve the identification of more patients for enrollment, those patients undergoing laparoscopic procedures to collect more contact tapping data for calibration of HRP with total hemoglobin concentration. In the case of FTTTS, the main necessary steps include (1) use of fiber contact mode to ensure more reliable data collection, (2) making use of calibration data determined in laparoscopic study and (3) implementation of a wider band source to include NIR wavelengths and more reliably discern veins and arteries using isosbestic points, as in pulse oximetry.

Chapter 6

Conclusions

6.1 Thesis Summary

The preceding chapters discuss both device engineering fundamentals and new applications of biomedical spectroscopy. A summary of the findings in each chapter on these two different facets is discussed below followed by some concluding remarks.

6.1.1 Microspectrometers

Chapter 1 discusses fundamental technologies currently used to create miniature spectrometers, both LC and non-LC based. Micro-machined grating and FT devices, acousto-optic filters, tunable Fabry-Pérot filters, and thermally actuated Bragg filters are among those investigated as possible modes of ultra-miniature spectrometer fabrication. Following a brief overview of the most significant properties of liquid crystalline materials, an overview is presented of applications of LC's in microspectrometers. Several configurations of tunable LC spectrometer are presented including tunable Lyot filters, LC phase modulators in FT devices, and LC variable retarders at waveguide interfaces. Lastly, implications of patterned LC switches and passive variable retarders are discussed in the scope of Hadamard transform spectrometers and static LC phase plate/focal plane array spectrometers, respectively.

Chapter 2 expands upon the technologies discussed in Chapter 1 with a new tunable LC spectrometer based on ferroelectric liquid crystals. Ferroelectric liquid crystals are most often used in microspectrometers as binary waveplates either in the DHFLC or SSFLC configuration. We disclose a new way of using the DHFLC configuration in an analog tunable mode, such that deforming the helical structure in these materials with temperature or applied electric field creates a tunable photonic crystal/Bragg grating. This chapter discloses all relative properties of the VA-DHFLC filter, including the polarization sensitivity, experiemental and theoretical filter performance, and wavelength tuning characteristics. Filters with no polarization sensitivity, tuning ranges across the visible spectral regime, and resolution capabilities from 15-30 nm, depending on the central wavelength, are fabricated. The ability of this device to resolve spectral information was characterized by testing its ability to recreate emission spectra from various souces, including a mercury lamp, white LED, and LCD panel emission. This chapter also discussed the capability of implementing these devices as spectral imaging device; replacing the single point photodiode in the microspectrometer setup with a focal plane array. Lastly, an increase in resolution was observed in the spectral signatures by applying either the Lucy-Richardson or blind deconvolution algorithm to the spectral signatures.

A second class of LC spectrometer is disclosed in Chapter 3 using a new type of LC polymer composite phase retarder. Stressed liquid crystal polymers have been investigated previously as a result of their μs switching times, however, the alignment of LC in these materials by sheared polymers throughout the volume of the LC layer allows ultrathick variable retarders to be realized. As the resolution in an FT spectrometer is dependent on the maximum phase delay, or retardance, in the sample, SLC phase modulators have the capability of single panel FT devices. A single pass FT device of 100 μm thickness was shown to resolve single frequency emission with resolution of 160 nm while a double pass FT device was subsequently shown to resolve laser emission with resolution of 60 nm.

6.1.2 Clinical Applications

Chapter 4 discusses the focal application of this thesis, the investigation of a method for non-invasive hemoglobin detection based on diffuse reflectance spectroscopy from the palpebral conjunctiva. Anemia definitions, pathological causes, and alternative attempts at a noninvasive detection scheme are discussed to justify the need for such a technology. Tissue diffusion theory is presented assuming the conjunctiva is a finite thickness layer medium and the scattering is relatively constant from patient to patient. A predictive model using a combination of nonlinear fitting and the partial least squares algorithm is presented as the best approach to predict hemoglobin from unknown diffuse reflectance spectra. Results from two clinical trials using different optical systems showed the ability of this predictive model to determine hemoglobin with a mean error of 0.781 g/dL ($r = 0.931$, $n = 30$) and 1.02 g/dL ($r= 0.818$, $n = 101$). Sensitivity and specificity of anemia detection for these two clinical trials was found to be 86% and 91% for the initial trial and 81% and 91% for the follow-up trial.

Chapter 5 examines an extension of the conjunctiva application where hemoglobin detection is performed using a single fiber from an individual blood vessel. In fetal twin to twin transfusion syndrome, local hemoglobin concentration in a individual blood vessel aids in determining if the blood vessel is properly adjoined to the maternal vessels. The capability of using a single fiber to detect shifts in hemoglobin concentration is clinically investigated during endoscopic procedures both in the fetus, and in standard laparoscopic procedures. In the laparoscopic procedures, various sampling techniques were tested in order to optimize repeatability of data collection from the individual fiber and it was found that in order to achieve reliable data, the fiber has to be touched against the vessel interest. In fetal endoscopy, vessels from the donor and recipient twin in FTTTS were discerned using reflectance profiles.

Appendix 1, appearing following these conclusions, explored a tangential application of biomedical diffuse reflectance spectroscopy. Vascular leak is an important biological response to monitor during infection, as changes in permeability of the vascular endothelium release immune cells, but also fluid into the site. The behavior of proteins in inhibiting or promoting this leak is assesses

through the Miles assay, in which a dye is injected into an animal and leak events induced, producing high dye absorption events in areas of leak. Diffuse reflectance spectroscopy is applied here as way to quantify the degree of leak, and provide a method for tracking the leak over time. Results in multiple animal studies showed the capability of diffuse reflectance spectroscopy to quantify immune reaction to mustard oil, vascular endothelial growth factor, and an investigative protein CAP37 suspected to cause endothelial permeability changes.

6.2 Concluding Remarks

Anemia is a single largest global illness adversely affecting mortality estimated to afflict 3.5 million people in the U.S. and 2 billion worldwide. Although anemia is often perceived by the general population to be a minor medical condition; it is a significant ailment physicians and other health care professionals have recognized as a serious condition. Current methods of hemoglobin measurement are invasive and involve a time delay ranging from minutes to hours because there is no clinically accepted non-invasive real-time method of measuring hemoglobin. The primary application discussed in this thesis fits this need as the method is capable of delivering real-time result of quantitative total hemoglobin concentration. Anemia is encountered across a breadth of medical specialities not limited to oncology, pediatrics, obstetrics, gynecology, anesthesiology, infectious disease, gastroenterology, cardiology, nephrology, geriatrics, and urology. Users of this technology can include physicians, nurses, lab technicians, paramedics and blood bank personnel, giving these studies an exceptionally broad impact.

Additionally, this technology significantly benefits from LC or other simple microspectroscopy technologies as it allows implementation and distribution of the device as an ultra-inexpensive and compact rapid screening tool in the hospital, family physicians office, blood bank, and the third world (where anemia is most prevalent and needle reuse runs rampant). The need for the technology is also evident in global HIV/AIDS guidelines state that a hemoglobin estimation, coupled with an HIV test, are the absolute minimum before administering anti-retroviral (ARV) therapy, meaning that simple, reliable and affordable screening tools must be widely available to support global initiatives

aimed at providing widespread ARV treatments. Implementing a spectrometer technology that is durable, inexpensive, and reliable in a device that is intuitive to use, requires no disposable (no patient contact), and can be operated by low level health providers is the end goal of this project, of which many steps have been completed in the scope of this thesis

Appendix A

Optical quantification of Vascular Leak in Rodents

A.1 Introduction: Vascular Leak

The vascular endothelium is not a simple, passive barrier to the passage of soluble and cellular blood components but instead is subject to highly active and tightly regulated biological control. Under pathological conditions, barrier function may become compromised leading to vascular leakage and concurrent associated tissue edema and inflammation. Diseases such as pulmonary edema, myocardial and cerebral infarction, diabetic retinopathy, and cancer metastasis all can benefit from the control and inhibition of vascular leak [189, 190]. In this regard, mediators of permeability such as vascular endothelial growth factor (VEGF) and other potential downstream signaling molecules are excellent potential targets for anti-vascular leak therapy [190, 191]. The lack of methods for quantifying vascular leak in an *in vivo* system which also allow for repeated measurements limit in vivo pharmacokinetic analysis of candidate anti-leak molecules. This limitation is because the Miles Assay for vascular permeability measurement *in vivo* is currently only quantified either by observation, planimetry or by tissue extraction. These methods are inherently limited by imprecision or by restriction to a single measurement, respectively. The present study demonstrates the feasibility

of diffuse reflectance spectroscopy in the quantification of vascular leak. Diffuse reflectance signals are collected using a reflectance probe similar to that applied in the fiber-optic conjunctiva study discussed in Chapter 4.

This noninvasive procedure is reproducible and can be used to acquire repeated measures over time allowing for pharmacokinetic analyses. Verification of this procedure used topical application of mustard oil or intradermal injection of recombinant vascular endothelial growth factor (VEGF) into mice or rats to elicit vascular leak. Preliminary experiments also included intradermal injection of recombinant CAP37 (cationic acidic protein of 37kD), a secretory protein released by neutrophils at sites of inflammation which has been shown to compromise endothelial barrier function in vitro [192, 193].

A.2 Animal Trial Data Collection Methods

The ability of diffuse reflectance spectroscopy to quantify vascular leak was demonstrated in multiple animal trials. Concurrently, the ability of a fiber reflectance probe to quantify leak, determine the time constant of the leak, roughly estimate the spatial uniformity of the leak spot and, most importantly, compare the amount of leak occurring from various proteins/peptides were examined.

A.2.1 Rodent Preparation and Injection

Rats and mice were treated with both topical and injected irritant agents and controls over the course of this study. Fisher-344 rats (160-180 g; VAF-plus; Charles River Laboratories, Wilmington, MA) or BALB/c mice (∼25g; Charles River Laboratories) were housed in barrier cages and fed rat chow and water *ad libitum*. VAF-plus rats and mice were certified free of common rat pathogens by the supplier and were monitored by Brown University/ RIH veterinary personnel. All animal studies followed current NIH guidelines for the Use of Laboratory Animals and were performed according to Institutional Animal Care and Use Committee-approved protocols.

Vascular leak events were enhanced for measurement through the Miles Assay, requiring injection of a dye conjugated with small bloodstream protein. Animals were anesthetized with 3% Isoflurane

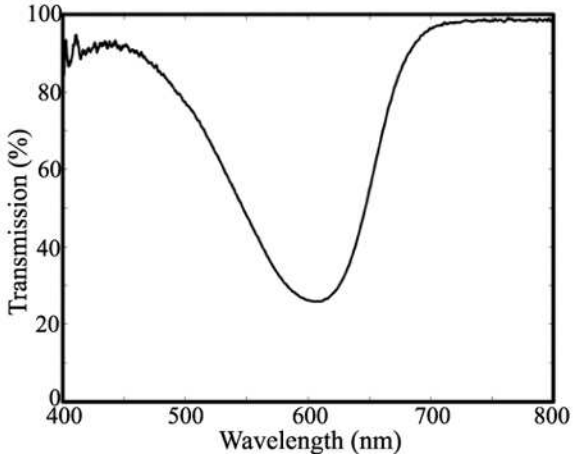

Figure A.1: Transmission spectra of Evans blue dye diluted to 0.1% with saline and with 1 cm pathlength. Note this solution is diluted from animal injected 2% solution due to longer cuvette pathlength.

and shaved prior to intravenous injection with Evans blue dye -conjugated bovine serum albumin as a 2% saline solution [191]. The optical absorption spectra of Evans blue is shown in Figure A.1. Dye-conjugated albumin was sterile filtered and warmed to 37° C prior to use. Rats were injected with 400 μls and mice with 200 μls of the dye-conjugated albumin solution and edema was initiated immediately following injection using test agents. All mice/rats were shaved prior to data collection to eliminate hair absorption defects.

A.2.2 Signal Collection and Analysis

The severity of leak was assessed qualitatively using digital photographs with post-processing image analysis techniques, and assessed quantitatively using a fiber optic array diffuse reflectance probe. The fiber probe is similar to the commercial probe discussed in Section 4; a metal ferrule with six 200 μm glass fibers oriented in a hexagonal pattern around a single 200 μm collection fiber manufactured by Ocean Optics (Dunedin, FL). In this case, the ferrule was placed directly in contact with the animal and therefore no collimation optics were required. A white LED was used for illumination along the six irradiation fibers and collection fiber was affixed to a miniature static grating spectrometer with optical resolution of $\sim$ 1 nm and operating range of 200-900 nm (USB4000, Ocean Optics, Dunedin, FL). Signal integration time ranged from 300-500 ms dependent on skin

pigment of the animal with white LED source broadband output optical power of 50 μW.

Following injection of Evans blue and prior to introduction of agent, reflectance spectra were collected to assess and remove baseline skin absorption characteristics. Spectra collected from treated spots were then post-processed in multiple steps. First, spectra were ratioed with skin baseline spectra to remove both skin background and LED emission characteristics from signal. Second, spectra were normalized to the intensity at one spectral point ($\lambda_{norm} = 725$ nm) to eliminate overall biasing of signals. This biasing is due to small fluctuations in probe orientation causing shifts in the overall amount of light introduced to the tissue. The normalization point of 725 nm was selected as a point beyond the dye absorption to scale spectra to a uniform baseline unaffected by dye concentration. The subsequent data processing steps makes this normalization insignificant for data processing; however, it is applied only to improve the visual appearance of signals. Lastly, a linear fit was applied from two spectral points at the periphery of the Evans blue absorption spectra, $\lambda_1 = 450$ nm and $\lambda_2 = 725$ nm. This line was then subtracted from the spectra to eliminate any warping of the spectral signatures attributed to heterogeneity in the optical absorption and scattering coefficients of the skin. Removal of this fit line isolates the depth of the Evans blue absorption peak independently from any broad spectral variations in background absorption profiles from spot to spot on an individual animal. Following post-processing, the intensity of the Evans blue peak absorption at $\lambda_{max} = 620$ nm is used as the quantifier of vascular leak.

A.3 Control for Pressure and Spatial Leak Variability

Two relevant parameters to consider regarding the reliability and repeatability of fiber probe data collection are the effects of spatial variability with repeated sampling and variability in the probe against skin pressure. Both factors were explored before additional investigation.

Vascular leak was introduced to a dye-injected mouse using a topical application of 1% mustard oil on the torso along with topical application of Acetone as a control. Pressure variation was quantified by collecting multiple spectra in succession starting with the probe gently resting on the leak spot with an approximate force of 100 mN and subsequently increasing the pressure to approximately

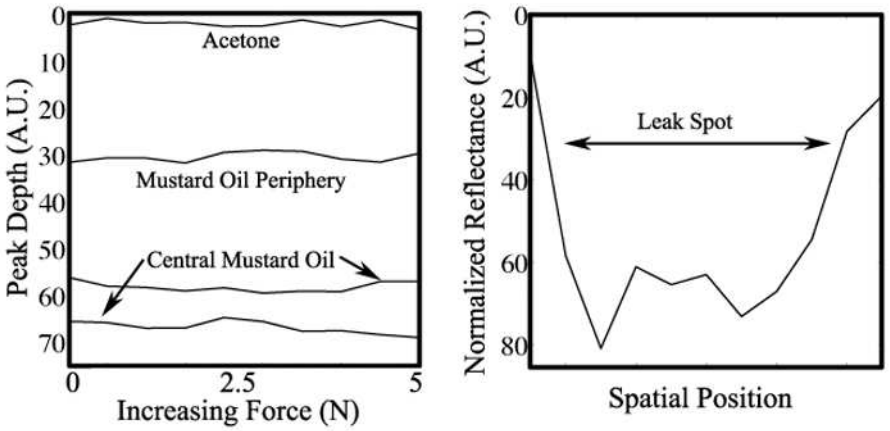

Figure A.2: Plot of the Evans blue peak depth as a function of the approximate force of probe pressed against skin for an acetone treatment, the periphery of a mustard oil leak spot, and the two positions on the center of a mustard oil leak spot (a). Plot of the Evans blue peak depth as a function of position as the probe is scanned across the spot

1N. This was performed on three different spatial locations of the mustard oil treatment site (two at the central location, one at the periphery) and one location on the acetone treatment site. As shown in Figure A.2(a), the intensity of the leak spot is highly uniform with pressure for all three spots on the mustard oil treatment site with standard deviation (SD) $< 3\%$ of mean peak depth in all three spots, and SD of all three spots all within 1% of the max peak depth.

Spatial probe positioning was observed to add more variability in the quantification of leak than pressure variation. An order of magnitude assessment of spatial variation in a vascular leak spot was obtained using the same mustard oil treatment and scanning multiple points in succession along one dimension across the spot. A plot of dye absorption versus spatial position is show in Figure A.2(b). Variability in the peak depth at the central of the leak spot is of significance in this case as the SD is 7% of the mean peak intensity at the center of the mustard oil spot, which may be a result of dye diffusion in subcutaneous and cutaneous layers, blood vessel positioning, injection variability, or any number of other effects. This analytical result of this fluctuation will be noise introduction to curves tracking the vascular leak quantifier as function of time. Spatial fluctuations can be removed by either (1) fixing the probe over the leak spot to reduce spatial variation with each time sampling point or (2) applying an averaging filter to create a function representative of the average time course leak across the spot. The latter method is employed here as a scanning average filter is applied to

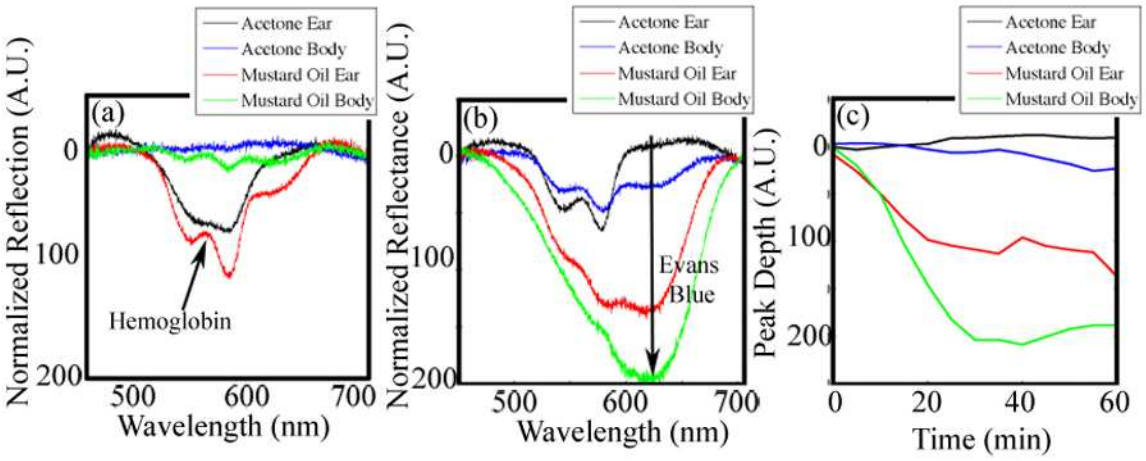

Figure A.3: Diffuse reflectance spectra of mustard oil and acetone treatment on mouse skin at the ear and on the skin shown right after application (a), and after 60 min elapsed time (b). Note the appearance of the signature of hemoglobin most prevalently in the Ear measurements as optical signal is recording hemoglobin still in blood vessels through thin skin and not vascular leak. A plot of the depth of the Evans blue dye peak as a function of time for mustard oil and saline on the ear and skin is shown in (c).

the time course functions generated in following experiments to smooth the noise generated through spatial variability and obtain a more accurate representation of physiological phenomena.

A.4 Animal Trial Vascular Leak Quantification Results

Three sets of experiments were conducted to validate the operation of the probe, two on mice and one on rats. Identical data collection techniques were applied in all studies as overviewed above.

A.4.1 Topical Mustard Oil and Acetone in Mice

Vascular leak was initiated by topical application of 1% mustard oil to one ear and one spot on the body of a mouse. An acetone control was applied in the contralateral ear and a separate spot on the body. Background spectra were collected prior to topical application but following introduction of dye to blood stream, and spectra were collected at 5 minute intervals for 60 minutes. A plot of the post-processed spectra at 0 minutes and 60 minutes are shown in Figure A.3(a) and (b) respectively. These spectra show the anticipated increase in Evans blue absorption from 0 min to 60 minutes for both the ear and body treatment compared with spectra from Acetone. Additionally, in both the

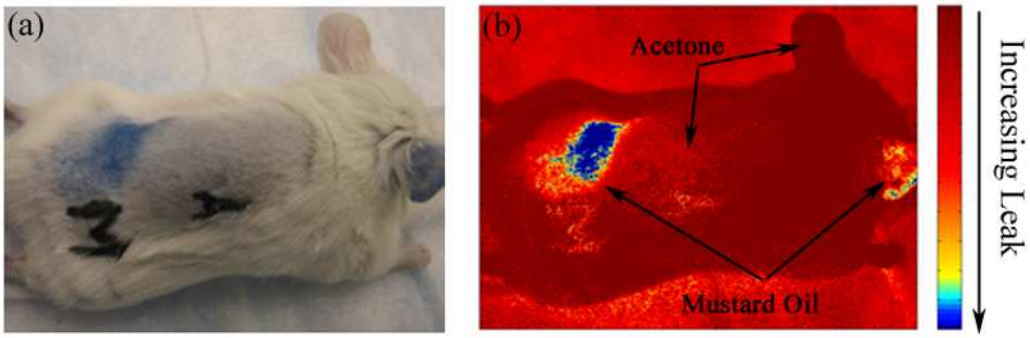

Figure A.4: A digital image of the mouse with topical irratations of mustard oil and control of acetone on the body and ear (a) and the color normalized version of the image calculated as described above.

mustard oil and acetone ear treatments at time 0 and 60 minutes, an absorption signature from hemoglobin (double peak around 550 nm) is observed. The contamination of pure dye signals from hemoglobin is not removed by background subtraction and post-process fitting because hemoglobin has sharper spectral features and overlaps the Evans blue dye absorption spectra. Because this effect adds additional noise to the quantifier of vascular leak, the skin is a preferred location for more precise dye measurement.

The time progression of the mustard oil leak is plotted in Figure A.3(c) showing the increase in leak for the mustard oil in the ear and body compared to acetone. As anticipated, more leak is observed in the body as a result of higher vascular density responding to the topical irritation. This results of this experiment were representative of two additional experiments with mustard oil and acetone topical treatments on mice.

Vascular leak may also be visualized and qualitatively studied using digital imaging. A raw digital image of the mouse analyzed above is shown in Figure A.4(a). Furthermore, the intensity of blue dye can be enhanced by normalizing the blue image channel with red image channel, applying false coloring based on the intensity range of the dye spot area, and plotting the resulting intensity values. This simple algorithm enhances areas of the image with high absorptions in the red wavelength domain, as occurs in the Evans blue. While not providing reliable quantitative readings, this technique is effective for qualitative observation on mouse skin under conditions of extensive vascular leak because of the high scattering uniformity from its white color.

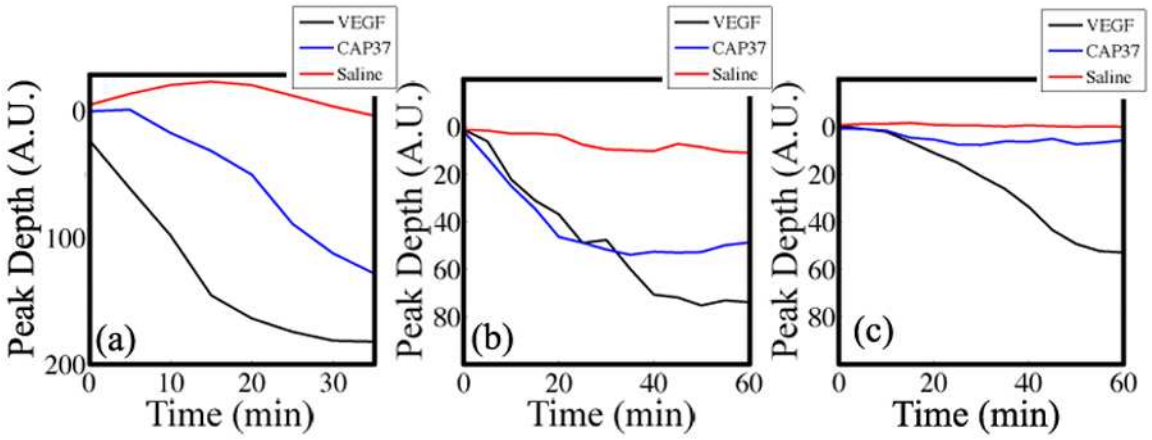

Figure A.5: Plot of the Evans blue peak depth as a function of time for subcutaneous injections of VEGF, CAP37, and Saline in three different subjects (a)-(c) denoted mouse 1-3, respectively.

A.4.2 Subcutaneous VEGF, CAP37 and Saline in Mice

Subdermal injections were subsequently examined using the same probe configuration. Three materials, mouse vascular endothelial growth factor (mVEGF, BioSource, Camarillo, CA), CAP37 (cationic acidic protein of 37kD), were used as agents in the study. Recombinant human CAP37 was the kind gift of H.A. Peireira (University of Oklahoma, Oklahoma City, OK). Explicitly, vascular endothelial growth factor was investigated as a well-known mediator of vascular leak, saline was used as a control to observe leak effects of the injection itself, and CAP37 was introduced as an investigational study with a protein reported to cause leak *in vitro*. Subcutaneous injections of 100 μL of VEGF at 10 μg/mL μg/mL, 100 μL CAP37 at 394 μg/mL and 100 μL of saline were introduced in three separate animals. Post-processing steps above were applied to data and the peak dye absorption plotted versus time for at least 40 minutes in 5 minute intervals, as shown in Figure A.5.

The increase in dye absorption at VEGF spot was observed as the maximum effect in all three mice while saline was observed to have comparatively less absorption effects. The maximum dye peak in the CAP37 injection site was between 60% and 70% of the VEGF absorption peak in mice 1-2. In mouse 3, considerably less absorption effects were observed with CAP37 injection site having approximately 20% of maximum VEGF absorption intensity and comparable to the leak levels of the saline. Mouse 3 had less leak with the VEGF treatment than the other two mice as well, meaning

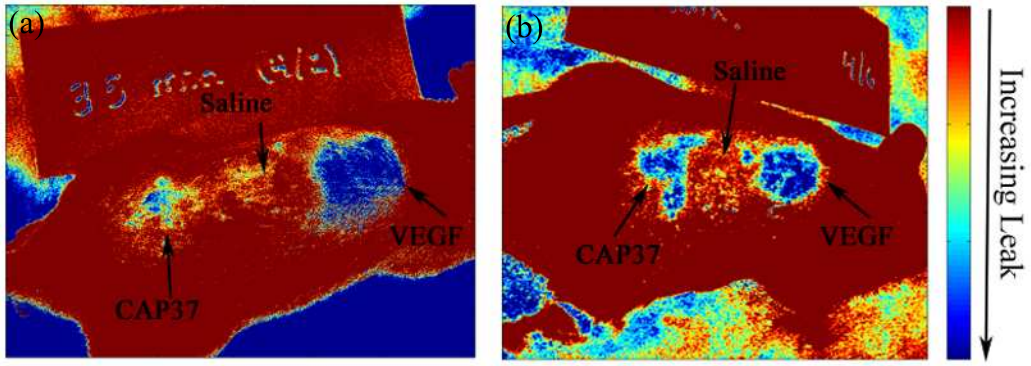

Figure A.6: Color normalized images of two of the mouse subjects, mouse 1 (a) and 2 (a) , showing leak spots of CAP37, VEGF and saline.

the stifled leak effects could be a function of purely physiological variation. The variability in the amount of VEGF leak between three mice may be also be a result of numerous factors including the depth of injection, age and weight of animal, and localization of vasculature. In all three animals, the time course progression of the leak is roughly that of an inverse exponential, showing the majority of leak occurs at the early stages of injection and continues for as much as 50 minutes after the initial irritation.

Digital images of one of the three mice, mouse 1, are shown in Figure A.6 in the raw form (a) and color normalized version (b). This image again shows an approximation, using false color, of the three intradermal injection sites and approximate leak intensity. It is emphasized that these images show spatial distribution of color only, but are unreliable as quantitative measures of leak.

A.4.3 Subcutaneous VEGF, CAP37 and Saline in Rats

The greater thickness of rat skin as compared to mice permits intradermal injections that produce a more spatially homogeneous dye spot; therefore, rats were subsequently investigated in a similar experiment to the mouse VEGF/CAP37/Saline experiment. Of two rats included in data analysis, one received subcutaneous injections of 100 μm of mouse VEGF at 2 μg/mL, the intact CAP37 protein at 394 μg/mL and saline. The second rat received subcutaneous injections of 100 μm of rat VEGF (BioSource, Camarillo, CA) at 10 μg/mL, 100 μm of a peptide corresponding to amino acids 20-44 of CAP37 at 394 μg/mL, and saline. Data was again collected at 5 minute increments for 60

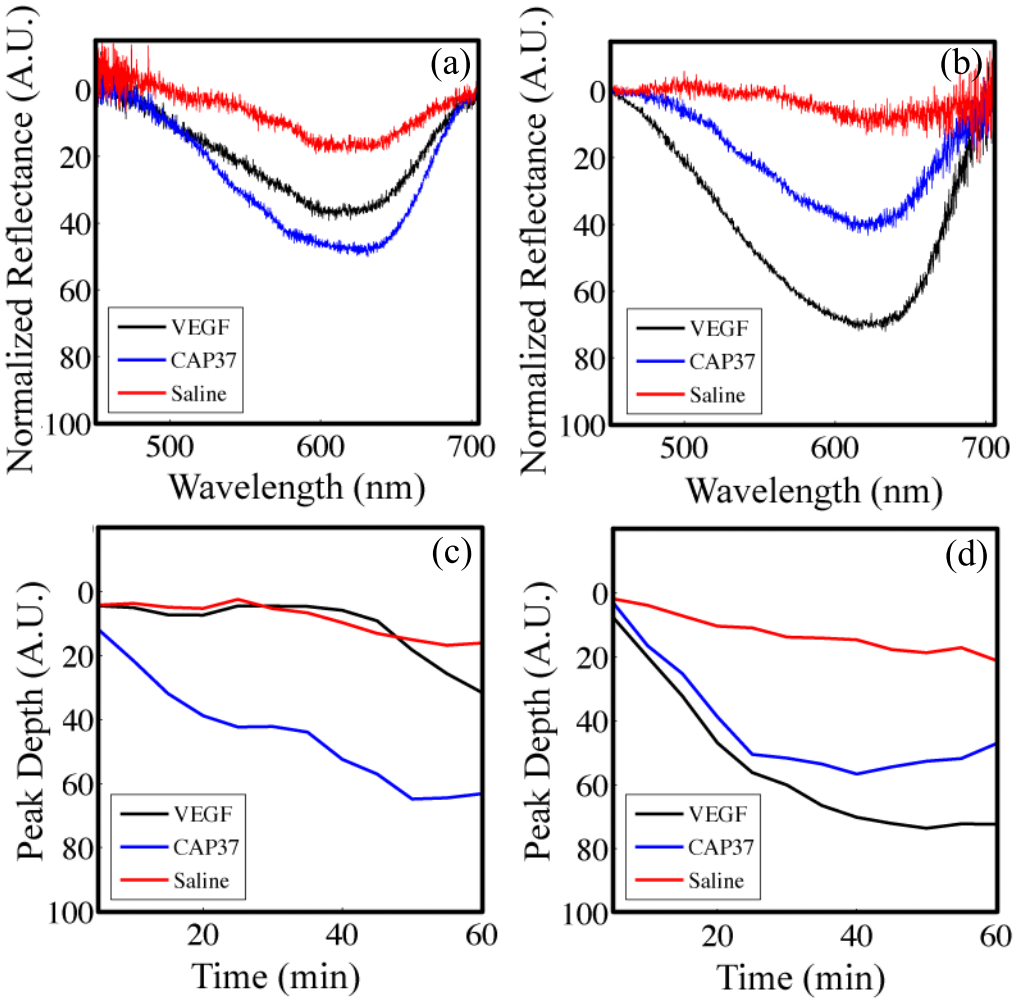

Figure A.7: Plot of reflection spectra at T = 60 min for two rat subjects, rat 1 with injections of Mouse VEGF, intact CAP37 protein, and saline (a) and rat 2 with injections of rat VEGF, CAP37 peptides, and saline. Plot of the Evans blue peak depth as a function of time for rat 1(c) and rat 2 (d).

minutes in each animal with post-processing applied. The reflection spectra at time of 60 minutes for rat 1 and rat 2 is shown in Figure A.7 (a) and (b), respectively, with resulting peak intensity as a function of time is plotted for both rats as shown below in Figure A.7 (c) and (d). The peak depth vs. time plots show a relatively comparable leak amount and rate for both the CAP37 intact protein and peptides in the two rats, while the recombinant rat VEGF is shown to induce much more leak than the mouse VEGF, as expected. Saline in both cases again has negligible effect in these animals.

Color corrected images were more difficult to construct in rats because of the stronger skin

pigment distorting the color channels such that the spots are not clearly visible, and as such the data is not pictured here.

A.5 Conclusions

The target goal of the above study was two-fold, one in identifying suitability of a new noninvasive technique in quantifying leak and two in investigating the leak inducing ability of CAP37 in its intact and fragmented peptide form. The above results validate the ability of quantification of vascular leak through collection of diffuse reflectance and signal processing to eliminate much of the background variability. It was noted that spatial variability in leak due to diffusion of dye has an effect and needs to be controlled through data collection or noise reduction. Regarding the CAP37, cursory studies on three mice and two rats have shown its potential to induce vascular leak; however ongoing studies are needed to establish additional controls, test additional peptides, and increase the data set number to more reliably infer the effects of CAP37. It is clear that based on specific activity, given the greater amount of CAP37 injected as compared to VEGF, the potency of CAP37 in causing vascular leak is substantially less than VEGF.

Bibliography

[1] E. Scapa, G. Meron, A. Glukhovsky, D. Gat, H. Jacob, R. Shreiber, M. N. Appleyard, and P. Swain. Wireless capsule colonoscopy. *Gastrointestinal Endoscopy*, 53(5):AB111, 2001.

[2] F. Riemenschneider, I. Sagnes, G. Bohm, H. Halbritter, M. Maute, C. Symonds, M. C. Amann, and P. Meissner. A new concept for tunable long wavelength VCSEL. *Optics Communications*, 222(1-6):341–350, 2003.

[3] E.G. Louwen and E Popov. *Diffraction Gratings and Applications*, volume 1. CRC Publishing, 1st edition, 1997.

[4] C Palmer. *Diffraction Grating Handbook*, volume 1. Newport Publishing, 6th edition, 2005.

[5] D. Brennan, J. Alderman, L. Sattler, J. Walshe, J. Huang, B. O'Connor, and C. O'Mathuna. Development of a micro-spectrometer system for process control application. *Infrared Physics and Technology*, 43(2):69–76, 2002.

[6] S. Grabarnik, R. Wolffenbuttel, A. Emadi, M. Loktev, E. Sokolova, and G. Vdovin. Planar double-grating microspectrometer. *Optics Express*, 15(6):3581–3588, 2007.

[7] S. Bidnyk, A. Balakrishnan, M. Pearson, M. Gao, H. Schriemer, and T. Hall. Cascaded optical microspectrometer based on additive dispersion planar gratings. *IEEE Photonics Technology Letters*, 18(1-4):247–249, 2006.

[8] K. Chaganti, I. Salakhutdinov, I. Avrutsky, and G. W. Auner. A simple miniature optical spectrometer with a planar waveguide grating coupler in combination with a plano-convex lens. *Optics Express*, 14(9):4064–4072, 2006.

[9] P. Cheben, I. Powell, S. Janz, and D.X. Xu. Wavelength-dispersive device based on a fourier-transform michelson-type arrayed waveguide grating. *Optics Letters*, 30(14):1824 – 1826, 2005.

[10] D. Sander and J. Muller. Selffocussing phase transmission grating for an integrated optical microspectrometer. *Sensors and Actuators A - Physical*, 88(1):1–9, 2001.

[11] D. Sander, O. Blume, and J. Muller. Microspectrometer with slab-waveguide transmission gratings. *Applied Optics*, 35(21):4096–4101, 1996.

[12] I. Avrutsky, K. Chaganti, I. Salakhutdinov, and G. Auner. Concept of a miniature optical spectrometer using integrated optical and micro-optical components. *Applied Optics*, 45(30):7811–7817, Oct 2006.

[13] G. Lammel, S. Schweizer, and P. Renaud. Microspectrometer based on a tunable optical filter of porous silicon. *Sensors and Actuators A - Physical*, 92(1-3):52–59, 2001.

[14] J. H. Correia, G. de Graaf, S. H. Kong, M. Bartek, and R. F. Wolffenbuttel. Single-chip CMOS optical microspectrometer. *Sensors and Actuators A - Physical*, 82(1-3):191–197, 2000.

[15] J. H. Correia, G. de Graaf, M. Bartek, and R. F. Wolffenbuttel. A CMOS optical microspectrometer with light-to-frequency converter, bus interface, and stray-light compensation. *IEEE Transactions on Instrumentation and Measurement*, 50(6):1530–1537, 2001.

[16] J. H. Correia, G. de Graaf, M. Bartek, and R. F. Wolffenbuttel. A single-chip CMOS optical microspectrometer with light-to-frequency converter and bus interface. *IEEE Journal of Solid-State Circuits*, 37(10):1344–1347, 2002.

[17] S. W. Wang, C. S. Xia, X. S. Chen, W. Lu, M. Li, H. Q. Wang, W. B. Zheng, and T. Zhang. Concept of a high-resolution miniature spectrometer using an integrated filter array. *Optics Letters*, 32(6):632–634, 2007.

[18] J. T. McWhirter and A. J. Sievers. Time-resolved spectroscopy with fourier-transform spectrometers - maintaining the fellgett advantage. *Applied Spectroscopy*, 45(9):1391–1394, 1991.

[19] O. Manzardo, H. P. Herzig, C. R. Marxer, and N. F. de Rooij. Miniaturized time-scanning Fourier transform spectrometer based on silicon technology. *Optics Letters*, 24(23):1705–1707, 1999.

[20] O. Manzardo, P. Kipfer, H. P. Herzig, H. Teichmann, M. T. Gale, and P. Ehbets. Micro-sized Fourier spectrometers. In *Optical Spectral Analysis Microsystem, Engleberg*, volume 16, pages 52–53, Zurich, Switzerland, 1998.

[21] S. D. Collins, R. L. Smith, C. Gonzalez, K. P. Stewart, J. G. Hagopian, and J. M. Sirota. Fourier-transform optical microsystems. *Optics Letters*, 24(12):844–846, 1999.

[22] M. J. Padgett, A. R. Harvey, A. J. Duncan, and W. Sibbett. Single-pulse, Fourier-transform spectrometer having no moving parts. *Applied Optics*, 33(25):6035–6040, 1994.

[23] A. R. Harvey, M. Begbie, and M. J. Padgett. Stationary Fourier transform spectrometer for use as a teaching tool. *American Journal of Physics*, 62(11):1033–1036, 1994.

[24] J. Courtial, B. A. Patterson, A. R. Harvey, W. Sibbett, and M. J. Padgett. Design of a static Fourier-transform spectrometer with increased field of view. *Applied Optics*, 35(34):6698–6702, 1996.

[25] B. A. Patterson, M. Antoni, J. Courtial, A. J. Duncan, W. Sibbett, and M. J. Padgett. An ultra-compact static Fourier-transform spectrometer based on a single birefringent component. *Optics Communications*, 130(1-3):1–6, 1996.

[26] D. Steers, W. Sibbett, and M. J. Padgett. Dual-purpose, compact spectrometer and fiber-coupled laser wavemeter based on a Wollaston prism. *Applied Optics*, 37(24):5777–5781, 1998.

[27] D. Komisarek, K. Reichard, D. Merdes, D. Lysak, P. Lam, S. D. Wu, and S. Z. Yin. High-performance nonscanning Fourier-transform spectrometer that uses a Wollaston prism array. *Applied Optics*, 43(20):3983–3988, 2004.

[28] C. D. Tran. Infrared multispectral imaging: Principles and instrumentation. *Applied Spectroscopy Reviews*, 38(2):133–153, 2003.

[29] C. D. Tran. Principles and analytical applications of acousto-optic tunable filters, an overview. *Talanta*, 45(2):237–248, 1997.

[30] C. D. Tran. Acousto-optic tunable filter: A new generation monochromator and more. *Analytical Letters*, 33(9):1711–1732, 2000.

[31] L. Bei, G. I. Dennis, H. M. Miller, T. W. Spaine, and J. W. Carnahan. Acousto-optic tunable filters: fundamentals and applications as applied to chemical analysis techniques. *Progress in Quantum Electronics*, 28(2):67–87, 2004.

[32] O. Khait, S. Smirnov, and C. D. Tran. Time-resolved multispectral imaging spectrometer. *Applied Spectroscopy*, 54(12):1734–1742, 2000.

[33] N. Gupta, D. R. Suhre, and M. Gottlieb. Long-wave infrared spectral imager with an 8 cm^{-1} passband acousto-optic tunable filter. *Optical Engineering*, 44(9), 2005. 094601.

[34] N. Gupta and V. Voloshinov. Hyperspectral imaging performance of a TeO_2 acousto-optic tunable filter in the ultraviolet region. *Optics Letters*, 30(9):985–987, 2005.

[35] M. E. Martin, M. Wabuyele, M. Panjehpour, B. Overholt, R. DeNovo, S. Kennel, G. Cunningham, and T. Vo-Dinh. An AOTF-based dual-modality hyperspectral imaging system (DMHSI) capable of simultaneous fluorescence and reflectance imaging. *Medical Engineering and Physics*, 28(2):149–155, 2006.

[36] T. Vo-Dinh, D. L. Stokes, M. B. Wabuyele, M. E. Martin, J. M. Song, R. Jagannathan, E. Michaud, R. J. Lee, and X. G. Pan. A hyperspectral imaging system for *in vivo* optical diagnosis. *IEEE Engineering in Medicine and Biology Magazine*, 23(5):40–49, 2004.

[37] Y. Inoue and J. Penuelas. An AOTF-based hyperspectral imaging system for field use in ecophysiological and agricultural applications. *International Journal of Remote Sensing*, 22(18):3883–3888, 2001.

[38] M. B. Wabuyele, F. Yan, G. D. Griffin, and T. Vo-Dinh. Hyperspectral surface-enhanced Raman imaging of labeled silver nanoparticles in single cells. *Review of Scientific Instruments*, 76(6), 2005. 063710.

[39] R. Srivastava, U. G. Shenoy, S. R. Forrest, S. Chinnayelka, J. S. Mohammed, R. S. Besser, and M. J. McShane. Bulk micromachining of a mems tunable fabry-perot interferometer: effect of residual silicon on device performance. *Journal of Microlithography Microfabrication and Microsystem*, 3(4):579–588, 2004.

[40] A. J. Keating, K. K. M. B. D. Silva, J. M. Dell, C. A. Musca, and L. Faraone. Optical characterization of fabry-perot mems filters integrated on tunable short-wave ir detectors. *IEEE Photonics Technology Letters*, 18(9-12):1079–1081, 2006.

[41] H. Stiebig, D. Knipp, S. R. Bhalotra, H. L. Kung, and D. A. B. Miller. Interferometric sensors for spectral imaging. *Sensors and Actuators A - Physical*, 120(1):110–114, 2005.

[42] P. C. Beard. Interrogation of free-space fabry-perot sensing interferometers by angle tuning. *Measurement Science and Technology*, 14(11):1998–2005, 2003.

[43] L.T. Creagh and A.R. Kmetz. Mechanism of surface alignment in nematic liquid crystals. *Molecular Crystals And Liquid Crystals*, 24(1-2):59–68, 1973.

[44] K. Y. Wu, W. Y. Chen, C. H. Wang, J. Hwang, C. Y. Lee, Y. L. Liu, H. Y. Huang, H. K. Wei, and C. S. Kou. Liquid crystal alignment on plasma beam scanned alkylsiloxane self-assembled monolayers. *Journal of Electrochemical Society*, 155(9):J244–J247, 2008.

[45] J.N. Eakin, R.A. Pelcovits, G.P. Crawford, and M.D. Radcliffe. Polarization holographic patterned alignment of nematic liquid crystals. *Molecular Crystals And Liquid Crystals*, 438:1749–1757, 2005.

[46] JH Kim, M Yoneya, J Yamamoto, and H Yokoyama. Nano-rubbing of a liquid crystal alignment layer by an atomic force microscope: a detailed characterization. *Nanotechnology*, 13(2):133–137, 2002.

[47] P. J. Collins and M. Hird. *Introduction to Liquid Crystal Chemistry and Physics*, volume 1. Taylor and Francis, Bristol, PA, 1997.

[48] T.G. Chrien, C. Chovit, and P.J. Miller. Imaging spectrometer using a liquid crystal tunable filter. *Proceedings of SPIE*, 1937:256–261, 1993.

[49] M. D. Evans, C. N. Thai, and J. C. Grant. Development of a spectral imaging system based on a liquid crystal tunable filter. *Transactions of the ASAE*, 41(6):1845–1852, 1998.

[50] R. W. Slawson, Z. Ninkov, and E. P. Horch. Hyperspectral imaging: Wide-area spectrophotometry using a liquid-crystal tunable filter. *Publications of the Astronomical Society of the Pacific*, 111(759):621–626, 1999.

[51] P.J. Miller. High-performance birefringent imaging interferometer. *Proceedings of SPIE*, 3920:32–39, 2003.

[52] J. Y. Hardeberg, F. Schmitt, and H. Brettel. Multispectral color image capture using a liquid crystal tunable filter. *Optical Engineering*, 41(10):2532–2548, 2002.

[53] B.P. Stevenson, W.B. Kendall, C.M. Stellman, and F.M. Olchowski. Phirst light: A liquid crystal tunable filter hyperspectral sensor. *Proceedings of SPIE*, 5093:104–113, 2003.

[54] P. Geladi, J. Burger, and T. Lestander. Hyperspectral imaging: calibration problems and solutions. *Chemometrics and Intelligent Laboratory Systems*, 72(2):209–217, 2004.

[55] M. Attas, T. Posthumus, B. Schattka, M. Sowa, H. Mantsch, and S. L. Zhang. Long-wavelength near-infrared spectroscopic imaging for *in vivo* skin hydration measurements. *Vibrational Spectroscopy*, 28(1):37–43, 2002.

[56] G. J. Fitzgerald. Portable hyperspectral tunable imaging system (phytis) for precision agriculture. *Agronomy Journal*, 96(1):311–315, 2004.

[57] M. E. Martin, M. B. Wabuyele, K. Chen, P. Kasili, M. Panjehpour, M. Phan, B. Overholt, G. Cunningham, D. Wilson, R. C. DeNovo, and T. Vo-Dinh. Development of an advanced hyperspectral imaging (HSI) system with applications for cancer detection. *Annals of Biomedical Engineering*, 34(6):1061–1068, 2006.

[58] M. E. Martin, M. B. Wabuyele, M. Panjehpour, M. N. Phan, B. F. Overholt, and T. Vo-Dinh. Hyperspectral fluorescence imaging system for biomedical diagnostics. *Proceedings of SPIE*, 6080:60800, 2006.

[59] B. B. Shah, H. D. Cavanagh, W. M. Petroll, Amogh D. Kothare, P. Gundabhat, K. Behbehani, and K. J. Zuzak. *In vivo* microvasculature visualization using hyperspectral imaging. *Proceedings of SPIE*, 6080(U), 2006.

[60] Y. Saito, T. Matsubara, T. Koga, F. Kobayashi, T. D. Kawahara, and A. Nomura. Laser-induced fluorescence imaging of plants using a liquid crystal tunable filter and charge coupled device imaging camera. *Review of Scientific Instruments*, 76(106103), 2005.

[61] P. J. Miller. Use of tunable liquid-crystal filters to link radiometric and photometric standards. *Metrologia*, 28(3):145–149, 1991.

[62] G. Hatakoshi and S. Tanaka. Coupled mode theory for a plane and cylindrical wave in optical waveguide bragg grating. *Journal of the Optical Society of America*, 71(1):40–48, 1981.

[63] Y. Q. Lu, F. Du, Y. H. Wu, and S. T. Wu. Liquid-crystal-based Fourier optical spectrum analyzer without moving parts. *Japanese Journal of Applied Physics Part 1-Regular Papers Short Notes and Review Papers*, 44(1A):291–293, 2005.

[64] K. Itoh, T. Inoue, T. Ohta, and Y. Ichioka. Liquid-crystal imaging Fourier-spectrometer array. *Optics Letters*, 15(11):652–654, 1990.

[65] G. D. Sharp, P. Wang, S. A. Serati, and T. K. Ewing. Liquid crystal Fourier transform spectrometer. *Proceedings of SPIE*, 3384:161–171, 1998.

[66] Y. Q. Lu, C. Wong, and S. T. Wu. A liquid crystal-based Fourier optical spectrum analyzer. *IEEE Photonics Technology Letters*, 16(3):861–863, 2004.

[67] T. H. Chao, H. Zhou, X. Xia, and S. A. Serati. Hyperspectral imaging using electro-optic Fourier transform spectrometer. *Proceedings of SPIE*, 5437:163–170, 2004.

[68] T. H. Chao, H. Zhou, X. Xia, and S. Serati. Near IR electro-optic imaging Fourier transform spectrometer. *Proceedings of SPIE*, 5816:163–172, 2005.

[69] S. R. Davis, M. H. Anderson, and S. D. Rommel. Liquid crystal waveguides: A new technology platform. *Molecular Crystals and Liquid Crystals*, 2006. submitted for publication.

[70] G. Boer, P. Ruffieux, T. Scharf, P. Seitz, and R. Dandliker. Compact liquid-crystal-polymer Fourier-transform spectrometer. *Applied Optics*, 43(11):2201–2208, 2004.

[71] G. Boer, T. Scharf, and R. Dandliker. Compact static Fourier transform spectrometer with a large field of view based on liquid-crystal technology. *Applied Optics*, 41(7):1400–1407, 2002.

[72] P. J. Bos and K. R. Beran. The π-cell – a fast liquid-crystal optical-switching device. *Molecular Crystals and Liquid Crystals*, 113(1-4):329–339, 1984.

[73] W. Kaye. Apparatus for minimizing beam collimation sensitivity in instruments including liquid crystal cells. United States Patent,4,497,542, 1981.

[74] D. J. Funk and D. S. Moore. Fourier-transform spectroscopy using liquid-crystal technology. *Optics Letters*, 22(23):1799–1801, 1997.

[75] H. S. Bellamy, P. K. Dasgupta, J. L. Lopez, and E. L. Loree. A liquid crystal shutter-array spectrometer. *Spectroscopy*, 10(6):50, 1995.

[76] D. C. Tilotta, R. M. Hammaker, and W. G. Fateley. Visible near-infrared Hadamard transform spectrometer based on a liquid crystal spatial light modulator array: A new approach in spectrometry. *Applied Spectroscopy*, 41(5):727–734, 1987.

[77] Q. S. Hanley, P. J. Verveer, and T. M. Jovin. Spectral imaging in a programmable array microscope by Hadamard transform fluorescence spectroscopy. *Applied Spectroscopy*, 53(1):1–10, 1999.

[78] J. Gourlay, P. McOwan, and D. G. Vass. Hadamard transform image processing and its optical implementation with ferroelectric liquid crystal spatial light modulators. *International Journal of Optoelectronics*, 10(1):51–58, 1995.

[79] A. E. Macgregor and R. I. Young. Hadamard transforms of images by use of inexpensive liquid-crystal spatial light modulators. *Applied Optics*, 36(8):1726–1729, 1997.

[80] A. P. Bohlke, J. M. Jarvis, J. S. White, J. D. Tate, J. V. Paukstelis, R. M. Hammaker, and W. G. Fateley. A new stationary Hadamard encoding mask for near-infrared Hadamard-transform Raman-spectrometry. *Journal of Molecular Structure*, 247:293–303, 1991.

[81] H. W. Tang, J. S. Zhou, T. Li, and G. Q. Chen. The applications and advances of Hadamard transform spectroscopy and imaging. *Chinese Journal of Analytical Chemistry*, 33(3):417–422, 2005.

[82] T. Hirschfield and G. Wyntjes. Fourier transform vs Hadamard transform spectroscopy. *Applied Optics*, 12(12):2876–2880, 1973.

[83] D. K. Yang, X. Y. Huang, and Y. M. Zhu. Bistable cholesteric reflective displays: Materials and drive schemes. *Annual Review of Materials Science*, 27:117–146, 1997.

[84] H. Q. Xianyu, S. Faris, and G. P. Crawford. In-plane switching of cholesteric liquid crystals for visible and near-infrared applications. *Applied Optics*, 43(26):5006–5015, 2004.

[85] M. Date, Y. Takeuchi, and K. Kato. A memory-type holographic polymer dispersed liquid crystal (HPDLC) reflective display device. *Journal of Physics D-Applied Physics*, 31(18):2225–2230, 1998.

[86] T.G. Fiske, L.D. Silverstein, J. Colegrove, and H. Yuan. HPDLC color separation device for image capture systems. *SID International Symposium Digest of Technical Papers*, 31:1134–1137, 2000.

[87] Y. J. Liu and X. W. Sun. Electrically tunable three-dimensional holographic photonic crystal made of polymer-dispersed liquid crystals using a single prism. *Japanese Journal fo Applied Physics Part 1*, 46(10A):6634–6638, 2007.

[88] A. Levstik, Z. Kutnjak, and C. Filipic. Dielectric method for dtermining the rotational viscosity in thick samples of ferroelectric chiral smectic c* liquid crystals. *Physical Review A*, 42:2204–2210, 1990.

[89] Deng-Ke Yang and Shin-Tson Wu. *Fundamentals of Liquid Crystal Devices*, volume 1. Wiley and Sons, West Sussex, England, 2006.

[90] N.A. Clark, M.A. Handschy, and S.T. Lagerwall. Ferroelectric liquid-crystal electro-optics using the surface stabilized structure. *Molecular Crystals And Liquid Crystals*, 94(1-2):213–234, 1983.

[91] H. R. Kim, Y. W. Lee, S. J. Kim, D. W. Kim, C. J. Yu, B. Lee, and S. D. Lee. A rotatable waveplate using a vertically aligned deformed-helix ferroelectric liquid crystal. *Ferroelectrics*, 312:479–484, 2004.

[92] M. Ozaki, M Kasano, D. Ganzke, W. Haase, and K. Yoshino. Mirrorless lasing in a dye-doped ferroelectric liquid crystal. *Advanced Materials*, 14(4):306–310, 2002.

[93] W. K. Choi, A. B. Davey, T. D. Wilkinson, and W. A. Crossland. Deformed helix ferroelectric liquid crystal fabry perot etalons. *Molecular Crystals And Liquid Crystals*, 304(329-337), 1997.

[94] A. D. Cohen, M. C. Parker, and R. J. Mears. Applications of flc slm dynamic holograms to wdm network components. *Ferroelectrics*, 214(1-2):775–782, 1998.

[95] D. H. You, C. J. Yu, and S. D. Lee. Reflective configuration of vertically aligned deformed-helix ferroelectric liquid crystal display. *Ferroelectrics*, 278:805–812, 2002.

[96] E. P. Pozhidaev, S. L. Smorgon, A. L. Andreev, I. N. Kompanets, V. Y. Zyryanov, and S. I. Kompanets. Low voltage and high optical quality polymer dispersed flc films. *Ferroelectrics*, 212(1-4):153–160, 1998.

[97] S. L. Smorgon, A. V. Barannik, V. Y. Zyryanov, E. P. Pozhidaev, A. L. Andreev, I. N. Kompanets, D. Ganzke, and W. Haase. Low voltage light modulator based on flc layer divided by polymer walls. *Molecular Crystals And Liquid Crystals*, 368:3975–3982, 2001.

[98] G. B. Cohen, R. Pogreb, K. Vinokur, and D. Davidov. Spatial light modulator based on a deformed-helix ferroelectric liquid crystal and a thin a-Si:H amorphous photoconductor. *Applied Optics*, 36(2):455–459, 1997.

[99] K. Sakoda. *Optical Properties of Photonic Crystals*. Springer Verlag, Dusseldorf, Germany, 2005.

[100] L.B. Lucy. An iterative technique for the rectification of observed distributions. *Astronomical Journal*, 79(6):745–754, 1974.

[101] D.A. Fish, A. M. Brinicombe, and Pike E.R. Blind deconvolution by means of the richardson-lucy alogorithm. *Journal of Optical Society of America A*, 12:58–75, 1995.

[102] Z. Zheng, J. Song, Y. Liu, F. Guo, J. Ma, and L. Xuan. Single-step exposure for two-dimensional electrically-tuneable diffraction grating based on polymer dispersed liquid crystal. *Liquid Crystals*, 35(4):489–499, 2008.

[103] T. Sasaki, H. Ono, N. Kawatsuki, and M. Kuwabara. Liquid crystal phase gratings using photoregulated photocrosslinkable polymer liquid crystals. *Applied Physics Letters*, 87(16), 2005.

[104] A. Ogiwara and T. Hirokari. Formation of anisotropic diffraction gratings in a polymer-dispersed liquid crystal by polarization modulation using a spatial light modulator. *Applied Optics*, 47(16):3015–3022, 2008.

[105] S. T. Wu and A. Y. G. Fuh. Electrical-frequency switchable multi-domain polymer dispersed liquid crystal Bragg mirror. *Japanese Journal of Applied Physics Part 1-Regular Papers Brief Communications & Review Papers*, 45(9A):7011–7016, 2006.

[106] Hiroshi Ono, Akira Hatayama, Akira Ernoto, and Nobuhiro Kawatsuki. Molecular reorientation in cross polarization gratings formed in thin photoreactive-polymer-liquid-crystal films. *Thin Solid Films*, 516(12):4178–4183, 2008.

[107] Y. J. Liu, X. W. Sun, P Shum, and X. J. Yin. Tunable fly's-eye lens made of patterned polymer-dispersed liquid crystal. *Optics Express*, 14(12):5634–5640, 2006.

[108] Y. J. Liu, X. W. Sun, and Q. Wang. A focus-switchable lens made of polymer-liquid crystal composite. *Journal of Crystal Growth*, 288(1):192–194, 2006.

[109] H. Sato, H. Fujikake, H. Kikuchi, and T. Kurita. Rollable polymer-stabilized ferroelectric liquid crystal device using thin plastic substrates. *Optical Review*, 10(5):352–356, 2003.

[110] J. W. Jung, Y. J. Lee, M. S. Shin, H. R. Kim, and J. H. Kim. Multi-domain liquid crystal alignment by micro-contact printed polymer layers. *Molecular Crystals And Liquid Crystals*, 470:183–190, 2007.

[111] H. R. Kim, J. W. Jung, Y. J. Lee, and J. H. Kim. Liquid crystal alignment with a molecular template of imprinted polymer layer during phase separation. *Applied Physics Letters*, 88(11), 2006.

[112] A. Parfenov, N. Tamaoki, and S. Ohni-Shi. Photoinduced alignment of nematic liquid crystal on the polymer surface microrelief. *Molecular Crystals and Liquid Crystals*, 359:487–495, 2001.

[113] G. J. Lee, J. J. Lee, J. S. Kim, U. J. Hwang, C. H. Oh, B. Park, Y. P. Lee, and S. H. Paek. Liquid crystal alignment by holographic surface relief grating inscribed on azo-polymer film. *Molecular Crystals and Liquid Crystals*, 424:75, 2004.

[114] H. Fujikake, M. Kuboki, T. Murashige, H. Sato, H. Kikuchi, and T. Kurita. Alignment mechanism of liquid crystal in a stretched porous polymer film. *Journal of Applied Physics*, 94(5):2864–2867, 2003.

[115] T. Murashige, H. Fujikake, H. Sato, H. Kikuchi, T. Kurita, and F. Sato. Liquid crystal alignment control using polymer filament and polymer layers coated on substrates. *Japanese Journal of Applied Physics Part 1-Regular Papers Brief Communications & Review Papers*, 44(4A):1862–1866, 2005.

[116] JL West, GQ Zhang, A Glushchenko, and Y Reznikov. Fast birefringent mode stressed liquid crystal. *Applied Physics Letters*, 86(3), 2005.

[117] J. L. West, K. Zhang, M. Zhang, E. Buyuanir, and A. Glushchenko. Stressed liquid crystals and their application. *Proceedings of SPIE*, 5936:1 – 10, 2005.

[118] B Wang, G. Q. Zhang, A. Glushchenko, J. L. West, P. J. Bos, and P. F. McManamon. Stressed liquid-crystal optical phased array for fast tip-tilt wavefront correction. *Applied Optics*, 44(36):7754–7759, 2005.

[119] G. Zhang, A. Glushchenko, J. L. West, I. Smalyukh, and O. Lavrentovich. A model of stressed liquid crystals: Close-packed, shaped liquid crystal droplets inside a sheared polymer matrix. *Proceedings of SPIE*, 5936:1 – 9, 2005.

[120] S. W. Ke, T. H. Lin, and A. Y. G. Fuh. Tunable grating based on stressed liquid crystal. *Optics Express*, 16(3):2062–2067, 2008.

[121] O. A. Aphonin, Y. V. Panina, A. B. Pravdin, and D. A. Yakovlev. Optical propertied of stretched polymer dispersed liquid crystal films. *Liquid Crystals*, 15(3):395–407, 1993.

[122] B. G. Wu, J. H. Erdmann, and J. W. Doane. Response-times and Voltage for PDLC Light Shutters. *Liquid Crystals*, 5(5):1453–1465, 1989.

[123] M.B. Pugh, editor. *Stedman's Medical Dictionary*. Lippincott, Williams and Wilkins, Baltimore, MD, 27th edition, 2000.

[124] World Health Organization. *Nutritional Anaemias: report of a WHO scientific Group*, Geneva, Switzerland, 1968.

[125] R.F. Weed, editor. *Hematology for Internists*. Little, Brown and Company, Boston, MA, 1st edition, 1971.

[126] A.H. Schmaier and L.M. Petruzzelli. *Hematology for the Medical Student*. Lippincott, Williams and Wilkins, Baltimore, MD, 1st edition, 2003.

[127] G.C. DeGruchy. *Clinical Haematology*. Blackwell Scientific Publications, Oxford, England, 2nd edition, 1964.

[128] J. M. Guralnik, W. B. Ershler, S. L. Schrier, and V. J. Picozzi. Anemia in the elderly: a public health crisis in hematology. *Hematology: American Society of Hematology Education Program*, 1:528–532, 2005.

[129] R. J. Stoltzfus. Defining iron-deficiency anemia in public health terms: A time for reflection. *Journal Of Nutrition*, 131(2):565S–567S, 2001.

[130] E.M. Couthino and S.J. Segal. *Is menstruation obsolete*. Oxford University Press, New York, NY, 1999.

[131] International Food Policy Research Institute. Iron deficiency in developing countries. *IFPRI Online http://www.ifpri.org/*, 2005.

[132] J. L. Abramson, C. T. Jurkovitz, V. Vaccarino, W. S. Weintraub, and W. McClellan. Chronic kidney disease, anemia, and incident stroke in a middle-aged, community-based population: The aric study. *Kidney International*, 64(2):610–615, 2003.

[133] G. Weiss. Pathogenesis and treatment of anaemia of chronic disease. *Blood Reviews*, 16(2):87–96, 2002.

[134] J.H. Brock, J.W. Halliday, Pippard M.J., and Powell L.W., editors. *Iron Metabolism in Health and Disease*. WB Saunders Company Ltd, London, England, 1994.

[135] A. N. Baer, E. N. Dessypris, S. B. Krantz, and E. Goldwasser. Blunted erythropoietin response to anemia in rheumatoid-arthritis. *Clinical Research*, 34(2):A450–A450, 1986.

[136] Virginia Minnich. Acute myelomonocytic leukemia, monocytic leukemia, and erythtoleukemia. *Marist College Online Seminars http://www.academic.marist.edu*, 1982.

[137] K. I. Yamakoshi, H. Shimazu, T. Togawa, M. Fukuoka, and H. Ito. Non-invasive measurement of hematocrit by electrical admittance plethysmography technique. *Ieee Transactions On Biomedical Engineering*, 27(3):156–161, 1980.

[138] K. I. Yamakoshi, K. S. Tanaka, and H. Shimazu. Electrical admittance cuff for noninvasive and simultaneous measurement of hematocrit, arterial pressure and elasticity using volume oscillometric method. *Medicine, Biology, Computing and Engineering*, 32:S99–S107, 1984.

[139] M. J. Rice, R. H. Sweat, Jr., J. M. Rioux, W. T. Williams, and W. Routt. Non-invasive measurement of blood components using retinal imaging, 2002.

[140] H. Kanashima, T. Yamane, T. Takubo, T. Kamitani, and M. Hino. Evaluation of noninvasive hemoglobin monitoring for hematological disorders. *Journal Of Clinical Laboratory Analysis*, 19(1):1–5, 2005.

[141] Y. Kinoshita, T. Yamane, T. Takubo, H. Kanashima, T. Kamitani, N. Tatsumi, and M. Hino. Measurement of hemoglobin concentrations using the astrim (tm) noninvasive blood vessel monitoring apparatus. *Acta Haematologica*, 108(2):109–110, 2002.

[142] R. G. Nadeau and W. Groner. The role of a new noninvasive imaging technology in the diagnosis of anemia. *Journal Of Nutrition*, 131(5):1610S–1614S, 2001.

[143] T. K. Aldrich, M. Moosikasuwan, S. D. Shah, and K. S. Deshpande. Length-normalized pulse photoplethysmography: A noninvasive method to measure blood hemoglobin. *Annals Of Biomedical Engineering*, 30(10):1291–1298, 2002.

[144] K. J. Jeon, S. J. Kim, K. K. Park, J. W. Kim, and G. Yoon. Noninvasive total hemoglobin measurement. *Journal Of Biomedical Optics*, 7(1):45–50, 2002.

[145] M. Rendell, E. Anderson, W. Schlueter, J. Mailliard, D. Honigs, and R. Rosenthal. Determination of hemoglobin levels in the finger using near infrared spectroscopy. *Clinical And Laboratory Haematology*, 25(2):93–97, 2003.

[146] D. Geva, B. Z. Sklar, E. Menashkin, and I. Fine. New approach in non-invasive measurement of hb/hct/sp0(2). *Anesthesiology*, 93(3A):U154–U154, 2000.

[147] L. D. Shvartsman and I. Fine. Optical transmission of blood: Effect of erythrocyte aggregation. *Ieee Transactions On Biomedical Engineering*, 50(8):1026–1033, 2003.

[148] I. Fine, D. Geva, O. Amir, and E. Monashkin. Clinical evaluation of non-invasive hemoglobin (hb) testing device. *American Society of Anesthesiologists Annual Meeting*, 1:A597, 2004.

[149] G. Zonios, J. Bykowski, and N. Kollias. Skin melanin, hemoglobin, and light scattering properties can be quantitatively assessed in vivo using diffuse reflectance spectroscopy. *Journal Of Investigative Dermatology*, 117(6):1452–1457, 2001.

[150] X. M. Wu, S. Yeh, T. W. Jeng, and O. S. Khalil. Noninvasive determination of hemoglobin and hematocrit using a temperature-controlled localized reflectance tissue photometer. *Analytical Biochemistry*, 287(2):284–293, 2000.

[151] E. Haak, T. Haak, P. Grozinger, G. Krebs, K. H. Usadel, and K. Kusterer. The impact of contralateral cooling on skin capillary blood cell velocity in patients with diabetes mellitus. *Journal Of Vascular Research*, 35(4):245–249, 1998.

[152] S. B. Zhang, B. R. Soller, S. Kaur, K. Perras, and T. J. Vander Salm. Investigation of noninvasive in vivo blood hematocrit measurement using nir reflectance spectroscopy and partial least-squares regression. *Applied Spectroscopy*, 54(2):294–299, 2000.

[153] D. M. Haaland and E. V. Thomas. Partial least-squares methods for spectral analyses. 1.relation to other quantitative calibration methods and the extraction of qualitative information. *Analytical Chemistry*, 60(11):1193–1202, 1988.

[154] D. M. Haaland and E. V. Thomas. Partial least-squares methods for spectral analyses. 2. application to simulated and glass spectral data. *Analytical Chemistry*, 60(11):1202–1208, 1988.

[155] I. Y. Petrova, R. O. Esenaliev, Y. Y. Petrov, H. P. E. Brecht, C. H. Svensen, J. Olsson, D. J. Deyo, and D. S. Prough. Optoacoustic monitoring of blood hemoglobin concentration: a pilot clinical study. *Optics Letters*, 30(13):1677–1679, 2005.

[156] R. O. Esenaliev, Y. Y. Petrov, O. Hartrumpf, D. J. Deyo, and D. S. Prough. Continuous, noninvasive monitoring of total hemoglobin concentration by an optoacoustic technique. *Applied Optics*, 43(17):3401–3407, 2004.

[157] D.S. Prough, Y. E. Petrov, M. H. Klasing, M. Motamedi, and R. Esenaliev. Continuous noninvasive optoacoustic monitoring of hemoglobin concentration: in vitro validation. *Anesthesiology*, 95:A155, 2001.

[158] T. N. Sheth, N. K. Choudhry, M. Bowes, and A. S. Detsky. The relation of conjunctival pallor to the presence of anemia. *Journal Of General Internal Medicine*, 12(2):102–106, 1997.

[159] A. R. Kent, S. H. Elsing, and R. L. Hebert. Conjunctival vasculature in the assessment of anemia. *Ophthalmology*, 107(2):274–277, 2000.

[160] R. S. Strobach, S. K. Anderson, D. C. Doll, and S. Ringenberg. The value of the physical examination in the diagnosis of anemia. *Arch Intern Med*, 148:831–832, 1988.

[161] R. J. Stoltzfus, A. Edward-Raj, M. L. Dreyfuss, M. Albonico, A. Montresor, M. D. Thapa, K. P. West, H. M. Chwaya, L. Savioli, and J. Tielsch. Clinical pallor is useful to detect severe anemia in populations where anemia is prevalent and severe. *Journal Of Nutrition*, 129(9):1675–1681, 1999.

[162] IUPUI Dept. of Anatomy. Basic histology of the eye. *Histology D502 Online Course Notes http://anatomy.iupui.edu*, 2004.

[163] O. L. Hung, N. S. Kwon, A. E. Cole, G. R. Dacpano, T. Wu, W. K. Chiang, and L. R. Goldfrank. Evaluation of the physician's ability to recognize the presence or absence of anemia, fever, and jaundice. *Academic Emergency Medicine*, 7(2):146–156, 2000.

[164] C. I. Sanchez-Carillo. Bias due to conjunctiva hue and the clinical assessment of anemia. *Journal of Clinical Epidemiology*, 42(8):751–754, 1989.

[165] C. I. Sanchez-Carillo, T. J. Ramirez-Sanchez, M. Zambrana-Castaneda, and B.J. Selwyn. Test of a noninvasive instrument for measuring hemoglobin. *International Journal of Technological Assessment in Heath Care*, 5(4):659–667, 1989.

[166] N. I. Shapiro, M. Stumpf, N. Chiota, M. Resciniti, J. Nicolet, and J. Ufberg. A standardized conjunctiva pallor tool predicts anemia. *Academic Emergency Medicine*, 11(5):478, 2004.

[167] M. Chowdhury, V. Chongsuvivatwong, A. F. Geater, H. H. Akhter, and T. Winn. Taking a medical history and using a colour scale during clinical examination of pallor improves detection of anaemia. *Tropical Medicine and International Health*, 7(2):133–139, 2002.

[168] A. Montresor, M. Albonico, N. Khalfan, R. J. Stoltzfus, J. M. Tielsch, H. M. Chwaya, and L. Savioli. Field trial of a haemoglobin colour scale: an effective tool to detect anaemia in preschool children. *Tropical Medicine and International Health*, 5(2):129–133, 2000.

[169] T. Getaneh, T. Girma, T. Belachew, and S. Teklemariam. The utility of pallor detecting anemia in under five years old children. *Ethiopian Medical Journal*, 38(2):77–84, 2000.

[170] S. P. Luby, P. N. Kazembe, S. C. Redd, C. Ziba, O. C. Nwanyanwu, A. W. Hightower, C. Franco, L. Chitsulo, and J. J. Wirima. Using clinical signs to diagnose anemia in african children. *Bulletin Of The World Health Organization*, 73(4):477–482, 1995.

[171] M. W. Weber, S. D. Kellingray, A. Palmer, S. Jaffar, E. K. Mulholland, and B. M. Greenwood. Pallor as a clinical sign of severe anaemia in children: an investigation in the gambia. *Bulletin Of The World Health Organization*, 75:113–118, 1997. Suppl. 1.

[172] F. K. Wurapa, M. K. Bulsara, and B. A. Boatin. Evaluation of conjunctival pallor in the diagnosis of anemia. *Journal Of Tropical Medicine And Hygiene*, 89(1):33–36, 1986.

[173] H. D. Kalter, G. Burnham, P. R. Kolstad, M. Hossain, J. A. Schillinger, N. Z. Khan, S. Saha, V. de Wit, N. Kenya-Mugisha, B. Schwartz, and R. E. Black. Evaluation of clinical signs to diagnose anaemia in uganda and bangladesh, in areas with and without malaria. *Bulletin Of The World Health Organization*, 75:103–111, 1997.

[174] K. Ernsting, S. Suner, and G. D. Jay. Use of digital imaging of conjunctiva to predict hemoglobin concentration. *Academic Emergency Medicine*, 8(6):528–529, 2001.

[175] S. Suner, G. P. Crawford, J. W. McMurdy, and G. D. Jay. Non-invasive determination of hemoglobin by digital photography of palpebral conjunctiva. *Journal of Emergency Medicine*, 33(2):105–111, 2007.

[176] S. Jacques. *Tissue Optics*. International Society for Optical Engineering, 2007.

[177] R. X. Liu, J. Kuang, Q. Gong, and X. L. Hou. Principal component regression analysis with spss. *COMPUTER METHODS AND PROGRAMS IN BIOMEDICINE*, 71(2):141–147, Jun 2003.

[178] A. J. Berger, T. W. Koo, I. Itzkan, and M. S. Feld. An enhanced algorithm for linear multivariate calibration. *ANALYTICAL CHEMISTRY*, 70(3):623–627, Feb 1998.

[179] S. S. Charschan and B. A. Rockwell. Update on ansi z136.1. *Journal Of Laser Applications*, 11(6):243–247, 1999.

[180] J.M. Bland and D.G. Altman. Statistical methods for assessing agreement between two methods of clinical measurement. *Lancet*, 1(8476):307–310, 1986.

[181] M. E. De Paepe, S. Burke, F. I. Luks, H. Pinar, and D. B. Singer. Demonstration of placental vascular anatomy in monochorionic twin gestations. *Pediatr Dev Pathol*, 5(1):37–44, 2002.

[182] S. R. Carr and M. P. Plevyak. Contemporary evaluation and management of twin-twin transfusion syndrome. *Medicine & Health Rhode Island*, 84(5):165–8, 2001.

[183] T. M. Crombleholme. The treatment of twin-twin transfusion syndrome. *Semin Pediatr Surg*, 12(3):175–81, 2003.

[184] E. Lopriore, H. T. Nagel, F. P. Vandenbussche, and F. J. Walther. Long-term neurodevelopmental outcome in twin-to-twin transfusion syndrome. *Am J Obstet Gynecol*, 189(5):1314–9, 2003.

[185] J. E. Dickinson, G. J. Duncombe, S. F. Evans, N. P. French, and R. Hagan. The long term neurologic outcome of children from pregnancies complicated by twin-to-twin transfusion syndrome. *Bjog*, 112(1):63–8, 2005.

[186] M. V. Senat, J. Deprest, M. Boulvain, A. Paupe, N. Winer, and Y. Ville. Endoscopic laser surgery versus serial amnioreduction for severe twin-to-twin transfusion syndrome. *N Engl J Med*, 351(2):136–44, 2004.

[187] K. Hecher, W. Diehl, L. Zikulnig, M. Vetter, and B. J. Hackeloer. Endoscopic laser coagulation of placental anastomoses in 200 pregnancies with severe mid-trimester twin-to-twin transfusion syndrome. *Eur J Obstet Gynecol Reprod Biol*, 92(1):135–9, 2000.

[188] A. Umur, M. J. van Gemert, P. G. Nikkels, and M. G. Ross. Monochorionic twins and twin-twin transfusion syndrome: the protective role of arterio-arterial anastomoses. *Placenta*, 23(2-3):201–9, 2002.

[189] G.P. van Nieuw Amerongen, C.M.L. Beckers, I.D. Achekar, S. Zeeman, R.J.P. Musters, and V.W.M. van Hinsbergh. Involvement of rho kinase in endothelial barrier maintenance. *Arteriosclerosis, Thrombosis and Vascular Biology*, 27(11):2332–2339, 2007.

[190] S. M. Weis and D. A. Cheresh. Pathophysiological consequences of vegf-induced vascular permeability. *Nature*, 487:497–505, 2005.

[191] J. Doukas, W. Wrasidlo, G. Noronha, E. Dneprovskaia, R. Fine, S. Weis, A. Hood, A. DeMaria, R. Soll, and D. A. Cheresh. Phosphoinositide 3-kinase / inhibition limits infarct size

after myocardial ischemia/reperfusion injury. *Proceedings of the National Academy of Science*, 103:19866–19871, 2006.

[192] N Gautam, AM Olofsson, H GHerwald, LF Iversen, E Lundgren-Akerlund, P Hedqvist, KE Arfors, H. Flodgaard, and L Lindbom. Heparin binding protein (hbp/cap37): A missing link in neutrophil-evoked alteration of vascular permeability. *Nature*, 7(10):1124–1129, 2001.

[193] T. D. Lee, M. L. Gonzales, P. Kumar, P. Grammas, and H. A. Pereira. Cap37, a neutrophil-derived imflammatory mediator, augments leukocyte adhesion to endothelial monolayers. *Microvascular Research*, 66:38–48, 2003.